A Thermodynamic Model for Noble Metal Alloy Inclusions in Nuclear Fuel Rods and Application to the Study of Loss-of-Coolant Accidents

by

MATTHEW HAIGH KAYE

A thesis submitted to

the Department of Materials and Metallurgical Engineering

in conformity with the requirements for

the degree of Doctor of Philosophy

Queen's University

Kingston, Ontario

September, 2001

Abstract

Metal alloy inclusions comprised of Mo, Pd, Rh, Ru, and Tc (the so-called "noble" metals) develop in CANDU fuel pellets as a result of fission. The thermochemical behaviour of this alloy system during severe accident conditions is of interest in connection with computations of loss of volatile compounds of these elements by reaction with steam-hydrogen gas mixtures that develop in the system as a result of water reacting with the Zircalloy cladding.

This treatment focuses on the development of thermodynamic models for the Mo-Pd-Rh-Ru-Tc quinary system. A reasonable prediction was made by modelling the ten binary phase diagrams, five of these evaluations being original to this work. This process provides a complete treatment for the five solution phases (vapour, liquid, bcc-solid, fcc-solid, and cph-solid) in this alloy system, as well as self-consistent Gibbs energies of formation for the Mo_5Ru_3 intermetallic phase, and two intermediate phases in the Mo-Tc system. The resulting collection of properties, when treated by Gibbs energy minimization, permits phase equilibria to be computed for specified temperatures and compositions.

Experimental work in support of this treatment has been performed. Measurements of the solidus and liquidus temperatures for Pd-Rh alloys were made using differential thermal analysis. These measurements confirm that the liquid solution exhibits positive deviation from Raoult's law. Experimental work as a visiting research engineer at AECL (Chalk River) was performed using a custom developed Knudsen cell/mass spectrometer. The Pd partial pressure was measured above multi-component alloys of known composition over a range of temperatures. These are correlated to

predicted activities of Pd from the developed thermodynamic model in the multi-component alloy.

The thermodynamic treatment developed for the noble metal alloy inclusions has been combined with considerable other data and applied to selected loss-of-coolant-accident scenarios to demonstrate the value of the improved alloy treatment. An original method of compressing voluminous data generated by extensive calculations (as undertaken previously by the author involving an ideal alloy model) is outlined. This technique permits the output from the thermodynamic computations with the models to be incorporated within the fission product release code.

Acknowledgements

I would like to thank my supervisor Dr W.T. Thompson of the Materials and Metallurgical Department at Queen's University and the Department of Chemistry and Chemical Engineering of the Royal Military College. I also thank Dr B.J. Lewis of the Department of Chemistry and Chemical Engineering of the Royal Military College, for providing guidance on the nuclear implications of this project. Their continued interest and enthusiasm have made my doctoral studies enjoyable and rewarding.

Dr F. Iglesias formerly of Ontario Hydro has also been supportive in terms of both financial assistance and interest. He was also instrumental in providing a liaison to the laboratories of the Atomic Energy of Canada Limited.

At AECL, Dr R. McEachern and later Dr S. Sunder provided me with the opportunity to direct experimental research that was of mutual interest. Together with their supporting technicians, Mr J. LeBlanc and Mr B. O'Connor, they treated me with kindness and gracious hospitality.

The support staff at Queen's University has been most generous with their time. Mr C. Cooney gave of his time and insight with regards to the Differential Thermal Analyser. Mr D. Deitrich supplied excellent machining assistance, especially with the difficult material tantalum. Finally, Mrs S. Donnelly was wonderful in her assisting me with administrative matters.

I can not say enough to thank Mrs Elizabeth Ells and the late Dr Charles Ells, to whose memory this work is dedicated, for their support and generosity to me during the experimental phase of my research. Not only did they provide me with accommodation;

they took an active interest in my research that stimulated my work.

To my many friends that have entertained and supported me through my years of study, I say thank you. The many conversations and discussions that we have shared have reminded me to keep a perspective on my work.

My thanks to my family, which have sustained me through all of my degrees and supported me at every stage of my professional development. Thank you to Mark and Linda for providing the cottage- a secure bastion in which to contemplate science and a retreat as well. To Rosie and Hamlet Katz for reminding me that there is magic in everyday. I owe a huge debt of gratitude to my parents for their unwavering confidence, support, patience, and interest; this is for them as much as it is a personal achievement.

Last on my list, but always first in my thoughts, my undying thanks to my wife Christina. As one chapter of life ends, the pages of the next beckon. This past year has been a whirlwind of wonderful experiences that promise many, many more, and the fact that we will face them together fills me with the greatest joy. Without you this simply would not be. *Nagyon szépen köszönöm.*

This work is dedicated to the memory of the late Dr Charles Edward Ells

He was a brilliant metallurgist, and mentor.

More importantly to me- he was my friend.

"The release of atomic energy has not created a new problem. It has merely made more urgent the necessity of solving an existing one." *--Albert Einstein (1879-1955)*

"The discovery of nuclear chain reactions need not bring about the destruction of mankind any more than did the discovery of matches. We only must do everything in our power to safeguard against its abuse." *--Albert Einstein (1879-1955)*

Table of Contents

Table of Figures

List of Tables

List of Symbols and Acronyms

a, c	Lattice parameters (nm).
a_i	Activity of species i.
α	Solid face centred cubic (cF4) phase.
α_{Total}	Coefficient of reactivity.
α_T	Temperature coefficient.
α_{Void}	Void coefficient.
α_{Others}	Other minor coefficients that contribute to α_{Total}.
A_0, B_0, A_1, B_1	Constants in the linear representation for p_0, p_1, *etc.*.
A_α-A_ε	Ends of a tie line between α and ε phases.
AECB	Atomic Energy Control Board
AECL	Atomic Energy of Canada Limited
ASM	American Society for Metals
ASTM	American Society for Testing and Materials
b, m	Intercept and slope in the linear relationship $y = mx + b$.
bcc	Body centred cubic
β	Solid body centred cubic (cI2) phase.
BAPD	Binary Alloy Phase Diagrams
BWR	Boiling-Water Reactor
$c^\bullet$	A constant.
C_P	Heat capacity (J/mol·K).
CANDU	Canadian Deuterium Uranium
CNSC	Canadian Nuclear Safety Commission
cph	Close packed hexagonal
DTA	Differential Thermal Analysis
emf	Electromotive force
EPMA	Electronprobe microanalysis
ε	Solid close packed hexagonal (hP2) phase.
f	Orifice correction factor.
fcc	face centred cubic
FACT	Facility for the Analysis of Chemical Thermodynamics
FORM	Fuel Oxidation and Release Model
ΔG_M	Gibbs Energy of melting (J/mol).
ΔG_A^M	Gibbs Energy of mixing for phase A (J/mol).
$\Delta \overline{G}_A^E$	Relative partial excess Gibbs Energy for component A (J/mol).
$\overline{G}_A^{E\,fcc}$	Partial excess Gibbs Energy for component A in the fcc-phase (J/mol).

$\overline{G}_A^{E\,cph}$	Partial excess Gibbs Energy for component A in the cph-phase (J/mol).
ΔG_i^E	Excess Gibbs Energy for phase *i* (J/mol).
$\Delta G_A^{\circ\,fcc}$	Lattice stability of element A in the fcc-crystal structure (J/mol).
$\Delta G_A^{\circ\,cph}$	Lattice stability of element A in the cph-crystal structure (J/mol).
γ_A	Activity coefficient of component *A*.
γ_i	Number of atoms per molecule of *i*.
γ_{x_i}	Mass sensitivity correction factor for isotope *x* of species *i*.
GCFBR	Gas-Cooled Fast Breeder Reactor
h_i	Enthalpy contribution in i^{th} term of an excess Gibbs Energy series (J/mol).
ΔH_{298}°	Standard enthalpy of formation at 298K (J/mol).
ΔH_A°	Standard enthalpy of A (J/mol).
ΔH_M	Enthalpy of melting (J/mol).
HTR	High Temperature Reactor
I_{x_i}	Intensity of isotope *x* for species *i* (counts).
IMCP	Improved Method of Chemical Potentials
k	Multiplication factor related to the number of neutrons born in one generation as a result of each neutron absorbed from the previous generation; when k = 1, it implies a steady state condition.
k_i	Mass transport coefficient for species, or fission product, *i*.
k_{Std}	Instrument constant for mass spectrometer based on a standard substance.
k_{Ag}	Instrument constant for the mass spectrometer based on silver.
K_{eq}	Equilibrium constant.
κ	A simple cubic (cP8) solid; in this work it refers to Mo_9Tc_{11}.
LMFBR	Liquid-Metal Fast Breeder Reactor
LOCA	Loss-of-Coolant Accident
LWGR	Light Water Graphite Reactor
Magnox	Magnesium Oxide (Reactor)
${}_0^1n$	A neutron.
n_{x_i}	Isotopic abundance of isotope *x* for species *i*.
N_A	Avagadro's Constant (6.022×10^{23} mol^{-1}).
ORIGEN	Oak Ridge Isotope Generation code; ORIGEN2 is the second version.
p_i	Partial pressure of species *i* (atm).
p_{tot}	Total system pressure (atm).
p_0, p_1, p_2, p_3	Constants in the recursion formula for $\overline{G}^E$.
PWR	Pressurized-Water Reactor

R	Molar gas constant (8.314 J/mol·K).
R_i	Rate of mass transport of a particular species, i.
RBMK	Reaktory Bolshoi Moshchnosti Kanalynye (a Russian LWGR)
ρ	Departure of a system from criticality; also termed reactivity of a system.
s	Daily correction factor for Knudsen Cell/mass spectrometer.
s_i	Entropy contribution in i^{th} term of excess Gibbs Energy series (J/mol·K).
S	Exposed surface area of a fuel rod (m^2).
S°_{298}	Standard entropy at 298K (J/mol·K).
S°_A	Standard entropy of A (J/mol·K).
ΔS_M	Entropy of melting (J/mol·K).
σ	Solid tetragonal phase.
σ_i	Ionization cross-section of i (cm^2) measured at a specific eV.
T	Temperature; unless otherwise stated, temperature is measured in Kelvin.
T_c	Critical temperature.
T_M	Melting temperature.
T_{Onset}	Onset temperature.
$T_{Peak\ Min}$	Temperature at which DTA detection peak reaches its minimum value.
T_V	Vaporization temperature.
${}^{n}_{z}U$	Isotope of Uranium where n represents the atomic mass unit and z the number of protons (the atomic number). For example, ${}^{235}_{92}U$ is the radioactive isotope of Uranium with an atomic mass of 235 amu. The nucleus contains 92 protons (along with 143 neutrons). An m after the atomic mass unit number indicates that the isotope is radioactively metastable, e.g., ${}^{99m}_{43}Tc$.
x	Void fraction.
X_i	Mole fraction of species i.
X°_i	Initial concentration (mole fraction) of species i.
XMA	X-ray microanalysis

1. Introduction

1.1 Background

The Canadian Nuclear Safety Commission (CNSC), formerly the Atomic Energy Control Board (AECB), has developed guidelines that regulate the design and operation of all CANDU* reactors in Canada. One of the principal areas of concern for the CNSC is safety, a relatively broad topic that includes design of systems to ensure reliability, redundancy, testability, and independence. In assessing safety, the main objective is to minimize risk- the product of probability and consequence.

Operational "abnormal" events may be classified in three categories: those of moderate frequency; those of low probability; and those of very low probability. Events of moderate frequency may arise from operational practice but have minimal consequence and thus low risk. The events of low probability generally result from mechanical failure or human error, but because of the design criteria only result in small, if any, radioactive releases outside of the plant. Once again the risk is low. Finally, there are the events of very low probability, which have potentially serious consequences (e.g., flooding, severe accidents, earthquakes, spent-fuel handling accidents, and loss-of-coolant accidents). It is this final class of accidents that is important in reactor safety analysis, and for the purpose of this work the principal concern is loss-of-coolant accidents (LOCA), which are considered as design basis accidents.

Before a discussion of loss-of-coolant accidents can be initiated, it is necessary to review some of the principles behind reactors and reactor safety and the implications

---

* CANadian Deuterium Uranium, a registered trademark of Atomic Energy of Canada Limited.

these principles have on reactor design, since some of the design features have important ramifications as to the nature of the LOCA.

Nuclear reactors generate heat as a result of nuclear fission within the fuel, which is generally composed of pellets of UO_2. Exceptions are UC_2 which is used in High Temperature Reactors (HTR), $^{239}PuO_2$ in depleted UO_2 in liquid-metal or gas-cooled fast breeder reactors (LMFBR and GCFBR), and U metal in the Magnox reactor (Mg/Al alloy used to clad fuel with graphite moderator). Where uranium is the principal component of the fuel, the only useful naturally fissile isotope of uranium is $^{235}_{92}U$, which has an isotopic abundance of 0.72%. Atoms of $^{235}_{92}U$ decay by a fission reaction, **(1.1)**:

$$^{235}_{92}U + {}^{1}_{0}n \rightarrow 2\,fragments + x\left({}^{1}_{0}n\right) + heat \qquad \textbf{(1.1)}$$

where n represents a neutron, and x can have a value of 2 or 3[1].

The neutrons produced in **(1.1)** are considered to be "fast" neutrons since they have energies of approximately 190×10^6 kJ/mol, and these neutrons are inefficient at sustaining the fission reaction, especially when compared to "slow" or "thermal" neutrons that have energies of approximately 2.4 kJ/mol. Thus, two options present themselves in terms of developing and maintaining a chain reaction:

1. Increase the fraction of $^{235}_{92}U$ in the fuel (i.e., fuel enrichment);
2. Slow down the "fast" neutrons (i.e., moderate the fuel), to promote the chain reaction.

The American and French (and others) have developed pressurized-water reactors (PWR) and boiling-water reactors (BWR) which operate with enriched UO_2 fuel, (i.e., fuel with 2-3% $^{235}_{92}U$). These reactors do not need a specialized moderator, so natural (light) water can be used.

The Canadian experience exploits the principles embodied in option 2. The CANDU reactor was developed to use natural uranium with 0.72% $^{235}_{92}U$. However, a special moderator is required and D_2O (so called heavy water*) is used for this purpose. The use of D_2O as a moderator highlights another difference between the CANDU reactor and the PWR and BWR, which use H_2O as their moderator. In the CANDU, heavy water passes over the fuel, absorbs energy and is heated to a temperature near 310°C. This heavy water is under pressure and is pumped to a steam generator where the heat is extracted by boiling natural water in a separate system. The steam created here, drives the turbines, producing electricity and then is recycled back to the steam generator. The heavy water from the steam generator also recycles back to the reactor.

Pressurized-water and boiling-water reactors use natural water as the moderator. For BWRs the water that collects the heat in the reactor core is also the water that is converted to steam to drive the turbines. This water is recycled back to the reactor. In PWRs the steam generators are in a separate heat transfer loop.

A second consequence of reaction **(1.1)** is that two fragments are created in place of the atom of $^{235}_{92}U$. These fragments are termed fission products and their inventory increases in a predictable manner over the service lifetime of the fuel. The ORIGEN2 code[2] has been developed to determine the concentrations of the fission products at various stages of fuel burn up under different operating conditions.

Therefore, there are three consequences of the radioactive decay of $^{235}_{92}U$: the

---

* Deuterium (D) is an isotope of hydrogen. It has a nucleus of 1 neutron and 1 proton, unlike hydrogen that has only a single proton as its nucleus. Deuterium has a natural abundance of 0.0156%[1].

generation of heat, which ultimately boils water to provide electrical energy; more neutrons, that are used to sustain the chain reaction and promote decay of more $^{235}_{92}U$, and an increasing inventory of fission products that stay trapped in the remaining fuel.

1.1.1 Loss-of-Coolant-Accidents

A schematic diagram of a typical CANDU reactor system[3] is shown in Figure 1-1. The worst potential rupture in the water system is postulated to occur at the inlet header (indicated on Figure 1-1). A break in the system at this point would prevent water coolant from reaching the core, and the remaining coolant would be pulled from the reactor by the outlet header or flow back and out the inlet header. The end result is that the core would no longer be cooled and an accident would have commenced.

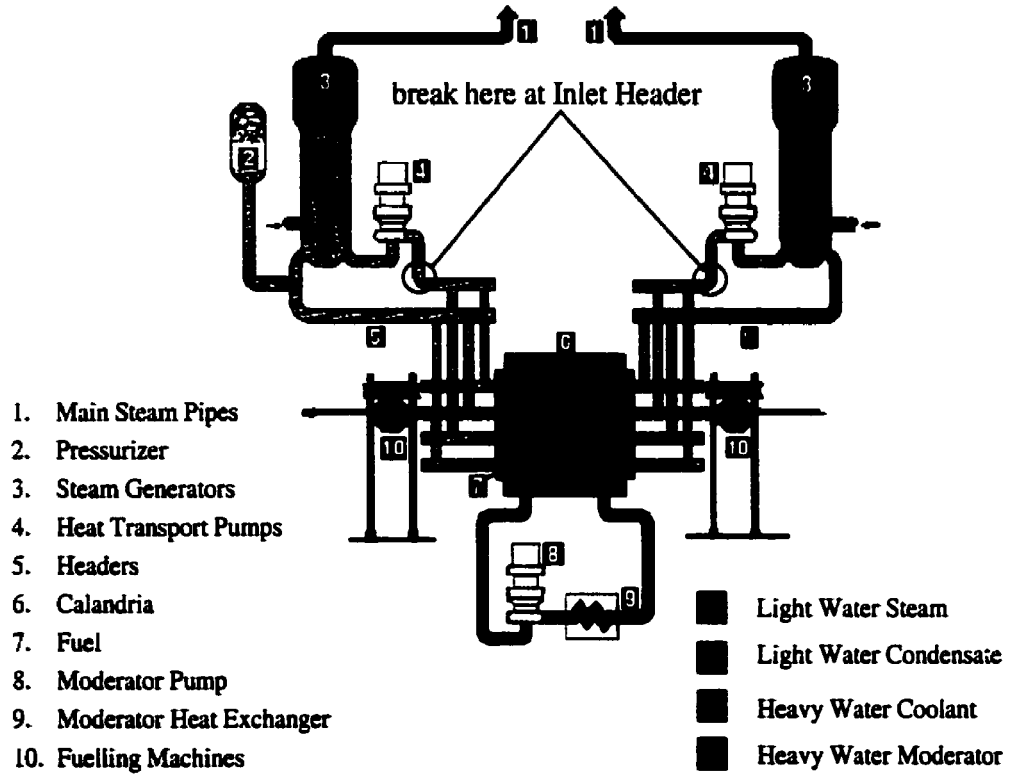

Figure 1-1. The CANDU reactor system[3], showing the postulated break in the reactor inlet header, which leads to the beginning of a LOCA.

Once an accident has begun, the temperature of the fuel rises, since it is no longer being cooled. One possible scenario is that as the temperature of the fuel rapidly increases, water is once again introduced into the system. This water, as it comes into contact with the hot fuel, can rapidly vaporize and in the process provide a vehicle for transporting chemical species from the fuel. The steam also interacts exothermically with the Zircalloy cladding to yield hydrogen, a reaction that will determine the type of atmosphere (i.e., reducing or less oxidizing) which will further affect interactions with the fuel.

As the temperature in the fuel increases, fission products within the fuel may be removed from the surface layers of the fuel, because the temperature provides a second driving force for diffusion of chemical species within the fuel from the central region (high concentration) to the perimeter region (lower concentration).

A further complication arises due to the nature of the reactivity within the reactor/fuel system. From reaction **(1.1)**, it was seen that one neutron is required to initiate the radioactive decay of $^{235}_{92}U$, but in the process 2 to 3 neutrons (on average) are released. The multiplication factor, k, is related to the number of neutrons born in one generation, as a result of each neutron in the previous generation being absorbed. Thus, when $k = 1$, every neutron absorbed in previous generation results in one new neutron in the next generation. In terms of neutrons, this represents a steady state condition, and the reactor is said to have gone critical.

The fractional departure of a system from criticality, or the reactivity of a system, is defined by equation **(1.2)**, where k is defined above[4,5]:

$$\rho = \frac{(k-1)}{k} \tag{1.2}$$

From equation **(1.2)**, if $k > 1$, then $\rho > 0$, and the system displays positive reactivity, while if $k < 1$, then $\rho < 0$, negative reactivity results. Note that while ρ may be both positive or negative, k is always positive.

The coefficient of reactivity, α_{Total}, is defined by equation **(1.3)**.

$$\alpha_{Total} = \alpha_T + \alpha_V + \alpha_{others} \tag{1.3}$$

where $\alpha_T = \frac{d\rho}{dT}$, the temperature coefficient; $\alpha_V = \frac{d\rho}{dx}$, the void coefficient, x represents the void fraction; and α_{others} represents other minor coefficients (e.g., the moderator coefficient[4]) that would be considered in a thorough analysis.

Differentiating equation **(1.2)** with respect to temperature gives,

$$\alpha_T = \frac{d\rho}{dT} = \frac{1}{k^2}\frac{dk}{dT} \tag{1.4}$$

and since $k \approx 1$, $k^2 \approx k$, therefore, the following is reasonably valid:

$$\alpha_T \approx \frac{1}{k}\frac{dk}{dT} \tag{1.5}$$

The implications of equations **(1.2)**, **(1.3)**, and **(1.5)** on the operation of a reactor are important in a potential accident scenario. Consider the implications to a reactor if either α_T or α_V were the only governing constraint. During normal or stable operation the temperature in the reactor and the power generated are expected to be nearly constant. If α_T were positive, and the temperature in the reactor increased slightly, since $\frac{dk}{dT} > 0$, k would increase and this would increase the reactivity, ρ, in the reactor, which in turn would increase the power generated. If more power were generated, a further

temperature increase would be caused and this escalating cycle would continue until either the core melted or outside intervention occurred. On the other hand, if the temperature in the reactor initially decreased slightly, a downward cycle would occur and the reactor would shutdown. In either case, a positive α_T term is inherently unstable.

The situation is much improved if α_T is negative. In this case, an increase in the temperature results in a decrease in k, and the power generated drops. This provides a self-correcting mechanism and the reactor returns to its original state. The same is true for a decrease in temperature. Commercially operated power reactors must have a temperature coefficient that is negative in order to obtain an operating licence.

A similar analysis can be extended to the void coefficient, α_V. Voids develop around the fuel at places where the liquid boils. This situation arises for either a liquid moderated (CANDU) or liquid cooled (PWR) reactor. Unlike the pressurized-water reactor, in the CANDU (and Russian RBMK*) system, α_V is positive, which means that as the void fraction increases the reactivity increase, and the power generated increases, causing more liquid to boil. This in turn increases the void fraction, and the system would become unstable, if, and only if, the void coefficient were the only variable that controls α_{Total}.

Fortunately, this is not the situation. In the CANDU reactor, because α_V is positive, α_T is negative, and this counteracts the α_V term.

It is also clear from the above, that one of the potential problems with the

---

* RBMK is an acronym for "Reaktory Bolshoi Moshchnosti Kanalynye". These reactors are also termed LWGR- that is graphite moderated with boiling light water coolant.

CANDU during a LOCA derives from the positive void coefficient. As coolant exits the system as a result of a break, the amount of voids in the coolant increases, and as a result the void coefficient increases. This effect will exert a tendency to increase the reactivity of the system, and also the power generated, which if unchecked or unbalanced by the temperature coefficient would lead to a melting of the reactor core.

1.1.2 Classification of Fission Products

Prussin et al.[6] classified fission products in three distinct groups based on their significant radioactive contributions in the event of a loss-of-coolant accident, and these are:

1. Inert/Noble gases- Xe and Kr;
2. Volatiles- I, Br, Cs, Rb, Te, Se, and Sb
3. Nonvolatiles (Not-so-volatile)- Ba, Sr, **Mo**, **Tc**, **Ru**, **Rh**, **Pd**, Y, La, Ce, Pr, Nd, Pm, Sm, Eu, Np, Pu, Zr, and Nb.

These groupings of elements are marked by their degree of volatility and their chemical properties.

Kleykamp[7-9] and others[10] have provided a different and more specific classification scheme based more on the chemical state of the fission products. The four classes are:

1. Fission gases and other volatile fission products- Kr, Xe, Br and I;
2. Fission products forming metallic precipitates- **Mo**, **Tc**, **Ru**, **Rh**, **Pd**, Ag, Cd, In, Sn, Sb, and Te;
3. Fission products forming oxide precipitates- Rb, Cs, Ba, Zr, Nb, Mo, and Te;
4. Fission products dissolved as oxides in the fuel matrix: Sr, Zr, Nb, Y, La, Ce, Pr, Nd, Pm, Sm, and Eu.

It is important to realize that the classification scheme proposed by Kleykamp places some elements (e.g., Mo and Nb) in more than one category. This is due to the

fact that transitions from one group to the next are based on solubility limits of the given fission products and also to changes in the chemical potential of oxygen during fuel burn up.

1.1.3 The Role of the "Noble Metals" as Fission Products

In both classification schemes, the so-called "Noble Metals", namely Mo, Pd, Rh, Ru, and Tc have been highlighted because of their importance to this work. Prussin et al.[6] placed them in the nonvolatile group and Kleykamp[7-9,11] classified them as elements that form metallic precipitates. Both these classification schemes suggest that instead of forming chemical species that readily escape from fuel during an accident, they instead form metallic inclusions within the fuel. This behaviour suggests that in any mass transport model developed to predict fission product behaviour, special consideration would be necessary for these elements, since they would tend to act as a solution.

1.1.4 Fission Product Release Models

A schematic diagram illustrating the fission product release model is shown in Figure 1-2.

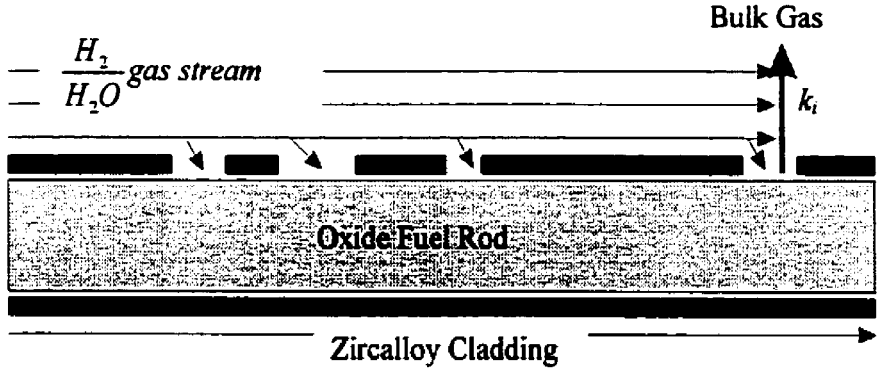

Figure 1-2. A schematic diagram of the Fission Product Release Model

During a loss-of-coolant accident, it is assumed that the flow of the coolant to the

fuel rod is interrupted, and the temperature of the rod rises. If water were to be reintroduced to the system, it would very rapidly vaporize upon coming into contact with the fuel rod, resulting in the production of steam. The subsequent interaction of this steam with the zirconium in the Zircalloy would result in the production of zirconia and hydrogen gas, as shown in reaction **(1.6)**.

$$Zr_{(solid)} + 2H_2O_{(vapour)} \xrightleftharpoons{elevated\ T} ZrO_{2(solid)} + 2H_{2(vapour)} \qquad \textbf{(1.6)}$$

As the hydrogen and steam gas mixture passes along the fuel rod, reactions occur between the gas and the elements in the fuel, and this allows fission products to be transported into the bulk gas.

The rate of mass transport of a particular species, *i*, into the bulk gas is given by equation **(1.7)**[12]:

$$R_i = S \cdot N_A \cdot \gamma_i \cdot k_i \left(X_i - X_i^\circ \right) atoms/s \qquad \textbf{(1.7)}$$

where S represents the exposed surface area of the fuel rod; N_A represents Avagadro's number; γ_i represents the number of atoms per molecule of fission product i; k_i represents the mass transport coefficient of fission product i; X_i represents the mole fraction of species i at the surface of the fuel; and X_i° represents the initial concentration of species i in the bulk gas stream (generally $X_i^\circ = 0$).

For species i at the surface of the fuel rod, the mole fraction is:

$$X_i = \frac{p_i}{p_{tot}} \qquad \textbf{(1.8)}$$

where p_i represents the partial pressure of species i, and p_{tot} represents the total system pressure.

It can be seen that this is a complex problem, which can be subdivided into three problems that occur in series. The first problem is to model the behaviour of the fuel and how the elements are transported within the fuel, subject to possible temperature and concentration gradients. The second problem is to determine the speciation of the elements in the fuel as they interact with the surrounding atmosphere and/or other elements, and the implications that this has on release of these fission products. The third problem involves the transport of the fission products in whatever chemical form away from the fuel rod and into the reactor containment system.

Of the problems outlined above, the first and third employ principles of mass transport and mass kinetics. The second problem is, in essence, a metallurgical problem, that requires an understanding of the thermodynamic properties of the species and solutions that are generated both within the fuel and at the surface of the fuel.

In previous work by this author and colleagues a preliminary analytical model was developed to describe the behaviour of low-volatile fission products under accident conditions[12]. This work brought together the kinetic and mass transport models developed to simulate the behaviour of the fission products in the fuel and as they were transported from the fuel, with calculations that established the chemical speciation predicted by thermodynamic considerations. Building on the work of Cubicciotti[13-16], this endeavour set a new standard for fission product release models.

In any model, assumptions are made in order to facilitate calculations. At the completion of the calculations, the assumptions are reviewed and areas in which the model falls short are subjected to further review and revision. For the preliminary analytical model the following assumptions were made:

1. The gas phase that forms is an ideal gas, therefore $p_i = X_{i(vapour)} p_{tot}$;
2. All metallic liquids form an ideal metallic liquid solution, if they form a solution phase at all, therefore $a_{i(in\ liquid)} = X_{i(in\ liquid)}$;
3. All solids (i.e., intermetallics, oxides, and spinels) are treated as pure separate phases; and if $a_{solid} = 1$ the solid forms, but if $a_{solid} < 1$ the solid does not form.

The first assumption is reasonable, since the system pressures that are being considered are not extreme nor justify a real gas treatment. The third assumption is reasonable for oxides and spinels. The second assumption and the simplification of treating solid metal components as mutually insoluble, was recognized as being only a first approximation to facilitate computations in the absence of data.

Once the concept had been shown to have merit, the next improvement to the model was to provide a better treatment of the metal elements, both in the liquid and solid phases. In particular, attention was placed on the noble metals, Mo-Pd-Rh-Ru-Tc, which are known to form white inclusions within nuclear fuel. It was felt that a proper thermodynamic treatment of this quinary system would provide a significant and justifiable enhancement to the fission product release model.

1.2 Objectives

The first objective of this research is to develop a complete thermodynamic model for the Mo-Pd-Rh-Ru-Tc Quinary system. **Chapter 2** introduces the reader to the five noble metals and provides a summary of thermodynamic and physical data that has been published in the literature. Since these five elements represent the components of the Mo-Pd-Rh-Ru-Tc Quinary system, it is essential that a consistent foundation be established (e.g., selecting a melting temperature for each element) before the thermodynamic model of the quinary system be constructed. The second tier of the

model, comprising models for the ten binary systems*, is presented in **Chapter 3**. The complete model for the multi-component system is assembled in **Chapter 4**.

The second objective is to validate the thermodynamic model with experimental data that is either self-generated or available in the literature. In **Chapter 4** comparison of the complete model to the limited data available in the literature is made. The experimental procedure is outlined in **Chapter 6**, using techniques explained in detail in **Chapter 5**. The experimental results are presented and discussed in **Chapter 7**. The experimental results are also compared to the model.

The final objective is to show how to incorporate the thermodynamic model into a series of fission product release calculations. **Chapter 8** details how the thermodynamic model, previously developed, is used to calculate fission product equilibrium concentrations- boundary conditions in the release model.

1.3 Original Research

Since there are five noble metals, there are ten binary systems to consider. As will be outlined in **Chapter 3**, prior investigators have thermodynamically modelled five of these systems (i.e., the systems Mo-Pd, Mo-Rh, Pd-Rh, Pd-Ru, and Rh-Ru). However, for one of these five systems, namely palladium-rhodium (Pd-Rh), experimental work at the solidus-liquidus boundary has not previously been performed.

Furthermore, in order to provide a complete thermodynamic model for systems that involve the noble metals, it was necessary to thermodynamically model the

---

* For a five component system there are $\binom{5}{2}$=10 binary, $\binom{5}{3}$=10 ternary, and $\binom{5}{4}$=5 quaternary sub-systems.

remaining five binary systems (i.e., the systems: Mo-Ru, Mo-Tc, Pd-Tc, Rh-Tc, and Ru-Tc). This original modelling is outlined in **Chapter 3**, along with all the earlier experimental work that pertains to phase equilibria in the appropriate binary systems.

Once the ten binary systems were thermodynamically modelled, an interpolation procedure with small departure terms was used to provide a five component model for the noble metals. These models are also original to this research. These models were compared to previous experimental data and to physical measurements performed as part of this work, the results of which are outlined in **Chapter 7-Experimental Results and Discussion.**

Finally, the model derived for the noble metal alloys is incorporated into the Fission Product Release Model. This incorporation of the developed thermodynamic model is also original to this research. The noble metal solution models are introduced into a Gibbs energy minimization program[17], which incorporates other data for hydrogen and oxygen containing species (nearly five hundred). The results of these computations are captured using a numerical technique developed specifically for this project. The Gibbs energy computations involving the noble metal alloy model from this research are in this way accessible to a generalized fission product release program, the Fuel Oxidation Release Model (FORM 2.0)[18].

2. The Noble Metals

2.1 Preliminary Remarks

In the past 50 years considerable research has been performed to acquire comprehensive tables of thermodynamic data. While some laboratories have closely guarded their privately developed data[19], the majority have not, and lately there has been a movement towards adopting standard values[20-24], and maintaining a strict formalism (e.g., expressing the heat capacity, C_P, as: $C_p = a + bT + cT^{-2} + dT^2$).

In order to develop a quinary model that predicts the behaviour of alloys that comprise the five elements, Mo, Pd, Rh, Ru, and Tc, it is essential that standard values, such as melting and boiling temperatures, be defined. The following chapter defines the heat capacity, ΔH°_{298}, S°_{298}, and transition temperatures for all phases (both real and hypothetical) of each element. Crystal structure, isotopic abundance, and ionization cross-section data for each element are also presented, thus providing the background data for the elements that will be used in subsequent chapters.

2.2 Thermodynamic Data for Mo, Pd, Rh, Ru, and Tc

2.2.1 Heat Capacity

Linear regression was performed on the heat capacity, C_P, data from the literature for all five elements (Mo[21], Pd[22], Rh[23,24], Ru[23,24], and Tc[22,24]) in the solid phase to obtain an expression of the form $C_p = a + bT + cT^{-2} + dT^2$, for the temperature range 298 - 3000K. The same equation was adopted for the liquid phase over the same temperature range.

Figure 2-1 shows the C_P for the condensed phases of each element plotted against

temperature. The filled symbols represent the values from the Facility for the Analysis of Chemical Thermodynamics (FACT) database[17], while the lines represent the regression data. For all the elements, except technetium, there is reasonable agreement.

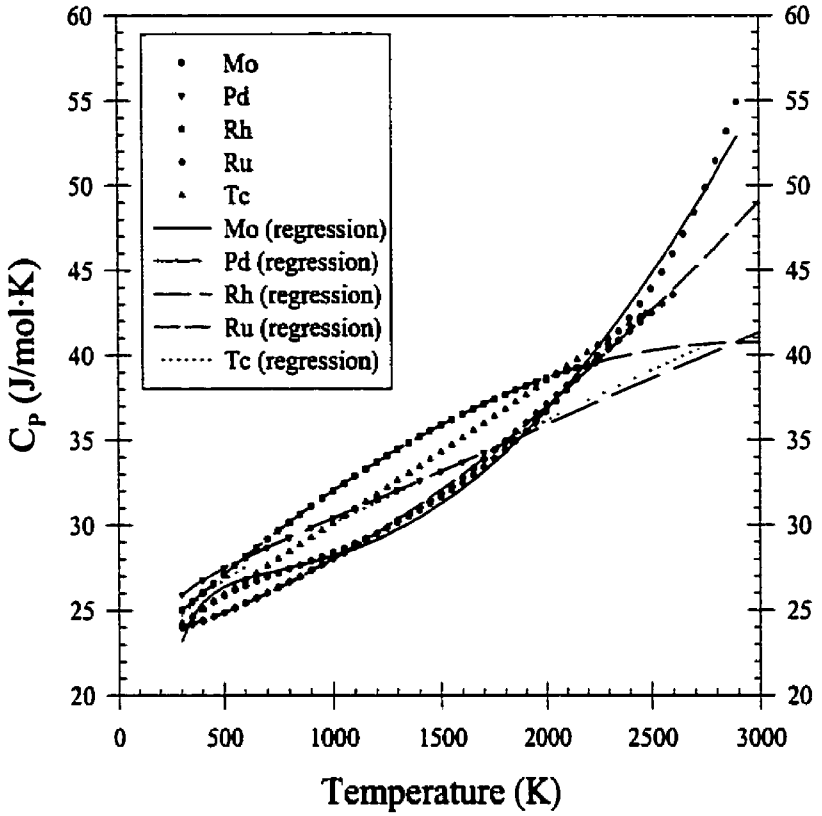

Figure 2-1. C_P data for the condensed forms of Mo, Pd, Rh, Ru, and Tc. The filled symbols are the measured data as reported in the FACT database[17], while the lines represent the fit data.

The heat capacities for the solid and liquid phases, shown in Table 2-1, are given for the temperature range 298-3000K.

Table 2-1. C_P data for Mo, Pd, Rh, Ru, and Tc in the condensed phases.

	$C_p = a + bT + cT^{-2} + dT^2$ (J/mol·K)					
Element	**a**	**bx10^3**	**c**	**dx10^6**	**T_{Min} (K)**	**T_{Max} (K)**
$Mo_{(bcc)}$	30.861	-7.2934	-534070	5.1509	298	3000
$Mo_{(liq)}$	30.861	-7.2934	-534070	5.1509	298	3000
$Mo_{(liq)}$	55.280	--	--	--	3000	4919
$Pd_{(fcc)}$	25.028	5.4404	-67548	--	298	3000
$Pd_{(liq)}$	25.028	5.4404	-67548	--	298	3237
$Rh_{(fcc)}$	20.811	13.4000	33942	-2.2679	298	3000
$Rh_{(liq)}$	20.811	13.4000	33942	-2.2679	298	3000
$Rh_{(liq)}$	40.747	--	--	--	3000	3970
$Ru_{(cph)}$	22.236	4.1437	40607	1.6015	298	3000
$Ru_{(liq)}$	22.236	4.1437	40607	1.6015	298	3000
$Ru_{(liq)}$	49.085	--	--	--	3000	4423
$Tc_{(cph)}$	24.339	5.9095	-127217	--	298	3000
$Tc_{(liq)}$	24.339	5.9095	-127217	--	298	4538

The C_P data for the monatomic gaseous phase of the elements, Table 2-2, were determined by fitting C_P data from the literature[22,24,29,30].

Table 2-2. C_P data for Mo, Pd, Rh, Ru, and Tc in the gaseous phase.

	$C_p = a + bT + cT^{-2} + dT^2 + eT^{-1} + fT^{-\frac{1}{2}}$ (J/mol·K)						T_{Min}	T_{Max}
Element	**a**	**bx10^3**	**c**	**dx10^6**	**e**	**f**	**(K)**	**(K)**
$Mo_{(gas)}$	110.886	-26.399	-2206221	4.8623	41776.1	-3814.35	298	5000
$Pd_{(gas)}$	20.766	--	--	--	--	--	298	600
$Pd_{(gas)}$	-1660.360	360.392	78544724	-43.1102	-1058487.7	74130.74	600	2700
$Rh_{(gas)}$	121.368	-21.559	-1401627	2.6359	38248.4	-3568.60	298	5000
$Ru_{(gas)}$	-52.257	9.072	4749159	0.1140	-66009.4	4128.10	298	5000
$Tc_{(gas)}$	21.075	--	--	--	--	--	298	500
$Tc_{(gas)}$	654.001	-0.131	18582271	15.0784	336236.8	-26145.60	500	3500

2.2.2 Crystal Structures, Transition Temperatures, Enthalpies, and Entropies

The five elements can be classified according to their stable crystal structure in

the solid phase: Mo is body-centred cubic; Pd and Rh are face-centred cubic; and Ru and Tc are close-packed hexagonal. Table 2-3 shows selected physical data for each of the five elements. It should be noted that none of these elements exhibit allotropic behaviour at atmospheric pressure.

Table 2-3. Physical data for Mo, Pd, Rh, Ru, and Tc.

Element	Atomic Mass (amu)	Density ($g \cdot cm^{-3}$)	Stable Crystal Structure	Atomic Radius (nm)	Lattice Parameters at 273K (nm)	References
Mo	95.94	10.22	cI2/bcc	0.136	a=0.3147	22,25,26,28
Pd	106.42	12.04	cF4/fcc	0.138	a=0.3890	22,25,26,28
Rh	102.91	12.42	cF4/fcc	0.134	a=0.3803	22,25,26,28
Ru	101.07	12.45	hP2/cph	0.132	a=0.2706; c=0.4282	22,25,26,28
Tc	98.91	11.40	hP2/cph	0.132	a=0.2740; c=0.4400	22,25,26

In order to maintain a consistent set of data, melting and boiling temperatures for each of the elements were chosen that agreed with values published in the *Journal of Phase Equilibria*[27] and the Binary Alloy Phase Diagrams[28]. The melting and boiling temperatures from these sources are presented in Table 2-4, along with the corresponding uncertainties. For comparison the values in the FACT[17] database are also presented here. The uncertainty of the boiling temperatures for the elements was not provided in the literature. The melting temperatures for molybdenum were already in agreement at 2896K, but for palladium and rhodium there was a difference of up to 3K between the adopted values of 1827K and 2236K, and 1825K and 2233K from the FACT database. The melting temperature for ruthenium given in the FACT database was 2523K, which is considerably lower than the selected value of 2607K. The melting temperature for technetium was 4K lower in the FACT database[17] than the selected value of 2477K from the Binary Alloy Phase Diagrams[28], but well within the uncertainty of temperature

measurement. On the whole the boiling temperatures were not in reasonable agreement, but it should be noted that the data at these extreme temperatures is limited and generally, based on extrapolated vapour pressures measured at much lower temperature.

Table 2-4. A comparison of the transition temperatures from FACT[17] with those of the present work.

Element	Transformation	FACT (K)	Uncertainty (K)	Present Work (K)	Uncertainty (K)
Mo	Melting	2896	±8	2896	±8
Mo	Vaporization	4957	not reported	4919	not reported
Pd	Melting	1825	±3	1827	±3
Pd	Vaporization	3385	not reported	3237	not reported
Rh	Melting	2233	±3	2236	±3
Rh	Vaporization	4230	not reported	3970	not reported
Ru	Melting	2523	±10	2607	±10
Ru	Vaporization	4606	not reported	4423	not reported
Tc	Melting	2473	±50	2477	±50
Tc	Vaporization	5584	not reported	4538	not reported

The enthalpies and entropies of formation at 298K for the solid, liquid, and gas for each element are given in Table 2-5. For the solid phase of each element, the enthalpy and entropy shown are for the stable crystal structure, as noted. The entropy at 298K, S°_{298}, was adopted from the FACT database[17]. For convenience, the melting and vaporization temperatures (T_M and T_V) are also provided.

Table 2-5. Standard Enthalpy and Entropy of Formation (at 298K) data for the elements Mo, Pd, Rh, Ru, and Tc.

Element	ΔH°_{298} (J/mol)	S°_{298} (J/mol·K)	Transformation Temperature (K)	Temperature Range (K)	Ref.
$Mo_{(bcc)}$	0	28.61	$T_M = 2896$	298-3000 K	28,29
$Mo_{(liq)}$	41403	42.90	$T_V = 4919$	298-3000 K	28,29
$Mo_{(gas)}$	738347	227.84		298-5000 K	28,29
$Pd_{(fcc)}$	0	37.82	$T_M = 1827$	298-3000 K	22,24,28
$Pd_{(liq)}$	16480	46.84	$T_V = 3237$	298-3237 K	28,30
$Pd_{(gas)}$	381565	168.94		298-600 K	28,30
$Pd_{(gas)}$	378970	161.36		600-2700 K	28,30
$Pd_{(gas)}$	346872	128.11		2700-5000 K	28,30
$Rh_{(fcc)}$	0	31.51	$T_M = 2236$	298-3000 K	24,28
$Rh_{(liq)}$	26568	43.39	$T_V = 3970$	298-3000 K	28,30
$Rh_{(gas)}$	555125	186.93		298-3970 K	28,30
$Ru_{(cph)}$	0	28.53	$T_M = 2607$	298-3000 K	24,28
$Ru_{(liq)}$	38589	43.34	$T_V = 4423$	298-3000 K	28,30
$Ru_{(gas)}$	677613	195.21		298-5000 K	28,30
$Tc_{(cph)}$	0	33.47	$T_M = 2477$	298-3000 K	28
$Tc_{(liq)}$	33290	46.91	$T_V = 4538$	298-3000 K	24,28
$Tc_{(gas)}$	650608	190.90		298-500 K	24,28
$Tc_{(gas)}$	650597	190.86		500-3500 K	24,28
$Tc_{(gas)}$	690777	231.41		3500-5000 K	24,28

In order to model the ten binary systems, ten ternary systems, five quaternary systems, and one quinary system, that can be constructed from these five elements, it was necessary to consider hypothetical crystal structures (e.g., Mo as fcc or cph). Then reasonable, yet still hypothetical, enthalpies of melting and corresponding transformation temperatures, were assigned, since these are required for the Gibbs energy of mixing expression for a particular phase (e.g., fcc-solid). The procedure for this is outlined in **Section 3.1**. Table 2-6 shows the thermodynamic data for each of the four elements,

including the assigned hypothetical properties for hypothetical crystal structures. These data may be considered to be the "lattice stabilities" with respect to the liquid phase.

For technetium, the data for hypothetical face-centred cubic, body-centred cubic, and tetragonal structures were assumed in a manner consistent with the values of the close-packed structure, and in the absence of data to the contrary, chosen to facilitate the assemblage of the binary phase diagrams of technetium.

Table 2-6. Thermodynamic data for $Metal_{(Solid)} \rightarrow Metal_{(Liquid)}$.

Phase	ΔH_M	ΔS_M	T_M	Reference
Mo (bcc)	41403	14.30	2896.0	31,32
Mo (fcc)	26203	14.93	1755.5	31,32
Mo (cph)	29853	14.30	2088.1	31,32
Pd (fcc)	16480	9.02	1827.1	31,33-35
Pd (cph)	12300	14.88	826.6	31,34,35
Pd (bcc)	12300	12.37	994.3	31
Rh (fcc)	26568	11.88	2236.4	32-34
Rh (cph)	25910	12.51	2071.1	32,34
Rh (bcc)	19664	16.27	1208.6	32
Ru (cph)	38589	14.80	2607.1	34
Ru (fcc)	21019	8.94	2350.6	34,35
Ru (bcc)	30420	12.51	2431.7	35
Tc (cph)	33290	13.44	2477.0	22,28
Tc (fcc)	30000	14.00	2142.9	
Tc (bcc)	28000	12.00	2333.3	
Tc (tetra)	20000	13.50	1481.5	

2.2.3 Phase Diagrams for the Elements

Because some of the experimental work that was performed for this project used a Knudsen cell coupled to a mass spectrometer to measure vapour pressures on the order of 10^{-4} to 10^{-10} atm, it was important to understand the relationship between temperature and

vapour pressure for the five elements. From Figure 2-2 it can be seen that palladium is the most volatile, followed by rhodium, ruthenium, technetium, and molybdenum in that order.

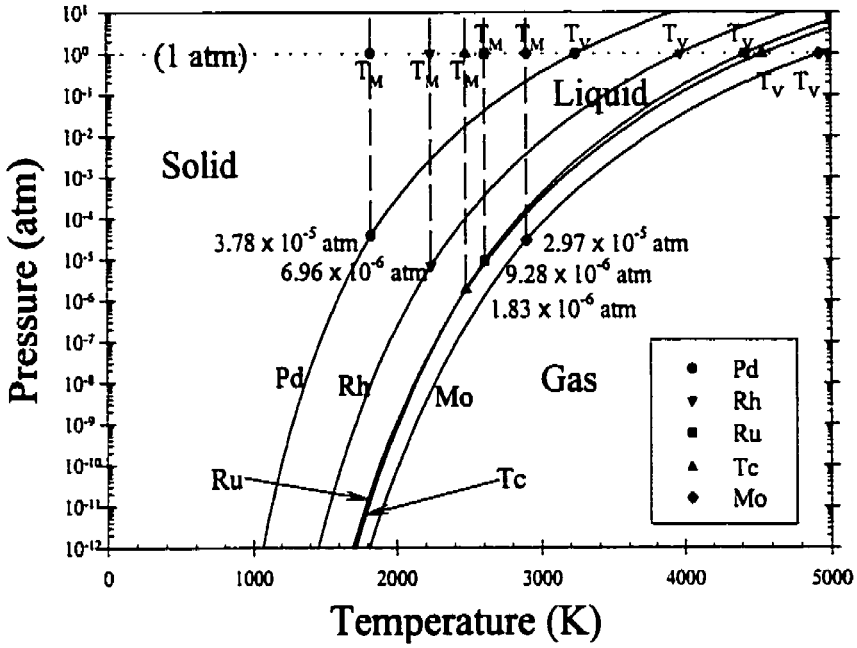

Figure 2-2. The Unary Phase Diagrams (superimposed) for Mo, Pd, Rh, Ru, and Tc, showing the relative partial pressures and their respective triple points.

Table 2-7 summarizes the triple point temperatures and corresponding pressures for Mo, Pd, Rh, Ru, and Tc.

Table 2-7. The triple point temperatures and corresponding pressures for the elements.

Element	Triple Point Temperature (K)	Pressure at Triple Point (atm)
Mo	2896	2.972×10^{-5}
Pd	1827	3.782×10^{-5}
Rh	2236	6.957×10^{-6}
Ru	2607	9.275×10^{-6}
Tc	2477	1.832×10^{-6}

2.3 Isotope Abundance and Ionization Cross-Section Data

Mass spectrometry measurements require knowledge of the relative abundance of the isotopes for each of the five elements, as well as their ionization cross-section. Of the 26 isotopes for molybdenum listed in the CRC Handbook of Chemistry and Physics[36] only seven have a natural abundance above one percent. For palladium there are six important isotopes, for rhodium only one, and for ruthenium seven. Because technetium is an artificial element, there are not any naturally occurring isotopes[36]. Table 2-8 summarizes the relative abundance for the various isotopes of Mo, Pd, Rh, and Ru.

Table 2-8. The relative abundance of the main isotopes of Mo, Pd, Rh, and Ru[36].

Isotope (amu)	Mo (%)	Pd (%)	Rh (%)	Ru (%)
92	14.84	---	---	---
94	9.25	---	---	---
95	15.92	---	---	---
96	16.68	---	---	5.53
97	9.55	---	---	---
98	24.13	---	---	1.89
99	---	---	---	12.71
100	9.63	---	---	12.61
101	---	---	---	17.01
102	---	1.02	---	31.62
103	---	---	100	---
104	---	11.14	---	18.72
105	---	22.33	---	---
106	---	27.33	---	---
108	---	26.46	---	---
110	---	11.72	---	---

In order to calculate the partial pressure of a particular element, it is necessary to know the maximum ionization cross-section. The data for the maximum ionization

cross-section for each element relative to argon[37] is presented in Table 2-9. The maximum ionization cross-section for argon at 32eV was reported as 2.83×10^{-16} cm^2 in the literature[37].

Table 2-9. Data for the maximum ionization cross-section of the noble metals[37].

Element	Ionization Cross-Section (cm^2) at 32eV
Mo	7.39×10^{-16}
Pd	6.55×10^{-16}
Rh	6.61×10^{-16}
Ru	7.20×10^{-16}
Tc	6.31×10^{-16}

2.4 Technetium

For the present work, technetium provided a special challenge. The most stable isotope ^{99}Tc, is not readily available commercially and the radioactive nature of Tc, especially ^{99m}Tc, which has a half-life of 6.01 hours[1], makes experimental work involving Tc difficult at best and generally hazardous to the extent that apparatus can become radioactively contaminated. Because of the safety hazards posed by Tc, experimental work, particularly the Knudsen Cell/Mass Spectrometry (described in **Sections 5.3** and **6.3**) did not include Tc in the noble metal alloys. However, for modelling purposes, the element was included.

2.5 Palladium

As mentioned previously in **Section 2.2.3**, palladium is the most volatile of the noble metals. Because of this, the Knudsen Cell/Mass Spectrometry experimental work, described in **Sections 5.3** and **6.3**, targeted the vapour pressure of palladium in the noble

metal alloys. However, before the four component alloys were examined, the apparatus was calibrated on a pure palladium sample, and comparison with the literature values for the vapour pressure of Pd was made (See Figure 7-7 in **Section 7.3.1.2**, p.132).

3. Critical Assessment of the Binary Alloy Phase Diagrams

3.1 Preliminary Remarks

There are ten binary systems that can be formed from the noble metals, Mo, Pd, Rh, Ru, and Tc. Although the Binary Alloy Phase Diagrams (BAPD) published by the American Society for Metals (ASM)[28] contains diagrams for nine of these systems, Ru-Tc being absent, there currently are only five systems that also have self-consistent thermodynamic evaluations presented in the literature. This lack of thermodynamic evaluations does not mean that these systems have not been studied. On the contrary, the importance of these five metals as alloy inclusions in nuclear fuel has been recognized for many years[7-9,38,39]. In this chapter each binary system will be critically examined, with a presentation of the experimental work that has previously been performed, and the subsequent conclusions that were drawn. Where appropriate, previous equilibrium phase diagrams will be included in order to demonstrate the progress of knowledge and to highlight areas of agreement and disagreement over nearly 50 years of research.

In order to present a comprehensive thermodynamic treatment for each of the ten binary systems, it is necessary to develop Gibbs energy expressions for each phase that is present in the binary system. It should be noted that the thermodynamic data for the "lattice stabilities" (both real and hypothetical) for the components in the ten binary systems were presented in **Table 2-6** of **Section 2.2.2** (p.21). These data comprise only part of the necessary Gibbs energy expressions for each phase present. The complete expression for the Gibbs energy for any phase in a binary system A-B, is given in equation **(3.1)**, where: the first two terms represent the energy components attributable to the lattice stabilities of A and B, respectively; the third term expresses the ideal mixing

term, which is a function of the proportion of A and B present in the phase, and the temperature; and the fourth term is an expansion series which accounts for deviations from ideal mixing.

$$\Delta G^{M}_{phase} = X_A \underbrace{(H^{\circ}_A - TS^{\circ}_A)}_{\text{lattice stability for A}} + X_B \underbrace{(H^{\circ}_B - TS^{\circ}_B)}_{\text{lattice stability for B}} + \underbrace{RT(X_A \ln X_A + X_B \ln X_B)}_{\text{ideal mixing term}} + \underbrace{\sum_{i=0} X_A X_B \left[(h_i - s_i T) X_B^i\right]}_{\text{excess Gibbs energy}} \quad \textbf{(3.1)}$$

where X_A and X_B represent the mole fractions of A and B, T the absolute temperature, R the gas constant, H° and S° the enthalpy and entropy contributions to the lattice energy, and h_i and s_i the enthalpy and entropy contributions in the excess Gibbs energy series.

It should be noted that the main purpose of thermodynamically modelling these ten binary systems is to develop a multi-component model. It is necessary, therefore, in systems that only contain two phases (e.g., Pd-Rh), to include Gibbs energy of mixing terms for all hypothetical crystal structures (e.g., a hypothetical close-packed hexagonal phase in the Pd-Rh system) in the modelling endeavour. With such hypothetical mixing terms it is thus possible to construct a multi-component model (details of this are explained in **Chapter 4**) using interpolation procedures.

Each binary system will be examined in terms of previous experimental work, most recent and thus "accepted" evaluation, including those evaluations original to this research, and thermodynamic properties. Only the expressions for the excess Gibbs energy of mixing will be presented, since the lattice stabilities were presented in **Table 2-6** of **Section 2.2.2** (p.21). Furthermore, a plot of a Gibbs energy isotherm, showing the various Gibbs energy of mixing curves as functions of composition at 1800K, is included, since the phase diagram was ultimately derived from a series of these over the given

temperature range.

3.2 Mo-Pd

3.2.1 Previous Studies of the Mo-Pd System

One of the first studies of the molybdenum-palladium system was performed by Raub[40] in 1954. For a series of alloys both the crystal structure and lattice parameter were determined at 1073K, 1123K and 1473K. At these three temperatures for alloys of molybdenum composition less than 32.26 atomic percent, only a face-centred cubic phase was observed (i.e., palladium–rich solid solution). In the range 44 to 77.18 atomic percent molybdenum, two phases, namely face-centred and body-centred cubic, were observed. Results for alloys extremely rich in molybdenum were not reported. It is noteworthy that Raub did not find evidence for any intermediate compounds, especially at the lower temperatures.

Haworth and Hume-Rothery examined the molybdenum-rich side of this system using classic metallographic techniques and X–ray diffraction[41]. The results are shown in Figure 3-1. The important discovery was the presence of a high temperature close-packed hexagonal (cph) ε-phase that exists between 50 and 60 atomic percent Pd. The temperature range for the ε-phase extends from above 1988K to slightly below 1673K.

In 1964, the palladium-rich side of the Mo-Pd phase binary diagram was studied in some detail by Anderson[42]. Anderson confirmed the presence of the ε-phase and the results indicated that there was a narrow compositional range at about 52 atomic percent Pd. Furthermore, an estimation of the maximum solubility of palladium was made to be 6.5 atomic percent at the peritectic temperature of 2028K ±10K. Together with the work

of Haworth and Hume-Rothery[41], Anderson provided a complete graphical representation above 1623K for the Mo-Pd system. This is reproduced in Figure 3-2.

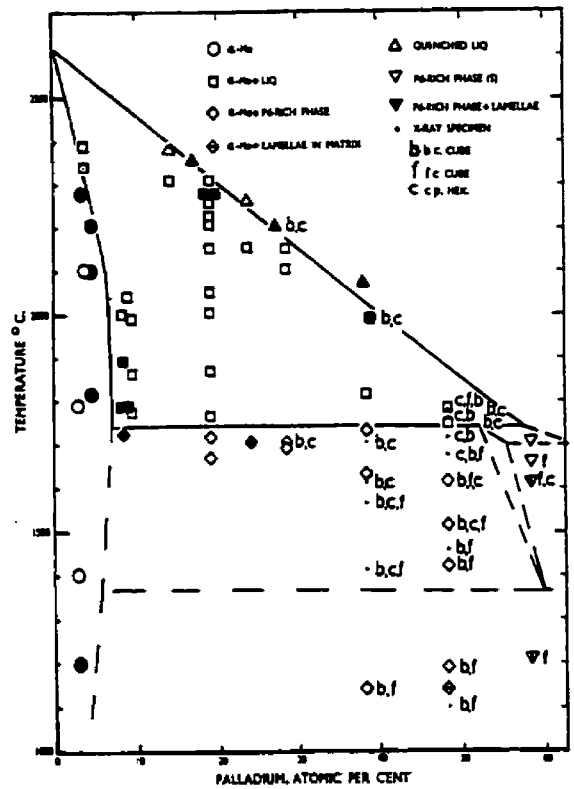

Figure 3-1. The molybdenum-rich half of the Mo-Pd binary diagram from Haworth and Hume-Rothery[41].

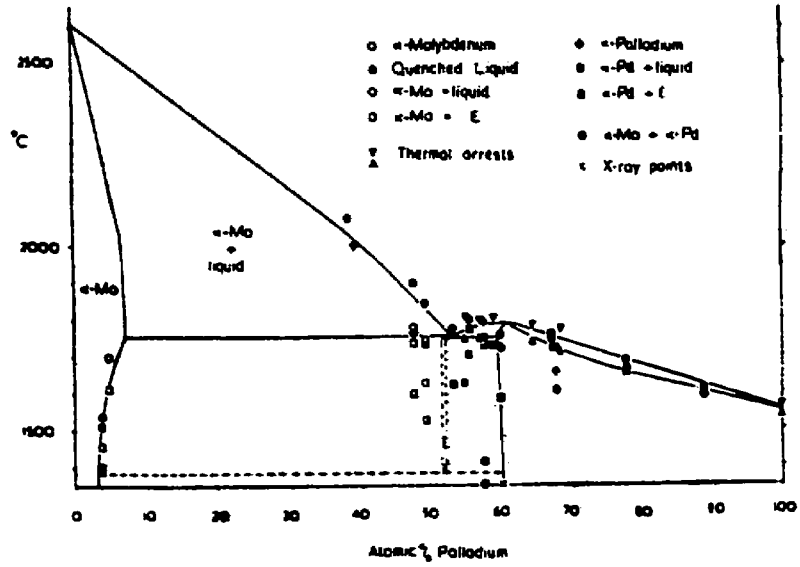

Figure 3-2. Molybdenum-palladium equilibrium diagram from Anderson[42].

Also in 1964, Savitskii et al.[43] used several methods to investigate Mo-Pd alloys across the complete compositional range, and published a different equilibrium diagram. Although there are differences between this evaluation and the previous investigations of Haworth and Hume-Rothery[41] and Anderson[42], Savitskii et al. confirmed the presence of the cph ε phase (composition of approximately 53.5 atomic percent Pd), which was reported to form at 2023K ±25K via a peritectic reaction, Liquid + (Mo) → ε, and decomposed at 1698K ±25K via an eutectoid reaction, ε → (Mo) + (Pd). Savitskii et al. also reported the absence of any low temperature intermetallic compounds.

Discrepancies occur in two major areas of the diagram, namely at the extremes of composition in the regions of solid solubility. Savitskii et al.[43] reported that the maximum solubility of Pd in molybdenum lies between 9 and 14 atomic percent, values higher than that of Anderson[42]. On the palladium-rich side of the diagram, it was reported that the maximum solubility of Mo in palladium extended only to 33 atomic percent, as opposed to the 40 atomic percent of Anderson[42]. Both papers agreed that these values change little with decreasing temperature. Also, Savitskii et al. suggested that there exists a peritectic reaction of Liquid + ε → (Pd), which produces, as a consequence of this postulated behaviour, a liquidus curve that is dramatically distended towards the palladium side of the phase diagram.

The results showing higher solubilities of Mo in palladium were confirmed by Zaiss et al.[44], who used quantitative electron-probe-microanalysis to study diffusion processes in the Mo-Pd system, and thereby determined the solvus line for the fcc palladium-rich phase. Their results are summarized in Table 3-1.

Table 3-1. Solubilities of Molybdenum in Palladium from Zaiss et al.[44].

Temperature (K)	Solubility of Mo in Pd (Atomic % Pd)
1273	65.0
1373	64.0
1473	62.0
1573	60.5
1763	57.0
1873	54.0

In the literature the first calculated evaluation for the Mo-Pd binary system was presented by Rand and Potter[35], although the mathematical expressions for the Gibbs energies were not published. This evaluation is shown in Figure 3-3.

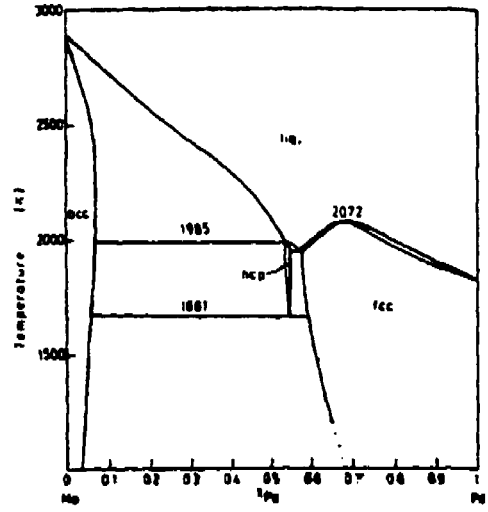

Figure 3-3. Computer generated evaluation of Rand and Potter[35].

The evaluation published by Rand and Potter was, as they themselves noted[35], based predominantly on the work of Haworth and Hume-Rothery[41], and Anderson[42], and as a consequence accepted the solubilities of Pd in molybdenum reported by these authors as opposed to the higher solubilities reported by Savitskii et al.[43] and the extremely high solubility of over 25 atomic percent Pd in Mo that was reported in 1956 by Greenfield and Beck[45]. The latter examined only two alloy compositions from this

system. Furthermore, the evaluation of Rand and Potter accepted the idea of a congruent melting point and a eutectic transformation on the palladium side of the diagram suggested by Anderson[42], instead of the peritectic reaction proposed by Savitskii et al.[43].

Although Raub, Haworth and Hume-Rothery, Anderson, and Savitskii et al.[40-43], quite distinctly reported the absence of any intermetallic compounds, Maldonado and Schubert[46] claimed that an ordered compound $MoPd_2$ exists below 1273K. The evaluation of Rand and Potter conveniently avoids addressing this issue by limiting their evaluation to a temperature range above 1300K. Brewer, in his comprehensive review of molybdenum[25], includes $MoPd_2$ in his proposed phase diagram, shown in Figure 3-4, for the Mo-Pd binary system, and this is the current evaluation published by the ASM[28].

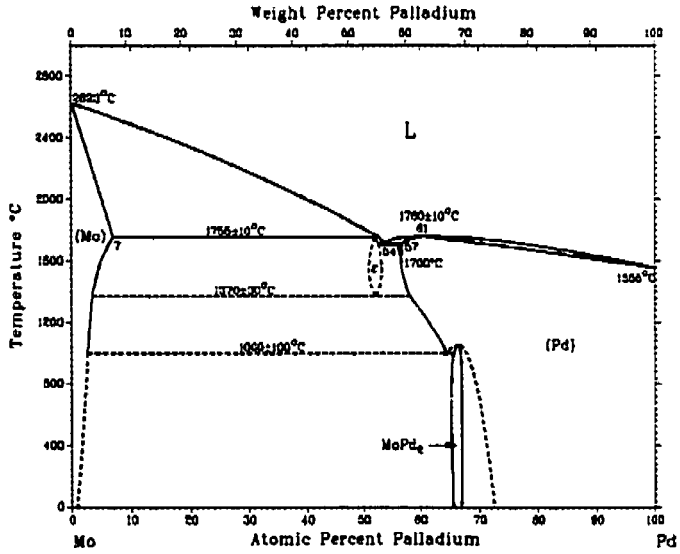

Figure 3-4. Mo-Pd equilibrium diagram from BAPD[28,25].

In order to clarify the various discrepancies within the Mo-Pd system, Kleykamp reinvestigated the system over the whole composition range from 1143K to 2273K[47]. This evaluation is shown in Figure 3-5.

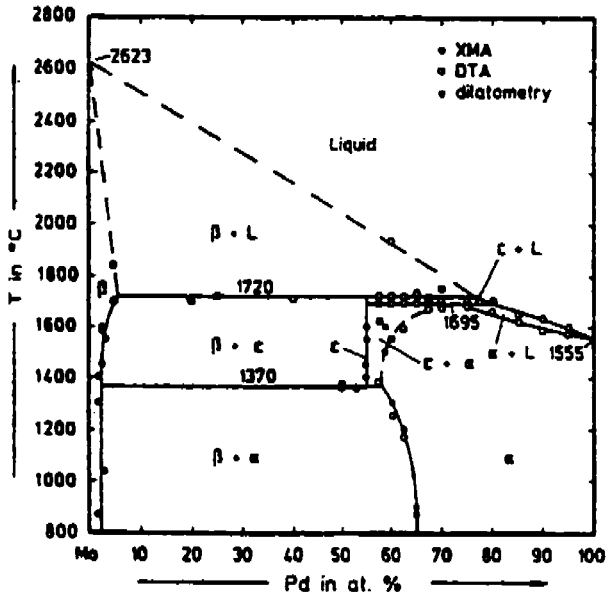

Figure 3-5. Phase diagram proposed for the Mo-Pd system by Kleykamp[47].

The extensive study by Kleykamp both clarifies and obscures the controversial aspects of the Mo-Pd phase diagram. On the Mo-rich side of the diagram, differential thermal analysis (DTA) of a 95%Mo/5%Pd alloy indicates a solvus temperature at 1973K and a solidus temperature of 2108K[47]. This result, together with X-ray microanalysis results for a series of alloys, indicated a limited solubility of Pd in molybdenum, thus confirming the results of Haworth and Hume-Rothery. Kleykamp also confirmed the existence of the ε-phase, but he placed it at 55 atomic percent Pd, a value slightly closer to the palladium rich side of the diagram.

As far as the existence of the compound $MoPd_2$, there was not any evidence at the lowest temperatures, i.e., 1143K and 1173K.

As can be seen from Figure 3-5, Kleykamp proposed the peritectic reaction, Liquid + ε → (Pd), on the palladium side of the binary system. But, it should be noted that there were inconsistent results here. X-ray microanalysis suggested that the solvus

boundary between the $\varepsilon + \alpha$ region and the α-phase region are at 59 atomic percent Pd at 1773K and 1873K. However, irreproducible differential thermal analysis peaks were interpreted, as shown in Figure 3-5, to be indicative of a solvus that extends toward the palladium rich side of the diagram. Finally, the presence of a liquidus DTA result at 60 atomic percent Pd at 2203 or 2213K, suggested that the β + Liquid region, and by extension the Liquid + ε region, was distended towards the palladium side of the diagram. Such a result, if accurate, would exclude the possibility of a eutectic reaction and congruent melting point involving the liquid and α phases. Unfortunately, Kleykamp did not offer any comment.

Kleykamp reported on the possible existence at temperatures above 1273K of the compound Mo_3Pd, but as he noted the possibility that this phase was stabilized by the presence of oxygen, it is not included on the binary phase diagram.

By using electromotive force (emf) techniques and the galvanic cell shown in **(3.2)**, the relative partial molar Gibbs energy of molybdenum in the Mo-Pd system was measured from 973K to 1373K.

$$(-)Re|Fe, FeO_{0.95}|Zr(Ca)O_2|MoO_2, Mo-Pd\ alloy|Re(+) \qquad \textbf{(3.2)}$$

At 1200K the relative partial molar excess Gibbs energy of molybdenum at infinite dilution in palladium was measured to be: $\overline{\Delta G}^{E}_{Mo\ at\ X_{Pd}=1} = -94kJ/mol$ [47].

Another re-investigation of the Mo-Pd binary system was made by Gürler and Pratt[48], who used ultra-rapidly solidified samples to achieve equilibrium much more quickly upon subsequent annealing. The alloys studied were in the temperature range 1153K to 1373K, and the results are presented in Figure 3-6.

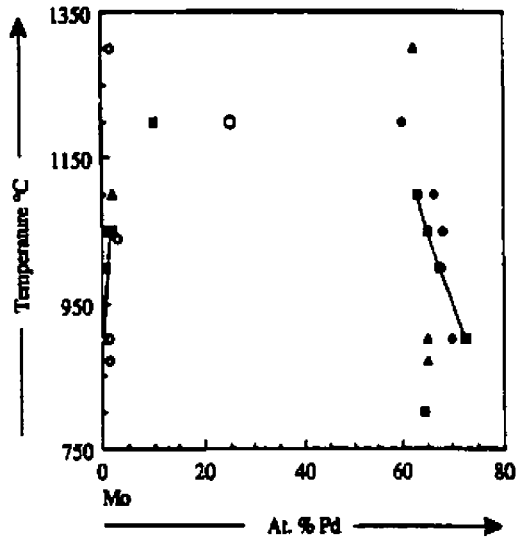

. The Mo–Pd phase diagram showing revised phase boundaries in the temperature range 1100–880 °C: ⊡ f.c.c., X-ray present study; ♦ f.c.c., SEM present study; △ f.c.c., SEM [47]; ● f.c.c., X-ray [LC]; ■ f.c.c.[40]; □ b.c.c., X-ray present study; ▲ b.c.c., SEM present study; ○ b.c.c., SEM [47]; ■ b.c.c., X-ray [LC]; ○ b.c.c. [45].

Figure 3-6. Comparison of results from Gürler and Pratt[48] with others.*

The results from Gürler and Pratt[48] indicated that there was not any evidence for the formation of either $MoPd_2$ or Mo_3Pd at temperatures above 1153K. Furthermore, this investigation confirmed the limited solubility of Pd in molybdenum, and the results are in agreement with Zaiss et al.[44] on the solubility of molybdenum in palladium.

The Mo-Pd was thermodynamically evaluated by Gürler[31] and summarized by Okamoto† in the *Journal of Phase Equilibria*[49]. This evaluation is shown in Figure 3-7, but it should be noted that there is a problem with the placement of the ε-phase, which is depicted to extend to 46 atomic percent Pd, when in the evaluation of Gürler[31] it clearly extends to 52 atomic percent Pd. Also of note is that this evaluation assumes the eutectic

---

* Note that X-ray data points referenced [LC] are referenced internally by Gürler and Pratt[48], and are from: L.A. Cornish, *PhD Thesis*, Birmingham University, (1985).

† The summary by Okamoto contains typographical errors in the table of thermodynamic data. All the Gibbs energy data for Pd is labelled Rh, and the Gibbs energy expression for the Pd-bcc structure should read: -12300 + 12.37T J/mol (not 12.35T); as in accordance with Gürler[31].

reaction and congruent melting point on the palladium side of the diagram, thereby disregarding the seemingly erroneous liquidus data point reported by Kleykamp[47].

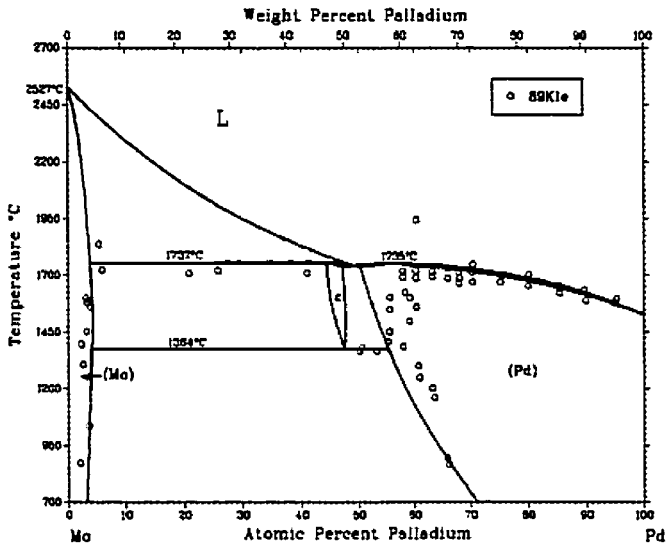

Figure 3-7. The updated ASM diagram based on Gürler[31,49].

3.2.2 Accepted Evaluation for the Mo-Pd System

The Mo-Pd phase diagram as evaluated by Gürler[31] is shown in Figure 3-8. This evaluation has a eutectic reaction, Liquid $\rightarrow \varepsilon$ + (Pd) at 2005K, and a congruent melting point at 2008K and 61.6 atomic percent Pd. It can be seen that unlike Figure 3-7, the ε-phase straddles the centre of the diagram and is positioned more in keeping with the results of Haworth and Hume-Rothery[41], and Anderson[42]. The possible compound $MoPd_2$ has not been included in this evaluation. The evaluation by Gürler[31] has been accepted in the present work.

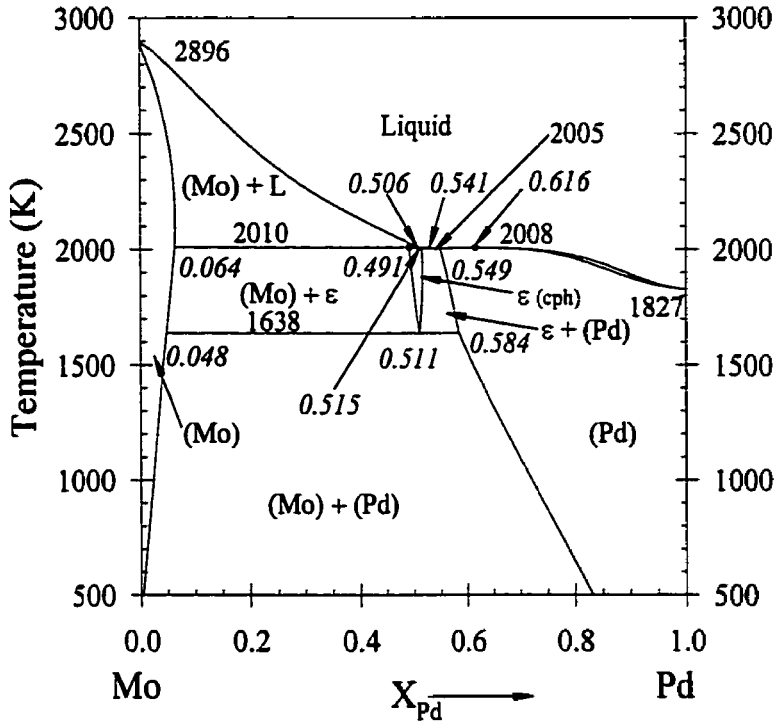

Figure 3-8. The Mo-Pd system as evaluated by Gürler[31], showing critical features.

A detailed view of the eutectic reaction at 2005K, shown in Figure 3-8, is clearly presented in Figure 3-9. The Phase Rule is obeyed in the regions bordering the ε-phase.

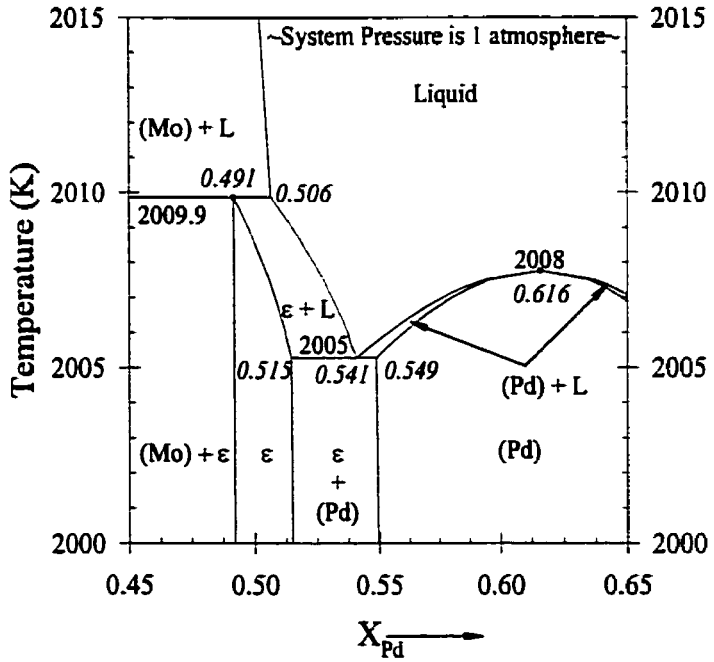

Figure 3-9. Computed detail of the Mo-Pd phase diagram near the eutectic reaction.

3.2.3 Thermodynamic Properties for Mo-Pd Binary System

Although it has been shown that there has been extensive experimental work performed in this system, there has been only limited thermodynamic data measured. As mentioned previously, Kleykamp measured the relative partial molar Gibbs energy of molybdenum from 973K to 1373K. At 1200K the relative partial molar excess Gibbs energy of Mo at infinite dilution in palladium* was: $\Delta\overline{G}^{E}_{Mo\ at\ X_{Pd}=1} = -94kJ/mol$ [47].

Although Rand and Potter[35] provided a mathematical evaluation of the Mo-Pd system, they did not report the coefficients of the Gibbs energy expressions that they used to determine that evaluation. However, in the evaluation by Gürler, shown in Figure 3-8, expressions for the excess Gibbs energies of mixing, as well as the Gibbs energies for the lattice stabilities of the various phases are reported. The energy expressions for the lattice stabilities were summarized in ***Section 2.2.2 - Crystal Structures, Transition Temperatures, Enthalpies, and Entropies***. The excess properties of mixing for the four phases in the Mo-Pd system are [31]:

$$\Delta G^{E}_{Liquid} = X_{Mo}X_{Pd}\left[366904.56 - 478773X_{Pd} - (193.12 - 216.85X_{Pd})T\right] \text{ J/mol} \quad \textbf{(3.3)}$$

$$\Delta G^{E}_{bcc} = X_{Mo}X_{Pd}\left[40328.63 + 1220269X_{Pd} - (73.49 + 159.92X_{Pd})T\right] \text{ J/mol} \quad \textbf{(3.4)}$$

$$\Delta G^{E}_{fcc} = X_{Mo}X_{Pd}\left[71076.50 - 100416.81X_{Pd} - (50.59 - 27.84X_{Pd})T\right] \text{ J/mol} \quad \textbf{(3.5)}$$

$$\Delta G^{E}_{cph} = X_{Mo}X_{Pd}\left[11387.07 + 656.46X_{Pd} - (16.81 + 53.33X_{Pd})T\right] \text{ J/mol} \quad \textbf{(3.6)}$$

A plot of the Gibbs energy of mixing curves for the four phases of the Mo-Pd system at 1800K is shown in Figure 3-10.

---

* The standard state was not specified by Kleykamp, but it is reasonable to assume that it was bcc-Mo.

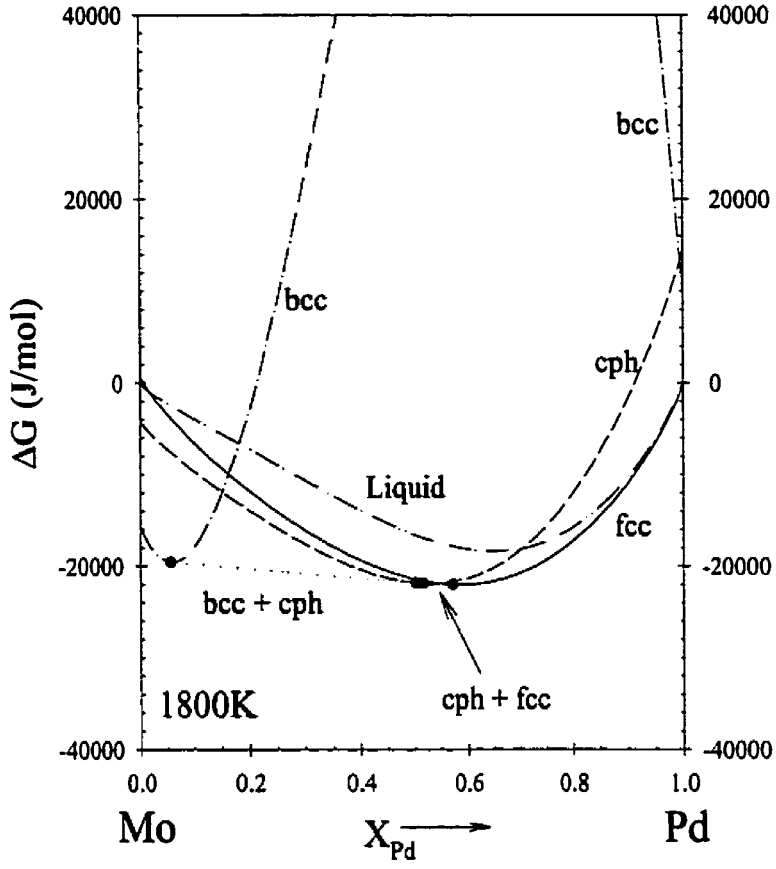

Figure 3-10. Gibbs Energy Isotherm at 1800K for Mo-Pd system.

3.3 Pd-Ru

3.3.1 Previous Studies of the Pd-Ru System

One of the earliest studies of the palladium-ruthenium binary system was performed by Rudnitskii and Polyakova[50]. These investigators used various techniques including X-ray analysis, thermo-emf measurements, differential thermal analysis, and measurements of hardness and electrical resistance to generate the phase diagram shown in Figure 3-11.

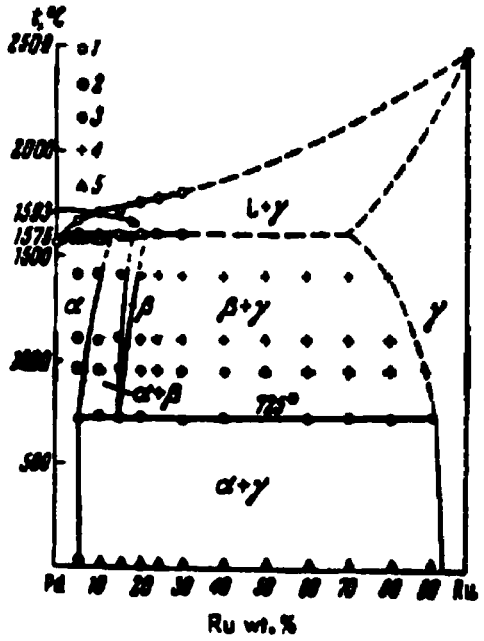

Figure 3-11. Pd-Ru diagram as evaluated by Rudnitskii and Polyakova[50].

As can be seen in Figure 3-11, there is reasonable mutual solubility of these two components in each other. In the case of ruthenium into Pd, the solubility limit was measured to lie between 10 and 15 atomic percent Ru. For palladium in Ru, the solubility was measured as about 10 atomic percent Pd in ruthenium at 1000K. Above 1000K the solubility of Pd was assumed to increase.

Perhaps the most interesting feature of this evaluation was the indicated presence of an intermediate phase region (labelled β-phase in Figure 3-11) around 15 atomic percent Ru. Rudnitskii and Polyakova[50] suggested that the intermediate β-phase is formed by a peritectic reaction of Liquid + Ru-rich solid → β at 1866K, and that a second peritectic reaction, Liquid + β → Pd-rich solid, occurs at 1848K.

Darling and Yorke[51] also examined the palladium-ruthenium system, but unlike Rudnitskii and Polyakova[50] they did not find evidence of an intermediate phase.

Obrowski and Zwingmann[52] were also unable to detect the presence of the intermediate phase in the palladium-ruthenium system. Although this work confined itself to the palladium-rich side of the system, the various experimental techniques, namely thermal and X-ray analysis, and microscopy, provided consistent evidence for the absence of the intermediate β-phase. Instead only one peritectic reaction, Liquid + Ru-rich solid → Pd-rich solid at 1858K, was observed. This agreed with the work of Darling and Yorke[51].

In their modelling of the Mo-Pd-Ru ternary system, Rand and Potter[35] briefly reviewed the aforementioned papers in order to summarize the data that were used in their evaluation. The result of their review was the phase diagram depicted in Figure 3-12, which was derived graphically from considering previous experimental work. Rand and Potter based this diagram predominantly on the work of Darling and Yorke[51], noting that the intermediate phase detected by Rudnitskii and Polyakova[50] may have been an artifact that resulted due to the presence of RuO_2 in some of the samples. Since Darling and Yorke used purer starting materials than Rudnitskii and Polyakova, the results of the former were preferred over those of the latter.

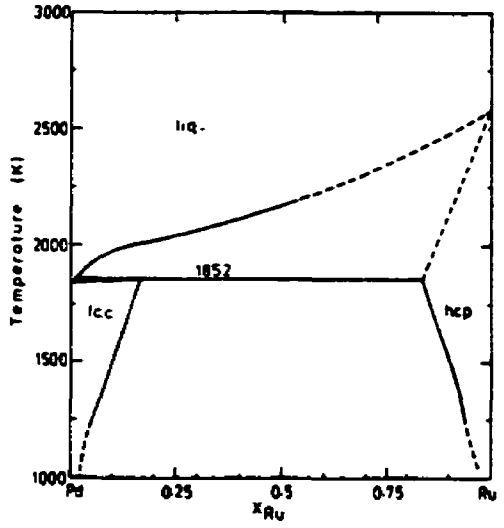

Figure 3-12. The Pd-Ru phase diagram suggested by previous experimental work[35].

The phase diagram calculated by Rand and Potter is shown in Figure 3-13. In this diagram the temperature of the peritectic reaction has been raised approximately 60K, and as a consequence the left-hand side of the peritectic tie-line has shifted to the right. Rand and Potter also commented that there was a lack of experimental thermodynamic data with which to base their evaluation, and so they estimated a few parameters based on values taken from their evaluations of Mo-Pd and Mo-Ru (mentioned in **Sections 3.2.1** and **3.6.1**, respectively). Unfortunately, the parameters used in the evaluation by Rand and Potter were not published.

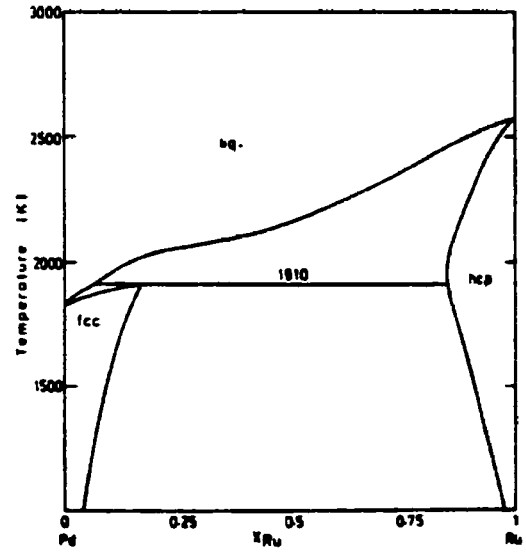

Figure 3-13. The Pd-Ru phase diagram calculated by Rand and Potter[35].

Using X-ray microanalysis and X-ray diffraction, Kleykamp[47] confirmed that the palladium-ruthenium system was a simple peritectic system as proposed by Darling and Yorke[51]. His proposed phase diagram is shown in Figure 3-14. It can be seen that the maximum solubility of palladium in Ru is relatively constant (at 7.7 ±0.3 at.%Pd) below the peritectic temperature of 1867K. This differs from previous work that suggested that solubility of palladium in Ru increased dramatically towards the peritectic temperature. On the palladium-rich side of the diagram, the maximum solubility of ruthenium in Pd is about 19 at.% Pd at the peritectic temperature.

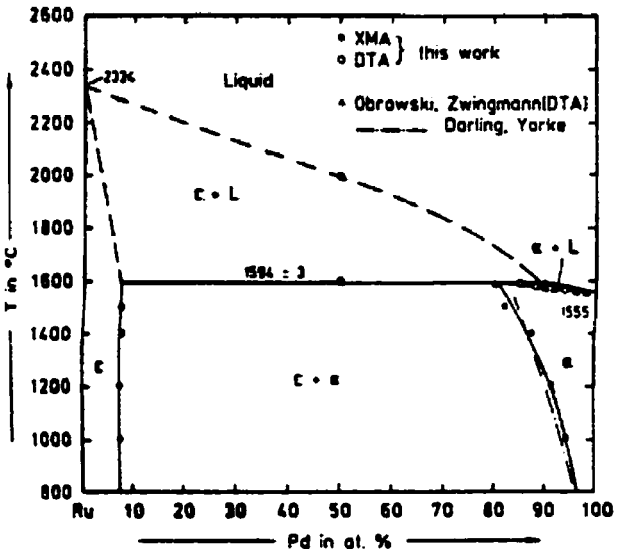

Figure 3-14. Pd-Ru phase diagram as proposed by Kleykamp[47].

Supplemental experimental data in the form of limited differential thermal analysis results confirmed the general form of the diagram, but unfortunately as a result of degradation of the thermocouples caused by the high palladium vapour pressure, data charting the liquidus was limited to one point at $X_{Pd} = 0.5$.

Kleykamp[47] also obtained the first thermodynamic data for this system by the emf method using a solid galvanic cell in the arrangement:

$$(-)Pt|Ru, RuO_2|Zr(Ca)O_2|RuO_2, Ru-Pd\ alloy|Pt(+) \qquad (3.7)$$

From this galvanic cell the activity of ruthenium was determined in the two phase region. At 1100K and 1200K, $\Delta\overline{G}_{Ru} = -5760J/mol$ and $\Delta\overline{G}_{Ru} = -6260J/mol$*, respectively, and the activity of ruthenium was calculated to be 0.53 at both temperatures.

Gürler provided a computer assessment of this system[34], based on the single peritectic description as suggested by the authors noted above. This evaluation, shown in

---

* The standard state was not specified by Kleykamp, but it is reasonable to assume that it was cph-Ru.

Figure 3-15, agrees with the features reported previously. The peritectic reaction occurs at 1867K, at $X_{Ru} = 0.185$.

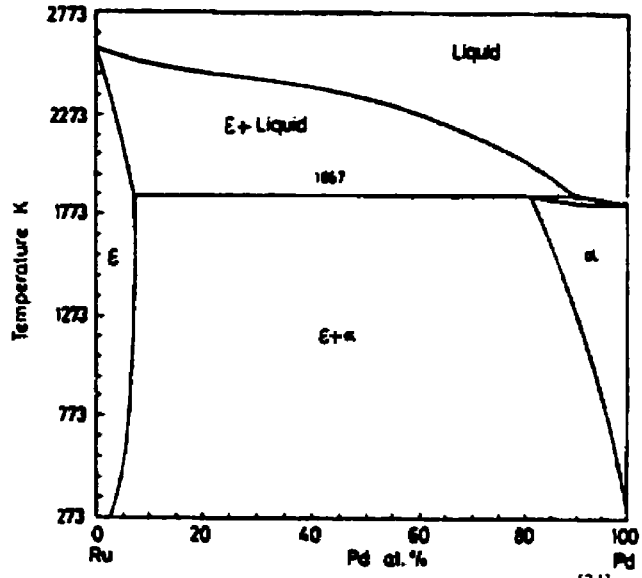

Figure 3-15. Evaluation proposed by Gürler[34].

A summary of the various evaluations of the palladium-ruthenium system was published in the *Journal of Phase Equilibria*[53], and is reproduced in Figure 3-16.

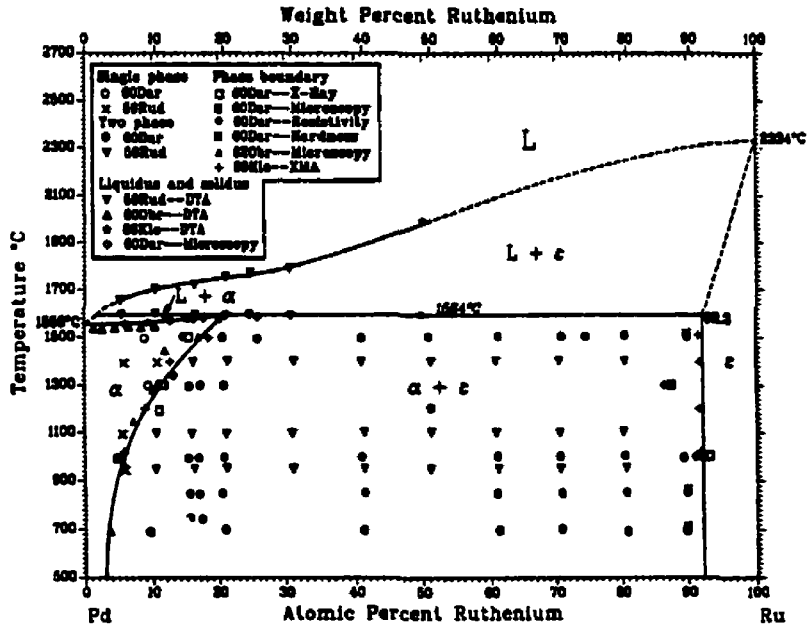

Figure 3-16. From the summary by Tripathi et al.[53], detailing experimental work performed in the palladium-ruthenium system.

The current evaluation published by the ASM[28] is presented in Figure 3-17.

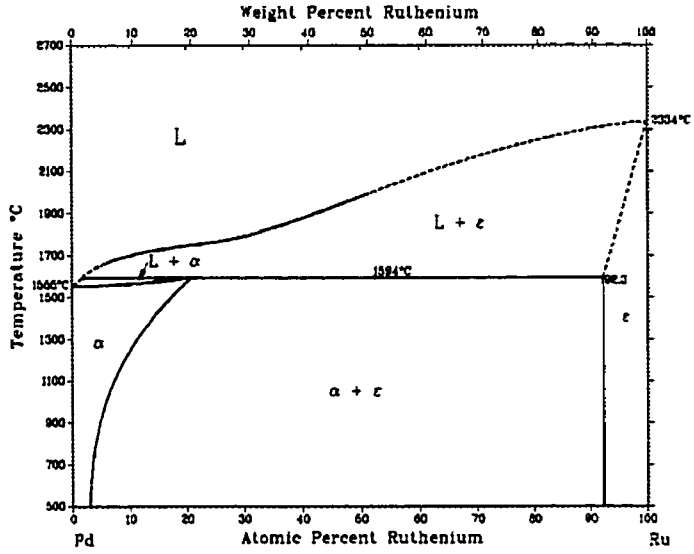

Figure 3-17. Pd-Ru equilibrium diagram from BAPD[28].

3.3.2 Accepted Evaluation for the Pd-Ru System

The currently accepted evaluation by Gürler[34] is shown in greater detail in Figure 3-18. This evaluation shows only terminal solid solutions with a two-phase region in between, and is characterized by the peritectic reaction, ε (cph-Ru) + Liquid → α (fcc-Pd). A further feature of interest, although it is not evident in Figure 3-18, is that the solidus boundary of the α + Liquid region, passes through a minimum at 1826.4K when $X_{Ru} = 0.0103$.

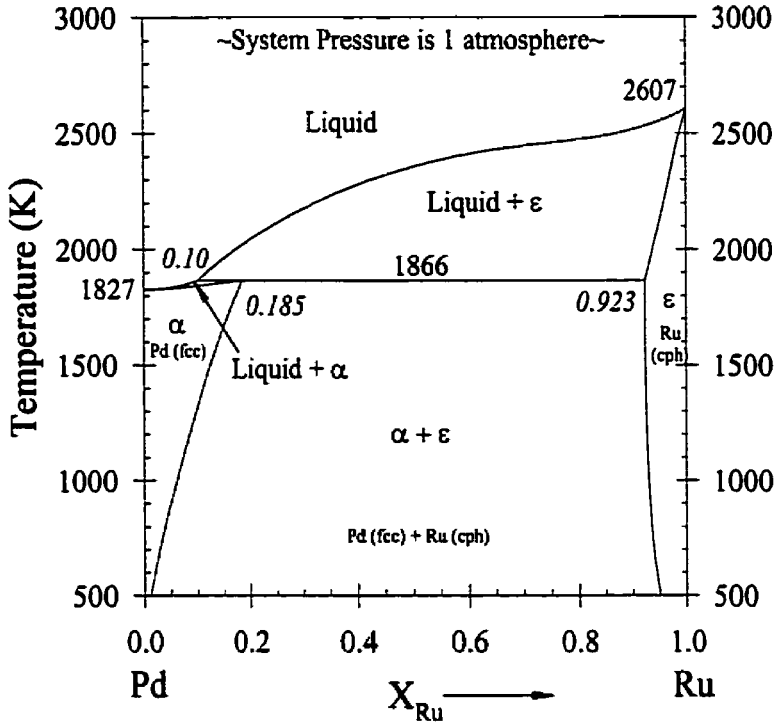

Figure 3-18. The Pd-Ru system as evaluated by Gürler[34].

3.3.3 Thermodynamic Properties for Pd-Ru Binary System

The excess properties of mixing for the four solution phases are [34]:

$$\Delta G^{E}_{Liquid} = X_{Pd}X_{Ru}\left[187564.062 - 62169.281X_{Pd} - \left(63.661 - 6.64X_{Pd}\right)T\right] \text{ J/mol} \quad \textbf{(3.8)}$$

$$\Delta G^{E}_{fcc} = X_{Pd}X_{Ru}\left[-5049.035 + 17.59T\right] \text{ J/mol} \quad \textbf{(3.9)}$$

$$\Delta G^{E}_{cph} = X_{Pd}X_{Ru}\left[-1524.818 + 14.933T\right] \text{ J/mol} \quad \textbf{(3.10)}$$

$$\Delta G^{E}_{bcc} = X_{Pd}X_{Ru}\left[20000\right] \text{ J/mol} \quad \textbf{(3.11)}$$

A plot of the Gibbs energy of mixing curves for the four solution phases of the Pd-Ru system at 1800K is shown in Figure 3-19.

As mentioned previously, Kleykamp[47] determined the partial free energy for ruthenium* to be $\Delta\overline{G}_{Ru} = -5760J/mol$ at 1100K and $\Delta\overline{G}_{Ru} = -6260J/mol$ at 1200K

---

* The standard state was not specified by Kleykamp, but it is reasonable to assume that it was cph-Ru.

and $a_{Ru} = 0.53$.

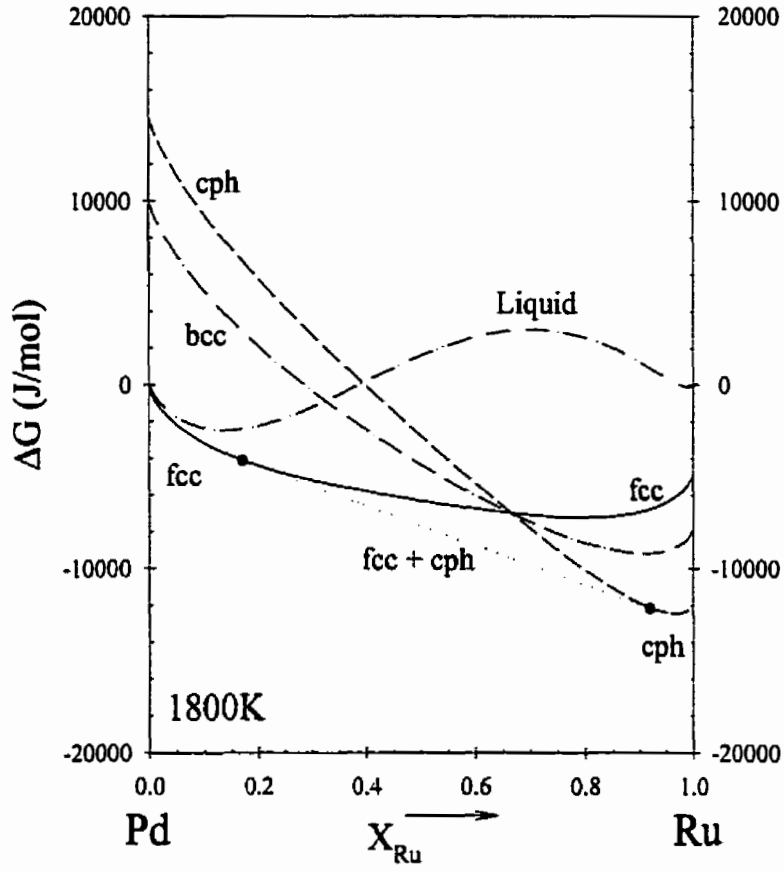

Figure 3-19. Gibbs Energy Isotherm at 1800K for Pd-Ru system.

3.4 Rh-Ru

3.4.1 Previous Studies of the Rh-Ru System

Of the six binary systems that do not include Tc, the fewest number of experimental studies pertain to the Rh-Ru system. Paschoal et al.[54,55] investigated the system using metallography, X-ray diffraction, DTA, electron microprobe, and microhardness measurements.

A summary of the results of Paschoal et al.[54,55] and two other minor papers concerning the changes in lattice parameters was made by Tripathi et al.[56]. The assessed

equilibrium diagram is presented in Figure 3-20.

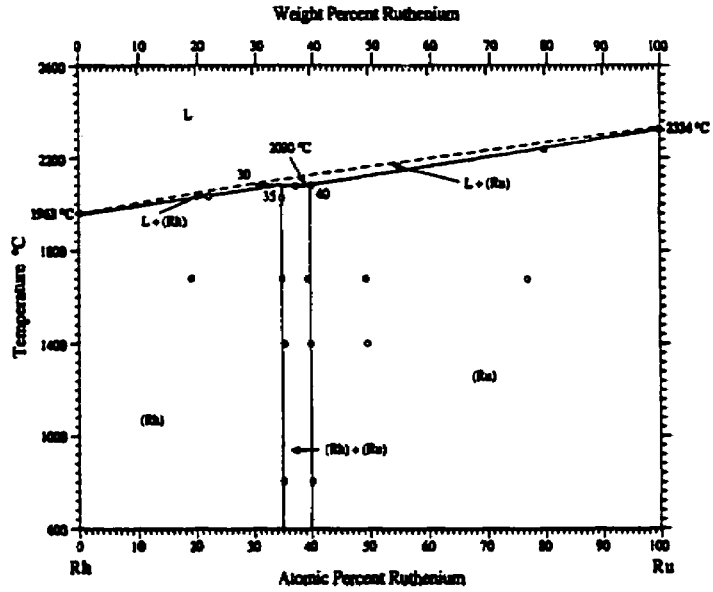

Figure 3-20. Rh-Ru equilibrium diagram from summary by Tripathi et al.[56].

The current evaluation published by the ASM[57] is presented in Figure 3-21.

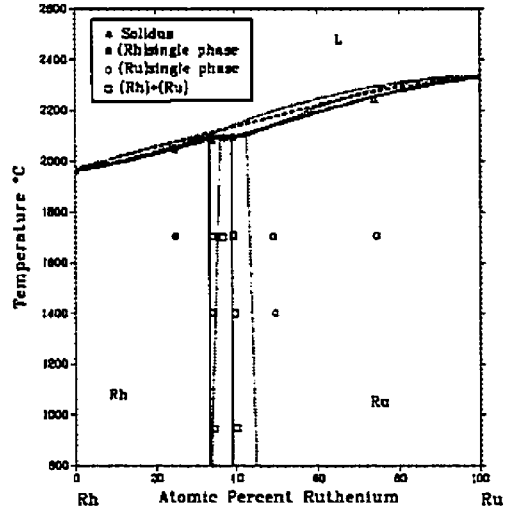

Figure 3-21. Rh-Ru equilibrium diagram[57].

3.4.2 Accepted Evaluation for the Rh-Ru System

The evaluation by Gürler [34] has been accepted and is shown in Figure 3-22. The diagram is characterized by a peritectic reaction, Liquid + $Ru_{cph} \rightarrow Rh_{fcc}$. The terminal

solid solutions dominate either edge of the diagram, with only a thin (less than 12 atomic percent) two phase region.

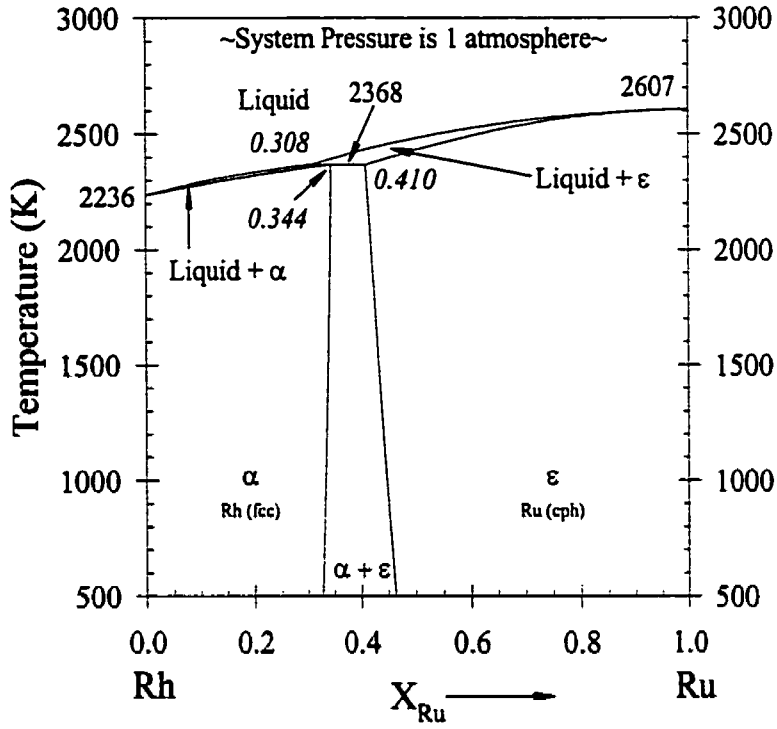

Figure 3-22. The Rh-Ru system as evaluated by Gürler[34].

3.4.3 Thermodynamic Properties for Rh-Ru Binary System

The excess properties of mixing for the four solution phases are [34]:

$$\Delta G^{E}_{Liquid} = X_{Rh}X_{Ru}\left[-35739.32+16.369T\right] \text{ J/mol} \quad \textbf{(3.12)}$$

$$\Delta G^{E}_{fcc} = X_{Rh}X_{Ru}\left[-53477.07+21.738T\right] \text{ J/mol} \quad \textbf{(3.13)}$$

$$\Delta G^{E}_{cph} = X_{Rh}X_{Ru}\left[-26440.004+10.445T\right] \text{ J/mol} \quad \textbf{(3.14)}$$

$$\Delta G^{E}_{bcc} = X_{Rh}X_{Ru}\left[0+0T\right] \text{ J/mol} \quad \textbf{(3.15)}$$

The Gibbs energy of mixing curves for the four solution phases of the Rh-Ru system at 1800K is shown in Figure 3-23.

It should be noted that there is an absence of direct thermodynamic data for this system.

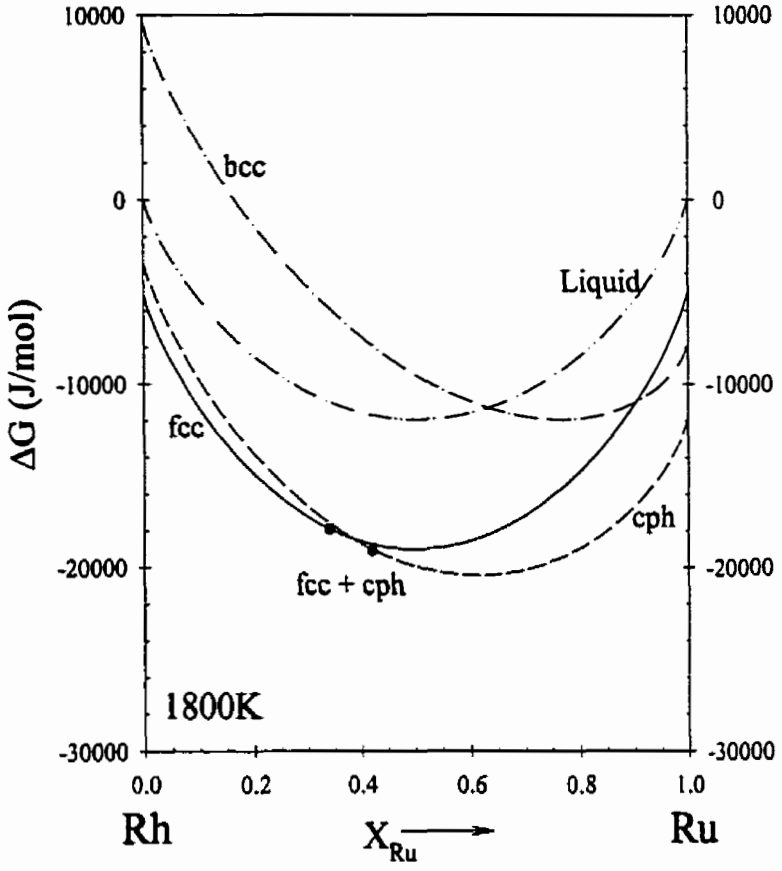

Figure 3-23. Gibbs Energy Isotherm at 1800K for Rh-Ru system.

3.5 Mo-Rh

3.5.1 Previous Studies of the Mo-Rh System

The work by Raub[40] examined the crystal structure of nine alloys in the Mo-Rh binary system. The results indicate that as well as terminal solids of body-centred-cubic Mo and face-centred-cubic Rh, there is an intermediate close-packed hexagonal ε-phase that spans over 30 atomic percent. Raub did not offer a phase diagram.

Haworth and Hume-Rothery examined this system using classic metallographic techniques[41], and studied alloys that varied from dilute rhodium alloys to rhodium percentages up to 60%. Their partial evaluation of the molybdenum-rich side of the

equilibrium diagram is shown in Figure 3-24.

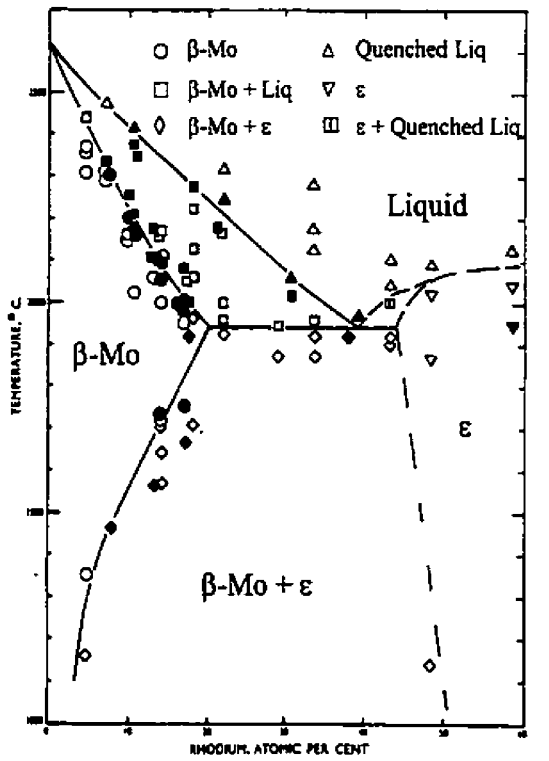

Figure 3-24. The molybdenum rich side of the Mo-Rh equilibrium diagram[41].

Haworth and Hume-Rothery determined that a eutectic transition occurred at approximately 40 atomic percent rhodium and 2213K ±15K. The maximum solubility of rhodium in molybdenum occurred at 20 atomic percent Rh and 2213K.

In 1960, Anderson and Hume-Rothery[58] investigated the rhodium side of the phase diagram at temperatures above 1773K. A complete equilibrium diagram was proposed that incorporated their results and those of Haworth and Hume-Rothery, and is shown in Figure 3-25.

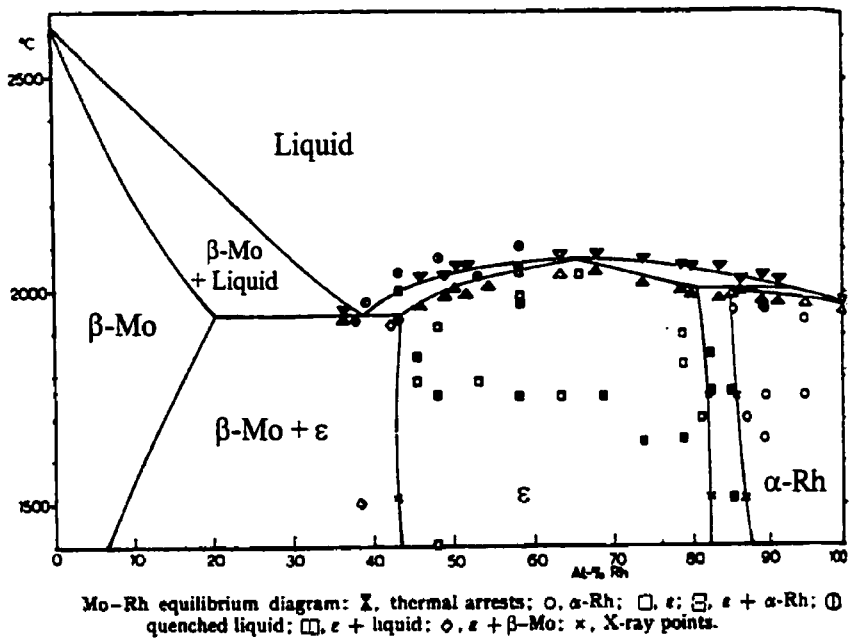

Mo–Rh equilibrium diagram: Ⅹ, thermal arrests; ○, α-Rh; □, ε; ⊟, ε + α-Rh; ⓘ quenched liquid; ⊞, ε + liquid; ◇, ε + β-Mo; ×, X-ray points.

Figure 3-25. Mo-Rh Equilibrium diagram from Anderson and Hume-Rothery[58].

As can be seen in Figure 3-25, Anderson and Hume-Rothery[58] postulated that the intermediate ε-phase extended from roughly 45 to 82 atomic percent Rh, and that there was a congruent melting at approximately 67 atomic percent Rh and 2348K ±10K. Furthermore, on the rhodium side of the diagram, there was a peritectic transformation of ε + Liquid → α-(Rh), where α- (Rh) is an fcc crystal structure, at 2273K ±10K. The maximum soluibility of Mo in rhodium was found to be 15 atomic % at the peritectic[58].

The phase diagram proposed by Brewer has been adopted as the current evaluation published by the ASM[25,28], and is presented in Figure 3-26.

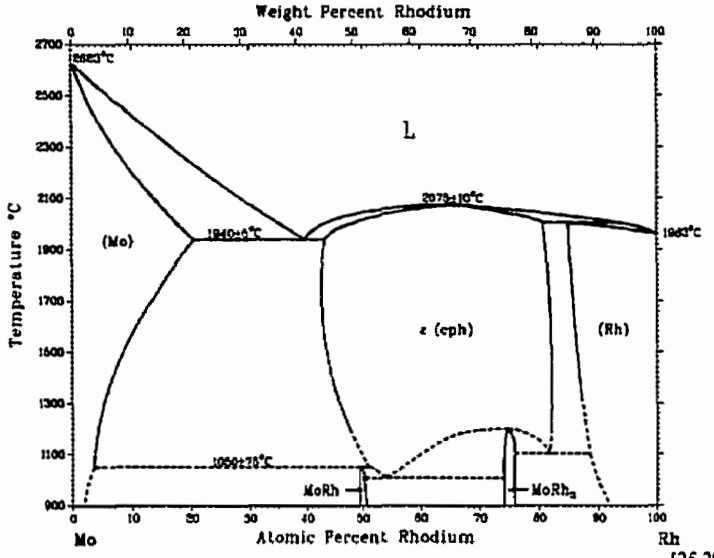

Figure 3-26. Mo-Rh equilibrium diagram from BAPD[25,28].

3.5.2 Accepted Evaluation for the Mo-Rh System

The Mo-Rh system was evaluated by Gürler and Pratt and summarized by Okamoto* for the *Journal of Phase Equilibria* [32,59]. The evaluation and thermochemical data by Gürler and Pratt were accepted but it was discovered in reprocessing their thermochemical data that at temperatures above 3200K the face-centred cubic phase reappeared (i.e., became stable) when $0.4 \leq X_{Rh} \leq 0.5$. Since this is physically unreasonable, the limitation that $0.54 \leq X_{Rh} \leq 1$ for the equations representing the fcc-phase was made.

The Mo-Rh phase diagram is shown in Figure 3-27. It should be noted that the model from Gürler and Pratt does not account for the compounds MoRh and $MoRh_3$, which do exist at lower temperatures[60]. Giessen et al. showed that a 50 at.% Mo-50

---

* Once again the summary by Okamoto[59] contains a typographical error, namely that the second part of the expression for the excess properties of the cph phase has the signs reversed on both constants.

at.% Rh alloy annealed at 1223K for 36 hours exhibited an ordered oP4 structure*. They also interpreted previous results by Anderson and Hume-Rothery[58] to indicate the presence of $MoRh_3$, and suggested a structure type of hP8†.

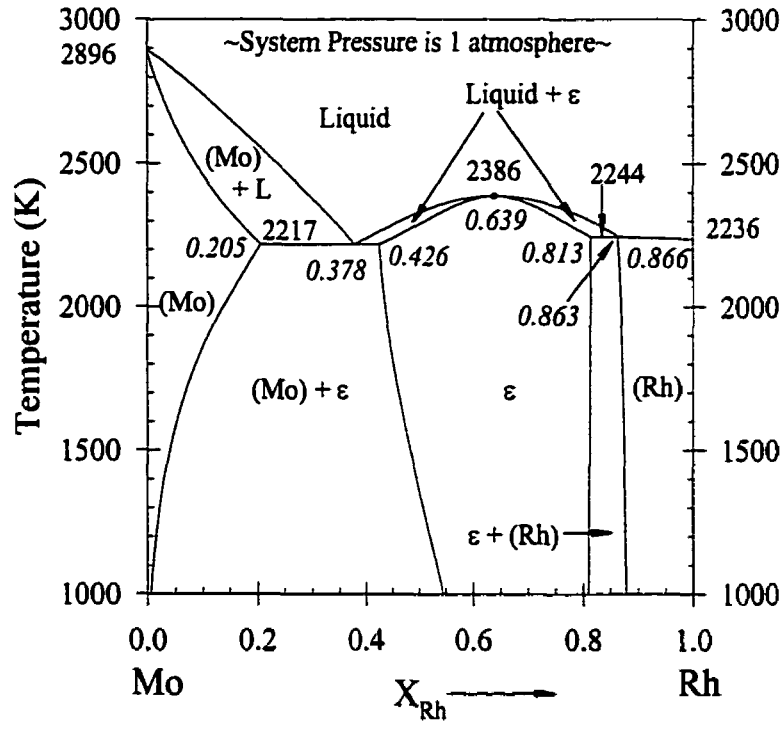

Figure 3-27. The Mo-Rh system computed using the data of Gürler and Pratt[32], with appropriate compositional limitations placed on the data for the fcc phase.

3.5.3 Including MoRh and $MoRh_3$ into an Improved Evaluation

The current accepted evaluation for the Mo-Rh binary system, that included data estimated for the compounds MoRh and $MoRh_3$, was evaluated specifically for this work and is shown in Figure 3-28. It can be seen that above 1500K the diagrams shown in Figure 3-27 and Figure 3-28 are identical.

---

*This is a simple orthorhombic structure. Giessen et al.[60] reported it by the Strukturbericht designation B19-MgCd.

† A simple hexagonal structure, reported by Giessen et al.[60] as Strukturbericht designation $D0_{19}$-$MgCd_3$.

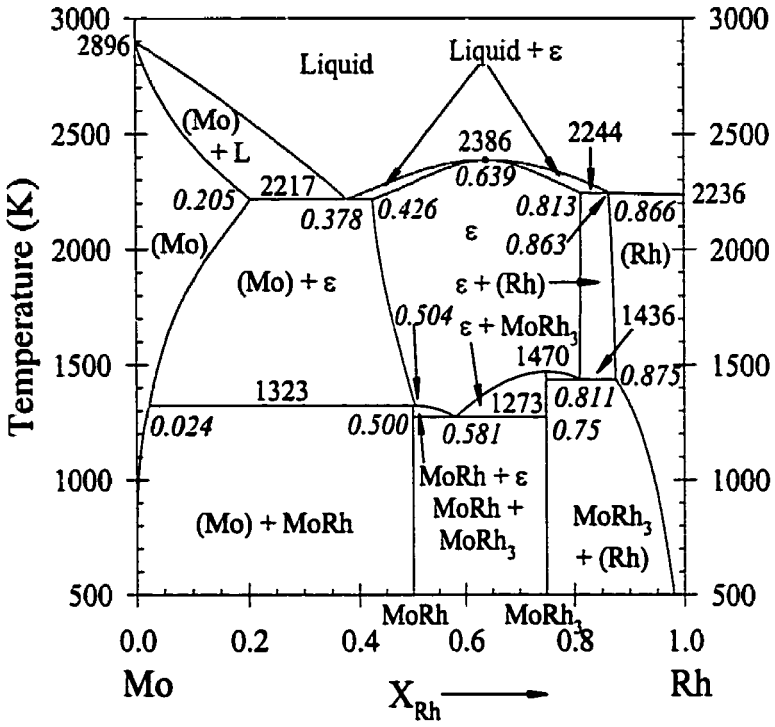

Figure 3-28. The Mo-Rh system incorporating the models of Gürler and Pratt[32], and also the data estimated for the compounds MoRh and $MoRh_3$.

3.5.4 Thermodynamic Properties for Mo-Rh Binary System

The excess properties of mixing for the four solution phases in the Mo-Rh system are [32]:

$$\Delta G^{E}_{Liquid} = X_{Mo}X_{Rh}\begin{bmatrix}-60261.04-84654.63X_{Rh}-27.78X^{2}_{Rh}\\-\left(-18.39-44.14X_{Rh}-0.22X^{2}_{Rh}\right)T\end{bmatrix}\ \text{J/mol} \qquad (3.16)$$

$$\Delta G^{E}_{bcc} = X_{Mo}X_{Rh}\left[22507.43-41776.92X_{Rh}-\left(5.48+7.67X_{Rh}\right)T\right]\ \text{J/mol} \qquad (3.17)$$

$$\Delta G^{E}_{fcc} = X_{Mo}X_{Rh}\left[110113.559-199401.5X_{Rh}-\left(65.004-99.42X_{Rh}\right)T\right]\ \text{J/mol} \qquad (3.18)$$

$$\Delta G^{E}_{cph} = X_{Mo}X_{Rh}\left[-8453.152-60006.5X_{Rh}-\left(5.495-25.872X_{Rh}\right)T\right]\ \text{J/mol} \qquad (3.19)$$

For the compounds, MoRh and $MoRh_3$, the Gibbs energy expressions used were:

$$\Delta G^{\circ}_{MoRh} = -47100+16.7477T\ \text{J/mol (per ½ mol of MoRh)} \qquad (3.20)$$

$$\Delta G^{\circ}_{MoRh_3} = -50339.2+20T\ \text{J/mol (per ¼ mol of } MoRh_3) \qquad (3.21)$$

Note that equations **(3.20)** and **(3.21)** refer to molybdenum and rhodium in their liquid states (i.e, $Mo_{(liq)}$ and $Rh_{(liq)}$). These equations were derived in a manner that provided a peritectoid reaction at 1323K, and eutectoid reactions at 1273K and 1436K.

A plot of the Gibbs energy of mixing curves for the four solution phases and the two stoichiometric compounds of the Mo-Rh system at 1800K is shown in Figure 3-29.

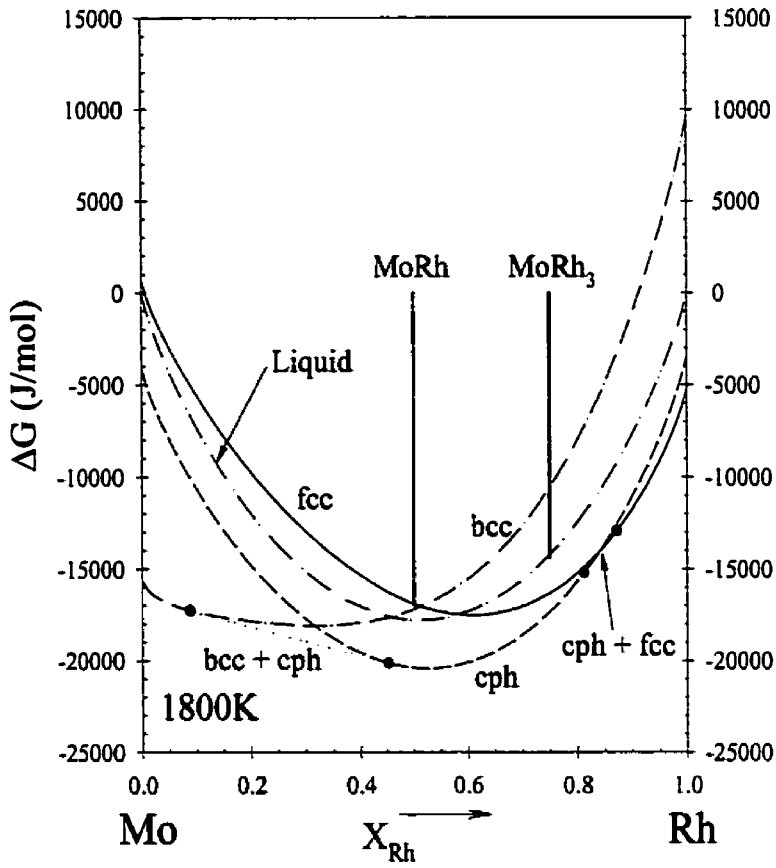

Figure 3-29. Gibbs Energy Isotherm at 1800K for Mo-Rh system.

3.6 Mo-Ru

3.6.1 Previous Studies of the Mo-Ru System

Anderson and Hume-Rothery[61] studied the Mo-Ru system using X–ray diffraction and classic metallographic techniques. They characterized this system with a

body-centred cubic phase on the Mo-rich side, a close-packed hexagonal phase on the Ru-rich side, and an intermediate tetragonal phase (σ-phase) with the approximate stoichiometry of Mo_5Ru_3. Their proposed equilibrium diagram is shown in Figure 3-30, but it should be noted that a thermodynamic evaluation was not offered by these authors.

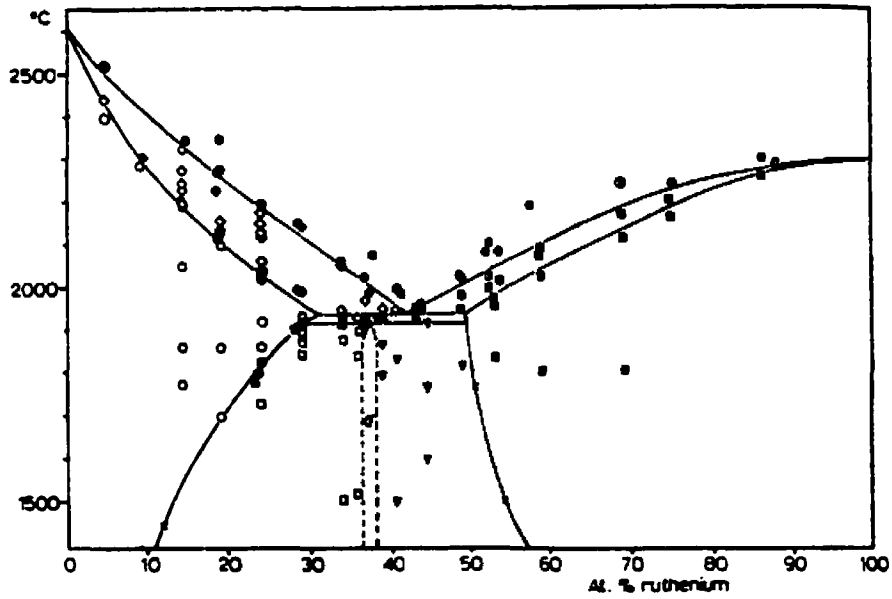

Molybdenum–ruthenium equilibrium diagram. × refer to X-ray points. The full points refer to specimens analysed after the experiments. For the open points, the compositions are either taken to be the same as the analytical values for another specimen of the same bar, or are the synthetic values: ○, α-Mo; ◐, quenched liquid; ◊, α-Mo + liquid; □, α-Mo + σ; ⊟, α-Ru; ▣, α-Ru + liquid; ◇, α-Ru + σ; △, α-Mo + α-Ru.

Figure 3-30. Mo-Ru equilibrium diagram from Anderson and Hume-Rothery[61].

An investigation of the ternary systems molybdenum-rhenium-niobium and molybdenum-rhenium-ruthenium by Kieffer and Sedlatschek[62] generally confirmed the features proposed by Anderson and Hume-Rothery[61] for the Mo-Ru binary system. One important distinction between the two diagrams is that Kieffer and Sedlatschek centred the σ-phase at a stoichiometry of Mo_3Ru_2, while Anderson and Hume-Rothery placed the σ-phase at Mo_5Ru_3. Furthermore, Kieffer and Sedlatschek proposed an eutectoid reaction involving $\sigma \rightarrow Mo_{(bcc)} + Ru_{(cph)}$ at approximately 1550K. The equilibrium diagram that was proposed by Kieffer and Sedlatschek is shown in Figure 3-31.

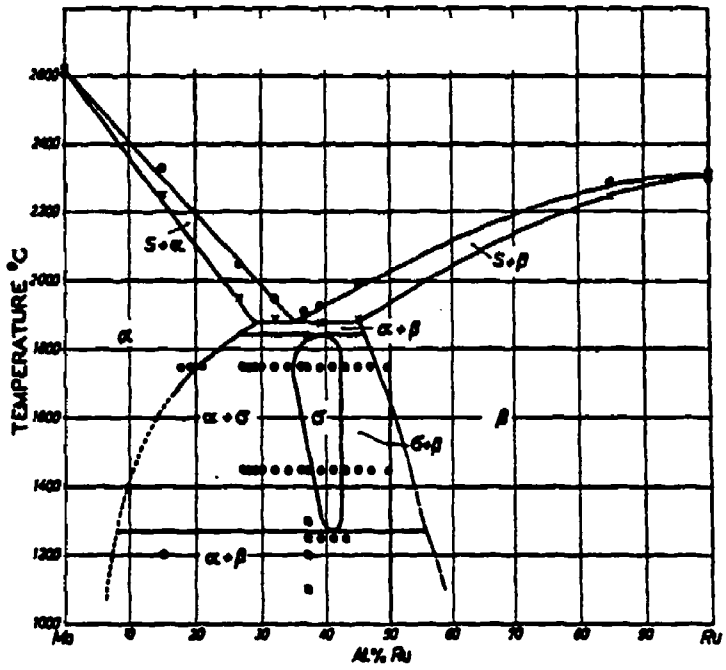

Figure 3-31. Equilibrium diagram proposed by Kieffer and Sedlatschek[62].

Rand and Potter[35] based their modelling efforts on the experimentally determined features depicted in Figure 3-32. In this work they treated the σ-phase as a stoichiometric (line) compound with the composition Mo_5Ru_3.

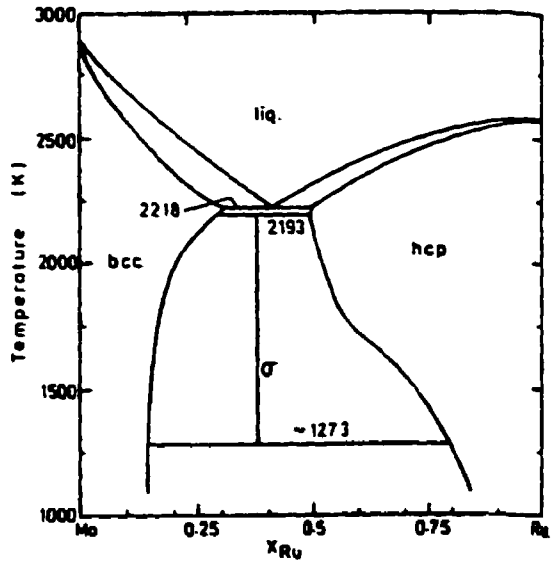

Figure 3-32. Experimentally based phase diagram for Mo-Ru, from which Rand and Potter derived a mathematical model[35].

The phase diagram that was mathematically determined by Rand and Potter is shown in Figure 3-33. It can be seen that the solidus and liquidus lines did not provide as narrow a two phase region as that suggested by the experimental results which were graphically represented in Figure 3-32. While Rand and Potter conceded this point, they maintained that for their purposes the temperature range of interest was below 2200K, and that in this region reasonable agreement was demonstrated between Figure 3-32 and Figure 3-33. They also pointed to the limited amount of thermodynamic data published for this system as a factor hindering the development of a better thermodynamic model. Unfortunately, as was the case for their model of the Mo-Pd system, the parameters derived for this model were not published in the literature[35].

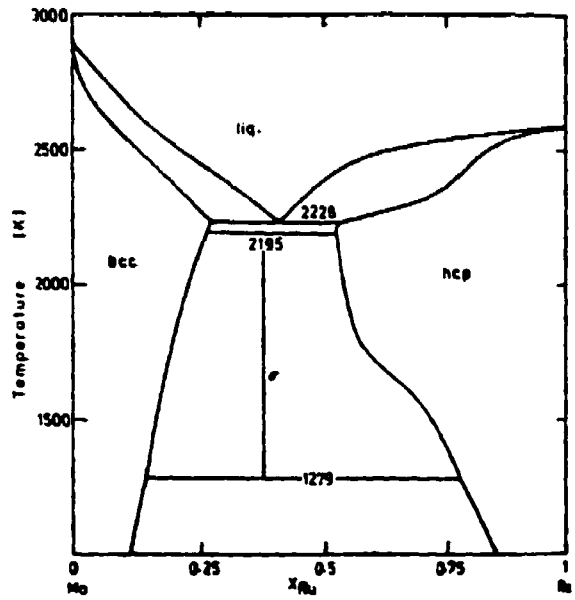

Figure 3-33. The phase diagram for Mo-Ru as modelled by Rand and Potter[35].

A second intensive experimental examination of the Mo-Ru binary system was undertaken by Kleykamp[47,63,64], and these experiments, while including traditional techniques such as metallography, X-ray diffraction, and DTA to establish phase boundaries, also employed the emf method to measure thermodynamic properties.

By using DTA, Kleykamp established that the eutectic temperature in this system was 2228K ±10K. Also using the DTA and dilatometry, the peritectoid and eutectoid reactions that involve bcc-solid rich Mo, cph-solid rich Ru, and σ phases, were determined to occur at 2188K and 1416K, respectively[63].

Results from the X–ray microanalysis (XMA) of a series of alloys heat treated at various temperatures, were used to graphically determine the solvus lines in the Mo-Ru system[63]. These results, along with the DTA and dilatometry results, are shown in Figure 3-34.

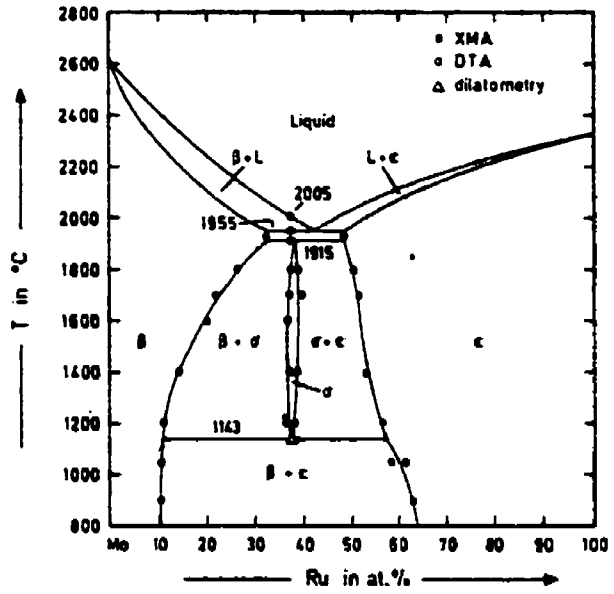

Figure 3-34. Experimental results from Kleykamp[63].

Using the solid galvanic cell schematically shown in **(3.22)**, the relative partial molar Gibbs energy of molybdenum in the Mo-Ru system was measured from 1150K to 1350K.

$$(-)\,Re\left|Fe, FeO_{0.95}\right|Zr(Ca)O_2\left|MoO_2, Mo-Ru\ alloy\right|Re\,(+) \qquad \textbf{(3.22)}$$

The relative partial molar excess Gibbs energy of molybdenum with respect to

bcc-Mo at infinite dilution in ruthenium was reported as follows: at 1200K, $\Delta\overline{G}^{E}_{Mo,w.r.t.bcc} = -43$ kJ/mol, and at 1300K, $\Delta\overline{G}^{E}_{Mo,w.r.t.bcc} = -40$ kJ/mol.

3.6.2 The Current ASM Evaluation

The current evaluation published by the ASM[28] is presented in Figure 3-35. This evaluation is derived completely from the graphically representation proposed by Kleykamp[63], and as yet, a thermodynamic model has not been published in the literature.

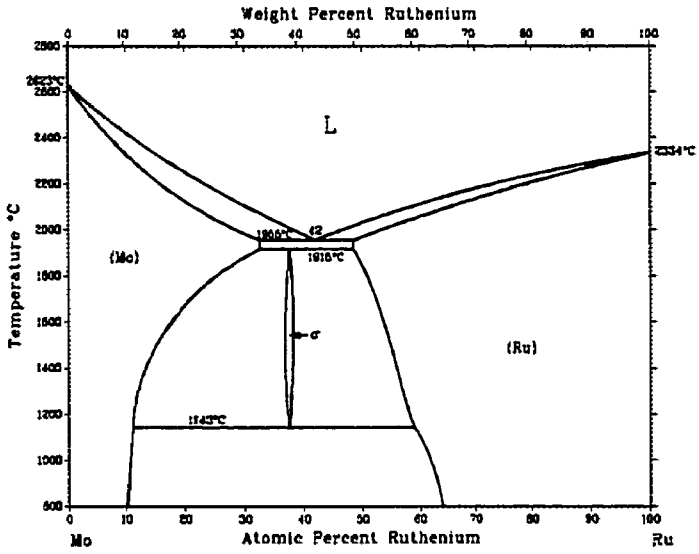

Figure 3-35. Mo-Ru equilibrium diagram from BAPD[28].

3.6.3 Evaluation for the Mo-Ru System Original to this Work

An original thermodynamic model was evaluated for the Mo-Ru system, as part of this thesis. Since there was limited thermodynamic data available[64], and only two major experimental papers (Anderson and Hume-Rothery[61] and Kleykamp[63]), there were not any major conflicting data that had to be resolved*. Instead, by using the lowest

---

* For an example of conflicting data, the reader is referred to the Mo-Pd system, where the conflicting data involved the possible existence of $MoPd_2$ and Mo_3Pd at lower temperatures, or the Pd-Ru system, where an intermediate compound was proposed in an early investigation.

common tangent approach, equilibria between the bcc-solid and cph-solid were established using the features proposed by Kleykamp[63] and illustrated on Figure 3-34. As a further defining condition for the thermodynamic model, the relative partial molar excess Gibbs energies of molybdenum at infinite dilution in ruthenium that had been measured by Kleykamp at 1200K and 1300K[64], were used. This original evaluation is shown in Figure 3-36. The σ-phase is treated as a stoichiometric (line) compound with composition Mo_5Ru_3.

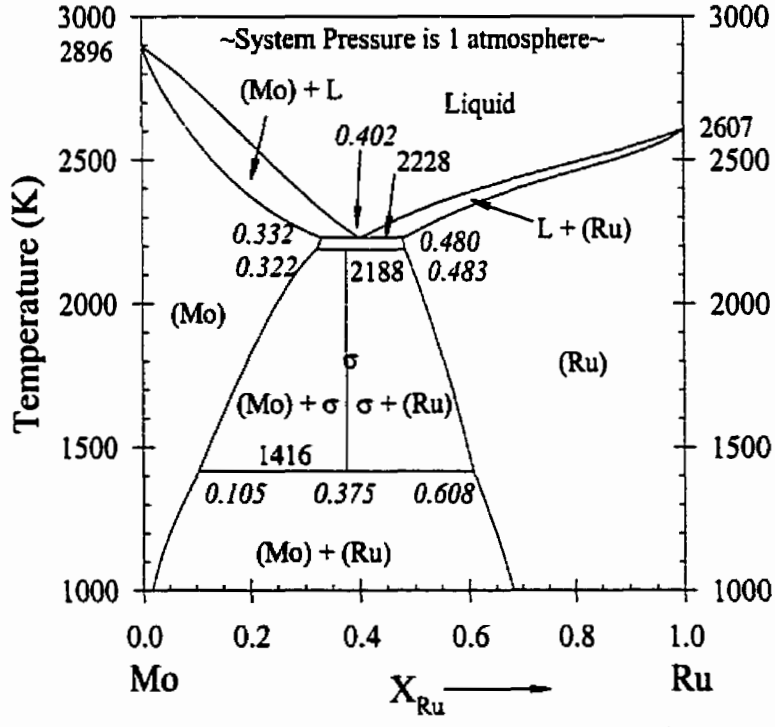

Figure 3-36. The Mo-Ru system as evaluated for this work.

3.6.4 Thermodynamic Properties for Mo-Ru Binary System

The excess properties of mixing for the solution phases in the Mo-Ru system are:

$$\Delta G^{E}_{Liquid} = X_{Mo}X_{Ru}\left[-46277+26370X_{Ru}\right] \text{ J/mol} \quad (3.23)$$

$$\Delta G^{E}_{bcc} = X_{Mo}X_{Ru}\left[33863+730.47X_{Ru}-18.335T\right] \text{ J/mol} \quad (3.24)$$

$$\Delta G^{E}_{cph} = X_{Mo}X_{Ru}\left[78174-169180X_{Ru}-(50-80X_{Ru})T\right] \text{ J/mol} \quad (3.25)$$

$$\Delta G^{E}_{fcc} = X_{Mo} X_{Ru} [15000] \text{ J/mol} \quad (3.26)$$

As mentioned previously, Kleykamp provided partial molar excess Gibbs energies at infinite dilution of Mo in cph-Ru solid solution[47,63]. From **(3.25)**, the partial molar excess Gibbs energy for Mo with respect to cph-solid is given by:

$$\Delta \overline{G}^{E}_{Mo,\,w.r.t.\,cph} = X^{2}_{Ru} \left[247354 - 338360 X_{Ru} - (130 - 160 X_{Ru}) T \right] \text{ J/mol} \quad (3.27)$$

At infinite dilution of Mo, $X_{Ru} = 1$, and **(3.27)** simplifies to:

$$\Delta \overline{G}^{E}_{Mo,\,w.r.t.\,cph} = [-91006 + 30T] \text{ J/mol} \quad (3.28)$$

Kleykamp reported that $\Delta \overline{G}^{E}_{Mo,\,w.r.t.\,bcc} = -43$ kJ/mol and -40 kJ/mol, at 1200K and 1300K, respectively[64]. By solving **(3.28)** and using the difference in Gibbs energy from Table 2-6 to convert from cph-solid as the reference state in **(3.28)**, to a bcc-solid reference state (in other words: +11550 J/mol), values of $\Delta \overline{G}^{E}_{Mo,\,w.r.t.\,bcc} = -43.46$ kJ/mol and –40.46 kJ/mol, at 1200K and 1300K, respectively, were obtained.

For the compound Mo_5Ru_3, $\Delta H^{\circ}_{298} = 35440$ J/mol, $S^{\circ}_{298} = 290.1092$ J/mol·K and $C_P = 221.0131 - 0.02404T - \frac{2548550}{T^2} + 3.05593 \times 10^{-5} T^2$ J/mol·K (all values per mol Mo_5Ru_3). The C_P expression for Mo_5Ru_3 was calculated from the C_P data for Mo and Ru.

$$C_{P\,Mo_5Ru_3} = 5C_{P\,Mo_{(bcc)}} + 3C_{P\,Ru_{(cph)}} \quad (3.29)$$

The expression $\Delta G^{\circ}_{Mo_5Ru_3} = 4430 - 7.68495T$ J/mol, (per mol of $Mo_{\frac{5}{8}}Ru_{\frac{3}{8}}$, with respect to $Mo_{(bcc)}$ and $Ru_{(cph)}$) was used to calculate ΔH°_{298} and S°_{298}. For ΔH°_{298}, the following equation was used:

$$\Delta H^{\circ}_{298} = 8(4430) = 35440 J / mol_{Mo_5Ru_3} \quad (3.30)$$

For S°_{298} the relationships expressed in **(3.31)** and solved in **(3.32)** were used.

$$\Delta S^{\circ}_{298\ Mo_5Ru_3} = S^{\circ}_{298\ Mo_5Ru_3} - 5S^{\circ}_{298\ Mo} - 3S^{\circ}_{298\ Ru} \quad (3.31)$$

$$S^{\circ}_{298\ Mo_5Ru_3} = 8(7.68495) + 5(28.605) + 3(28.53488) = 290.1092 J/K/mol_{Mo_5Ru_3} \quad (3.32)$$

A plot of the Gibbs energy of mixing curves for the four solution phases and the compound Mo_5Ru_3 of the Mo-Ru system at 1800K is shown in Figure 3-37.

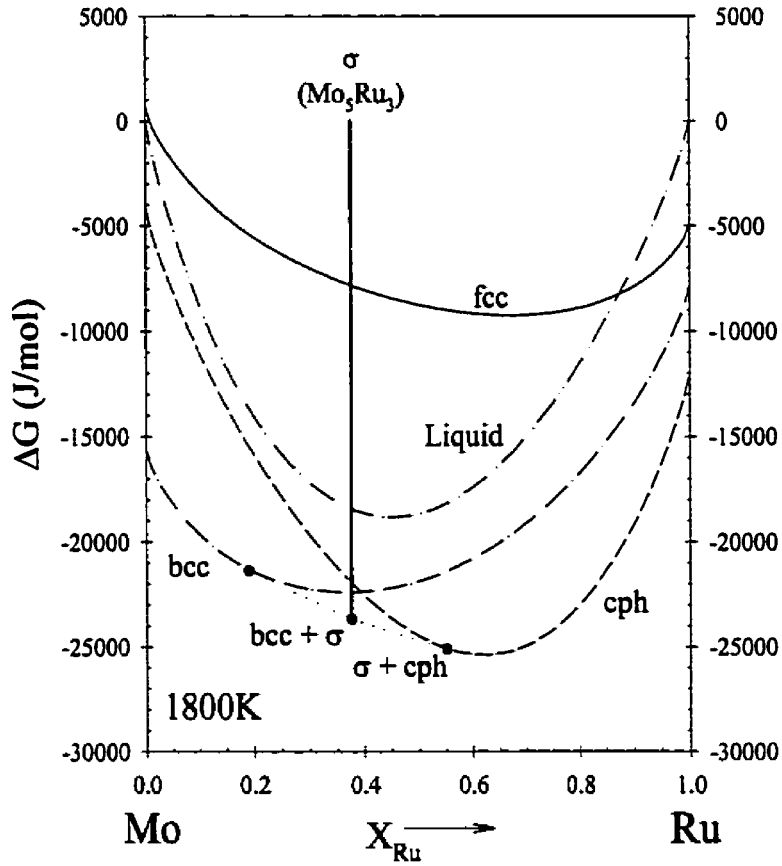

Figure 3-37. Gibbs Energy Isotherm at 1800K for Mo-Ru system.

In order to assess the validity of the proposed evaluation, it was necessary to critically compare the proposed phase diagram with previous experimental work. As was shown with equations **(3.25)**, **(3.27)**, and **(3.28)**, the values measured by Kleykamp[64] were in agreement with the values that were obtained from the proposed evaluation. Furthermore, the eutectic, peritectoid, and eutectoid temperatures found by Kleykamp[63]

agree exactly with those predicted by the model. These facts are not surprising, since the proposed model was developed from these data.

However, Kleykamp also determined the positions of the solvus lines for this system using X-ray microanalysis. A comparison of these values with the proposed evaluation is shown in Figure 3-38. The boxed values shown on the diagram represent the difference between the values of Kleykamp, and those predicted by the model. Negative values indicate that the Kleykamp point is to the left (i.e., Mo-rich) of the predicted value.

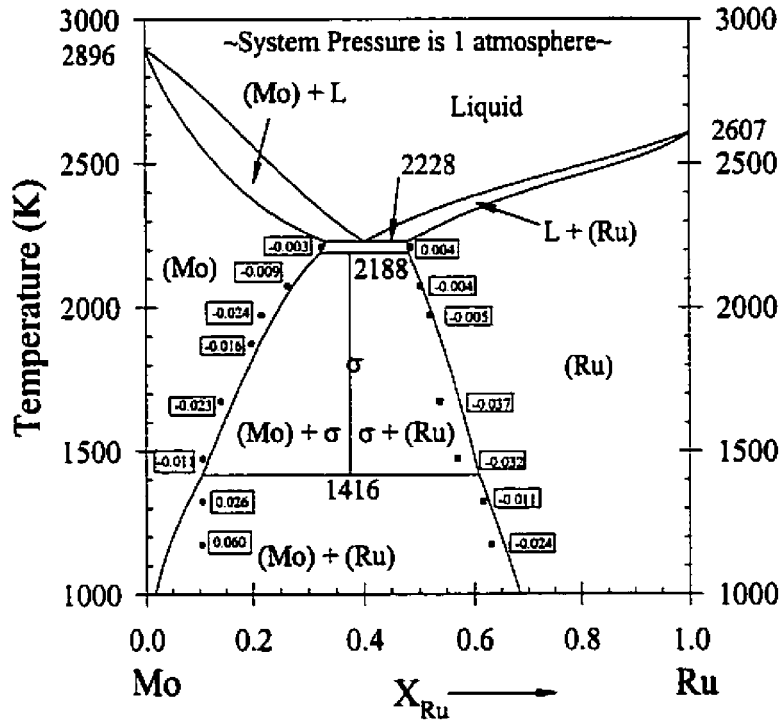

Figure 3-38. Comparison of the data of Kleykamp with the new evaluation. The boxed values represent the difference between the proposed evaluation and the data of Kleykamp. Negative values indicate that the data point from Kleykamp is to the left.

In general the agreement is respectable, as indicated by the boxed values on the diagram, which represent differences between the current evaluation and the data given by Kleykamp[63], except possibly at temperatures below 1416K on the Mo-rich side of the

diagram. The sample preparation in the work of Kleykamp[63] involved arc melting under reduced argon pressure, high purity powders of both Mo and Ru. Homogenization at various temperatures was performed under high vacuum. Discrepancies here may be a result of incomplete solid state diffusion in the alloys tested, this problem being especially relevant at lower temperatures. In his experimental work Kleykamp annealed one alloy at 1173K for seven weeks and a second alloy at 1323K for four weeks. However, if homogenization were incomplete, it would be expected that the composition of the bcc-Mo solid would be rich in Mo, while the composition of the cph-Ru solid would be light in Mo, as is the case.

Comparison of the predicted diagram with the results of Anderson and Hume-Rothery[61] are presented in Figure 3-39.

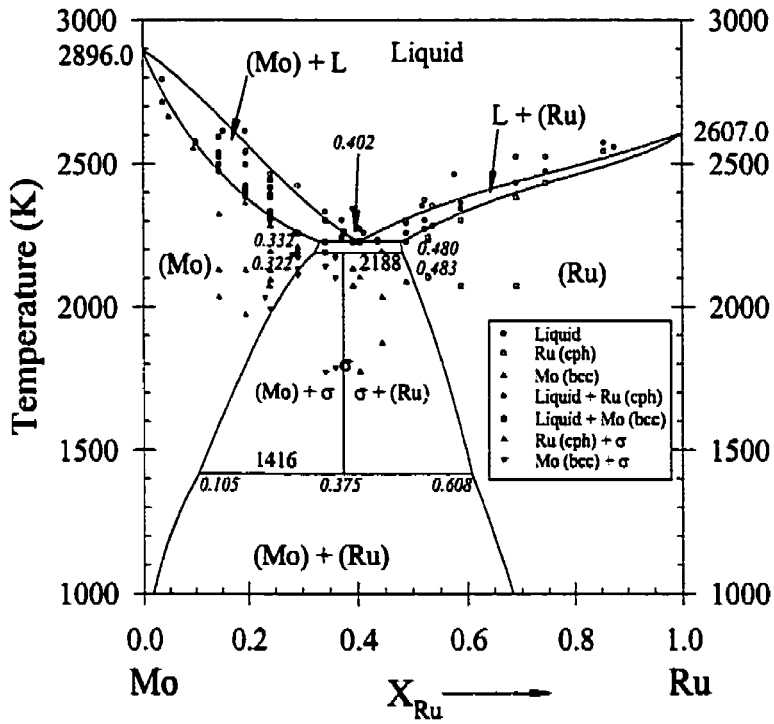

Figure 3-39. Comparison of experimental work from Anderson and Hume-Rothery[61] with the proposed evaluation of the Mo-Ru system.

In general there is good agreement between the observed phases and those predicted by the current evaluation. Discrepancies may be explained by difficulties in accurately measuring high temperatures, errors in calculating the data points as presented in the diagram of Anderson and Hume-Rothery[61], and compositional shifts of data points that could result from volatilization.

The proposed evaluation was presented at the 1998 Topical Meeting of the American Nuclear Society and published as part of the conference proceedings[65]. Subsequently, Gürler[66] has published experimental results that support the position of the solvus lines below the eutectoid temperature of 1416K. A comparison of the solvus compositions determined experimentally by Gürler[66] and those predicted by the proposed evaluation are presented in Table 3-2. The agreement shown here provides further credibility to the proposed model.

Table 3-2. Comparison of solvus compositions determined by Gürler[66] and those predicted by the current evaluation.

Temperature (K)	bcc Solvus from Gürler (at.% Ru)	bcc Solvus as Predicted (at.% Ru)	cph Solvus from Gürler (at.% Ru)	cph Solvus as Predicted (at.% Ru)
973	2.90	1.51	64.1	68.8
1073	3.25	2.72	63.5	67.2
1173	3.60	4.43	62.8	65.4
1223	3.75	5.47	62.2	64.5
1323	4.40	7.90	61.2	62.6
1388	5.25	9.69	60.4	61.4
1473	7.90	11.74	59.3	60.1

3.7 Mo-Tc

3.7.1 Previous Studies of the Mo-Tc System

Of the four binary systems that involve technetium, the Mo-Tc binary system has

been investigated the most and is also the most complex, since at least four solid phases have been identified. Although the first study to examine the system was that of Compton et al.[67], these investigators were concerned with determining the superconductivity properties of Mo-Tc alloys at extremely low temperatures.

Darby et al.[68,69] reported the first crystallographic data for eleven alloys annealed at temperatures between 773K and 1323K. Using X-ray diffraction they found that four solid phases existed, namely: a Mo-rich bcc-solid (β); a cP8 structure (κ)*; a σ-phase (tetragonal phase); and a Tc-rich cph-solid (ε). The composition of the cP8 structure was determined to lie within the narrow range of 54±2 atomic percent Tc, specifically the intermediate cubic structure must lie between $0.50 < X_{Tc} < 0.56$ at 873K, and a narrower range of $0.53 < X_{Tc} < 0.56$ at 1323K. The σ-phase, however, was found to have a wide compositional range that centred about 70 atomic percent Tc. At 973K the boundary between σ and the $\sigma + \varepsilon$ two phase region was found to be between 75 and 77 atomic percent Tc. The boundary between the σ and the $\sigma + \kappa$ two phase region was less well defined, lying between 60 – 70 at.% Tc at 973K.

The summary of molybdenum phase diagrams prepared by Brewer[25] reported the presence of five phases: the liquid, a terminal Mo-rich bcc phase extending to $X_{Tc} \approx 0.50$, a terminal Tc-rich cph phase extending to $X_{Tc} \approx 0.85$, an intermediate tetragonal phase centred at $X_{Tc} = 0.70$, and another intermediate cubic solid at $X_{Tc} = 0.55$. The equilibrium phase diagram proposed by Brewer is shown in Figure 3-40.

---

* Reported as an A15-Cr_3O type simple cubic structure by Darby and Zegler[68].

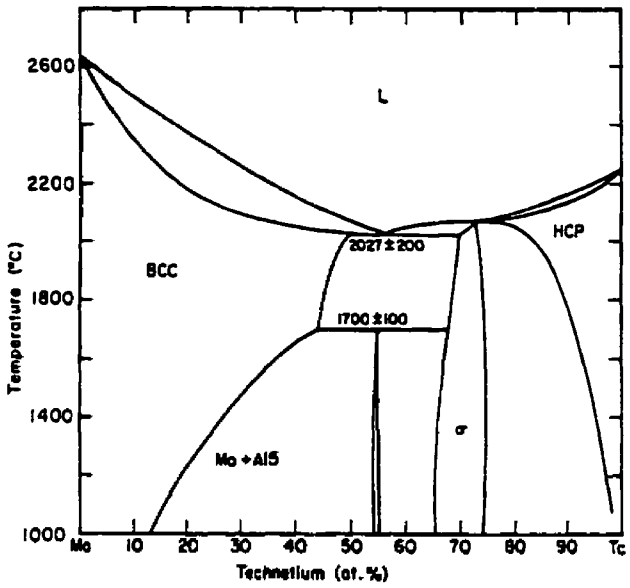

Figure 3-40. Mo-Tc equilibrium diagram as presented by Brewer[25].

As mentioned in **Section 2.4-Technetium**, experimental work with Tc is difficult. It is often useful to exploit the chemical similarities that exist between technetium and rhenium (both are group VIIB). By comparing Figure 3-40 to the Mo-Re phase diagram shown in Figure 3-41, similar features are apparent, although the σ-phase has shifted towards the higher Mo concentrations.

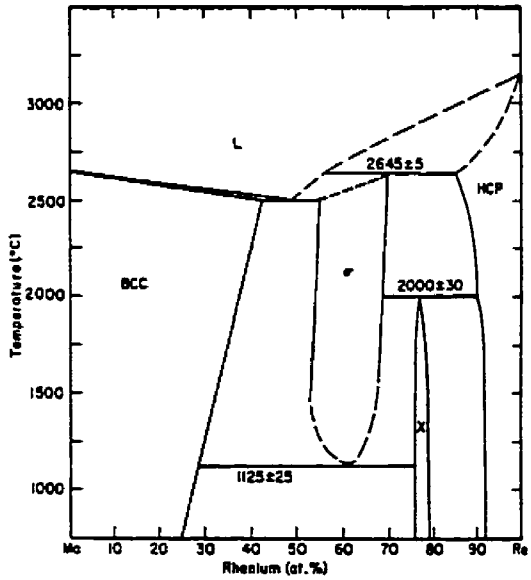

Figure 3-41. The equilibrium diagram for Mo-Re, as proposed by Brewer[25].

The current evaluation published by the ASM[28] is presented in Figure 3-42.

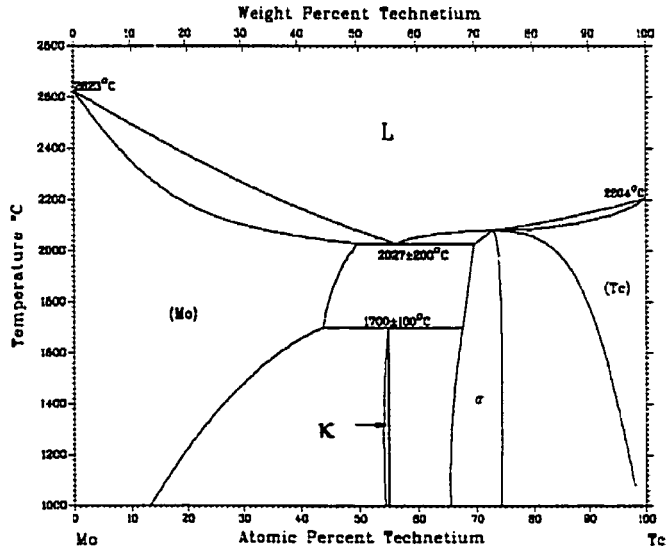

Figure 3-42. Mo-Tc equilibrium diagram from BAPD[28].

3.7.2 Evaluation for the Mo-Tc System Original to this Work

The foundations for the Mo-Tc evaluation were developed by considering data proposed by Brewer[25]. His attempt to define the liquidus over the complete compositional range was unsuccessful. Instead he suggested that the thermodynamic behaviour of the liquid for X_{Tc} = 0-0.67, could be represented by:

$$\ln \gamma_{Mo} = X_{Tc}^2 \left(\frac{100}{T} - 400 X_{Tc} \right) \tag{3.33}$$

and

$$\ln \gamma_{Tc} = X_{Mo}^2 \left(\frac{-500}{T} + \frac{400 X_{Mo}}{T} \right) + \frac{50}{T} \tag{3.34}$$

while for X_{Tc} = 0.67-1, the liquid behaviour was defined by:

$$\ln \gamma_{Mo} = X_{Tc}^2 \left(\frac{-325}{T} + \frac{350 X_{Tc}}{T} \right) - \frac{33}{T} \tag{3.35}$$

and

$$\ln \gamma_{Tc} = X_{Mo}^2 \left(\frac{200}{T} - \frac{350 X_{Mo}}{T} \right) \tag{3.36}$$

By considering these four equations, the critical temperatures and compositions for the eutectic and eutectoid reactions, and being mindful of the experimentally determined solubility limits for the σ-solid phase, it was possible to mathematically determine the equilibrium phase diagram. In this assessment the intermediate cubic structure, κ, was treated as a stoichiometric (line) compound, Mo_9Tc_{11}.

The Mo-Tc phase diagram is developed as shown in Figure 3-43. It can be seen from this diagram that the compositional requirements suggested by Darby et al.[68,69] are respected at 873K and 973K.

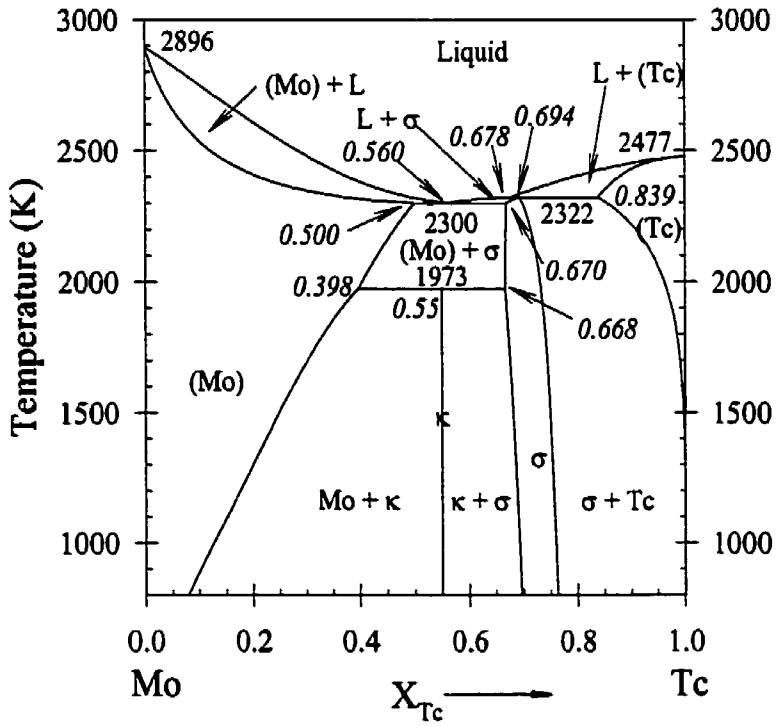

Figure 3-43. The Mo-Tc system as evaluated for this work.

3.7.3 Thermodynamic Properties for Mo-Tc Binary System

The excess properties of mixing for the solution phases in the Mo-Tc system are:

$$\Delta G^{E}_{Liquid} = X_{Mo}X_{Tc}\left[-4904.1+21680X_{Tc}\right] \text{ J/mol} \qquad \textbf{(3.37)}$$

$$\Delta G^{E}_{bcc} = X_{Mo}X_{Tc}\left[-3882.8-21442X_{Tc}+(11+11X_{Tc})T\right] \text{ J/mol} \quad \textbf{(3.38)}$$

$$\Delta G^{E}_{cph} = X_{Mo}X_{Tc}\left[59650+27437X_{Tc}-(20+10X_{Tc})T\right] \text{ J/mol} \quad \textbf{(3.39)}$$

$$\Delta G^{E}_{tetragonal} = X_{Mo}X_{Tc}\left[-28106-150380X_{Tc}-(10-50X_{Tc})T\right] \text{ J/mol} \quad \textbf{(3.40)}$$

$$\Delta G^{E}_{fcc} = X_{Mo}X_{Tc}\left[0+(0)T\right] \text{ J/mol} \quad \textbf{(3.41)}$$

For the compound, κ, Mo_9Tc_{11}, the following Gibbs energy expressions was used:

$$\Delta G^{\circ}_{Mo_9Tc_{11}} = \left[-42794.3+13.8253T\right] \text{ J/mol per } \tfrac{1}{20}\text{ mol } Mo_9Tc_{11} \quad \textbf{(3.42)}$$

Note that equation **(3.42)** refers to formation from molybdenum and technetium in their liquid states (i.e, $Mo_{(liq)}$ and $Tc_{(liq)}$).

A plot of the Gibbs energy of mixing curves for the five solution phases and one stoichiometric compound from the Mo-Tc system at 1800K is shown in Figure 3-44.

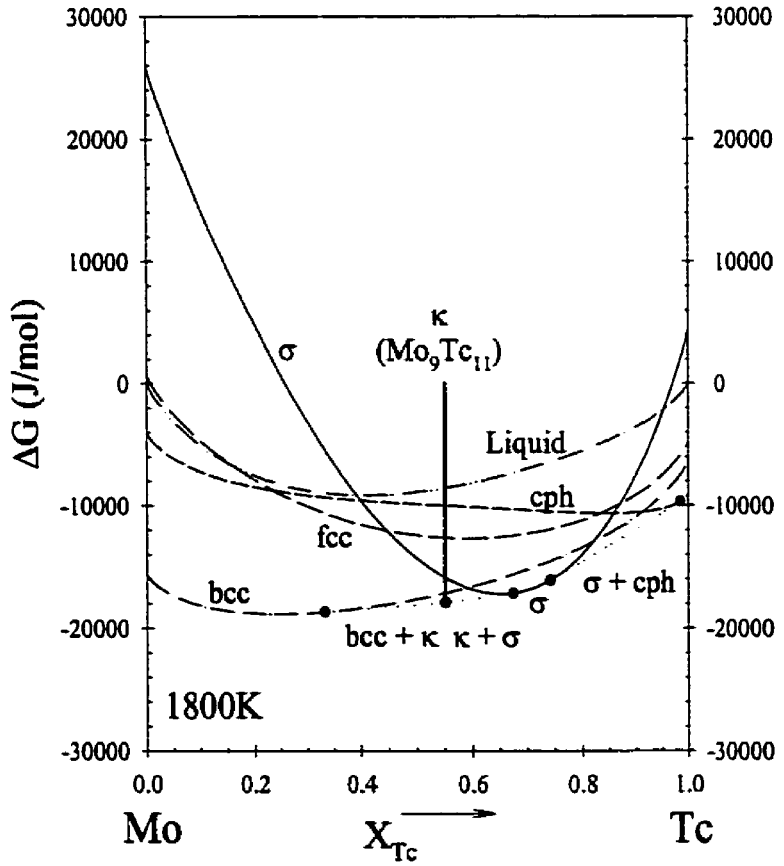

Figure 3-44. Gibbs Energy Isotherm at 1800K for Mo-Tc system.

3.8 Pd-Tc

3.8.1 Previous Studies of the Pd-Tc System

Experimental work in the Pd-Tc system has been very limited. It was speculated by Ageev et al.[70] and verified by others (e.g., Compton et al.[67] and Darby et al.[69]) that the alloying behaviour of rhenium and technetium would be similar, as they are both Group VIIB elements (i.e., the Mn group). Because of this similarity, it is speculated that the system will exhibit a peritectic reaction. It should be noted that Pd has a tendency to this behaviour with other hexagonal transition metals (e.g., Pd-Ru, Pd-Os, and Pd-Re[28]).

In 1962 Darby et al.[71] studied the system by examining, with X-ray metallography, alloys that had previously been annealed for 7 days at 1323K. The results suggested that the maximum compositional variation for the two phase mixture of terminal fcc-Pd and terminal cph-Tc lay in the range $0.5 < X_{Pd} < 0.75$. Furthermore, two phases were identified at $X_{Pd} = 0.666$.

A similar study in 1963 by Niemiec[72] examined alloys that were annealed for 20 hours at 1773K. From this work, the solvus between the terminal fcc-Pd and the two phase region must lie in the range $0.684 < X_{Pd} < 0.75$, approximately at $X_{Pd} = 0.73$. For the solvus between the terminal cph-Tc and the two phase mixture, the boundary must lie between $0.47 < X_{Pd} < 0.565$, approximately at $X_{Pd} = 0.49$.

The current evaluation published by the ASM[28] is presented in Figure 3-45.

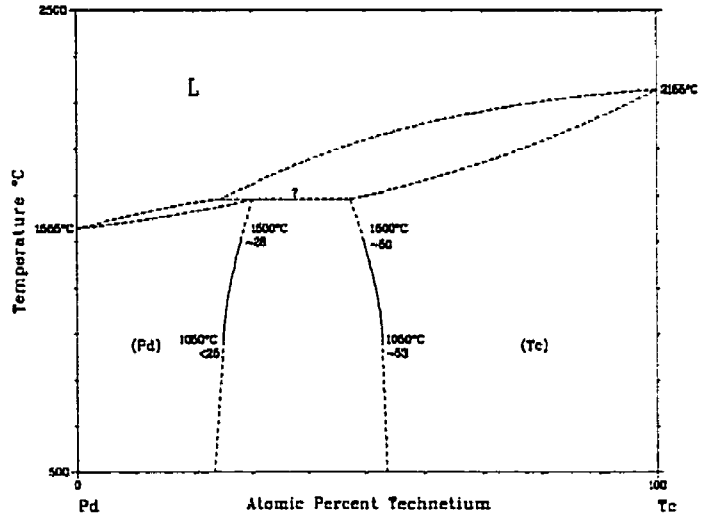

Figure 3-45. Pd-Tc equilibrium diagram from BAPD[28].

3.8.2 Evaluation for the Pd-Tc System Original to this Work

There was limited experimental data upon which to base the thermodynamic evaluation, but nonetheless, Gibbs energy expressions for the fcc-solid phase and cph-solid phase were developed from this limited data. A tie line between the fcc-solid and the cph-solid at 1773K, which satisfied the given data, was extended from the fcc-solid boundary at $X_{Pd} \cong 0.73$ and the cph-solid boundary at $X_{Pd} \cong 0.49$. At 1323K another tie line, which satisfied the data, was extended from the fcc-solid boundary at $X_{Pd} \cong 0.25$ and the cph-solid boundary at $X_{Pd} \cong 0.47$. From this information four independent equations were constructed that equated partial properties for each of the elements along these tie lines. For example, at every temperature along a tie line the partial properties of palladium in the fcc-solid and cph-solid are equal, therefore:

$$\overline{G}_{Pd}^{fcc} = \overline{G}_{Pd}^{cph} \tag{3.43}$$

which is equivalent to:

$$\left(\overline{G}_{Pd}^{fcc} - G_{Pd}^{\circ\, fcc}\right) = \left(\overline{G}_{Pd}^{cph} - G_{Pd}^{\circ\, cph}\right) + \left(G_{Pd}^{\circ\, cph} - G_{Pd}^{\circ\, fcc}\right) \quad \textbf{(3.44)}$$

Each of the three bracketed expressions were rearranged further. The first two expressions are equivalent to $RT \ln a_{Pd}$ in the particular phase. The third expression is simply the difference in the lattice stabilities of the two different phases, and is known (see **Section 2.2.2**). Therefore, equation **(3.44)** was rewritten as:

$$RT \ln X_{Pd}^{fcc} + \overline{G}_{Pd}^{E\, fcc} = RT \ln X_{Pd}^{cph} + \overline{G}_{Pd}^{E\, cph} + \left(G_{Pd}^{\circ\, cph} - G_{Pd}^{\circ\, fcc}\right) \quad \textbf{(3.45)}$$

Using the Margules formalism[73] in order to represent the excess term with a power series and a recursion relationship, the excess Gibbs energy terms in equation **(3.45)** were replaced with the following:

$$\overline{G}_{Pd}^{E\, fcc} = \left(X_{Tc}^{fcc}\right)^2 \left[(p_0 - p_1) + 2(p_1 - p_2) X_{Tc}^{fcc} + 3(p_2 - p_3)\left(X_{Tc}^{fcc}\right)^2 + \ldots\right] \quad \textbf{(3.46)}$$

$$\text{and } \overline{G}_{Pd}^{E\, cph} = \left(X_{Tc}^{cph}\right)^2 \left[(p_0 - p_1) + 2(p_1 - p_2) X_{Tc}^{cph} + 3(p_2 - p_3)\left(X_{Tc}^{cph}\right)^2 + \ldots\right] \quad \textbf{(3.47)}$$

where X_{Tc}^{fcc} and X_{Tc}^{cph} represent the concentrations of technetium at either end of the tie line, and p_0, p_1, p_2, p_3, etc., represent constants in the recursion formula. In general, there is little justification for more than two of these constants and thus values for p_2, p_3, etc. (i.e., the higher order terms) are set to zero. Equations **(3.46)** and **(3.47)** (with the higher order terms set to zero) were now substituted into equation **(3.45)** and rearranged to produce:

$$\begin{aligned} &RT \ln X_{Pd}^{fcc} - RT \ln X_{Pd}^{cph} - \left(G_{Pd}^{\circ\, cph} - G_{Pd}^{\circ\, fcc}\right) = \\ &\left(X_{Tc}^{cph}\right)^2 \left[(p_0 - p_1) + 2p_1 X_{Tc}^{cph}\right] - \left(X_{Tc}^{fcc}\right)^2 \left[(p_0 - p_1) + 2p_1 X_{Tc}^{fcc}\right] \end{aligned} \quad \textbf{(3.48)}$$

For equation **(3.48)**, the left-hand side is completely defined at a given temperature, T, and so this equation has only two unknowns, p_0 and p_1. In order to solve for p_0 and p_1 a second equation was necessary, and was derived by considering:

$$\overline{G}_{Tc}^{fcc} = \overline{G}_{Tc}^{cph} \tag{3.49}$$

which is equivalent to:

$$\left(\overline{G}_{Tc}^{fcc} - G_{Tc}^{\circ fcc}\right) = \left(\overline{G}_{Tc}^{cph} - G_{Tc}^{\circ cph}\right) + \left(G_{Tc}^{\circ cph} - G_{Tc}^{\circ fcc}\right) \tag{3.50}$$

By a similar mathematical procedure as outlined above, equation **(3.50)** was expressed as:

$$\begin{aligned} &RT\ln X_{Tc}^{fcc} - RT\ln X_{Tc}^{cph} - \left(G_{Tc}^{\circ cph} - G_{Tc}^{\circ fcc}\right) = \\ &\left(X_{Pd}^{cph}\right)^2\left[p_0 + 2p_1 X_{Tc}^{cph}\right] - \left(X_{Pd}^{fcc}\right)^2\left[p_0 + 2p_1 X_{Tc}^{fcc}\right] \end{aligned} \tag{3.51}$$

Solving equations **(3.48)** and **(3.51)** simultaneously gave values for p_0 and p_1 at a particular T. This process was repeated at a second temperature, which allowed a temperature dependence term to be introduced for both p_0 and p_1. In other words, $p_0 = A_0 + B_0 T$ and $p_1 = A_1 + B_1 T$. Once values for p_0 and p_1 were derived, a tentative phase diagram was determined.

Once tentative Gibbs energy expressions for the two solids had been determined, the liquid phase was introduced in a similar manner. Finally, fine adjustments to all the constants in the excess Gibbs energy expressions for some or all of the phases were made to better represent the features of the equilibrium phase diagram (e.g., an appropriate peritectic temperature).

The Pd-Tc phase diagram, evaluated as described above, is shown in Figure 3-46.

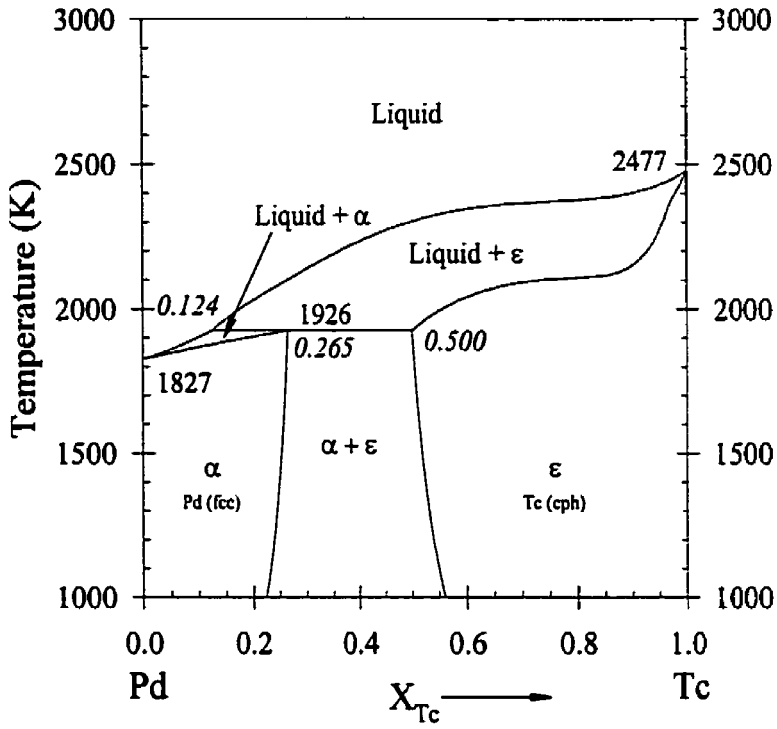

Figure 3-46. The Pd-Tc phase diagram as evaluated for this work.

A visual comparison of the phase diagram presented in Figure 3-46, above, and Figure 3-45, the diagram published by the ASM, reveals an obvious discrepancy between the solidus and liquidus lines as they approach the melting temperature of Tc. In order to resolve this, it is necessary to apply the following thermodynamic principle:

$$\overline{G}_{Tc}^{Liquid} = \overline{G}_{Tc}^{Solid} \tag{3.52}$$

where $\overline{G}_{Tc}^{Liquid}$ represents the partial Gibbs energy of Tc at the liquidus and $\overline{G}_{Tc}^{Solid}$ represents the partial Gibbs energy of Tc at the solidus. This is equivalent to:

$$\left(\overline{G}_{Tc}^{Liquid} - G_{Tc}^{\circ\ Liquid}\right) = \left(\overline{G}_{Tc}^{Solid} - G_{Tc}^{\circ\ Solid}\right) + \left(G_{Tc}^{\circ\ Solid} - G_{Tc}^{\circ\ Liquid}\right) \tag{3.53}$$

Finally, equation **(3.53)** can be re-written as:

$$\left(RT \ln X_{Tc}^{Liquid}\right) = \left(RT \ln X_{Tc}^{Solid}\right) + \left(\Delta H_{Tc}^{Melt} - T\Delta S_{Tc}^{Melt}\right) \tag{3.54}$$

where R represents the gas constant, T the temperature of interest, X_{Tc}^{Liquid} the mole

fraction of Tc at the liquidus, and X_{Tc}^{Solid} the mole fraction of Tc at the solidus.

Solving equation **(3.54)** at 2415K, where $X_{Tc}^{Liquid} \simeq 0.95$ and $X_{Tc}^{Solid} \simeq 0.99$ (taken from Figure 3-45), and using the value for $\Delta H_{Tc}^{Melt} = 33290\ J/mol$ provided in Table 2-6, a relationship for the entropy of melting for Tc can be calculated. Because the melting temperature for Tc on Figure 3-45 is 2428K, 49K below the currently excepted value of 2477K, the relationship $\Delta S_{Tc}^{Melt} = \frac{\Delta H_{Tc}^{Melt}}{T^{Melt}}$ can also be used to determine the melting temperature for Tc that will satisfy the equality expressed by equation **(3.54)**. This value for the melting temperature of Tc was calculated to be 2477K, which represents a contradiction between thermodynamic data and the ASM phase diagram. In fact the accepted value for the melting temperature of Tc is predicted.

On the other hand, using the values at 2450K from Figure 3-46, where $X_{Tc}^{Liquid} = 0.974$ and $X_{Tc}^{Solid} = 0.993$, the consequent melting temperature of Tc is 2481K, which is excellent agreement to the accepted value of 2477K. This means that the construction of the liquidus and solidus, illustrated in Figure 3-46, is self-consistent, while the dotted construction shown in Figure 3-45 is not.

A comparison of the current evaluation with the experimental work of Darby et al.[71] and Niemiec[72] is shown in Figure 3-47. The diagram is consistent with the limited experimental work. The position of the two phase region at 1323K suggested by Darby et al.[71] is correct. Furthermore, the boundaries proposed by Niemiec[72] at 1773K are respected.

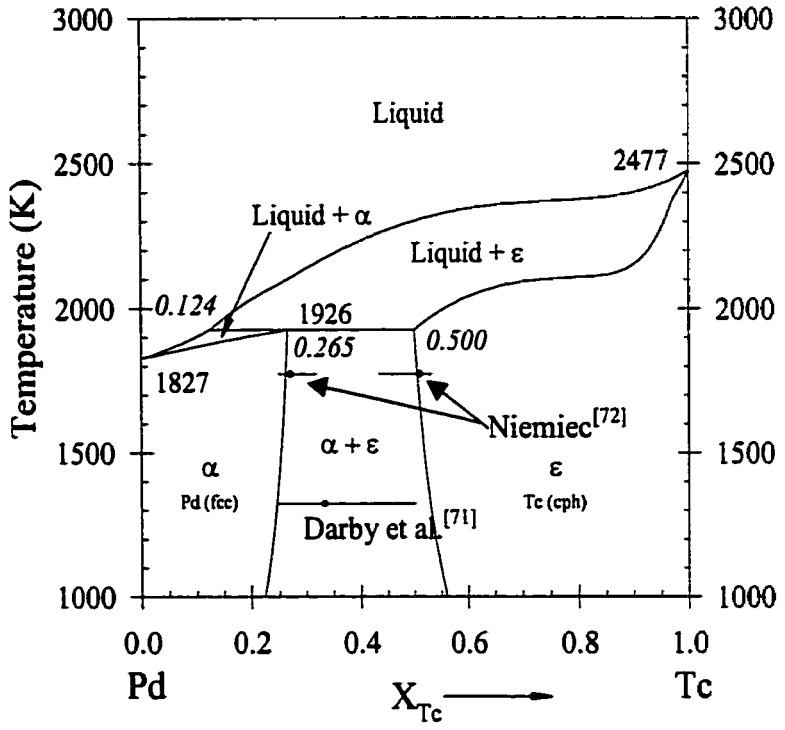

Figure 3-47. Comparison of Pd-Tc phase diagram as evaluated for this work with experimental data from Darby et al.[71] and Niemiec[72].

3.8.3 Thermodynamic Properties for Pd-Tc Binary System

The excess Gibbs energies for the four phases in the Pd-Tc system are:

$$\Delta G^{E}_{Liquid} = X_{Pd}X_{Tc}\left[187564 - 62169.3X_{Pd} - (63.661 - 6.64X_{Pd})T\right] \text{ J/mol} \quad \textbf{(3.55)}$$

$$\Delta G^{E}_{fcc} = X_{Pd}X_{Tc}\left[-500 + 12T\right] \text{ J/mol} \quad \textbf{(3.56)}$$

$$\Delta G^{E}_{cph} = X_{Pd}X_{Tc}\left[-5962.7 + 4296X_{Tc} - (12.92 - 27.13X_{Tc})T\right] \text{ J/mol} \quad \textbf{(3.57)}$$

$$\Delta G^{E}_{bcc} = X_{Pd}X_{Tc}\left[20000 + 0T\right] \text{ J/mol} \quad \textbf{(3.58)}$$

The excess Gibbs energy for the bcc-solid phase required a positive term (instead of 0) to prevent the phase becoming stable at high temperatures.

A plot of the Gibbs energy of mixing curves for the four solution phases of the Pd-Tc system at 1800K is shown in Figure 3-48.

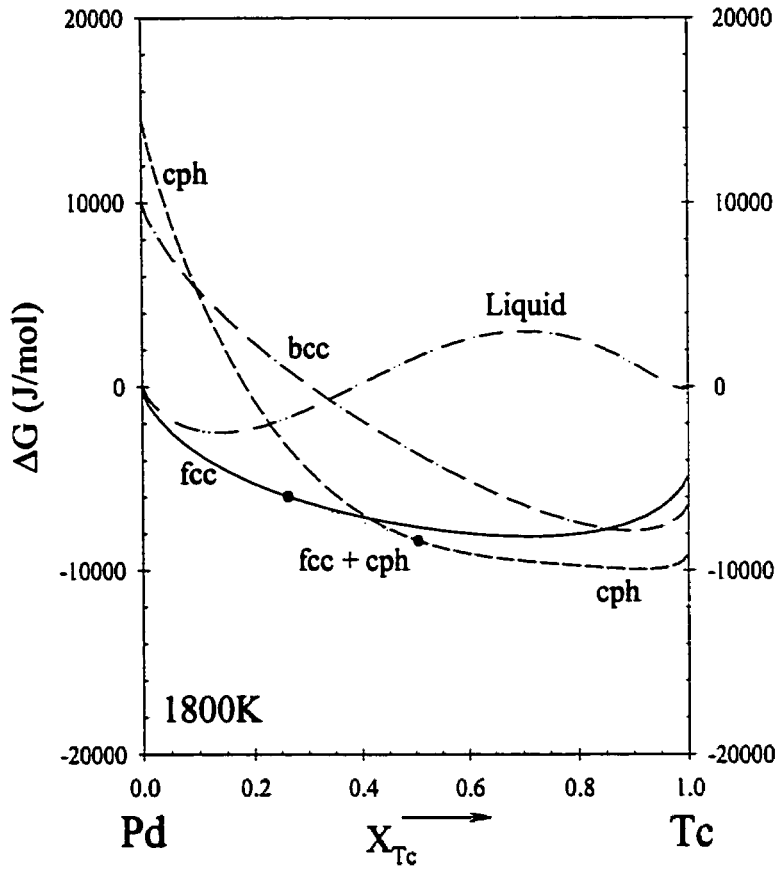

Figure 3-48. Gibbs Energy Isotherm at 1800K for Pd-Tc system.

3.9 Rh-Tc

3.9.1 Previous Studies of the Rh-Tc System

Experimental work in the Rh-Tc system has also been limited. Darby et al.[71] studied the system by examining, with X-ray metallography, alloys that had previously been annealed for 7 days at 1323K. The results suggested that the maximum compositional variation for the two phase mixture of terminal fcc-Rh and terminal cph-Tc lay in the range $0.5 < X_{Rh} < 1$. Furthermore, at $X_{Rh} = 0.75$, only a trace of the fcc-Rh phase was detected, suggesting that the solvus boundary between the cph-Tc phase and the two phase region was at a composition range of $0.65 < X_{Rh} < 0.75$.

A similar study in 1963 by Niemiec[72] studied alloys that were annealed for 20 hours at 1773K. From this work, the solvus between the terminal fcc-Rh and the two phase region must lie in the range $0.955 < X_{Rh}$, approximately at $X_{Rh} = 0.98$. For the solvus between the terminal cph-Tc and the two phase mixture, the boundary must lie between $0.658 < X_{Rh} < 0.763$, approximately at $X_{Rh} = 0.70$.

The current evaluation published by the ASM[28] is presented in Figure 3-49.

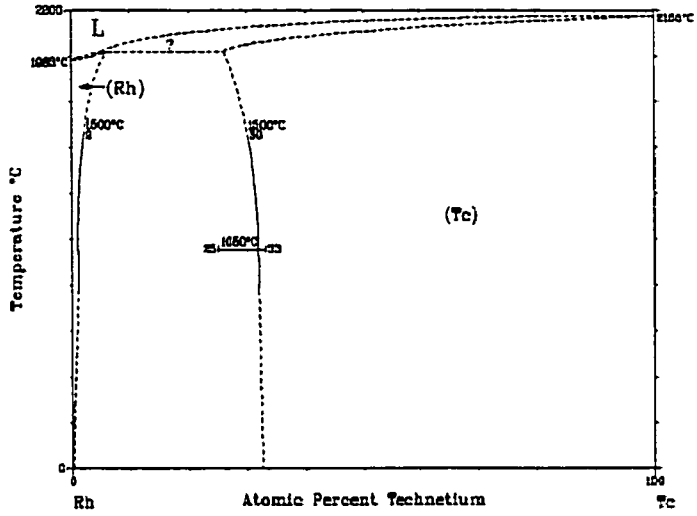

Figure 3-49. Rh-Tc equilibrium diagram from BAPD[28].

3.9.2 Evaluation for the Rh-Tc System Original to this Work

Once again there was limited experimental data to base the thermodynamic evaluation. Nonetheless, from this limited data Gibbs energy expressions for the fcc-solid phase and cph-solid phase were developed. A tie line between the fcc-solid and the cph-solid at 1773K, which satisfied the given data, was extended from the fcc-solid boundary at $X_{Rh} \cong 0.97$ and the cph-solid boundary at $X_{Rh} \cong 0.70$. At 1323K another tie line, which satisfied the data, was extended from the fcc-solid boundary at $X_{Rh} \cong 0.98$ and the cph-solid boundary at $X_{Rh} \cong 0.33$. From this information four independent equations

were constructed that equated partial properties for each of the elements along these tie lines, in exactly the same procedure described for the Pd-Tc system.

The current evaluation is shown in Figure 3-50.

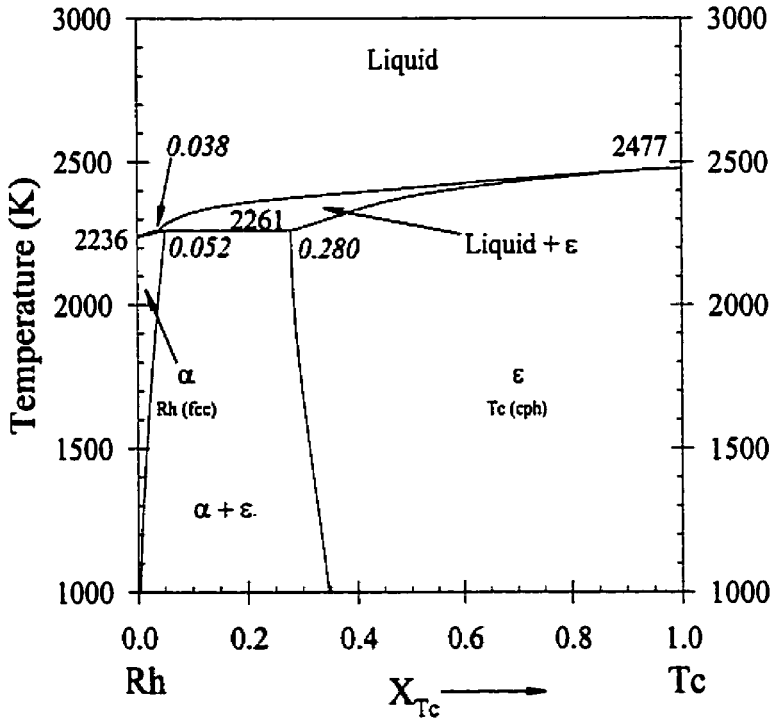

Figure 3-50. The Rh-Tc system as evaluated for this work.

A comparison of the current evaluation with the experimental work of Darby et al.[71] and Niemiec[72] is shown in Figure 3-51. The diagram is consistent with the limited experimental work. The position of the two phase region at 1323K suggested by Darby et al.[71] is correct. Furthermore, the boundaries proposed by Niemiec[72] at 1773K are respected.

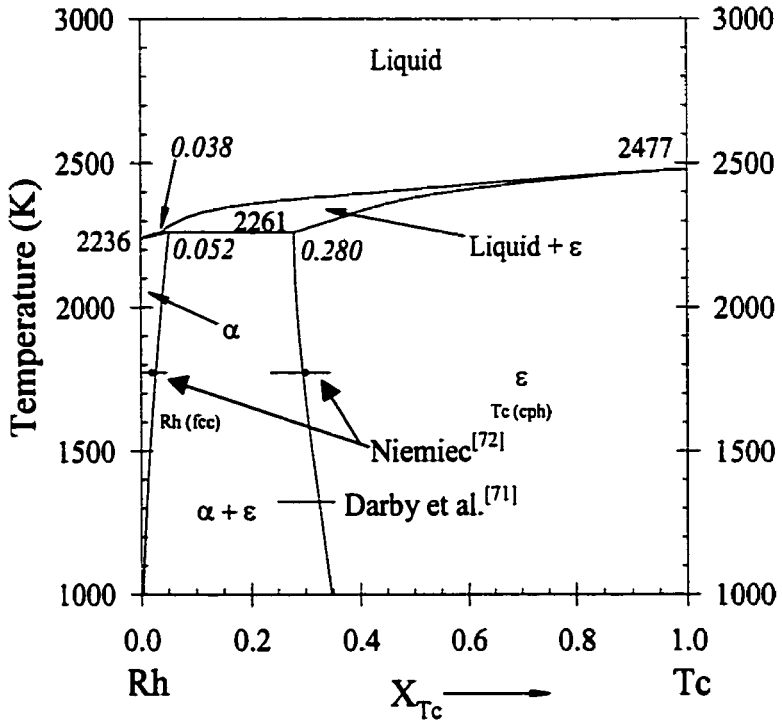

Figure 3-51. Comparison of the Rh-Tc system as evaluated for this work with the experimental work of Darby et al.[71] and Niemiec[72].

3.9.3 Thermodynamic Properties for Rh-Tc Binary System

The excess Gibbs energies for the four solution phases in the Rh-Tc system are:

$$\Delta G^{E}_{Liquid} = X_{Rh}X_{Tc}\left[293000-131000X_{Tc}-(113.54-43.75X_{Tc})T\right] \text{ J/mol} \quad \textbf{(3.59)}$$

$$\Delta G^{E}_{fcc} = X_{Rh}X_{Tc}\left[-9562.8+16T\right] \text{ J/mol} \quad \textbf{(3.60)}$$

$$\Delta G^{E}_{cph} = X_{Rh}X_{Tc}\left[-28250-111959X_{Tc}+(21.28+28.94X_{Tc})T\right] \text{ J/mol} \quad \textbf{(3.61)}$$

$$\Delta G^{E}_{bcc} = X_{Rh}X_{Tc}\left[0+0T\right] \text{ J/mol} \quad \textbf{(3.62)}$$

The Gibbs energy of mixing curves for the four solution phases at 1800K for the Rh-Tc system is shown in Figure 3-52.

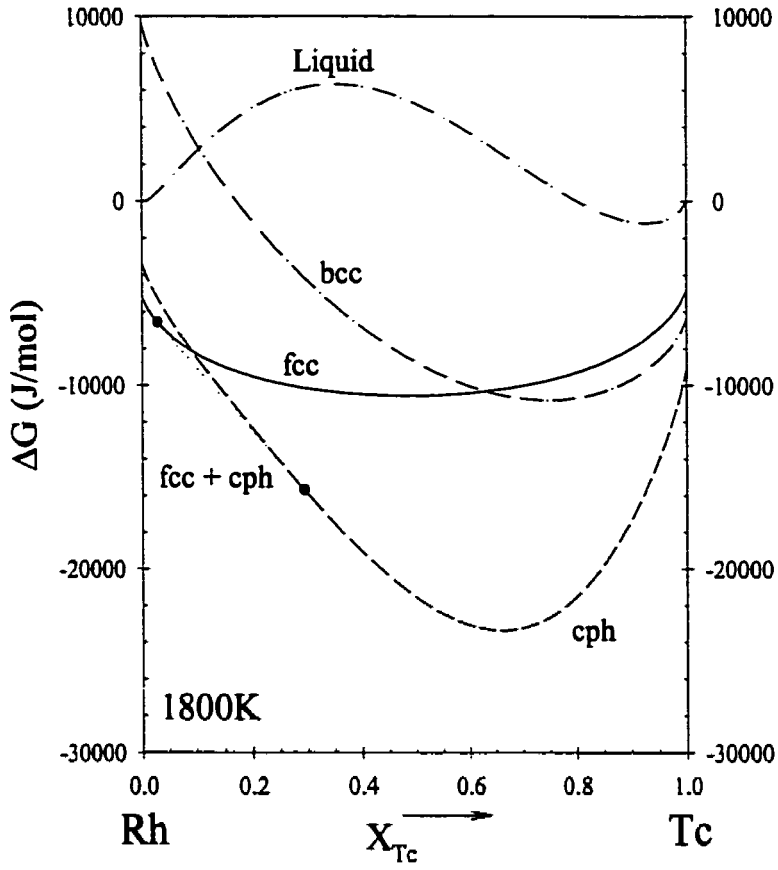

Figure 3-52. Gibbs Energy Isotherm at 1800K for Rh-Tc system.

3.10 Ru-Tc

3.10.1 Previous Studies of the Ru-Tc System

Darby et al.[69], using X-ray diffraction on a series of alloys previously annealed at 973K, determined that there was a continuous series of solid cph solutions in this binary system. Of course, these results do not preclude the possibility of a solid state miscibility gap at lower temperatures, much like the Pd-Rh binary system. However, for the purposes of this work, and in the absence of any other data, an ideal system was assumed. This means that the excess properties for the Ru-Tc binary system are:

$$\Delta G^{E}_{Liquid} = X_{Ru}X_{Tc}\left[0-(0)T\right] \text{ J/mol} \quad (3.63)$$

$$\Delta G^{E}_{cph} = X_{Ru}X_{Tc}\left[0-(0)T\right] \text{ J/mol} \quad (3.64)$$

$$\Delta G^{E}_{fcc} = X_{Ru}X_{Tc}\left[0-(0)T\right] \text{ J/mol} \quad (3.65)$$

$$\Delta G^{E}_{bcc} = X_{Ru}X_{Tc}\left[0-(0)T\right] \text{ J/mol} \quad (3.66)$$

3.10.2 Evaluation for the Ru-Tc System

The evaluation is shown in Figure 3-53. The diagram shows that the liquidus and solidus form a thin lens. It is also apparent from the diagram that there is not a miscibility gap in the solid phase.

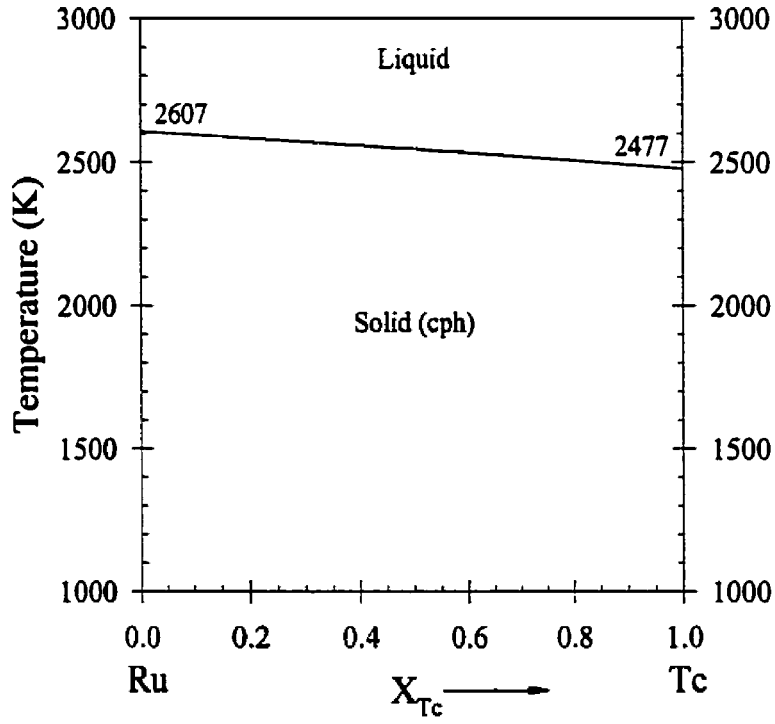

Figure 3-53. The Ru-Tc system as evaluated for this work.

3.10.3 Thermodynamic Properties for Ru-Tc Binary System

As mentioned previously the experimental work performed on this system is limited, and thermodynamic measurements have yet to be made.

3.11 Pd-Rh

3.11.1 Previous Studies of the Pd-Rh System

Raub et al.[74,75] were the first investigators to report the existence of a solid state miscibility gap in the palladium-rhodium system. By using X-ray diffraction and classic metallographic techniques they determined that the critical temperature of the miscibility gap was 1118K, and that this occurred at 51at.% Rh. Raub et al.[74,75] did not offer experimental data at temperatures approaching the solidus-liquidus region of the equilibrium diagram.

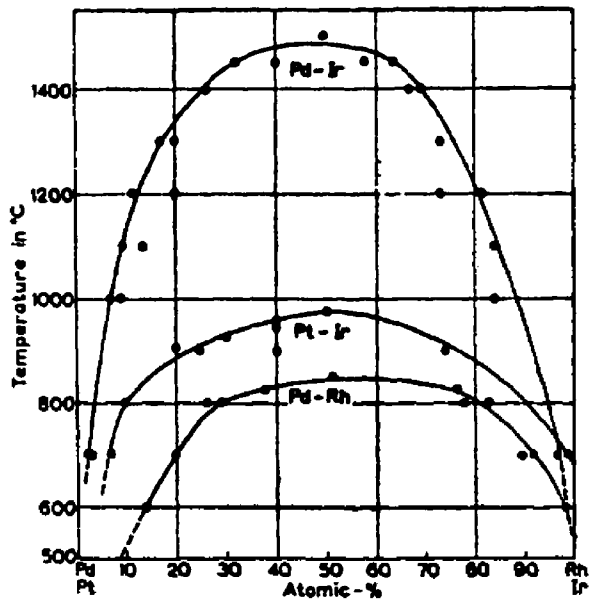

Figure 3-54. The solid miscibility gap in the Pd-Rh as determined by Raub et al.[74].

Myles[76] measured, using a torsion-effusion method, the vapour pressure of palladium over a series of Pd-Rh alloys. From these measurements, thermodynamic data at 1575K were calculated, and positive deviations from ideal behaviour were noted[76]. A phase diagram was not presented.

Shield and Williams[77] investigated the system using electrical resistivity

measurements on five Pd-Rh alloys. In general they found that decomposition of the alloy from single phase at high temperature to dual phase at low temperature occurred at temperatures slightly higher than those observed by Raub et al.[74,75]. The explanation presented by Shield and Williams was that their experimental technique was better able to distinguish phase separation on a fine scale[77]. The critical temperature of the miscibility gap was reported[77] as 1188K ±15K at X_{Rh} = 0.52 ±0.02, 70K above the temperature proposed by Raub et al.[74,75]. Shield and Williams offer only a refined version of the solid state miscibility gap, and do not comment on higher temperature features of the equilibrium phase diagram.

3.11.2 The Current ASM Evaluation

The Pd-Rh system was evaluated by Gürler et al. and summarized by Okamoto in the *Journal of Phase Equilibria* [33,78]. Contradictory data is presented on the excess properties of mixing for the liquid phase in the paper by Gürler et al.[33]. Furthermore, Okamoto, in his summary[78], confuses the excess properties of mixing for the liquid and the fcc-solid phase. The following excess properties of mixing were used in this work[33]:

$$\Delta G^{E}_{Liquid} = X_{Pd}X_{Rh}\left[20027 - 2260X_{Rh} - (2.74 - 0.56X_{Rh})T\right] \text{ J/mol} \qquad \textbf{(3.67)}$$

$$\Delta G^{E}_{fcc} = X_{Pd}X_{Rh}\left[21247 + 2199X_{Rh} - (2.74 - 0.56X_{Rh})T\right] \text{ J/mol} \qquad \textbf{(3.68)}$$

The excess properties for the hypothetical cph-solid and bcc-solid are given by equations **(3.69)** and **(3.70)**. It should be noted that these values are positive in order to prevent the inadvertent appearance of either of these phases at high temperatures.

$$\Delta G^{E}_{cph} = X_{Pd}X_{Rh}\left[20920\right] \text{ J/mol} \qquad \textbf{(3.69)}$$

$$\Delta G^{E}_{bcc} = X_{Pd}X_{Rh}\left[20920\right] \text{ J/mol} \qquad \textbf{(3.70)}$$

The current evaluation published by the ASM[28] is presented in Figure 3-55.

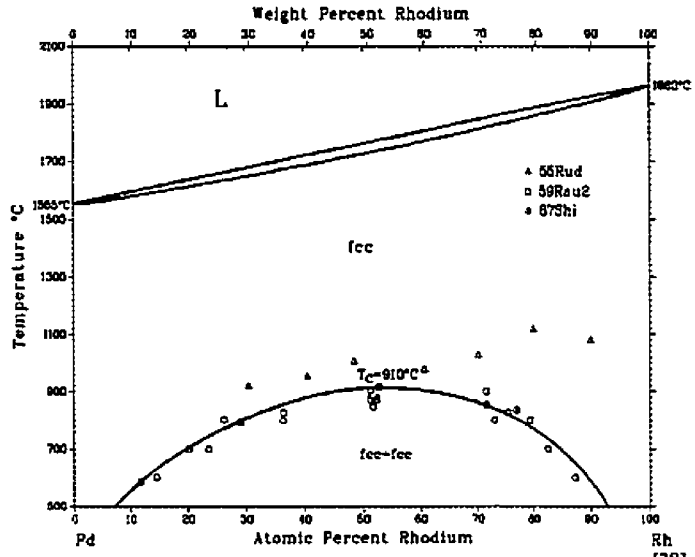

Figure 3-55. Pd-Rh equilibrium diagram from BAPD[28].

The evaluation made using equations **(3.67)** to **(3.70)** is shown in Figure 3-56.

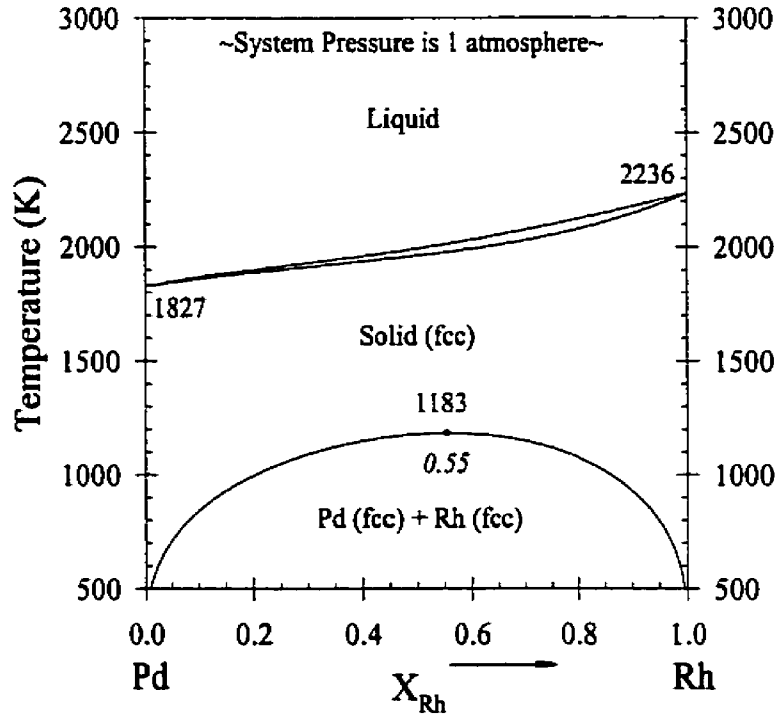

Figure 3-56. The Pd-Rh system as evaluated by Gürler et al.[33].

In a recent paper, Jacob et al.[79] measured the activity of rhodium in solid Pd-Rh alloys in the temperature range of 950 to 1350K using an emf technique. From their data they derived a pseudosubregular solution model for the excess properties of the solid

phase. Their results predict a solid-state miscibility gap at X_{Rh} = 0.55 ±0.02 with T_c = 1210 ±5K. This value is slightly higher than the T_c = 1188 ±15K at X_{Rh} = 0.52 ±0.02 from previous work by Shield and Williams[77]; the T_c = 1183 K at X_{Rh} = 0.55 predicted by Gürler et al., shown in Figure 3-56 [33]; and substantially higher than the early values of T_c = 1118K at X_{Rh} = 0.51 reported by Raub et al.[74].

The excess Gibbs energy of mixing for the fcc-solid phase, calculated by Jacob et al.[79], is given by the expression:

$$\Delta G^{E}_{fcc} = X_{Pd}X_{Rh}(31130+4585X_{Rh})-(10.44+1.51X_{Rh})T \text{ J/mol} \qquad (3.71)$$

and these authors propose a phase diagram, shown in Figure 3-57, for the Pd-Rh system which assumes ideal behaviour in the liquid phase.

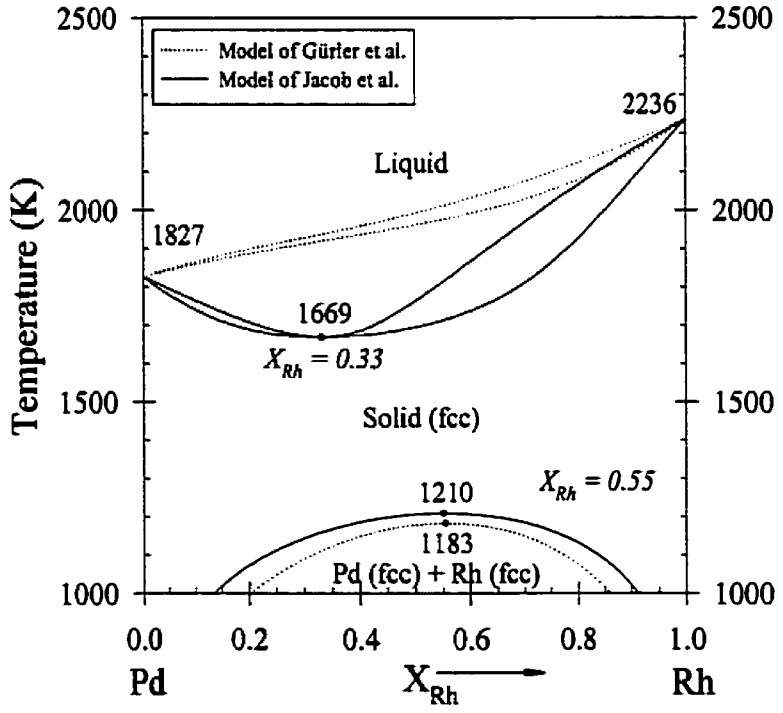

Figure 3-57. The Pd-Rh proposed by Jacob et al., assuming ideal behaviour in the liquid phase. For comparison the evaluation of Gürler et al.[33] is shown with dotted lines.

Because there were discrepancies in the literature concerning the position of the solidus and liquidus lines in this system, clarification was required. This is addressed in

the experimental work as differential thermal analysis was performed on a series of Pd-Rh alloys. The results from this original experimental work will show that the equilibrium phase diagram is similar to that modelled by Gurler et al.[33], which in turn suggests that the phases exhibit positive deviations from ideal behaviour as measured by Myles[76].

4. Thermodynamic Models for Multi-Component Alloys

4.1 Preliminary Remarks

In order to model the complete Mo-Pd-Rh-Ru-Tc alloy system accurately, it was necessary to model the ten individual binary systems, as illustrated in **Chapter 3**. These binary systems, became the framework from which a complete model for the multi-component system was derived.

The multi-component thermodynamic model was developed using the Kohler Interpolation scheme, described in **Section 4.2**. In subsequent sections, comparison of phase diagrams that have been developed using the model, with experimental data, will be presented. In this manner confidence in the model was acquired.

4.2 Kohler Interpolation

Interpolation methods may be used to estimate Gibbs energies based upon experimental studies for the binary metal combinations. While there are several different interpolation schemes for modelling a multi-component system from its constituent binary systems[80], the Kohler Interpolation scheme, that has been successfully applied to many other metallic systems was utilized for this work[81]. The Kohler Interpolation scheme, proportionally weights, from each binary system, the contribution of the thermodynamic property of interest, as given in equation (4.1).

$$G_p^E = (1-X_X)^2\, G_a^E + (1-X_Y)^2\, G_b^E + (1-X_Z)^2\, G_c^E \qquad \textbf{(4.1)}$$

This is illustrated in Figure 4-1, where the Gibbs energy of mixing at point ***p***, is estimated from the known Gibbs energy of mixing at points ***a***, ***b***, and ***c***, which are found by extending line segments from each of the corners on the ternary diagram, to the binary system on the opposing edge.

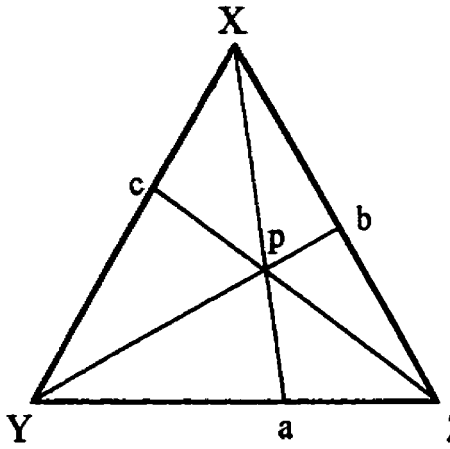

Figure 4-1. Representation of Kohler Interpolation; the property (G^E) at ***p*** may be estimated from a knowledge of properties at compositions ***a***, ***b***, and ***c***.[81]

The form of the interpolation scheme for the excess Gibbs energy is consistent with regular solution behaviour of each component dissolved in a solvent involving a fixed proportion of the other two components. This methodology has been found suitable in many cases as a predictive approach to provide ternary excess solution property estimates, when experimental data do not exist. As experimental data are gathered for the system, departure terms may be added to the basic interpolation. These terms take the form of products of all mole fractions raised to different powers multiplied by a temperature dependent coefficient. The correction terms vanish in the binary subsystems.

4.3 Comparison of Thermodynamic Model with Previous Research

4.3.1 Data from Kernforschungszentrum Karlsruhe (Paschoal et al.)

Paschoal et al.[82] have presented an extensive collection of data, derived from metallographic examination, X-ray diffraction, and electronprobe microanalysis (EPMA), for ternary and quaternary alloys in the Mo-Pd-Rh-Ru system at 1973K. A comparison of their results for the ternary alloys against the developed thermodynamic model is presented in this section. If the thermodynamic model were to be accepted without

ternary excess terms, the predicted ternary phase diagram at 1973K for the Mo-Pd-Rh system would be as shown in Figure 4-2 (Note: on page A-34 of **Appendix A**, an evaluation, previously published[65], that does not include ternary excess terms is shown). It can be seen that the liquid phase appears to be stable in two distinct fields and the ε-solid (cph) phase has only small fields near the Mo-Rh and Mo-Pd binary edges. Furthermore, there is poor agreement between this diagram and the experimental work (diagrams shown in **Appendix B**) of Paschoal et al.[82], for example, the two points labelled α+ε are shown to lie in a region labelled α+β. Also, the ε-solid (cph) phase was experimentally determined to extend well into the centre of the diagram.

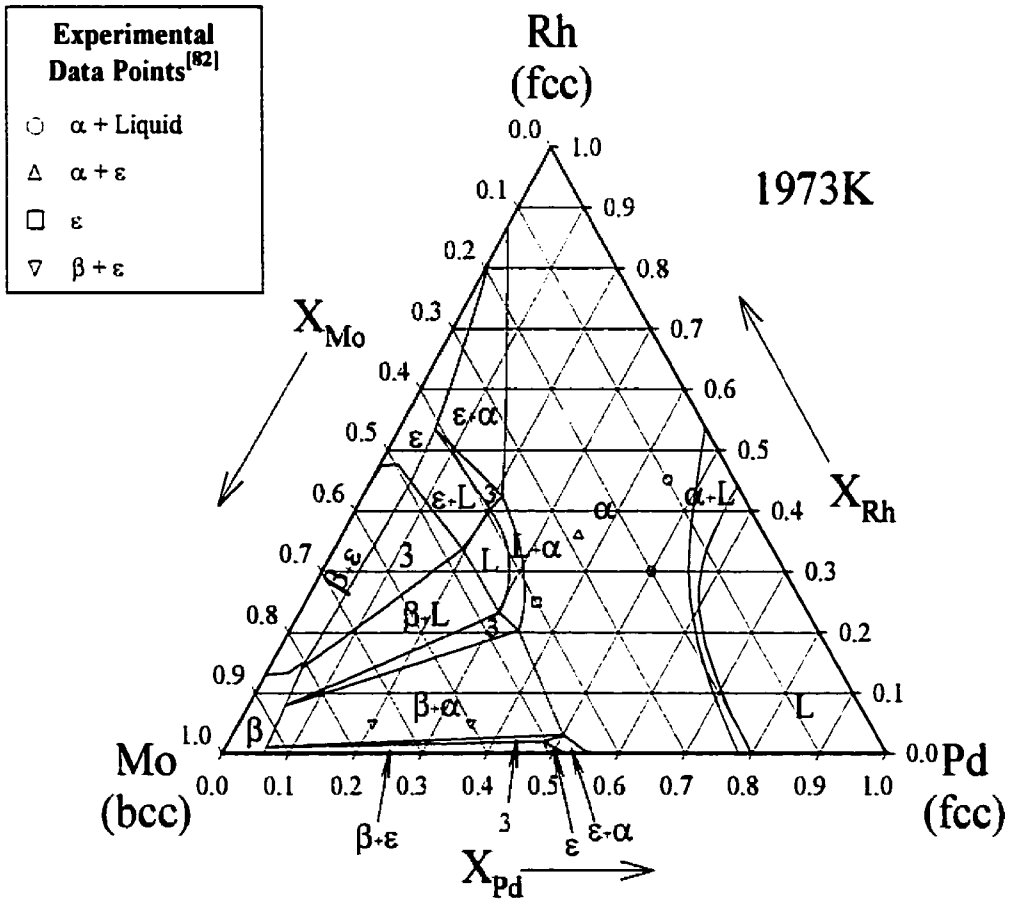

Figure 4-2. The Mo-Pd-Rh ternary diagram produced without the inclusion of ternary terms in the thermodynamic model. Experimentally determined phase compositions[82] are annotated in the legend, top left. Note: α = fcc; β = bcc; ε = cph; and L = Liquid.

Due to the major discrepancies between the experimental results from Paschoal et al.[82] and the thermodynamic model that is devoid of ternary excess energy terms, as illustrated in Figure 4-2, ternary excess energy terms were added to the thermodynamic model. These terms are listed below in Table 4-1.

Table 4-1. Ternary excess energy terms for the Liquid, fcc, bcc, and cph phases.

Phase	Components	Ternary Excess Gibbs Energy Term
Liquid	Mo, Pd, Rh	$G^{E}_{Liquid} = X_{Mo}X^{2}_{Pd}X_{Rh}(-9000)$
Liquid	Pd, Rh, Ru	$G^{E}_{Liquid} = X_{Pd}X_{Rh}X_{Ru}(-52500)$
bcc-solid	Mo, Pd, Rh	$G^{E}_{bcc} = X_{Mo}X_{Pd}X_{Rh}(-19730+10T)$
bcc-solid	Mo, Pd, Ru	$G^{E}_{bcc} = X_{Mo}X_{Pd}X_{Ru}(40000)$
bcc-solid	Mo, Rh, Ru	$G^{E}_{bcc} = X_{Mo}X_{Rh}X_{Ru}(-48000)$
cph-solid	Mo, Pd, Ru	$G^{E}_{cph} = X_{Mo}X_{Pd}X_{Ru}(-15000)+X^{2}_{Mo}X_{Pd}X_{Ru}(-130000)$
cph-solid	Mo, Pd, Rh	$G^{E}_{cph} = X_{Mo}X_{Pd}X_{Rh}(-89730+10T)$
cph-solid	Pd, Rh, Ru	$G^{E}_{cph} = X_{Pd}X_{Rh}X_{Ru}(-90000)$
fcc-solid	Mo, Pd, Rh	$G^{E}_{fcc} = X_{Mo}X_{Pd}X_{Rh}(-197300+100T)$
fcc-solid	Mo, Pd, Ru	$G^{E}_{fcc} = X_{Mo}X_{Pd}X_{Ru}(-115507+9T)$
fcc-solid	Pd, Rh, Ru	$G^{E}_{fcc} = X_{Pd}X_{Rh}X_{Ru}(-40000)$

The Mo-Pd-Rh phase diagram, developed with the ternary excess parameters listed in Table 4-1, is shown in Figure 4-3. It can be seen that there is much better agreement with the experimental data that had been determined by Paschoal et al.[82].

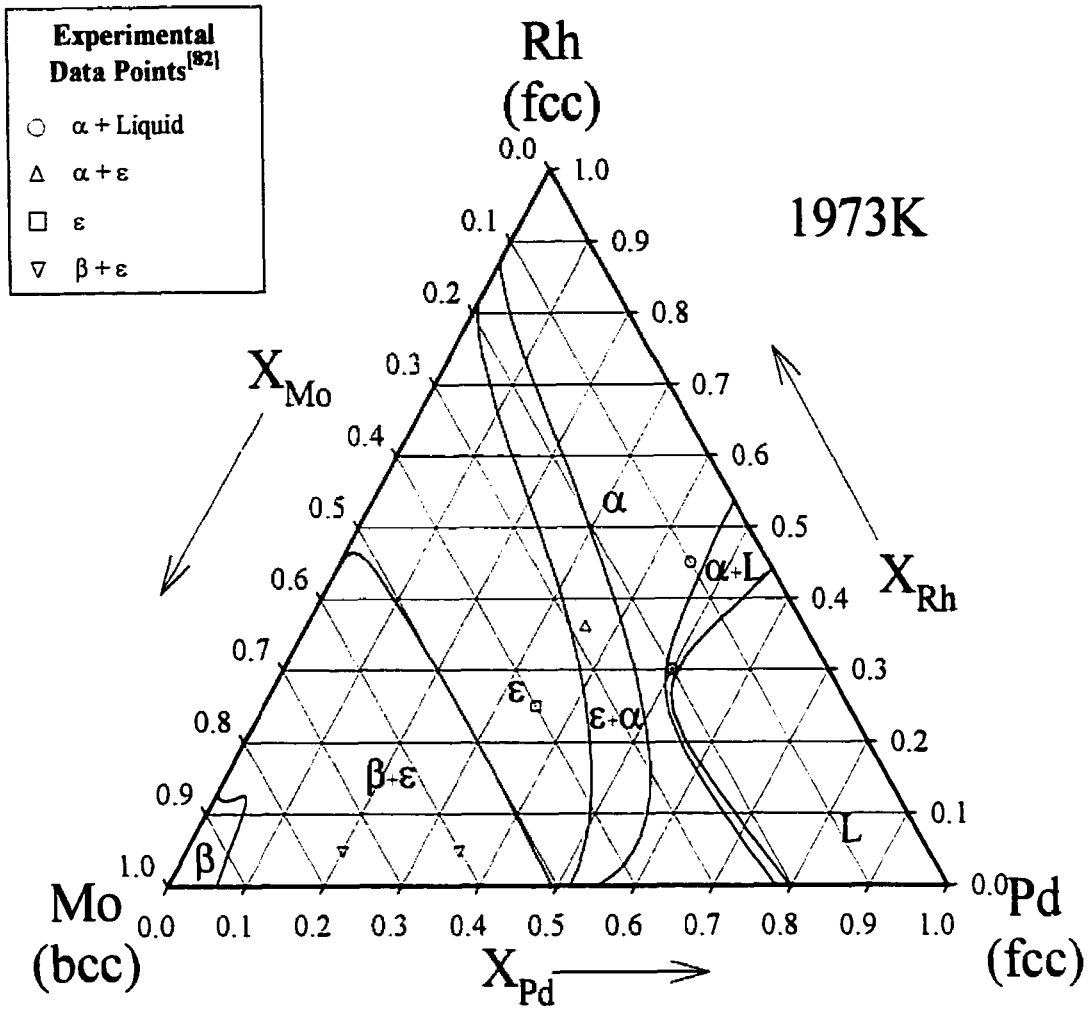

Figure 4-3. Mo-Pd-Rh. Note: α = fcc; β = bcc; ε = cph; and L = Liquid.

The Pd-Rh-Ru phase diagram is shown in Figure 4-4. Once again there is good agreement between the experimentally determined data for the phases present[82] and the diagram predicted by the improved thermodynamic model. It should be noted here that the diagrams of Paschoal et al.[82] are not well defined by the data. In essence, the boundaries between phases are sketched in such a manner that the phases observed are placed within the corresponding regions. An underlying thermodynamic model is not present, so these boundaries must be regarded as best estimates only.

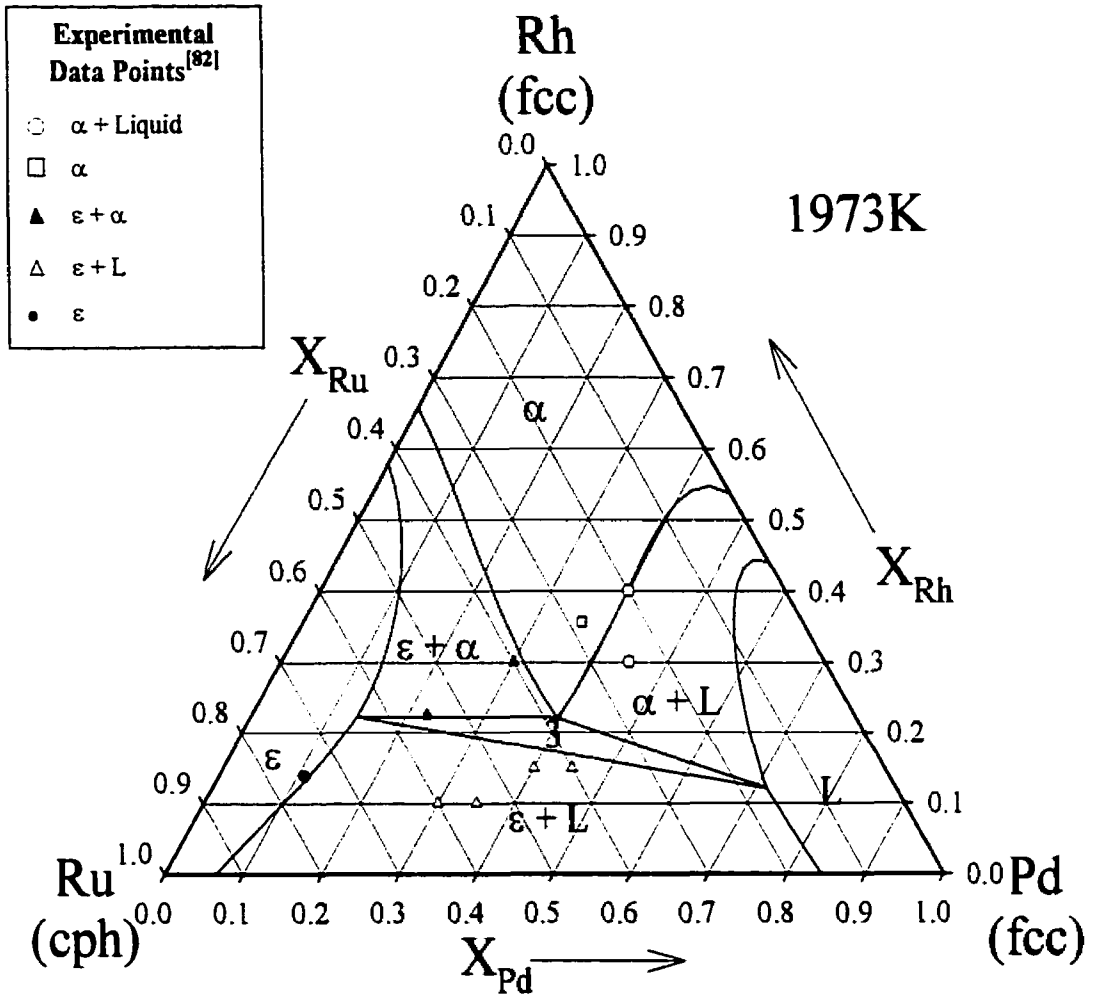

Figure 4-4. Pd-Rh-Ru. Note: α = fcc; ε = cph; and L = Liquid.

The Mo-Rh-Ru and Mo-Pd-Ru ternary phase diagrams are shown in Figure 4-5 and Figure 4-6, respectively. In both these diagrams there are two distinct regions: the region that extends from the central ε-solid phase to the right binary edge (either Rh-Ru or Pd-Ru); and the region that lies between the β-solid phase and the ε-solid phase. For the region that extends from the central ε-solid phase to the right binary edge, the agreement between the model and the experimental data is good.

Discrepancies occur in the region that lies between the β-solid and ε-solid phases, where the σ-solid phase is involved. Because the model treats Mo_5Ru_3 (σ-solid) as a

stoichiometric line compound, there is little flexibility to allow for the existence of σ-solid as a distinct phase region that can extend into the interior of the ternary diagram.

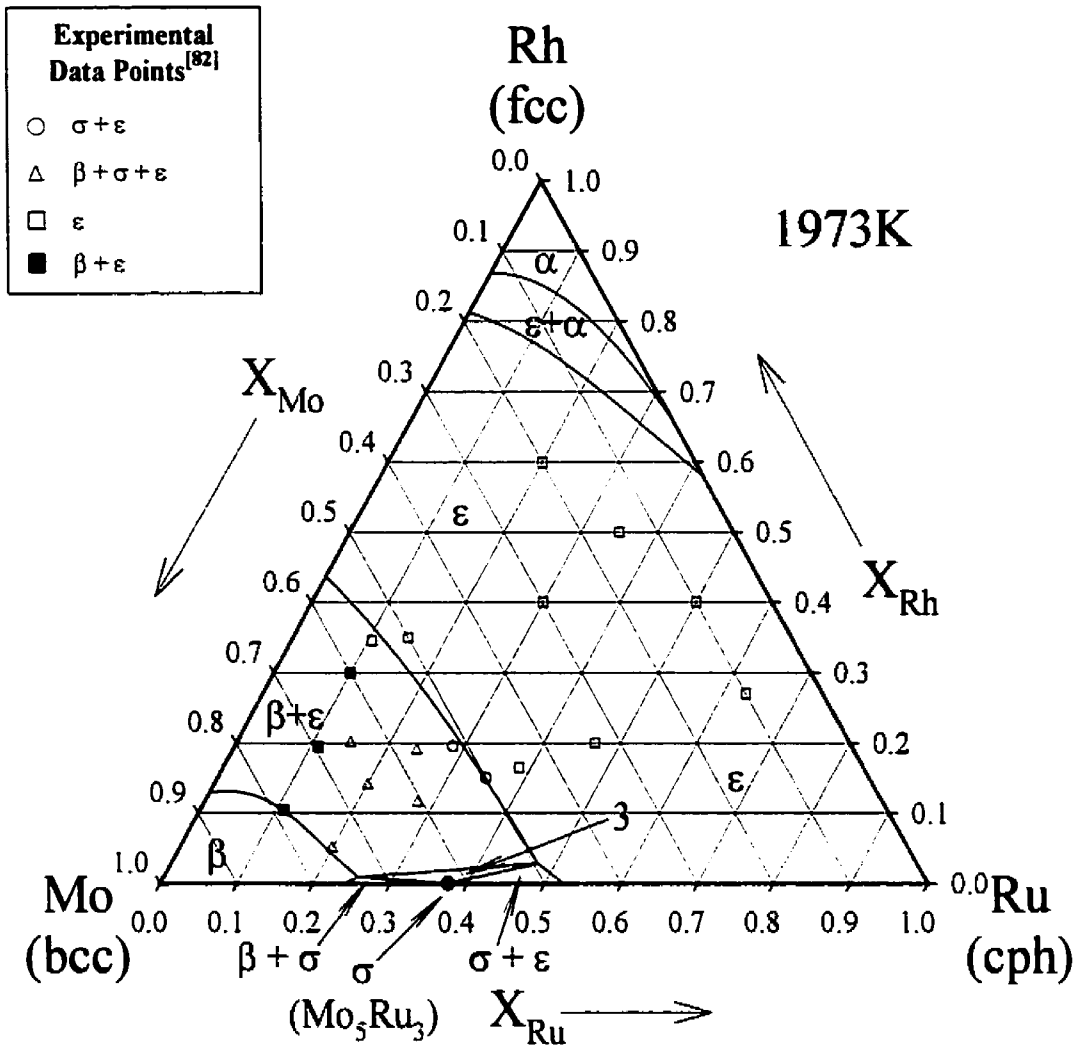

Figure 4-5. Mo-Rh-Ru. Note: α = fcc; β = bcc; ε = cph; and σ = tetragonal.

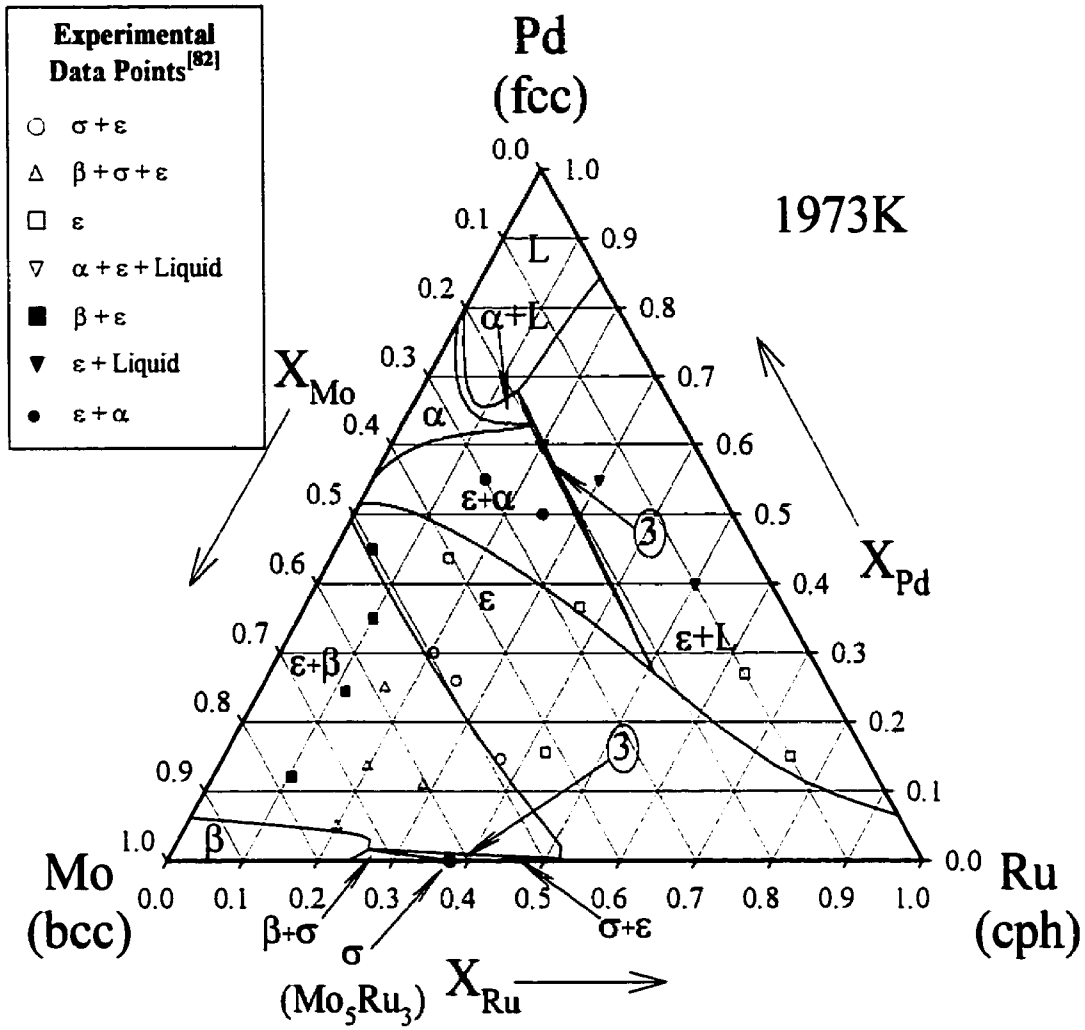

Figure 4-6. Mo-Pd-Ru. Note: α = fcc; β = bcc; ε = cph; σ = tetragonal; L = Liquid.

4.3.2 Data from Japan (Naito et al.)

K. Naito et al.[83] investigated the Mo-Pd-Ru ternary phase diagram using microscopy, X-ray diffraction, and vapour pressure measurements using a Knudsen cell coupled to a mass spectrometer. The results of their investigation are shown in Figure 4-7.

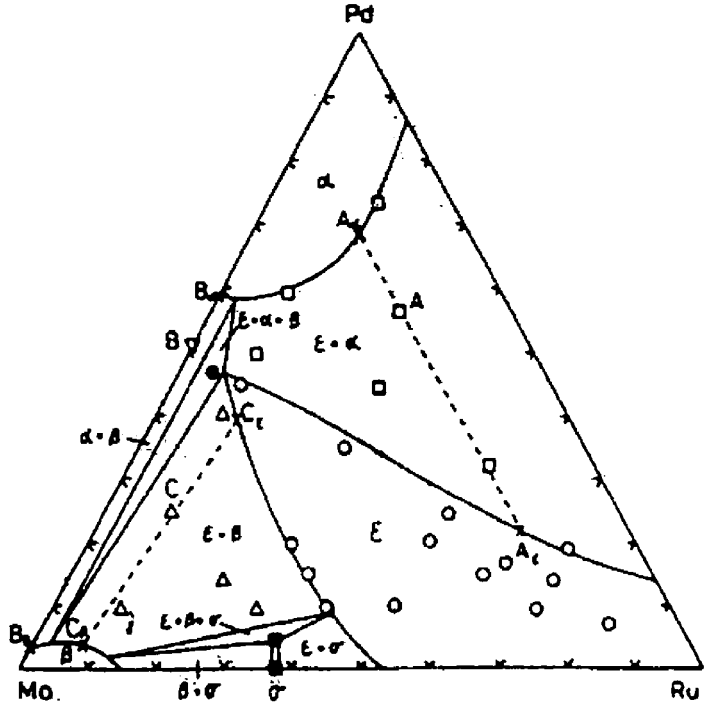

Phase diagram of the ternary Mo–Ru–Pd system at 1723 K from this experiment. α: solid solution (fcc); ϵ: solid solution (hcp); σ: intermetallic compound of Mo_5Ru_3 (tetragonal); β: solid solution (bcc); ○: ϵ; □: $\epsilon + \alpha$; △: $\epsilon + \beta$, ▽: $\alpha + \beta$, ●: $\epsilon + \alpha + \beta$; ■: σ.

Figure 4-7. The Mo-Pd-Ru diagram at 1723K, as proposed by Naito et al.[83].

It should be noted that there are problems with this diagram along the Mo-Pd binary edge. It can be seen that the accepted diagram for the Mo-Pd system, Figure 3-8, clearly indicates that an ε-solid phase exists around $X_{Mo} = 50$ atomic percent. This means that the phase labelled $\alpha + \beta$ is in error, as is the three phase region labelled $\varepsilon + \alpha + \beta$.

The Mo-Pd-Ru diagram at 1723K developed by the improved thermodynamic model (i.e., Kohler Interpolation with departure terms) is shown in Figure 4-8. There is excellent agreement between the experimental results of Naito et al.[83] and the model. The two tie lines suggested by Naito et al.[83], labelled A_α-A_ε and C_α-C_ε, are well replicated by the model. In fact there are only four ε-solid phase data points, indicated by

a filled circle in Figure 4-8, that do not lie within the ε-solid phase region. However, the three ε-solid phase points along the X_{Mo} = 50% line, are close to the phase boundary. The fourth point, along the Pd-Ru edge, represents a graphical contradiction in the work of Naito et al.[83], since on their diagram the point A_ε is at X_{Mo} = 16.1%, X_{Pd} = 17.3%, and X_{Ru} = 66.7%, which should be between the erroneous point and the Mo-Ru edge*.

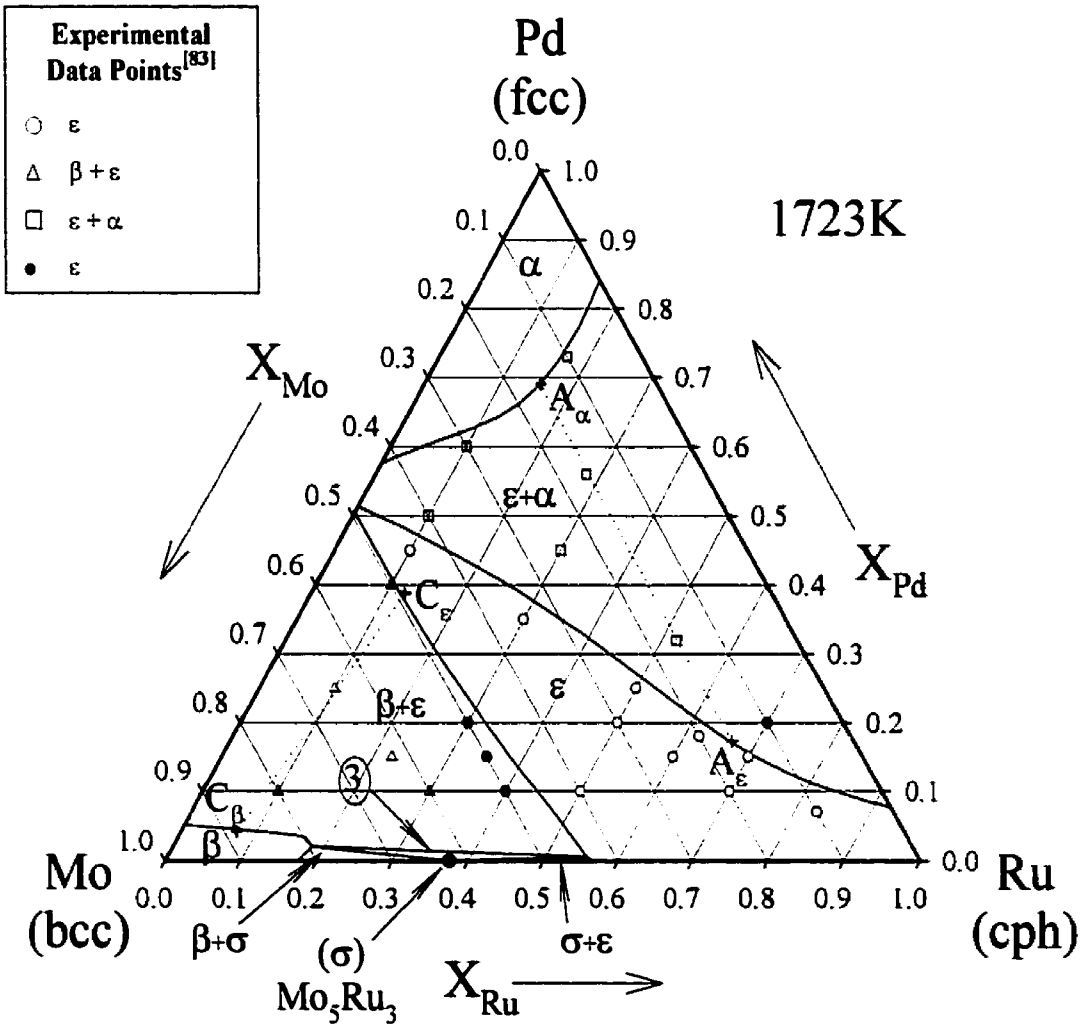

Figure 4-8. Comparison of the experimental data from Naito et al.[83] to the proposed Mo-Pd-Ru diagram. Note: α = fcc; β = bcc; ε = cph; and σ = tetragonal.

---

* In Figure 4-7 A_ε is clearly positioned above the X_{Pd} = 20 atomic percent. This permits the diagram to be drawn to include the debatable point within the ε-solid phase region.

4.3.3 Data from Birmingham, England (Gürler et al.)

Gürler and Pratt[84] annealed sixteen alloys in the Mo-Pd-Rh system, and studied the phase assemblages of each using optical microscopy, X-ray diffraction, SEM, and electron probe microanalysis. The results of their experimental work[84] were compared with the thermodynamic model for this ternary system at 1373K, shown in Figure 4-9. It should be pointed out that the compound $MoRh_3$ was withdrawn from the analysis to facilitate comparison, since Gürler and Pratt[84] did not consider it.

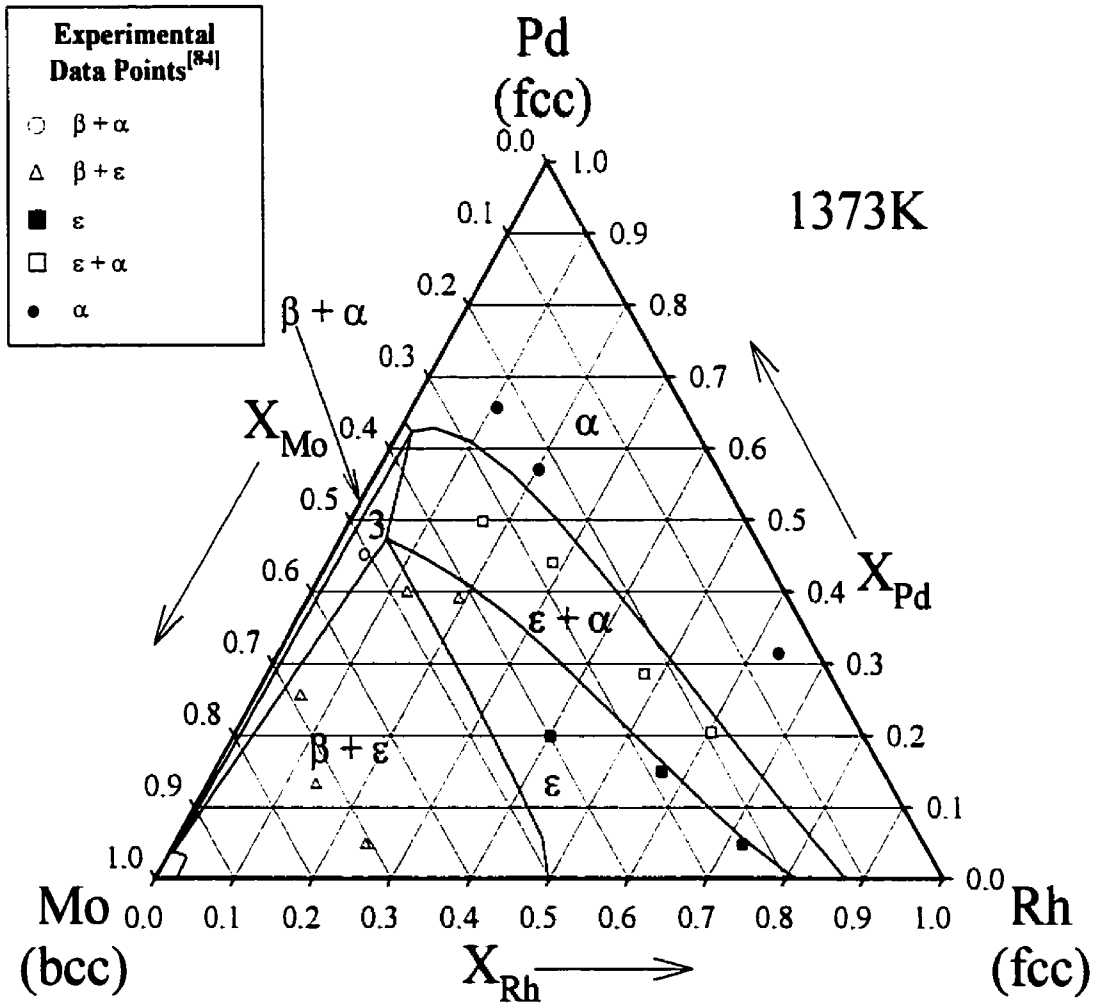

Figure 4-9. Mo-Pd-Rh. The experimentally determined points are from Gürler and Pratt[84]. Note: α = fcc; β = bcc; and ε = cph.

Gürler and Pratt used their experimental data to develop a computer calculation of

the Mo-Pd-Rh ternary phase diagram[85]. Their evaluation at 1373K is shown in Figure 4-10. By comparing the evaluation shown in Figure 4-9 with that of Figure 4-10, it can be seen that the model developed for this work better represents the experimental data in the central region of the diagram. A copy of the figure from the paper by Gürler and Pratt[85] which shows the experimental data is include in **Appendix B**.

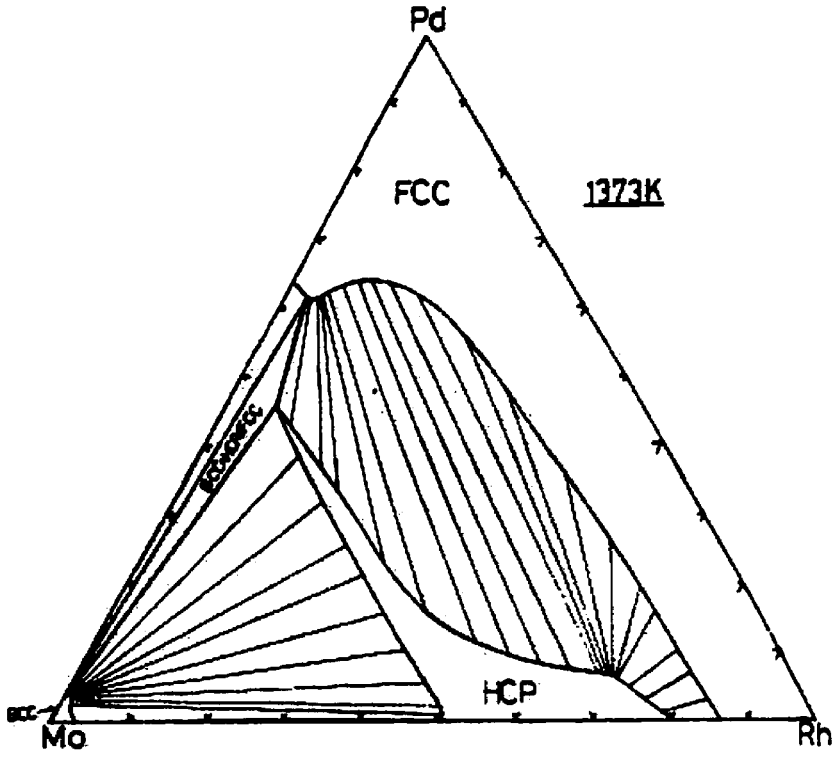

Figure 4-10. Mo-Pd-Rh ternary diagram at 1373K calculated by Gürler and Pratt[85].

4.3.4 Data from Harwell, England (Haines et al.)

Haines et al.[86] are the only researchers to propose ternary phase diagrams that involve Tc in combination with pairs of elements from amongst the noble metals. The methodology that Haines et al. employ is similar to that used in this work, that is building upwards from binary evaluations. However, it is clear from the diagrams of Mo-Tc, Pd-Tc, and Rh-Tc that their proposed models do not fit the limited experimental data that

exist for these binary systems. This means that the foundation of their ternary diagrams is seriously flawed.

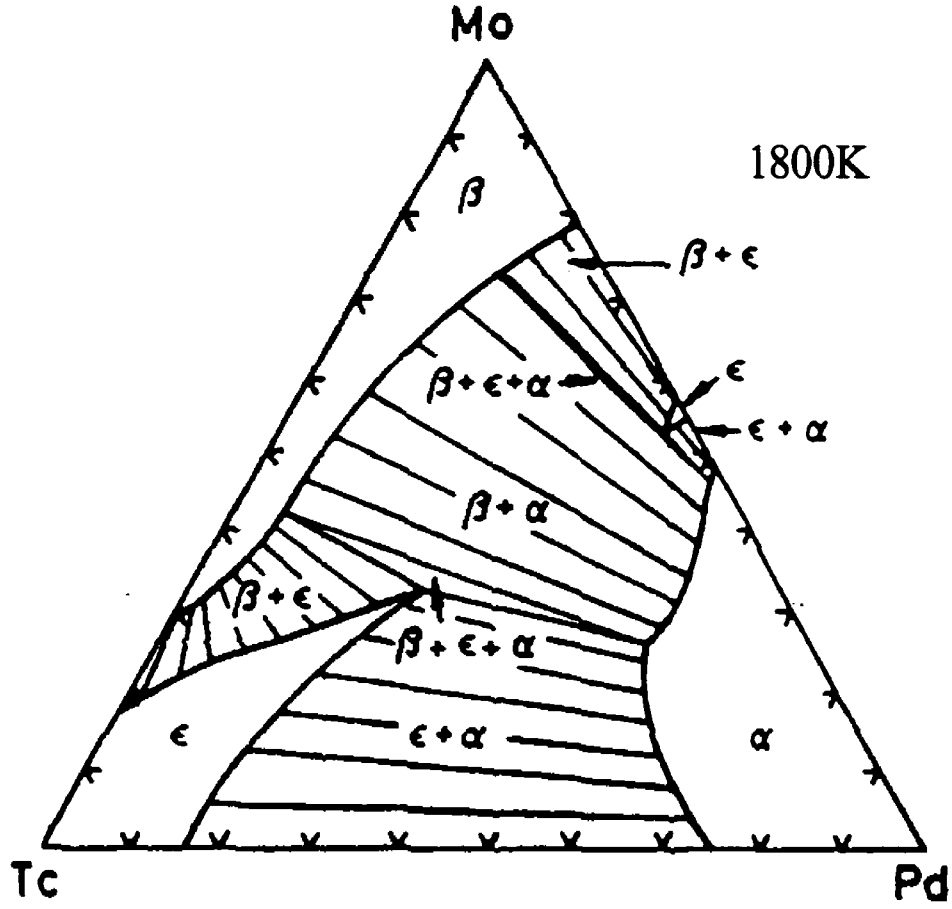

Figure 4-11. Mo-Rh-Tc from Haines et al.[86]. Note: α = fcc; β = bcc; ε = cph.

The ternary phase diagram predicted by the thermodynamic model for Mo-Pd-Tc is shown in Figure 4-12. Not that this diagram includes the tetragonal σ-phase and the compound Mo_9Tc_{11}.

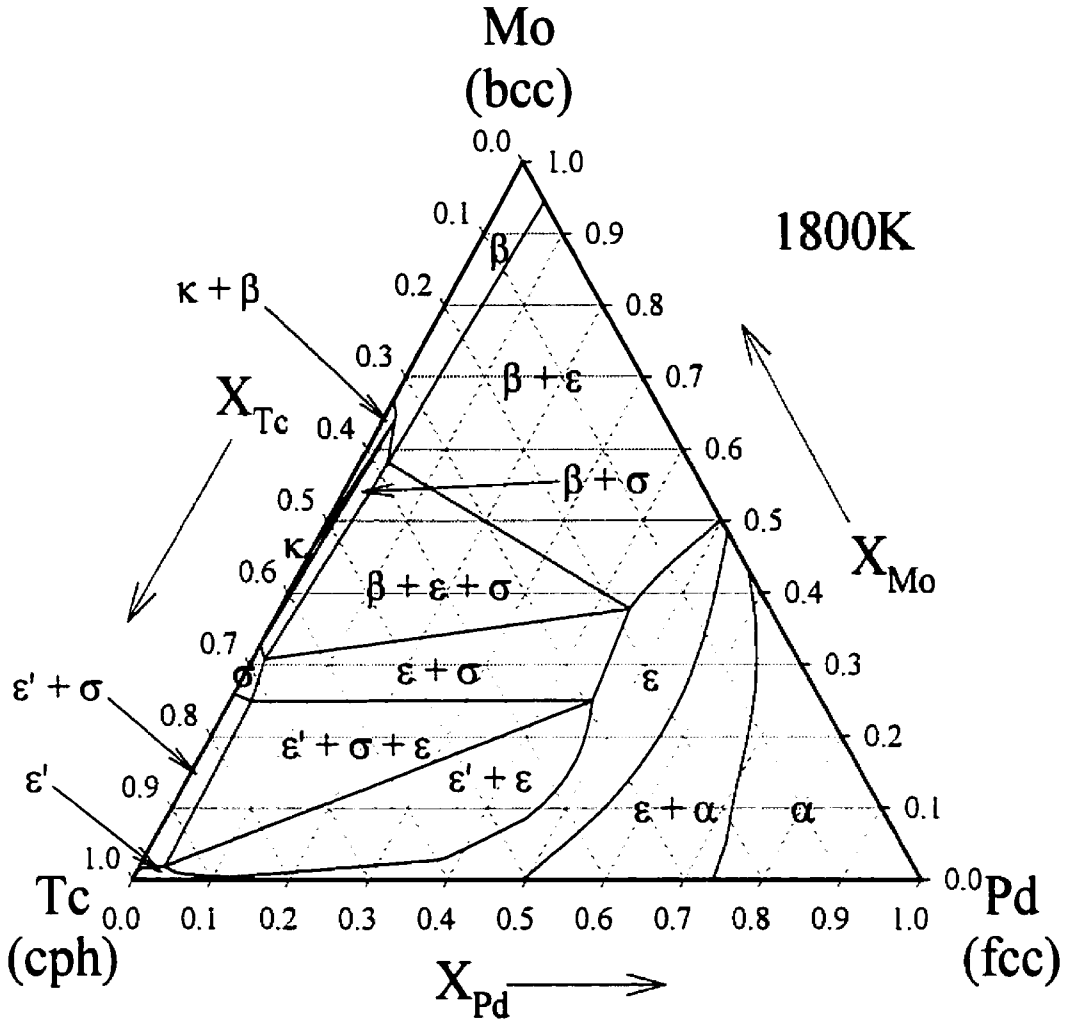

Figure 4-12. The Mo-Pd-Tc diagram predicted by the thermodynamic model. Note: α = fcc; β = bcc; ε = cph; ε' = cph; σ = tetragonal; and $\kappa = Mo_9Tc_{11}$.

5. Experimental Techniques

5.1 Preliminary Remarks

There are many experimental techniques that can be used to determine features of equilibrium phase diagrams and their underlying thermodynamic properties. A review of these techniques was recently co-authored by the author of this work[87], and has been included in **Appendix A**. With such a variety of techniques available, it was necessary to clearly establish the experimental objectives of this work and select the experimental techniques that would best achieve these ends.

There were two primary experimental techniques, namely differential thermal analysis and Knudsen cell mass spectrometry, used in this work. Differential thermal analysis was selected in order to resolve the controversy surrounding the placement of the solidus-liquidus on the Pd-Rh equilibrium phase diagram. This technique provides direct measurements of the critical temperatures that define the solidus and liquidus.

The second experimental technique, Knudsen cell mass spectrometry, measures vapour pressures above alloys. Since the primary goal of this thesis is to provide better insight into the thermodynamic properties of the noble metal alloys, it was felt that measurements of this nature for the noble metal alloys would be most useful.

This chapter will provide an overview of these techniques and how they can be used to provide thermodynamic information, that in turn can be used to validate the thermodynamic model developed in **Chapters 2** through **4**.

5.2 Differential Thermal Analysis

5.2.1 Overview of the Technique

The differential thermal analysis (DTA) technique measures the differences in temperature between a reference material and the sample while both are exposed to the same slow temperature change in a common thermal environment. In practice the reference material is chosen for its thermal stability over the temperature range of interest. This means that the reference material can not undergo a phase transition. Often high purity alumina is chosen since it fulfils this necessary requirement.

Because DTA measures temperature differences, it is well suited to detecting transition temperatures that involve significant enthalpy changes that are not sluggish, for example heats of melting; it is less suited to detecting kinetically slower solid-to-solid transitions (i.e., a transition across a solvus boundary). In the current work, an investigation of the solidus-liquidus region of the Pd-Rh binary system was made, but because of the limitations mentioned, the temperatures near the solid state miscibility gap were not explored. The latter, however, are not in dispute.

5.2.2 Interpreting the Results

A typical DTA curve is shown in Figure 5-1. For pure materials, according to the American Society for Testing and Materials (ASTM) standard E-967-83[88], the melting temperature is given at $T_{Peak\ min}$. For alloys the solidus temperature corresponds to T_{Onset}, while the liquidus temperature corresponds to $T_{Peak\ min}$.

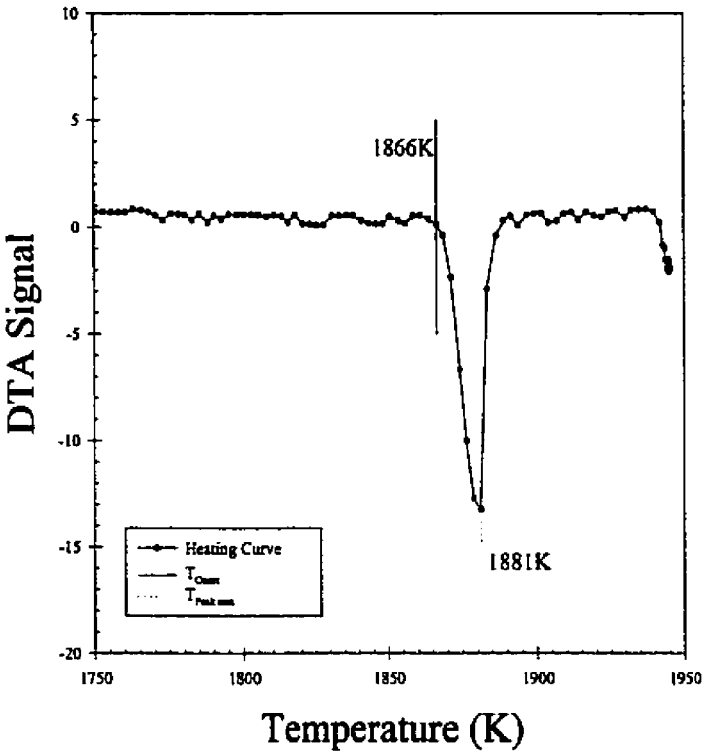

Figure 5-1. A typical DTA curve for an 80%/20% Pd/Rh alloy. The solidus temperature is 1866K and the liquidus occurs at 1881K.

5.3 Knudsen Cell Mass Spectrometry

5.3.1 Overview of the Technique

The Knudsen cell mass spectrometry technique measures the partial pressure of gases in a restricted volume. In the case of metals it is well understood that for any metal or alloy at equilibrium with its surroundings, there is an associated partial pressure (often quite low) of the component elements above the surface of that metal or alloy. Thermodynamically this means that atoms of a particular species are leaving the solid phase and entering the vapour phase at equal rates. In experimental work, this equality is approximated as a result of slow escape of vapour from the Knudsen cell.

A Knudsen cell is constructed from a suitably inert refractory material as shown

in Figure 5-2. There is a small cavity within the cell into which the vapour phase associated with the metal or alloy can develop to a near equilibrium value. The gaseous atoms will be travelling on random paths through this volume. Every so often, at a rate that is proportional to the partial pressure of the species of that particular atom, one atom will be travelling on the correct path that will allow it to leave via the pin-hole in the lid of the Knudsen cell. The escaping atom is then ionized and accelerated towards a detector that identifies it by its atomic mass.

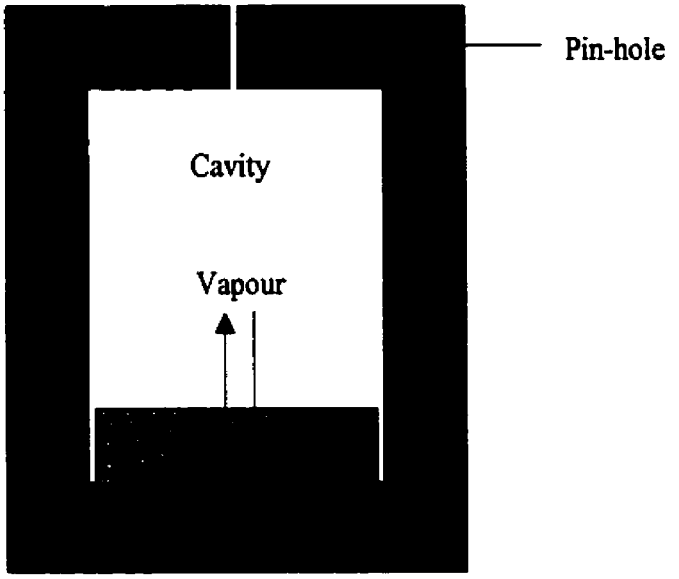

Figure 5-2. A typical Knudsen Cell.

5.3.2 Analysis of the Results

Upon heating the cell in a vacuum, a near equilibrated atmosphere is produced above the alloy. The orifice in the cell lid allows a limited beam of atoms to leave the cell, and these atoms are deflected towards a mass spectrometer, which then counts the number of atoms of a given atomic mass. Equation **(5.1)** is used to convert from the number of counts of an isotope of species *i*, to a pressure reading for species *i*:

$$p_i = \frac{I_{x_i} \cdot T}{k_{Std} \cdot \sigma_i \cdot \gamma_{x_i} \cdot n_{x_i} \cdot f \cdot s} \tag{5.1}$$

where, p_i represents the pressure of species i in atmospheres; I_{x_i} represents intensity, measured in counts of a particular isotope, x, of species i; T represents the absolute temperature; k_{Std} represents an instrument constant based on a standard substance, often silver; σ_i represents the ionization cross-section of i; γ_{x_i} represents the mass-sensitivity correction factor for the mass spectrometer, which is a ratio of the mass of the standard substance to that of species i; n_{x_i} represents a correction factor based on the isotopic abundance of isotope x; f represents the orifice size correction factor; and s represents a daily correction factor.

In the work presented here, a silver standard was used to determine the instrument constant. This instrument constant, k_{Ag} (= k_{Std}), is determined by calibrating the mass spectrometer against a silver standard. Equation **(5.2)** provides the relationship for k_{Ag}, where I_{Ag} represents the number of counts; T_{Ag} represents the absolute temperature; p_{Ag} represents the silver pressure; and σ_{Ag} represents the ionization cross-section of Ag.

$$k_{Ag} = \frac{I_{Ag} \cdot T_{Ag}}{p_{Ag} \cdot \sigma_{Ag} \cdot \gamma_{Ag}} = k_{Std} \tag{5.2}$$

The mass-sensitivity correction factor for the mass spectrometer, γ_{x_i}, is used to account for the variation in detection sensitivity as a function of ion mass.

The orifice size correction factor, f, is defined by **(5.3)**. This factor accounts for a possible orifice size difference between the day of the silver calibration and the day of the experiment. For the silver calibration experiment, the orifice diameter was 0.061mm (0.024 inches). For measurement convenience, the orifice diameter was measured in

thousandths of an inch, using carefully calibrated drill bits.

$$f = \frac{(orifice\ \ diameter)^2}{(0.024)^2} \tag{5.3}$$

Finally, the daily correction factor, s, is determined by comparing the relative intensity of the perfluorotributylamine (FC-43) during the experiment, with the intensity of the FC-43 from the silver calibration experiment. For this experimental work the FC-43 peaks at 100, 114, and 119 amu were used since they bracket the atomic masses of the species of interest. This variable accounts for daily variations within the apparatus and enables results from different days to be compared.

6. Experimental Procedures

6.1 Experimental Materials

6.1.1 Mo-Pd-Rh-Ru Alloy Preparation

Alloys were prepared from high purity powders of molybdenum, palladium, rhodium, and ruthenium obtained from Alfa Aesar. The specifications for these powders, as provided by Alfa Aesar, are presented in Table 6-1. The molybdenum, rhodium, and ruthenium were tested for impurities by spectrographic analysis, while the palladium was examined by d.c. arc emission spectroscopy.

Table 6-1. Specifications of the metal powders.

Element	Purity	Mesh Size	Detected Impurities (ppm)
Mo	99.999%	-325	Al (<0.2), B (<0.05), Ca (<0.25), Co (<0.02), Cr (<0.07), Cu (<0.10), Fe (<0.25), K (<0.05), Li (<0.005), Mg (<0.25), Mn (<0.02), Na (<0.05), Ni (<0.07), Pb (<0.02), W (<30), Zn (<0.1)
Pd	99.9985%	-22	Fe (2)
Rh	99.99+%	-22	Cu (14), Fe (<10), Fe (<10), Ir (16), Pt (<10), Si (<10)
Ru	99.95%	-325	Ag (9), Al (6), Au (4), Co (4), Cu (3), Fe (8), Ir (<10), Mn (<1), Ni (7), Os (8), Pb (<5), Pd (<20), Pt (<20), Rh (<10), Si (11)

6.2 Differential Thermal Analysis Apparatus

6.2.1 Sample Preparation

Appropriate proportions of palladium and rhodium powders were weighed (uncertainty ±0.1mg) and the powders were intimately mixed with an agate mortar and pestle. The compositions of each mixture, along with the atomic fraction for each element are presented in Table 6-2. Note that the total mass for each mixture was chosen to be approximately 0.1g.

Table 6-2. Mass data for Pd-Rh alloys.

Sample	Pd (g)	Rh (g)	Total mass (g)	Pd Mass %	Rh Mass %	X_{Pd}	X_{Rh}
A	0.1011	0.0000	0.1011	1.00	0.00	1.00	0.00
B	0.1083	0.0137	0.1220	0.89	0.11	0.88	0.12
C	0.0808	0.0198	0.1006	0.80	0.20	0.80	0.20
D	0.0900	0.0300	0.1200	0.75	0.25	0.74	0.26
E	0.0706	0.0312	0.1018	0.69	0.31	0.69	0.31
F	0.0785	0.0423	0.1208	0.65	0.35	0.64	0.36
G	0.0726	0.0493	0.1219	0.60	0.40	0.59	0.41
H	0.0611	0.0519	0.1130	0.54	0.46	0.53	0.47
J	0.0428	0.0785	0.1213	0.35	0.65	0.34	0.66
K	0.0238	0.0962	0.1200	0.20	0.80	0.19	0.81

6.2.2 Crucibles

The crucibles used were a 99.9% high purity Al_2O_3, stabilized with SiO_2. A schematic diagram of the crucible is shown in Figure 6-1. The crucible has been designed to allow a thermocouple to extend upwards into the centroid of the sample.

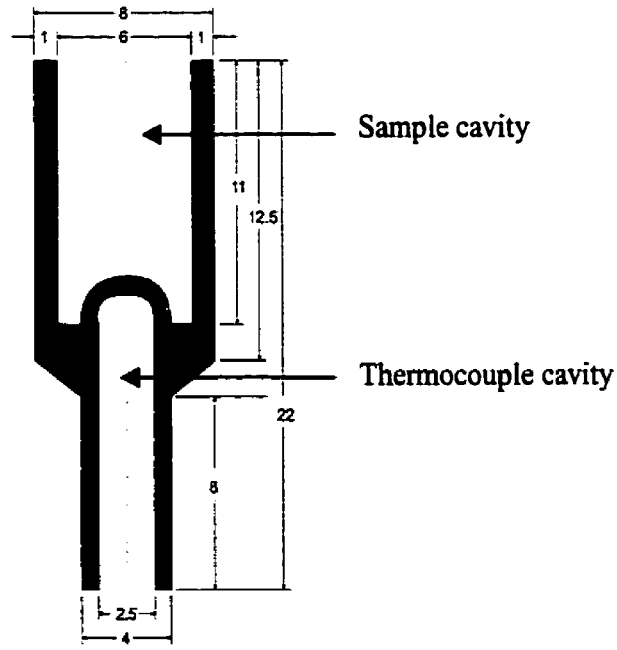

Figure 6-1. DTA crucible. All measurements are in millimetres.

6.2.3 Configuration of Differential Thermal Analyser

A Netzsch Simultaneous Thermal Analyzer STA429 was used to perform thermal analysis on a series of Pd-Rh alloys. The DTA, operating in its low temperature mode (i.e., T_{Max} = 2023K), uses two alumina crucibles, one which contains the sample of known mass, the other alumina powder which is chemically stable up to T_{Max}. The crucibles, manufactured by Netzsch, were bottom-capped cylinders 8mm in diameter and 13mm deep. A Type B thermocouple (Pt-30%Rh/ Pt-6%Rh) was used to measure the temperature from the bottom of the alumina crucible.

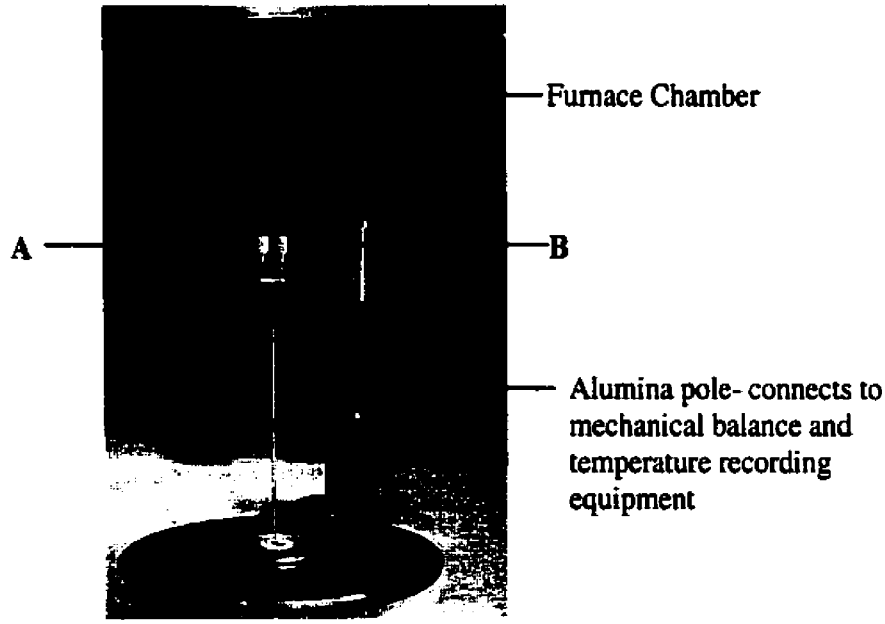

Figure 6-2. A photograph showing the "goal-post" configuration for the DTA sample holder. The crucible on the left **(A)** contains the sample, while the crucible on the right **(B)** contains an alumina reference sample.

6.2.4 Calibration of Thermal Analyzer

In order to calibrate the Netzsch Thermal Analyzer, high purity samples of silver and gold were used in accordance with ASTM standard E-967-83[88]. The accepted melting temperatures for silver and gold are 1236K and 1337K, respectively. Pure palladium was also used as a standard to verify accuracy. The accepted value for the

melting temperature of Pd of 1827 ±3K was confirmed in repeated trials.

6.2.5 Typical Experiment

For each experiment the appropriate masses of powders were measured (see Table 6-2) and intimately mixed with mortar and pestle. The powder was placed in a high purity alumina crucible and mounted within the DTA, along side the reference sample. A typical heating profile for each sample is shown in Figure 6-3. The temperature for each sample was cycled across the anticipated solidus-liquidus transition five times, in order to provide replicate data. The heating rate was 10C°/min for the first four runs, and then at 5C°/min for the fifth run, to ascertain the effect, if any, heating rate caused. To prevent oxidation, an inert atmosphere of high purity nitrogen* was passed into the furnace chamber at a rate of 100mL/min for the duration of the experiment. Furthermore, for each run the change in the mass of the sample was monitored continuously.

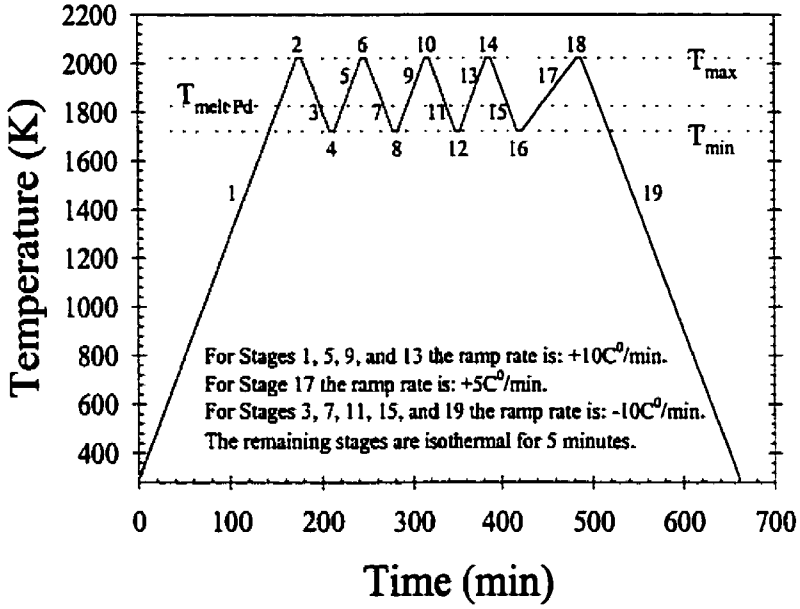

Figure 6-3. Typical heating profile for each DTA experiment.

* 99.999% N_2 containing impurities listed as: O_2 < 1ppm, H_2O < 3ppm, Total Hydrocarbons < 0.5ppm.

6.3 Mass Spectrometer-Knudsen Cell Apparatus

6.3.1 Sample Preparation

Appropriate proportions of molybdenum, palladium, rhodium, and ruthenium powders were weighed (uncertainty ±0.1mg) and the powders were intimately mixed with an agate mortar and pestle. The compositions of each mixture, along with the atomic fraction for each element are presented in Table 6-3. Initially the total mass for each mixture was chosen to be approximately 0.2g, but this restriction was loosened to approximately 0.5g after the first three experiments, in order to make the sample preparation easier.

Table 6-3. Compositions of alloys treated in the Knudsen cell-mass spectrometer.

Sample	Mo (g)	Pd (g)	Rh (g)	Ru (g)	X_{Mo}	X_{Pd}	X_{Rh}	X_{Ru}
1	0	0.1484	0	0	0	1	0	0
2	0	0.0584	0.1982	0	0	0.222	0.778	0
3	0	0.0885	0.0791	0	0	0.520	0.480	0
4	0.1309	0.1442	0.2751	0.1347	0.203	0.202	0.397	0.198
5	0.0938	0.1034	0.1498	0.1485	0.201	0.199	0.299	0.301
6	0.0948	0.1028	0.1003	0.1968	0.203	0.198	0.200	0.399
7	0.2384	0.0488	0	0.1999	0.505	0.093	0	0.402
8	0.3306	0.0528	0.0505	0.0498	0.700	0.100	0.100	0.100

6.3.2 Knudsen Cell and Crucibles

Knudsen cells were machined from 99.9% pure tantalum rods, obtained from Goodfellow Cambridge Limited or Robin Materials. A typical analysis of the tantalum, as provided by Goodfellow, is given in Table 6-4, while Table 6-5 shows the typical analysis of the tantalum rod supplied by Robin Materials. During machining and subsequent exposure to atmospheric conditions, it was expected that a surface layer of

Ta_2O_5 formed on the tantalum cell.

Table 6-4. Typical analysis for the impurities in the tantalum rod supplied by Goodfellow Cambridge Limited. Note that N.R. = not reported.

Element	Mass (ppm)	Element	Mass (ppm)	Element	Mass (ppm)
Al	5	H	N.R.	O	N.R.
B	N.R.	Mg	5	Si	10
C	N.R.	Mn	2	Sn	2
Ca	2	Mo	100	Ti	20
Cr	5	N	N.R.	V	5
Co	1	Na	10	W	100
Cu	2	Nb	<500	Zr	10
Fe	30	Ni	3		

Table 6-5. Typical analysis for the impurities in the tantalum rod supplied by Robin Materials. Note that N.R. = not reported.

Element	Mass (ppm)	Element	Mass (ppm)	Element	Mass (ppm)
Al	<5	H	<5	O	30
B	<1	Mg	<5	Si	10
C	10	Mn	<5	Sn	<5
Ca	<5	Mo	<5	Ti	<5
Cr	<5	N	<10	V	N.R.
Co	<5	Na	not detected	W	25
Cu	<5	Nb	75	Zr	<5
Fe	<5	Ni	<5		

Figure 6-4 shows a schematic diagram of the Knudsen Cell and the cell lid. It is important to realize that the diameter of the hole in the cell lid was not always exactly 0.610mm (0.024"), since machining to this specification is difficult in tantalum. The diameter of the hole was measured using drill bit penetration, accurate to ±0.025mm.

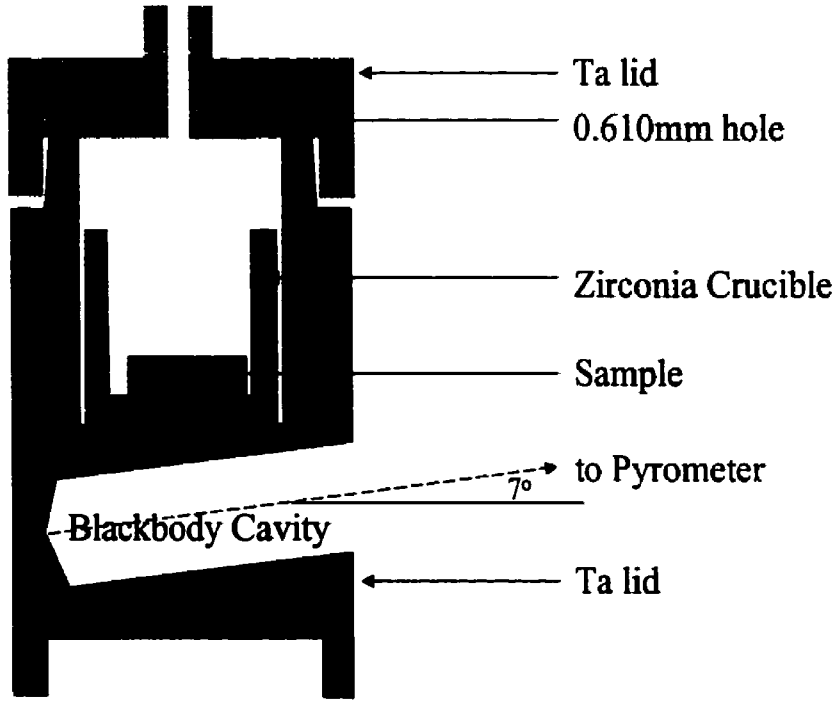

Figure 6-4. Schematic diagram of the Knudsen Cell.

After machining, the tantalum cells were cleaned in an acid solution of 23% HNO_3, 4% HF, and 73% H_2O for an hour, washed in acetone followed by methanol, and finally dried in a 150C oven for 30 minutes.

A zirconia crucible was used as an inner liner, in order to allow samples to be easily placed in the Knudsen cell and also to protect the tantalum crucible should accidental melting of the sample occur. From the Ellingham diagram[89] zirconia is inert to all of the noble metals. The zirconia crucibles were manufactured by Custom Tech Ceramics of Arvada Colorado. Three different lots of crucibles were prepared by Custom Tech for this experimental work. The first set of crucibles were purchased in 1997 (Pinawa batch), while the second (Batch 1) and third (Batch 2) were purchased in August of 1999.

6.3.3 Configuration of Knudsen Cell-Mass Spectrometer

The configuration of the Knudsen Cell-Mass Spectrometer is shown in Figure 6-5. The Knudsen Cell was positioned on its mounting tripod in such a manner as to allow a direct line of sight for the optical pyrometer to read the temperature within the blackbody cavity of the cell. It was also necessary for the vertical alignment to be such that the pin-hole in the cell lid was aligned with the top aperture, which led to the mass spectrometer. The furnace chamber and the quadrupole mass spectrometer manufactured by ABB Extrel were evacuated to at least 10^{-6}Pa, a process that took at least 12 hours.

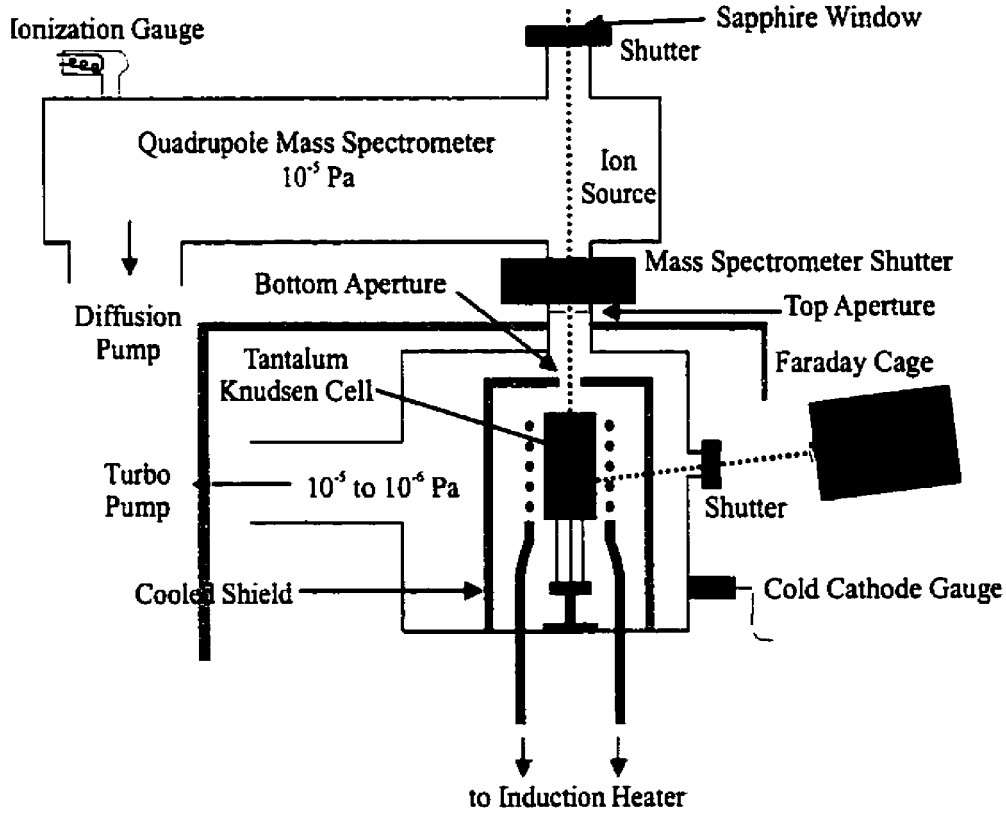

Figure 6-5. Schematic diagram of the Knudsen Cell-Mass Spectrometer apparatus.

6.3.4 A Typical Experimental Run

A sample was prepared in the appropriate proportions (Table 6-3) and placed in a zirconia crucible, which in turn was positioned in the central cavity of the Knudsen cell.

The diameter of the pin-hole opening in the lid was measured by drill bit penetration. The Knudsen cell was tightly sealed by the lid, and this unit was placed on a tripod stand.

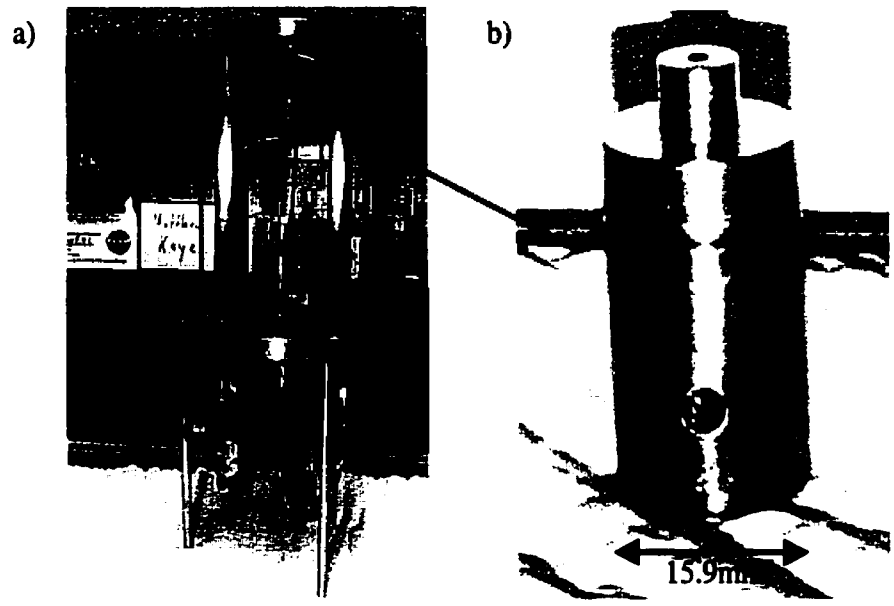

Figure 6-6. a) The Knudsen cell holder, showing the tripod that positions the cell in the midst of the copper induction coils. Coolant water flows through the four support columns, as well as the copper induction coils. Water enters and exits from the bottom. **b)** Knudsen cell, showing the black body cavity in the side and the exit hole in the lid. The arrow indicates the location for the placement of the cell within the induction coils.

6.3.5 Batch Conditions

In order to account for the possibility of experimental variations that might occur as a result of contaminants being contributed by pieces of the apparatus, a careful record was kept concerning various experimental details. For example, although the zirconia crucible should be inert to alloys of Mo-Pd-Rh-Ru, it is possible that one of the stabilizing compounds in the ceramic might be a problem*.

---

* Such a problem was discovered in preliminary work performed at AECL-Whiteshell. Two different crucible types were used (i.e., zirconia stabilized with calcia, and hafnia stabilized with calcia) and it was found that the measured partial pressure of Pd in a pure Pd sample was significantly different for each crucible type. The measured partial pressure of Pd was much lower for the hafnia crucible, and it was decided that these types of crucibles would be avoided in future work.

Table 6-6. Experimental parameters. Note that the sample type is differentiated on the basis of being a mixed powder (M) or a compressed pellet (C).

Run	Crucible Batch	Sample Type	Orifice Diameter (inches)	Orifice Size Correction Factor (f)	Average Daily Correction Factor (s_{avg})
1	Batch 2	M	0.0315	1.723	1.798
2	Pinawa	C	0.017	0.502	1.756
3	Batch 2	C	0.0305	1.615	0.850
4	Batch 1	M	0.021	0.766	1.333
5	Batch 1	M	0.0235	0.959	1.735
6	Batch 1	M	0.0225	0.879	1.625
7	Batch 1	M	0.032	1.778	0.896
8	Batch 1	M	0.033	1.891	1.170

The mass of the experimental assembly was determined before and after each experimental run. The experimental assembly consists of the Knudsen cell and lid, the sample crucible, and the sample (uncertainty in each measurement ±0.1mg). Mass lost during the experiment was attributed to vaporization of Pd. This data is presented in Table 6-7, along with the consequences of Pd vaporization on the compositional fraction of Pd in the sample.

Table 6-7. Comparison of the initial and final mass of the assembly for each run.

Run	Initial Mass (g)	Final Mass (g)	Mass Loss (g)	Initial X_{Pd}	Final X_{Pd}
1	75.0170	75.0114	0.0056	1	1
2	69.6397	69.6327	0.0070	0.222	0.200
3	75.0359	75.0307	0.0052	0.520	0.505
4	74.7346	74.7224	0.0122	0.202	0.188
5	68.2609	68.2589	0.0020	0.199	0.196
6	75.5186	75.5149	0.0037	0.198	0.192
7	74.9696	74.9474	0.0222	0.093	0.053
8	70.2522	70.2355	0.0167	0.100	0.071

7. Experimental Results and Discussion

7.1 Preliminary Remarks

The experimental results will be presented in two distinct sections: those results from the Differential Thermal Analysis of Pd-Rh alloys; and the results from Knudsen Cell– Mass Spectrometry for a series of Mo-Pd-Rh-Ru alloys.

7.2 DTA Experiments

The temperature data produced by the differential thermal analyzer came in three parts. The first piece of information was the temperature of the reference sample. The second piece of data was the difference in the temperature between the reference sample and the alloy being analyzed. During the heating of the alloy in either the solid or liquid phase region, the temperature difference was constant. At transition temperatures, this was not the case. The third piece of information produced was a record of the overall mass change in the system. For all runs, a mass change was not observed, which indicates that oxidation did not occur and that evaporation was insignificant.

Five runs were performed in succession for each sample. A typical set of results is shown in Figure 7-1. **Appendix C** contains similar figures for all the experimental runs. For the pure palladium sample, the average melting temperature was 1827.1K, which agrees with the literature value of 1827K. The uncertainty in the measurement was ±3K. A summary of all the results is presented in Table 7-1.

The results presented in Table 7-1 have been imposed on the phase diagram for Pd-Rh as proposed by Gürler et al.[33], shown in Figure 7-2 and in detail on Figure 7-3

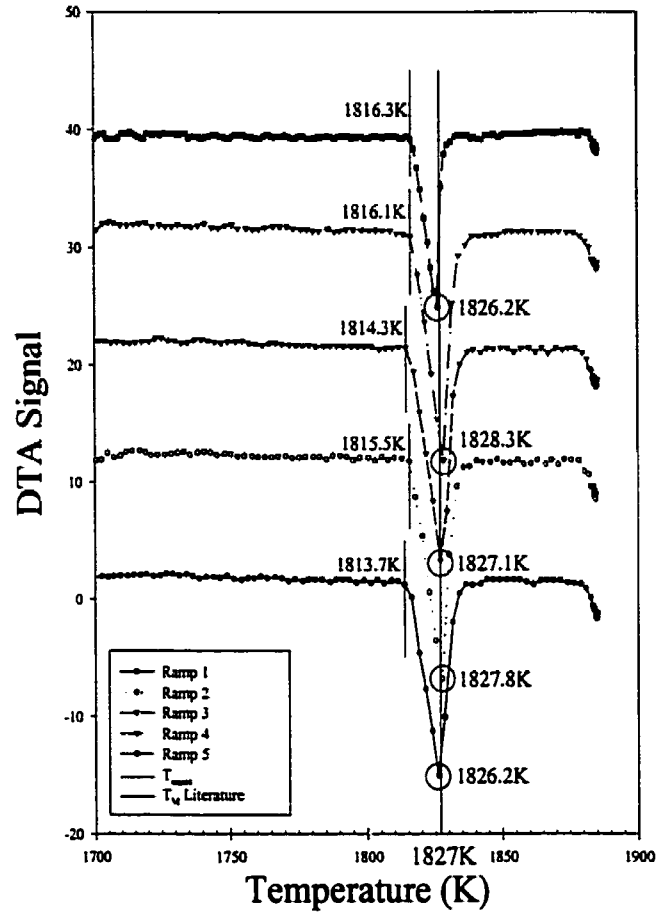

Figure 7-1. A typical set of results for the DTA experiments. In this case the sample was pure Pd. Five runs were performed.

Table 7-1. Summary of the results from the DTA experiments.

Sample	X_{Pd}	X_{Rh}	$T_{Solidus}$ (K)	$T_{Liquidus}$ (K)
A	1.00	0.00	1827±3	1827±3
B	0.88	0.12	1844±3	1856±3
C	0.80	0.20	1868±3	1880±3
D	0.74	0.26	1879±3	1895±3
E	0.69	0.31	1895±3	1911±3
F	0.64	0.36	1904±3	1919±3
G	0.59	0.41	1928±3	1939±3
H	0.53	0.47	1946±3	1958±3
J	0.34	0.66	1995±10	$T_{Liq} > 2023$
K	0.19	0.81	$T_{Sol} > 2023$	$T_{Liq} > 2023$

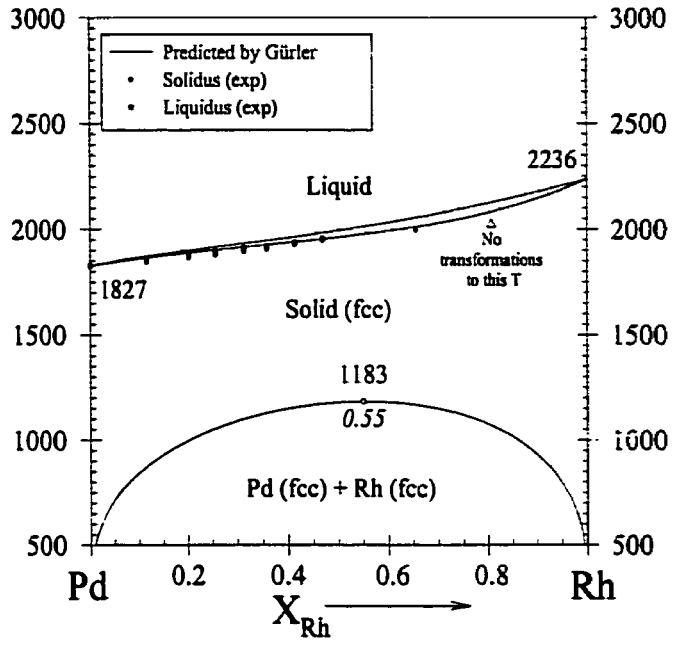

Figure 7-2. Comparison of the results from the current work with Gürler et al.[33].

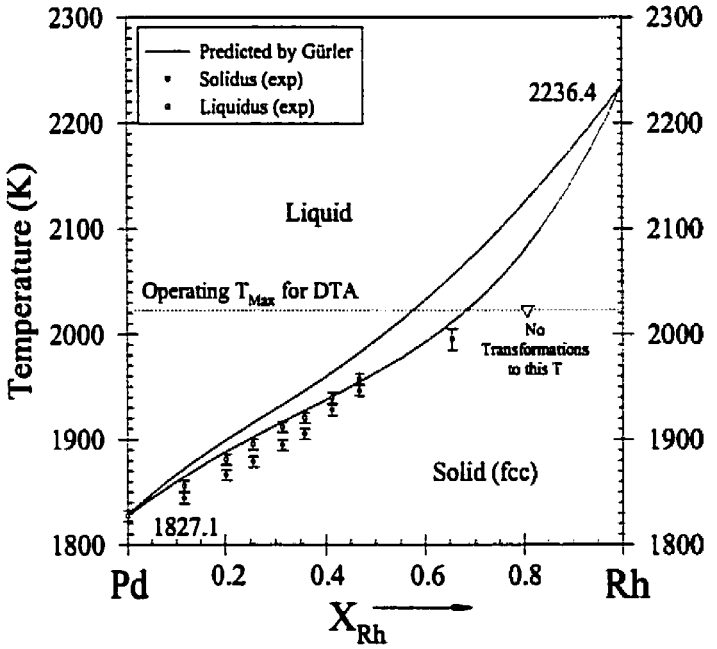

Figure 7-3. Enhanced diagram showing solidus and liquidus results from this work.

7.3 Knudsen Cell- Mass Spectrometry Experiments

For each experiment the data acquired consisted of a continuous spectrum of counts (representing intensity) at atomic mass units in intervals of 0.1amu. A typical

spectrum of intensity (in counts versus amu) is shown in Figure 7-4. There are two potential methods of recording and interpreting this data. The first is to determine the area under the peaks that correspond to a specific isotope of palladium. This method is based on the trapezoid rule, and the area for a particular isotope, ${}^{X}Pd$, is:

$$\textit{peak area for } {}^{X}Pd = \left(\frac{\Delta x}{2}\right)\left(\left(\sum_{y=-5}^{5} {}^{X+\frac{y}{10}}Pd\right)+\left(\sum_{y=-4}^{4} {}^{X+\frac{y}{10}}Pd\right)\right) \qquad (7.1)$$

where X = 102, 104, 105, 106, 108, or 110; Δx represents the interval at which counts are measured (in this case $\Delta x = 0.1$); and ${}^{X+\frac{y}{10}}Pd$ represents the measured number of counts at $X+\frac{y}{10}$ amu.

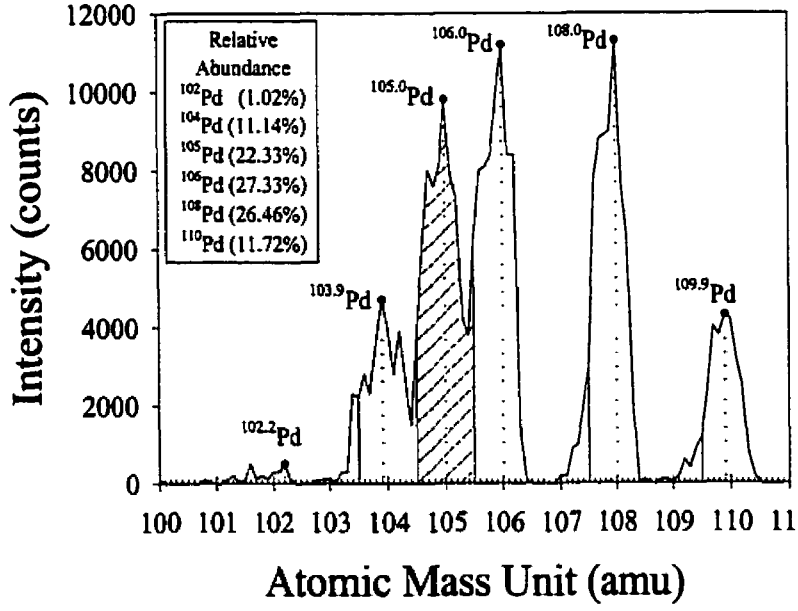

Figure 7-4. A typical spectrum of intensity versus amu, for the range of 100amu to 111amu. For the six Pd isotopes, the corresponding peak (maximum value) is indicated. The area under the intensity "curve" at ${}^{105}Pd$ is marked by the hatched region.

The second method for interpreting the intensity data is to consider the maximum intensity value at the corresponding peak. In the case illustrated in Figure 7-4, the maximum peaks and corresponding atomic mass unit are indicated.

A comparison of these two methods is provided in order to illustrate that there is little difference in either approach. For the example shown in Figure 7-4, the relative intensity values are provided in Table 7-2. From this data it can be seen that both methods provide nearly the same result, with the maximum intensity values being slightly closer to the expected natural abundance values. Computationally, the maximum intensity values are also easier to determine and so the values based on the maximum peak value will be reported.

Table 7-2. Comparison of peak area method to the maximum intensity (I_{Max}) method.

Isotope	Peak Area (counts)	Peak Area Relative Proportion	I_{Max} (counts)	I_{Max} Relative Proportion	Natural Abundance
^{102}Pd	215	0.8%	500	1.2%	1.02%
^{104}Pd	3135	12.2%	4700	11.2%	11.14%
^{105}Pd	6755	26.3%	9800	23.4%	22.33%
^{106}Pd	6680	26.0%	11200	26.8%	27.33%
^{108}Pd	6345	24.7%	11300	27.0%	26.46%
^{110}Pd	2600	10.1%	4300	10.3%	11.72%

For each of the eight experiments, *s*, the daily correction factor (from equation **(5.1)**) was calculated by analyzing the intensity of three peaks from a FC-43 spectrum, and comparing these values to a calibration standard. The results of these runs are shown in Table 7-3, along with the calibration standard and the value for *s*, determined for each experiment. The value for *s* is calculated by dividing the measured intensity of a particular FC-43 peak, by the corresponding peak intensity measured for the Ag standard.

The value of the orifice size correction factor, *f*, for each experiment is also presented in Table 7-3. This value was calculated using equation **(5.3)**.

Table 7-3. The data used to calculate the daily correction factor, s. Also the orifice size correction factor, f.

Run	100 amu	114 amu	119 amu	s_{100}	s_{114}	s_{119}	s_{avg}	f
Ag Std	614.6	218.9	477.0					
1	1130.0	362.0	907.4	1.839	1.654	1.902	1.798	1.723
2	977.9	418.0	843.7	1.591	1.910	1.769	1.756	0.502
3	537.6	176.6	414.0	0.875	0.807	0.868	0.850	1.615
4	531.4	201.4	430.2	0.865	0.920	0.902	0.896	1.778
5	623.0	394.3	565.2	1.014	1.801	1.185	1.333	0.766
6	820.0	500.2	756.5	1.334	2.285	1.586	1.735	0.959
7	781.7	470.0	694.9	1.272	2.147	1.457	1.625	0.879
8	620.4	291.8	557.0	1.009	1.333	1.168	1.170	1.891

The mass-sensitivity correction standard, γ_{x_i}, (equation **(5.1)**) is the ratio of the mass of the standard (in this case pure Ag) substance to that of the measured substance. Because Pd and Ag have nearly the same atomic mass, γ_{x_i} was assumed to be unity.

The isotopic abundance for Mo, Pd, Rh, and Ru were presented in Table 2-8. The principal element of interest was Pd, and a summary of its isotopic abundance is given in Table 7-4. The values for the isotopic abundance are represented by n_{x_i} in equation **(5.1)**.

Table 7-4. Isotopic abundance for palladium.

Isotope (amu)	Pd (%)	Isotope (amu)	Pd (%)
102	1.02	**106**	27.33
104	11.14	**108**	26.46
105	22.33	**110**	11.72

Finally, the ionization cross-section for Pd at 62eV, σ_{Pd}, was taken to be 5.50×10^{-16} cm^2. This value was estimated from the value presented in Section 2.3, which was for Pd at 32eV.

7.3.1 Results for Pure Elements

7.3.1.1 Silver Standard

In order to calibrate the Knudsen Cell-Mass Spectrometer, a silver standard was used. This experiment measured the vapour pressure of silver, in order that the instrument constant, k_{Ag}, from equation **(5.1)** be determined. It also provided a measure of the apparatus. The signal produced by introducing the FC-43 standard at the conclusion of the silver experiment allows the daily correction factor, s, to be calculated. These results for the daily correction factor, s, were shown in Table 7-3.

7.3.1.2 Sample 1 - Pure Palladium

The values for the maximum peak intensity of the six isotopes of palladium were measured above a sample of pure Pd. The results are shown in Table 7-5 at eight temperatures.

Table 7-5. Intensity (peak maximum) data for Sample 1.

Temperature (K)	^{102}Pd	^{104}Pd	^{105}Pd	^{106}Pd	^{108}Pd	^{110}Pd
1528	200	300	700	600	500	400
1585	100	600	700	900	700	500
1627	100	400	1100	1300	1000	1000
1652	400	900	1400	1500	1800	1300
1691	200	900	2400	2900	3300	2200
1718	300	2200	4200	5500	4700	1800
1753	300	3300	7300	7300	8000	4600
1772	500	4700	9800	11200	11300	4300

Equation **(5.1)** shows that the pressure for a given isotope of palladium is proportional to the intensity multiplied by the temperature. Table 7-6 shows these values with respect to the reciprocal of temperature.

Table 7-6. Intensity multiplied by temperature data for Sample 1.

Temperature^{-1} (1/K)	^{102}Pd	^{104}Pd	^{105}Pd	^{106}Pd	^{108}Pd	^{110}Pd
6.54×10^{-4}	305600	458400	1069600	916800	764000	611200
6.31×10^{-4}	158500	951000	1109500	1426500	1109500	792500
6.15×10^{-4}	162700	650800	1789700	2115100	1627000	1627000
6.05×10^{-4}	660800	1486800	2312800	2478000	2973600	2147600
5.91×10^{-4}	338200	1521900	4058400	4903900	5580300	3720200
5.82×10^{-4}	515400	3779600	7215600	9449000	8074600	3092400
5.70×10^{-4}	525900	5784900	12796900	12796900	14024000	8063800
5.64×10^{-4}	886000	8328400	17365600	19846400	20023600	7619600

A plot of the natural log of intensity multiplied by temperature versus the reciprocal of temperature for the pure Pd sample is shown in Figure 7-5. This plot shows a linear relationship between $\ln[I \cdot T]$ and $\frac{1}{T}$ as expected from equation **(5.1)**, when combined with the Van't Hoff equation[89], $\frac{d \ln P}{d\left(1/T\right)} = -\frac{\Delta H^{\circ}}{R}$.

Furthermore, the results should group themselves in three bands: the most abundant isotopes (each accounting for ≈25% of natural Pd) ^{105}Pd, ^{106}Pd, and ^{108}Pd at the top; ^{104}Pd and ^{110}Pd (each ≈11% of natural Pd) in the middle; and ^{102}Pd at the bottom.

Because equation **(5.1)** accounts for the isotopic abundance, (i.e., n_{x_i}), in theory the partial vapour pressure of Pd calculated using each isotope should be equivalent. Using the data from each of the six isotopes, it is now possible to determine the partial vapour pressure of Pd by six independent calculations using equation **(5.1)**. In the results that follow, total Pd pressures are reported, but expressed in terms of the isotope that was used in equation **(5.1)**.

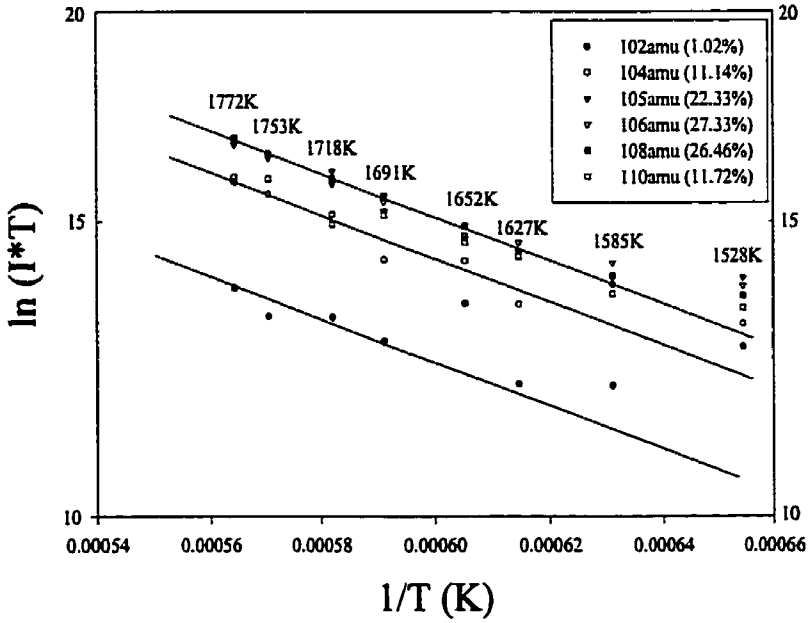

Figure 7-5. Natural log (I*T) versus 1/T for the primary isotopes of Pd for Sample 1. Three general trend lines has been added.

From this figure it can be seen that the intensity associated with the lowest temperature (i.e., 1528K) is insufficient to provide reasonable data. This data has been omitted in the subsequent regression analysis. Figure 7-6 shows the results of linear regression for each isotope of palladium.

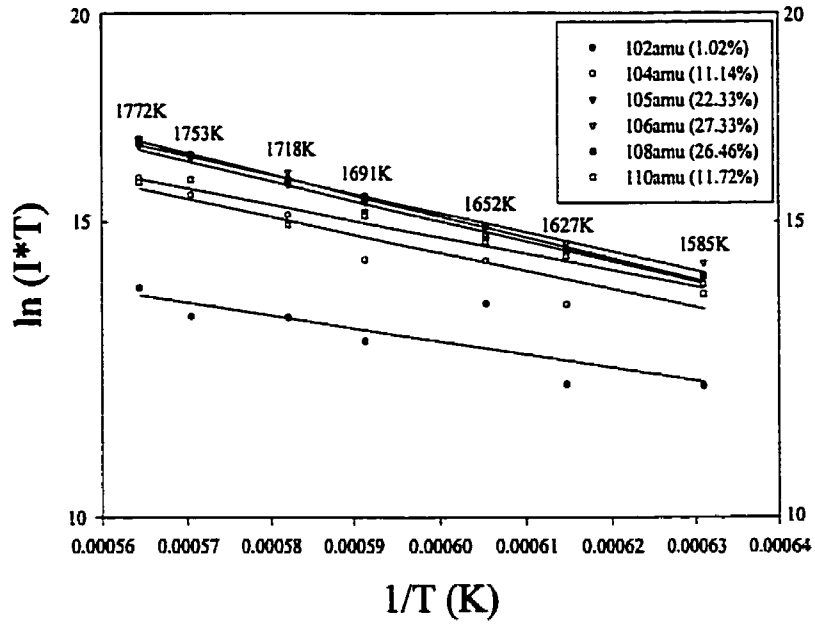

Figure 7-6. Results of the regression data for Sample 1.

The coefficients of the linear regression are presented in Table 7-7 along with an R^2 assessment of adequacy of fit. Only the three most abundant isotopes of Pd have an R^2 greater than 0.95. Since ^{102}Pd, ^{104}Pd, and ^{110}Pd are the least abundant of the six isotopes, the intensity of their signal was generally insufficient for analysis purposes, especially at lower temperatures. In this and subsequent analysis, only the three most abundant isotopes of Pd will be reported, since counting statistics were often poor for the three least abundant isotopes of Pd. The slopes of the linear regression lines for the three abundant isotopes are similar: mean value of –1206.5 and a standard deviation of 58.6.

Table 7-7. Data for the linear regression analysis for Sample 1.

Isotope	m (slope)	b (intercept)	R^2
^{102}Pd	-778.11	1.5716	0.6715
^{104}Pd	-1085.70	1.8088	0.8578
^{105}Pd	-1206.27	1.9002	0.9870
^{106}Pd	-1148.03	1.8700	0.9739
^{108}Pd	-1265.27	1.9385	0.9921
^{110}Pd	-985.38	1.7580	0.9497

Using values of $f = 1.723$, $s = 1.798$, $k_{Ag} = 8.28 \times 10^{27}$, and $\sigma_{Pd} = 5.5 \times 10^{-16}$ cm^2, the measured pressure for pure Pd was calculated using each isotope of Pd, Table 7-8.

Table 7-8. Computed partial pressures for Pd as calculated using the three abundant isotopes, along with the predicted values from the thermodynamic model.

T (K)	^{105}Pd (×10^{6}atm)	^{106}Pd (×10^{6}atm)	^{108}Pd (×10^{6}atm)	Model (×10^{6}atm)
1585	0.26	0.27	0.22	0.91
1627	0.41	0.40	0.32	1.88
1652	0.53	0.47	0.58	2.85
1691	0.94	0.92	1.09	5.32
1718	1.66	1.78	1.57	8.06
1753	2.95	2.41	2.73	13.53
1772	4.00	3.74	3.90	17.77

A plot of $\ln p_{Pd\,Measured}$ $vs\,\frac{1}{T}$ is shown in Figure 7-7.

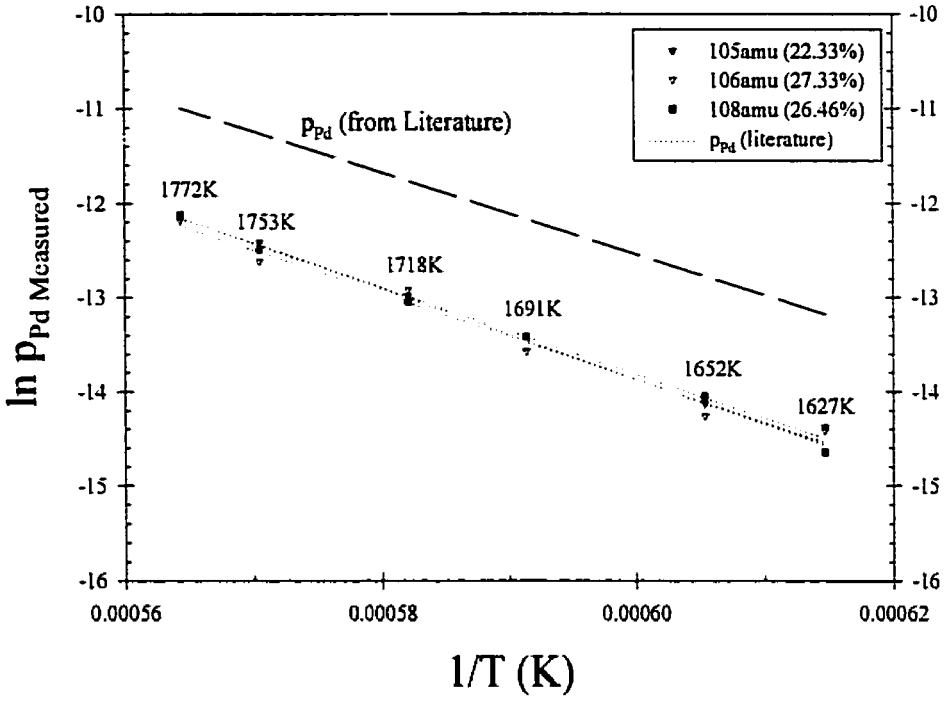

Figure 7-7. Plot of the Natural Logarithm of the Computed Partial Pressure for Pd against Reciprocal Temperature.

A linear regression analysis was performed and the results of the linear regression for the data are presented in Table 7-9.

Table 7-9. Data for the linear regression analysis for Figure 7-7.

Isotope	m (slope)	b (intercept)	R^2
^{105}Pd	-46558	14.115	0.9900
^{106}Pd	-45780	13.593	0.9815
^{108}Pd	-48001	14.930	0.9961

By taking the averages for the slope and intercept, an expression for the Pd partial pressure as a function of temperature was calculated to be:

$$\ln[p_{Pd}] = \frac{-46780}{T} + 14.213 \qquad (7.2)$$

This expression can be compared with the equivalent expression for the literature value[17]:

$$\ln[p_{Pd}] = \frac{-43353}{T} + 13.469 \qquad (7.3)$$

It can be seen that the agreement is respectable. From equation **(7.2)** the heat of sublimation is calculated as 388929 J/mol, while the literature value, obtained from equation **(7.3)**, is 360437 J/mol. The difference is 28492 J/mol or about 8%. Furthermore, because the calculated enthalpy of sublimation is within acceptable agreement, the effect being measured is that of Pd vaporizing, and not that of a side reaction such as Pd interacting with the tantalum crucible and then effusing.

The results for palladium provide a measure of how well Pd can be measured by the apparatus. By referring to Table 7-8, it was shown that the results for each of the abundant isotopes of Pd were approximately in error by a factor of 4 below the predicted pressure of Pd. There are several possible sources of error in the *absolute* determination of p_{Pd} in equation **(5.1)**, and these are summarized here:

1. *I*: the intensity was determined by subtracting two spectra- one measured when there was an open path to the detector and the other when the path was obstructed (i.e., a background count). Both measurements were rounded to the nearest 100 counts. In a 10000 count intensity reading the error would be less than 1%;
2. *T*: the pyrometer is rated to be accurate to 1% of the measured temperature;
3. *f*: the measurement of the orifice diameter is ±0.001 inches. For an orifice diameter of 0.030inches, this can result in a 7% error in the value of *f*. This error is compounded by the fact that there are two measurements involved- the sample and the silver standard;
4. *s*: the daily correction factor is calculated as the average of three ratios between FC-43 peaks measured for the Ag standard and the sample. If one assumes that the standard deviation of these three values is the error, then a reasonable estimate is between 15-20%;

5. σ_{Pd}: the ionization cross-section for Pd was estimated from literature values. As there is little experimental evidence to support the estimated value, it could in error by as much as a factor of 2. In other words, a value of 2.8×10^{-16} cm^2 is not unreasonable.
6. γ: this value was assumed to be 1. The associated error is just over 1%.
7. n: the isotopic abundance values for Pd were considered to be very accurate.

Of the sources of error listed above, the greatest uncertainty lies in the ionization cross-section for Pd. If the factor of 4, by which the experimental measurements differ from the literature values, were incorporated into this term, an ionization cross-section of 1.4×10^{-16} cm^2 would result. This value is not consistent with the literature, however, and has not been proposed.

In order to circumvent some of the uncertainties associated with calculating the absolute partial pressure of the palladium above each of the alloys the relative partial pressures of palladium will be used to compute the activity, a_{Pd}. Since,

$$\overline{G} - G^{\circ} = RT \ln\left[a_{Pd}\right] = RT \ln\left[\frac{c^{\bullet} p_{Pd\ alloy}}{c^{\bullet} p^{\bullet}_{Pd\ pure}}\right] \qquad \textbf{(7.4)}$$

where $c^{\bullet}$ represents the constants from the denominator of equation **(5.1)**.

From equation **(7.4)** it can be seen that the constant terms used to calculate the absolute pressures of Pd in both the alloy and the pure sample, cancel themselves. This removes the necessity for refining the precision in the ionization cross-section, σ_{Pd}. There is, however, error still associated with the experiment-to-experiment variables (e.g., f and s) that are not eliminated. In the subsequent results, the relative partial pressures of the alloy and pure palladium (calculated by equation **(7.2)**), will be reported, since this is all that is necessary to test the thermodynamic models.

7.3.2 Single Phase Alloys

7.3.2.1 Sample 2 – 22.8%Pd/77.2%Rh

The intensity results for Sample 2 are shown in Table 7-10. Only the three most abundant isotopes are reported. **Appendix D** contains complete results for Samples 2-8.

Table 7-10. Intensity (peak maximum) data for Sample 2.

Temperature (K)	^{105}Pd	^{106}Pd	^{108}Pd
1741	300	400	500
1799	700	900	800
1850	1200	900	1100
1893	2100	2000	1900
1922	3000	2700	3200
1953	2600	3100	2700
1982	3700	4800	4100
2015	5100	6300	5900
2031	6900	7000	7200

A plot of the natural log of intensity multiplied by temperature versus the reciprocal of temperature for the Sample 2 is shown in Figure 7-8. The results of linear regression for each isotope of palladium for Sample 2 are shown as well.

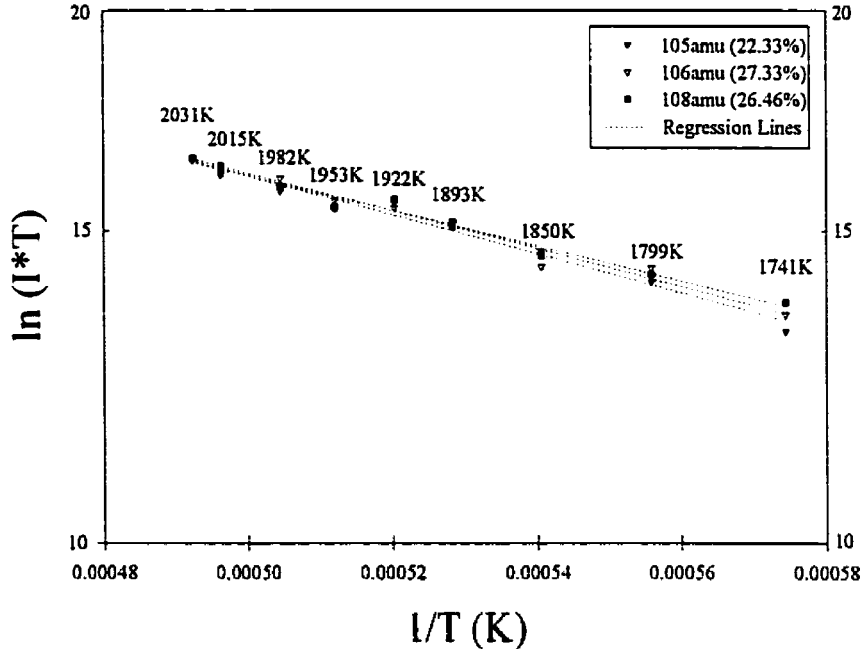

Figure 7-8. Natural log (I*T) versus 1/T for the isotopes of Pd for Sample 2. The lines represent linear regression results for each isotope.

The coefficients of the linear regression are presented in Table 7-11 along with an R^2 assessment of adequacy of fit. The slopes of the linear regression lines from the three most abundant isotopes have a mean value of –1055.5 and a standard deviation of 55.8.

Table 7-11. Data for the linear regression analysis for Sample 2.

Isotope	m (slope)	b (intercept)	R^2
^{105}Pd	-1102.2	1.7583	0.9766
^{106}Pd	-1070.6	1.7442	0.9799
^{108}Pd	-993.7	1.7042	0.9809

A plot of $\ln p_{Pd\,Measured}$ *vs* $\frac{1}{T}$ is shown in Figure 7-9.

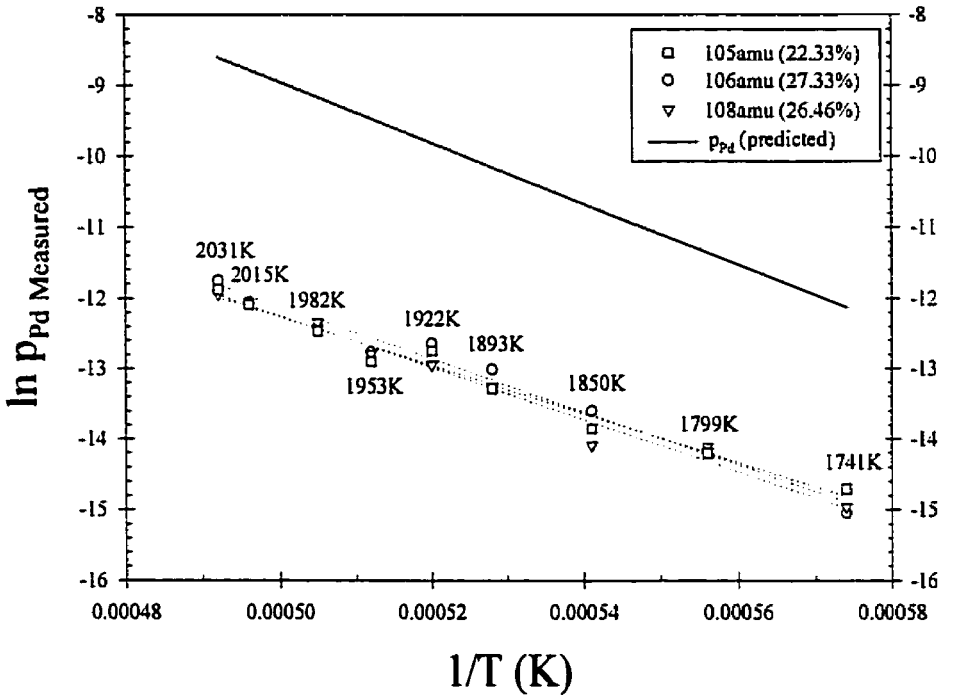

Figure 7-9. Plot of the Natural Logarithm of the Computed Partial Pressure for Pd against Reciprocal Temperature for Sample 2.

The coefficients of the linear regression are presented in Table 7-12 along with an R^2 assessment of adequacy of fit. The slopes of the linear regression lines in Figure 7-9 have a mean value of –36300 and a standard deviation of 1646.

Table 7-12. Linear regression analysis for Sample 2. The slope provides a measure of the partial heat of mixing for Pd.

Isotope	m (slope)	b (intercept)	R^2
^{105}Pd	-37532	6.649	0.9811
^{106}Pd	-36938	6.219	0.9803
^{108}Pd	-34431	4.946	0.9795
Model	-42928	12.512	

From the linear regression data, an expression for the partial pressure of Pd in this alloy can be derived, equation **(7.5)**.

$$\ln\left[p_{Pd\,(Sample\,2)}\right] = \frac{-36300}{T} + 5.938 \qquad (7.5)$$

From equation **(7.5)** the heat of sublimation in this temperature range is calculated as 302kJ/mol, which compares to the predicted value of 357kJ/mol. The difference is 55kJ/mol or 15% lower than predicted.

The calculated ratio of the partial pressure for Pd over the alloy to the measured partial pressure of pure Pd, along with the partial Gibbs energy of mixing for Pd in the alloy and as predicted by the model are listed in Table 7-13. A comparison of the measured partial Gibbs energy of mixing with the partial Gibbs energy of mixing predicted by the model is shown in Figure 7-10.

Table 7-13. Computed are: the ratio of the partial pressure for Pd over the alloy to the measured partial pressure of pure Pd; the partial Gibbs energy of mixing for Pd; and the partial Gibbs energy of mixing as calculated by the thermodynamic model for Sample 2.

Temperature (K)	**Experimental** $\frac{p_{Pd\,(alloy\,2)}}{p^{\circ}_{Pd\,(pure)}}$	**Experimental** $\Delta\overline{G}^{M}_{Pd}$ **(kJ/mol)**	**Model** $\Delta\overline{G}^{M}_{Pd}$ **(kJ/mol)**
1741	0.105	-32.6	-10.8
1799	0.086	-36.6	-11.6
1850	0.074	-40.1	-12.3
1893	0.065	-43.1	-12.9
1922	0.059	-45.1	-13.3
1953	0.055	-47.2	-13.7
1982	0.050	-49.2	-14.1
2015	0.046	-51.5	-14.6
2031	0.044	-52.6	-14.8

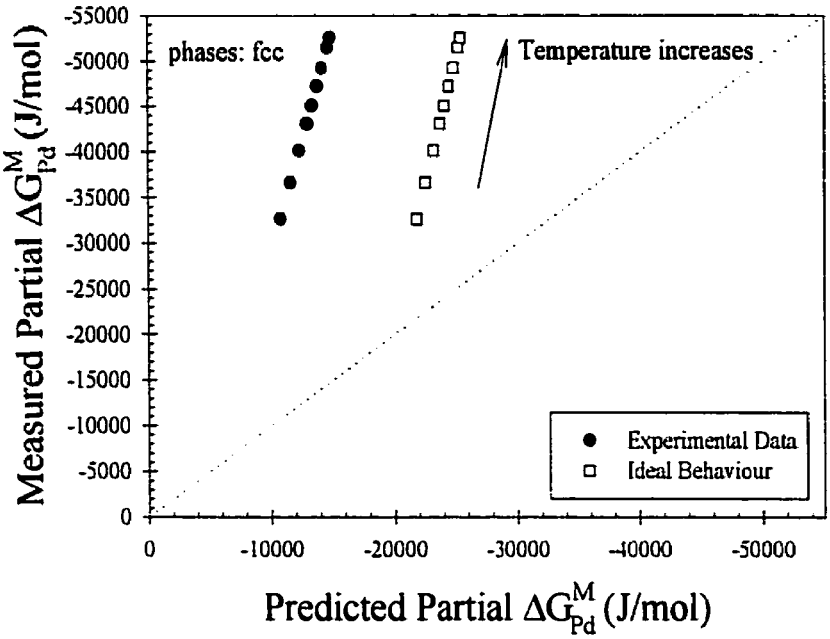

Figure 7-10. Comparison of Measured Partial Gibbs energy of mixing with the Partial Gibbs energy of mixing predicted by the model. Sample 2.

7.3.2.2 Sample 3 – 52.0%Pd/48.0%Rh

The intensity results for Sample 3 are shown in Table 7-14.

Table 7-14. Intensity (peak maximum) data for Sample 3.

Temperature (K)	^{105}Pd	^{106}Pd	^{108}Pd
1730	1100	1300	1200
1805	2600	3400	2800
1838	4400	4700	5000
1869	8000	9300	8400
1901	13100	14000	15000
1929	20600	23500	23000

A plot of the natural log of intensity multiplied by temperature versus the reciprocal of temperature for the 52.8%Pd/47.2%Rh sample is shown in Figure 7-11, along with the results of the linear regression analysis.

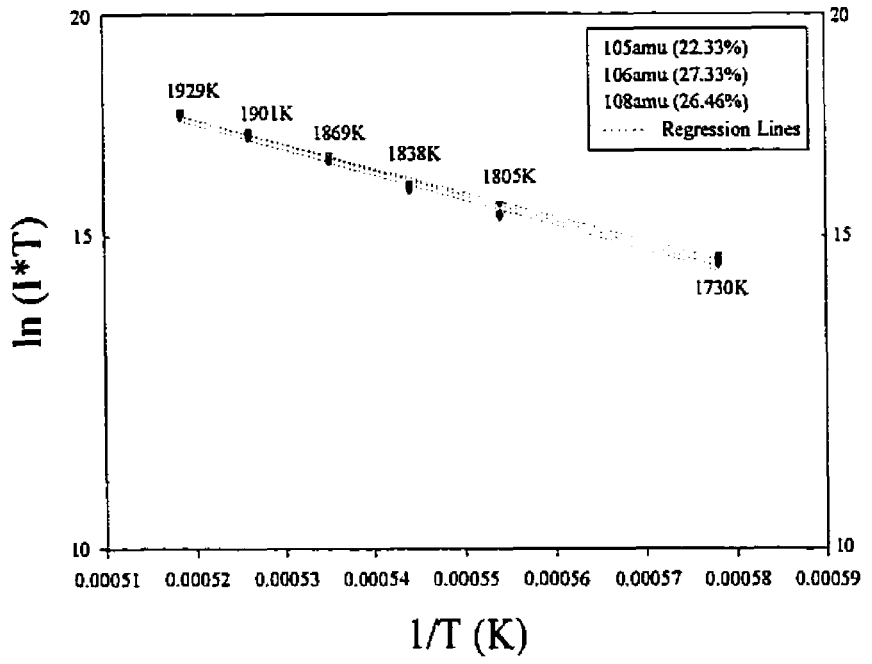

Figure 7-11. Natural log (I*T) versus 1/T for the primary isotopes of Pd for Sample 3 along with the results of the regression analysis.

The linear regression analysis for Sample 3 is shown in Table 7-15. The average slope was –1396.7 and the standard deviation was 33.7.

Table 7-15. Data for the linear regression analysis for Sample 3.

Isotope	m (slope)	b (intercept)	R^2
^{105}Pd	-1413.7	1.9738	0.9904
^{106}Pd	-1357.9	1.9474	0.9896
^{108}Pd	-1418.6	1.9791	0.9898

A plot of $\ln p_{Pd\,Measured}$ $vs\,\frac{1}{T}$ is shown in Figure 7-12.

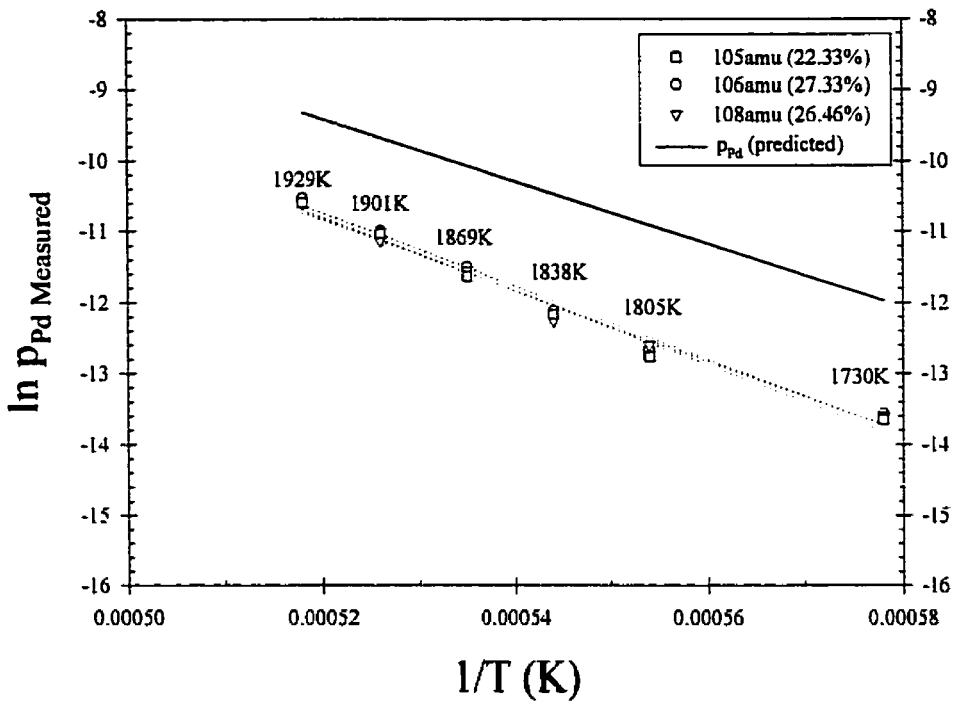

Figure 7-12. Plot of the Natural Logarithm of the Computed Partial Pressure for Pd against Reciprocal Temperature for Sample 3.

The coefficients of the linear regression are presented in Table 7-16 along with an R^2 assessment of adequacy of fit. The slopes of the linear regression lines in Figure 7-12 have a mean value of –51200 and a standard deviation of 1084.

Table 7-16. Linear regression analysis for Sample 3. The slope provides a measure of the partial heat of mixing for Pd.

Isotope	m (slope)	b (intercept)	R^2
^{105}Pd	-51558	16.070	0.9855
^{106}Pd	-49982	15.155	0.9847
^{108}Pd	-52060	16.270	0.9847
Model	-44202	13.578	

From the linear regression data, an expression for the partial pressure of Pd in this alloy can be derived, equation **(7.6)**.

$$\ln\left[p_{Pd\,(Sample\,3)}\right] = \frac{-51200}{T} + 15.832 \qquad (7.6)$$

From equation **(7.6)** the heat of sublimation in this temperature range is calculated as 426kJ/mol, which compares to the predicted value of 367kJ/mol. The difference is 58kJ/mol or 16% higher than predicted.

The calculated ratio of the partial pressure for Pd over the alloy to the measured partial pressure of pure Pd, along with the partial Gibbs energy of mixing for Pd in the alloy and as predicted by the model are listed in Table 7-17. A comparison of the measured partial Gibbs energy of mixing with the partial Gibbs energy of mixing predicted by the model is shown in Figure 7-13.

Table 7-17. Computed are: the ratio of the partial pressure for Pd over the alloy to the measured partial pressure of pure Pd; the partial Gibbs energy of mixing for Pd; and the partial Gibbs energy of mixing as calculated by the thermodynamic model for Sample 3.

Temperature (K)	**Experimental** $\frac{p_{Pd\,(alloy\,3)}}{p^{\circ}_{Pd\,(pure)}}$	**Experimental** $\Delta\overline{G}^{M}_{Pd}$ **(kJ/mol)**	**Model** $\Delta\overline{G}^{M}_{Pd}$ **(kJ/mol)**
1730	0.392	-13.5	-5.6
1805	0.436	-12.5	-6.1
1838	0.456	-12.0	-6.3
1869	0.474	-11.6	-6.5
1901	0.494	-11.2	-6.7
1929	0.511	-10.8	-6.8

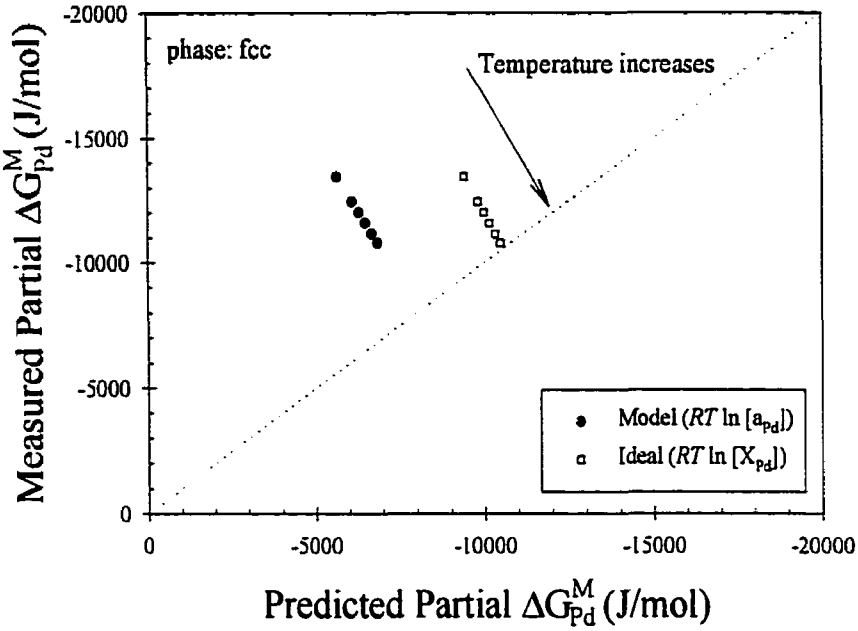

Figure 7-13. Comparison of Measured Partial Gibbs energy of mixing with the Partial Gibbs energy of mixing predicted by the model. Sample 3.

7.3.2.3 Sample 4 – 20.3%Mo/19.8%Ru/20.2%Pd/39.7%Rh

The intensity results for Sample 4 are shown in Table 7-18.

Table 7-18. Intensity (peak maximum) data for Sample 4.

Temperature (K)	^{105}Pd	^{106}Pd	^{108}Pd
1715	1100	900	800
1737	1200	1100	1300
1757	1400	1300	1400
1779	1600	1800	1400
1802	2000	2400	2100
1824	2200	3100	2400
1844	2800	3100	3200
1861	3200	3700	2900
1885	4000	3800	3700
1910	4800	4600	4200

A plot of the natural log of intensity multiplied by temperature versus the

reciprocal of temperature for Sample 4 is shown in Figure 7-14.

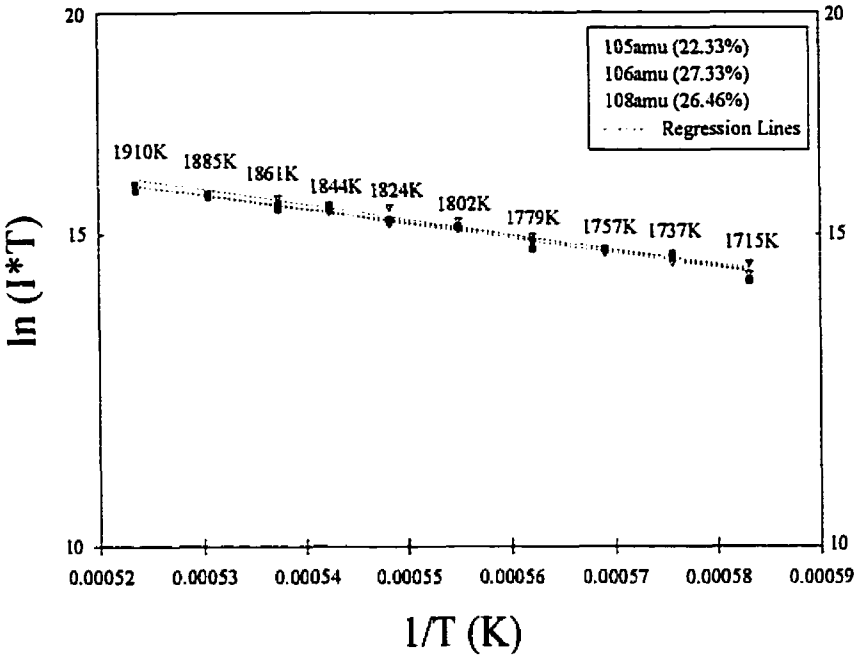

Figure 7-14. Natural log (I*T) versus 1/T for the primary isotopes of Pd for Sample 4 along with the results of the regression analysis.

The results of the linear regression are presented in Table 7-19. The data from the three most abundant isotopes is consistent with an average slope of –822.4 and a standard deviation of 43.7.

Table 7-19. Data for the linear regression analysis for sample Sample 4.

Isotope	m (slope)	b (intercept)	R^2
^{105}Pd	-781.4	1.6129	0.9913
^{106}Pd	-868.3	1.6621	0.9675
^{108}Pd	-817.6	1.6317	0.9612

A plot of $\ln p_{Pd\,Measured}$ $vs\,\frac{1}{T}$ is shown in Figure 7-7.

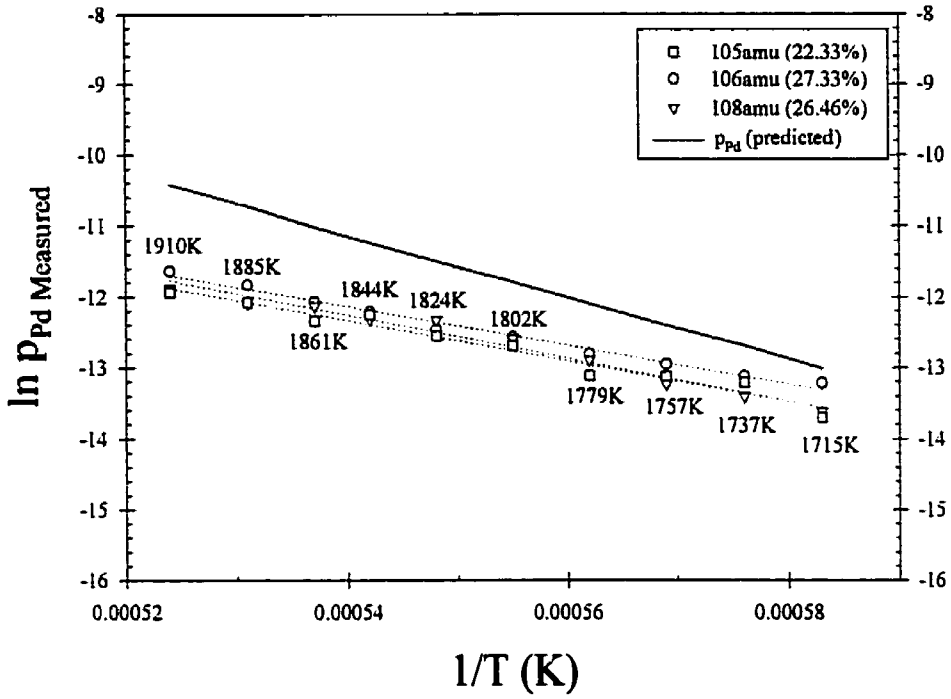

Figure 7-15. Plot of the Natural Logarithm of the Computed Partial Pressure for Pd against Reciprocal Temperature for Sample 4.

The coefficients of the linear regression are presented in Table 7-23 along with an R^2 assessment of adequacy of fit. The slopes of the linear regression lines in Figure 7-15 have a mean value of –28761 and a standard deviation of 1515.

Table 7-20. Linear regression analysis for Sample 4. The slope provides a measure of the partial heat of mixing for Pd.

Isotope	m (slope)	b (intercept)	R^2
^{105}Pd	-27415	2.664	0.9872
^{106}Pd	-30402	4.157	0.9739
^{108}Pd	-28467	3.035	0.9641
Model	-43848	12.550	

From the linear regression data, an expression for the partial pressure of Pd in this alloy can be derived, equation (7.7).

$$\ln\left[p_{Pd\,(Sample\,4)}\right] = \frac{-28761}{T} + 3.285 \qquad (7.7)$$

From equation **(7.7)** the heat of sublimation in this temperature range is calculated as 239kJ/mol, which compares to the predicted value of 365kJ/mol. The difference is 1255kJ/mol or 34% lower than predicted.

The calculated ratio of the partial pressure for Pd over the alloy to the measured partial pressure of pure Pd, along with the partial Gibbs energy of mixing for Pd in the alloy and as predicted by the model are listed in Table 7-21. A comparison of the measured partial Gibbs energy of mixing with the partial Gibbs energy of mixing predicted by the model is shown in Figure 7-16.

Table 7-21. Computed are: the ratio of the partial pressure for Pd over the alloy to the measured partial pressure of pure Pd; the partial Gibbs energy of mixing for Pd; and the partial Gibbs energy of mixing as calculated by the thermodynamic model for Sample 4.

Temperature (K)	**Experimental** $\frac{p_{Pd\,(alloy\,4)}}{p^{\circ}_{Pd\,(pure)}}$	**Experimental** $\Delta\overline{G}^{M}_{Pd}$ **(kJ/mol)**	**Model** $\Delta\overline{G}^{M}_{Pd}$ **(kJ/mol)**
1715	0.656	-6.0	-17.6
1737	0.574	-8.0	-17.9
1757	0.510	-9.8	-18.2
1779	0.450	-11.8	-18.6
1802	0.395	-13.9	-18.9
1824	0.350	-15.9	-19.3
1844	0.315	-17.7	-19.6
1861	0.288	-19.3	-19.9
1885	0.254	-21.5	-20.2
1910	0.224	-23.7	-20.6

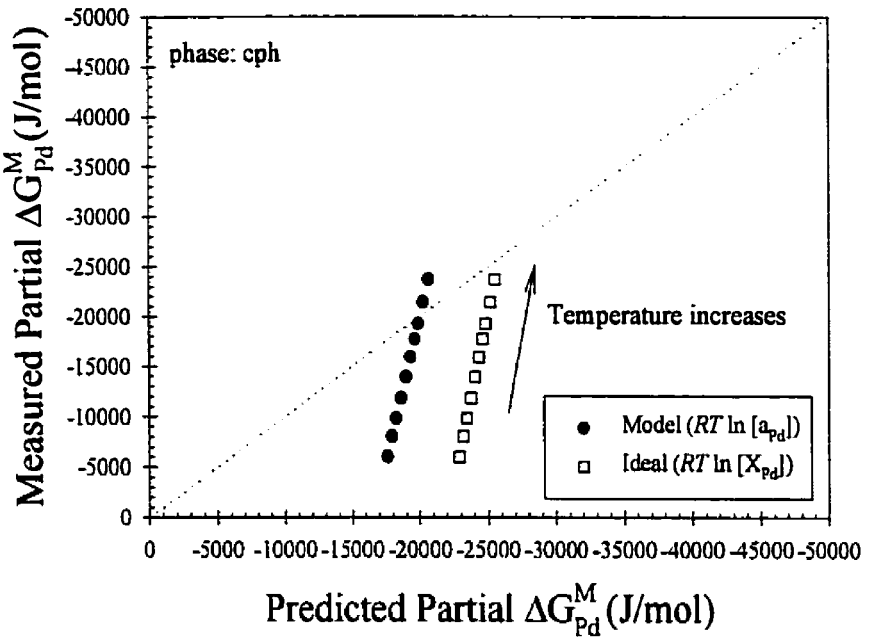

Figure 7-16. Comparison of Measured Partial Gibbs energy of mixing with the Partial Gibbs energy of mixing predicted by the model. Sample 4.

7.3.2.4 Sample 5 – 20.1%Mo/30.1%Ru/19.9%Pd/29.9%Rh

The intensity results for Sample 5 are shown in Table 7-22.

Table 7-22. Intensity (peak maximum) data for Sample 5.

Temperature (K)	^{105}Pd	^{106}Pd	^{108}Pd
1684	900	1200	700
1703	1200	1100	1000
1723	1800	1100	1300
1743	1500	2100	1800
1759	2700	3000	2400
1786	3200	2900	3100
1812	3700	3800	3800
1837	4700	5000	3800
1858	6000	5800	6200
1874	5900	6100	6000

A plot of the natural log of intensity multiplied by temperature versus the

reciprocal of temperature for Sample 5 is shown in Figure 7-17.

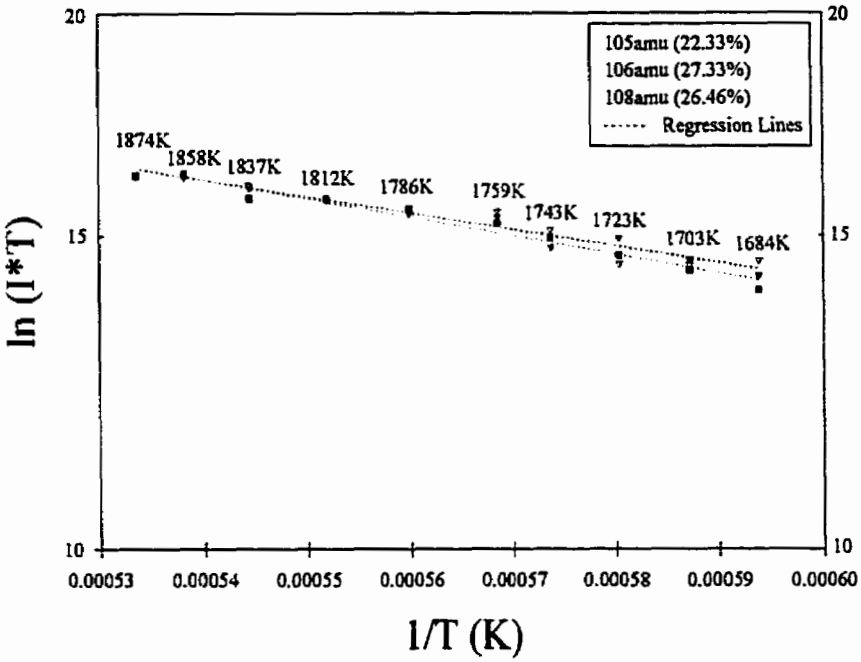

Figure 7-17. Natural log (I*T) versus 1/T for the primary isotopes of Pd for Sample 5 along with the results of the regression analysis.

The results from the linear regression analysis are presented in Table 7-23. The average slope of the line is –976.2 with a standard deviation of 65.4.

Table 7-23. Data for the linear regression analysis for Sample 5.

Isotope	m (slope)	b (intercept)	R^2
^{105}Pd	-943.3	1.7171	0.9621
^{106}Pd	-933.7	1.7121	0.9373
^{108}Pd	-1051.5	1.7755	0.9680

A plot of $\ln p_{Pd\,Measured}$ $vs\,\frac{1}{T}$ is shown in Figure 7-18.

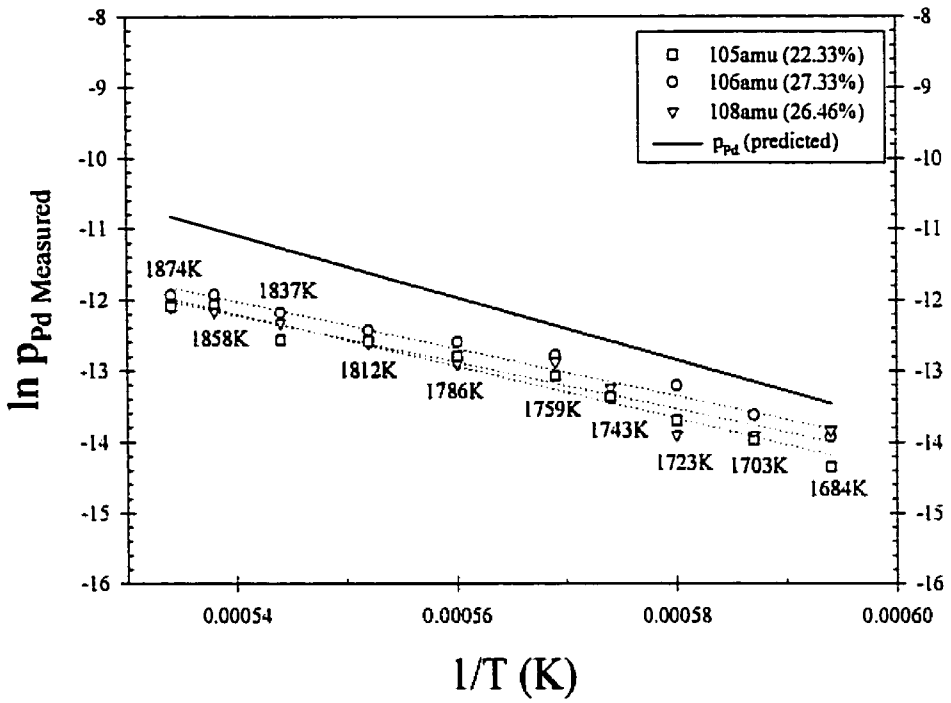

Figure 7-18. Plot of the Natural Logarithm of the Computed Partial Pressure for Pd against Reciprocal Temperature for Sample 5.

The coefficients of the linear regression are presented in Table 7-24 along with an R^2 assessment of adequacy of fit. The slopes of the linear regression lines in Figure 7-18 have a mean value of –34277 and a standard deviation of 2122.

Table 7-24. Linear regression analysis for Sample 5. The slope provides a measure of the partial heat of mixing for Pd.

Isotope	m (slope)	b (intercept)	R^2
^{105}Pd	-33242	5.920	0.9668
^{106}Pd	-32870	5.223	0.9372
^{108}Pd	-36718	7.622	0.9705
Model	-43800	12.559	

From the linear regression data, an expression for the partial pressure of Pd in this alloy can be derived, equation **(7.8)**.

$$\ln\left[p_{Pd\,(Sample\,5)}\right] = \frac{-34277}{T} + 6.255 \qquad (7.8)$$

From equation **(7.8)** the heat of sublimation in this temperature range is calculated as 285kJ/mol, which compares to the predicted value of 364kJ/mol. The difference is 79kJ/mol or 22% lower than predicted.

The calculated ratio of the partial pressure for Pd over the alloy to the measured partial pressure of pure Pd, along with the partial Gibbs energy of mixing for Pd in the alloy and as predicted by the model are listed in Table 7-25. A comparison of the measured partial Gibbs energy of mixing with the partial Gibbs energy of mixing predicted by the model is shown in Figure 7-19.

Table 7-25. Computed are: the ratio of the partial pressure for Pd over the alloy to the measured partial pressure of pure Pd; the partial Gibbs energy of mixing for Pd; and the partial Gibbs energy of mixing as calculated by the thermodynamic model for Sample 5.

Temperature (K)	**Experimental** $\frac{p_{Pd\,(alloy\,5)}}{p^{\circ}_{Pd\,(pure)}}$	**Experimental** $\Delta\overline{G}^{M}_{Pd}$ **(kJ/mol)**	**Model** $\Delta\overline{G}^{M}_{Pd}$ **(kJ/mol)**
1684	0.587	-7.5	-16.8
1703	0.540	-8.7	-17.1
1723	0.496	-10.0	-17.4
1743	0.456	-11.4	-17.7
1759	0.427	-12.4	-17.9
1786	0.384	-14.2	-18.3
1812	0.347	-15.9	-18.7
1837	0.316	-17.6	-19.1
1858	0.293	-19.0	-19.4
1874	0.276	-20.0	-19.6

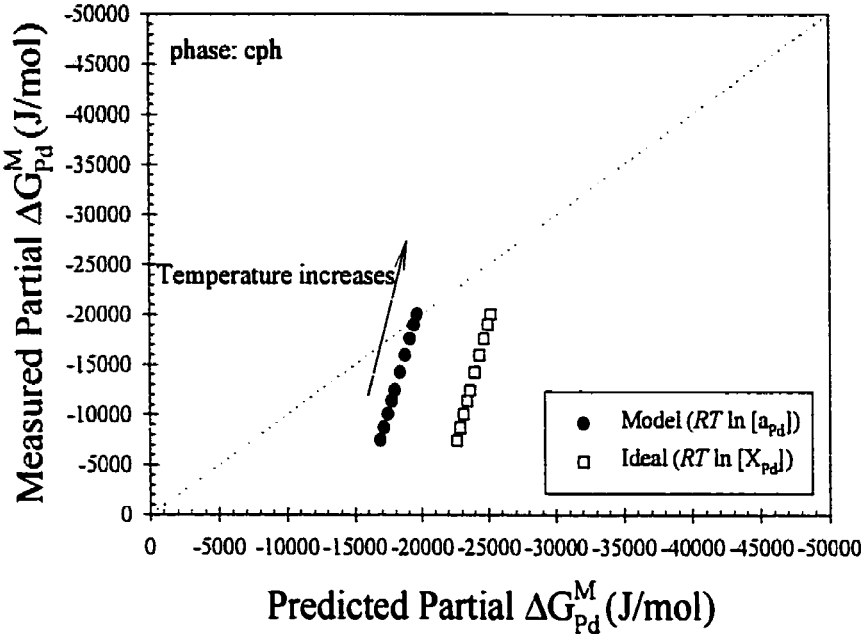

Figure 7-19. Comparison of Measured Partial Gibbs energy of mixing with the Partial Gibbs energy of mixing predicted by the model. Sample 5.

7.3.2.5 Sample 6 – 20.3%Mo/39.9%Ru/19.8%Pd/20.0%Rh

The intensity results for Sample 6 are shown in Table 7-26.

Table 7-26. Intensity (peak maximum) data for Sample 6.

Temperature (K)	^{105}Pd	^{106}Pd	^{108}Pd
1661	300	300	300
1686	400	500	400
1705	500	400	600
1734	900	800	600
1760	1000	700	700
1787	1600	1300	1400
1813	2300	2200	1500
1833	2200	2400	1600
1853	2800	3000	3200
1875	3900	3600	2800

A plot of the natural log of intensity multiplied by temperature versus the

reciprocal of temperature for Sample 6 is shown in Figure 7-20.

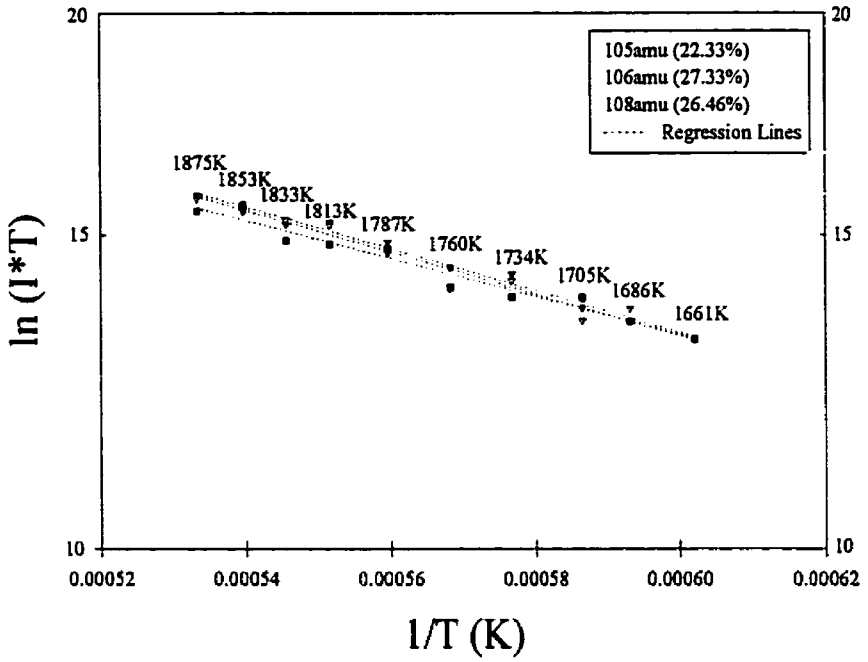

Figure 7-20. Natural log (I*T) versus 1/T for the primary isotopes of Pd for Sample 6 along with the results of the regression analysis.

The results from the linear regression analysis are presented in Table 7-27. The average slope of the line is −1135.4 with a standard deviation of 61.5.

Table 7-27. Data for the linear regression analysis for Sample 6.

Isotope	m (slope)	b (intercept)	R^2
^{105}Pd	-1171.5	1.8245	0.9868
^{106}Pd	-1170.4	1.8219	0.9643
^{108}Pd	-1064.4	1.7591	0.9601

A plot of $\ln p_{Pd\,Measured}$ $vs\ \frac{1}{T}$ is shown in Figure 7-21

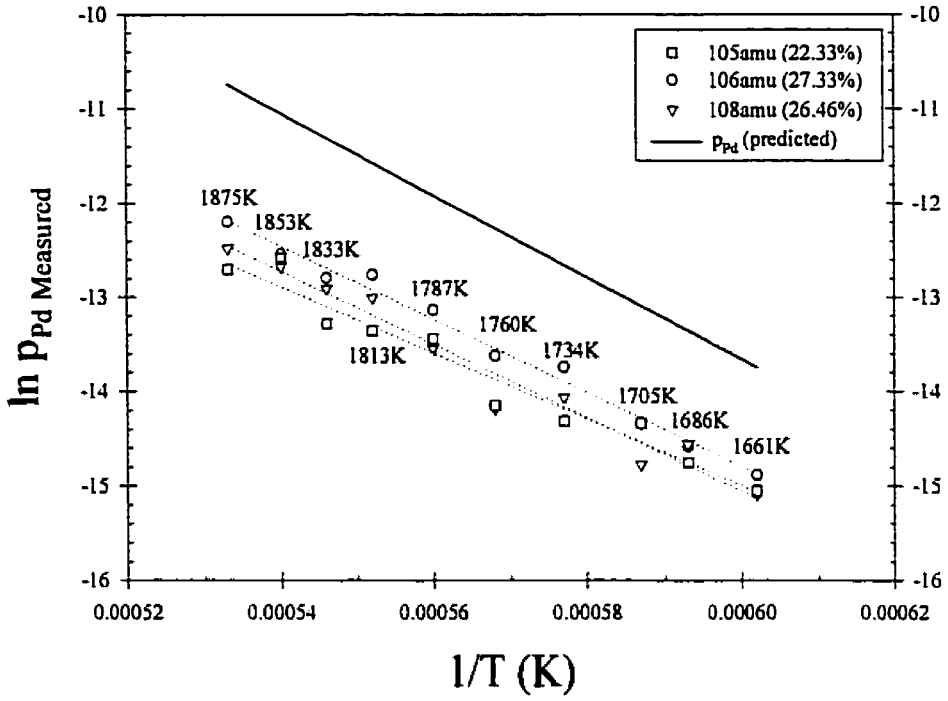

Figure 7-21. Plot of the Natural Logarithm of the Computed Partial Pressure for Pd against Reciprocal Temperature for Sample 6.

The coefficients of the linear regression are presented in Table 7-28 along with an R^2 assessment of adequacy of fit. The slopes of the linear regression lines in Figure 7-21 have a mean value of –37665 and a standard deviation of 2182.

Table 7-28. Linear regression analysis for Sample 6. The slope provides a measure of the partial heat of mixing for Pd.

Isotope	m (slope)	b (intercept)	R^2
^{105}Pd	-38942	8.572	0.9880
^{106}Pd	-38907	8.285	0.9631
^{108}Pd	-35145	6.089	0.9545
Model	-43548	12.469	

From the linear regression data, an expression for the partial pressure of Pd in this alloy can be derived, equation **(7.9)**.

$$\ln\left[p_{Pd\,(Sample\,6)}\right] = \frac{-37665}{T} + 7.649 \qquad (7.9)$$

From equation (7.9) the heat of sublimation in this temperature range is calculated as 313kJ/mol, which compares to the predicted value of 362kJ/mol. The difference is 49kJ/mol or 14% lower than predicted.

The calculated ratio of the partial pressure for Pd over the alloy to the measured partial pressure of pure Pd, along with the partial Gibbs energy of mixing for Pd in the alloy and as predicted by the model are listed in Table 7-29. A comparison of the measured partial Gibbs energy of mixing with the partial Gibbs energy of mixing predicted by the model is shown in Figure 7-22.

Table 7-29. Computed are: the ratio of the partial pressure for Pd over the alloy to the measured partial pressure of pure Pd; the partial Gibbs energy of mixing for Pd; and the partial Gibbs energy of mixing as calculated by the thermodynamic model for Sample 6.

Temperature (K)	Experimental $\frac{p_{Pd\,(alloy\,6)}}{p^{\circ}_{Pd\,(pure)}}$	Experimental $\Delta\overline{G}^{M}_{Pd}$ (kJ/mol)	Model $\Delta\overline{G}^{M}_{Pd}$ (kJ/mol)
1661	0.341	-14.9	-15.5
1686	0.314	-16.2	-15.9
1705	0.296	-17.3	-16.1
1734	0.271	-18.8	-16.5
1760	0.250	-20.3	-16.9
1787	0.231	-21.7	-17.2
1813	0.215	-23.2	-17.6
1833	0.204	-24.2	-17.9
1853	0.193	-25.3	-18.1
1875	0.182	-26.5	-18.4

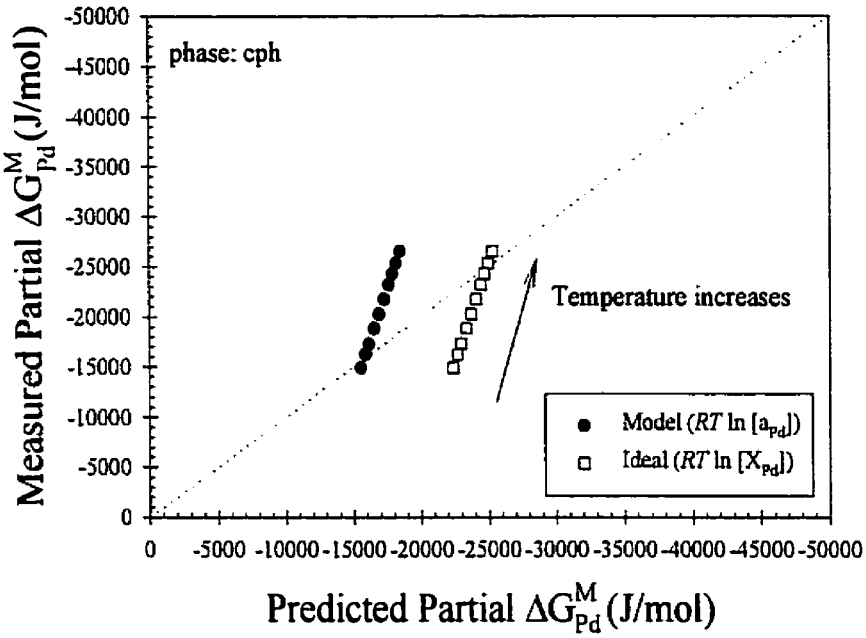

Figure 7-22. Comparison of Measured Partial Gibbs energy of mixing with the Partial Gibbs energy of mixing predicted by the model. Sample 6.

7.3.3 Two Phase Alloys

7.3.3.1 Sample 7 – 50.5%Mo/40.2%Ru/9.3%Pd

The intensity results for Sample 7 are shown in Table 7-30.

Table 7-30. Intensity (peak maximum) data for Sample 7.

Temperature (K)	^{105}Pd	^{106}Pd	^{108}Pd
1793	500	700	800
1827	900	1200	1200
1857	1100	2100	1300
1886	2000	1600	1700
1916	2300	2100	2800
1944	2300	2700	2800
1962	2300	2700	2600

A plot of the natural log of intensity multiplied by temperature versus the reciprocal of temperature for the Sample 7 is shown in Figure 7-23.

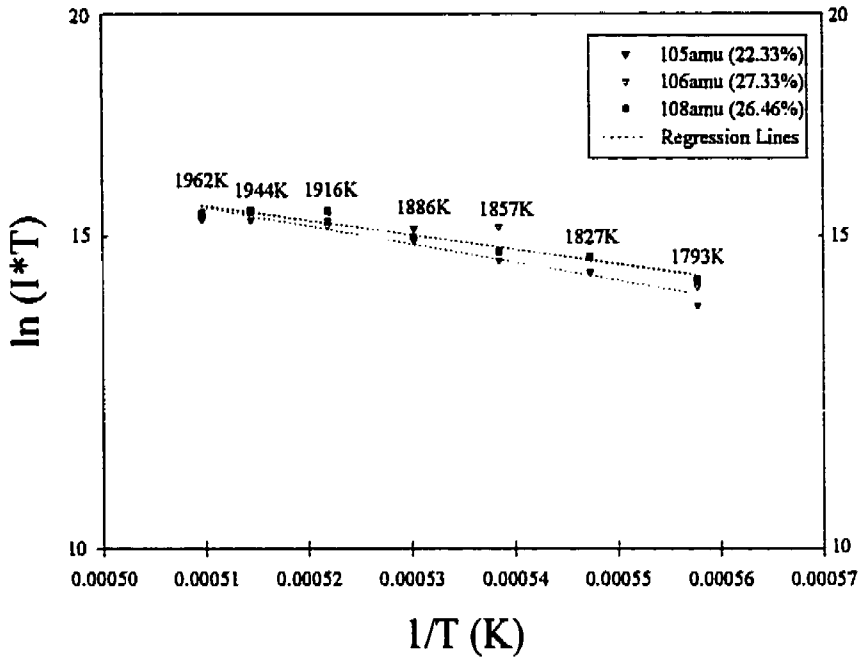

Figure 7-23. Natural log (I*T) versus 1/T for the primary isotopes of Pd for Sample 7 along with the results of the regression analysis.

The results from the linear regression analysis are presented in Table 7-31. The average slope of the line is –888.8 with a standard deviation of 118.1.

Table 7-31. Data for the linear regression analysis for Sample 7.

Isotope	m (slope)	b (intercept)	R^2
^{105}Pd	-1023.71	1.7140	0.9061
^{106}Pd	-803.94	1.6027	0.8580
^{108}Pd	-838.76	1.6212	0.9384

A plot of $\ln p_{Pd\,Measured}$ $vs\,\frac{1}{T}$ is shown in Figure 7-28.

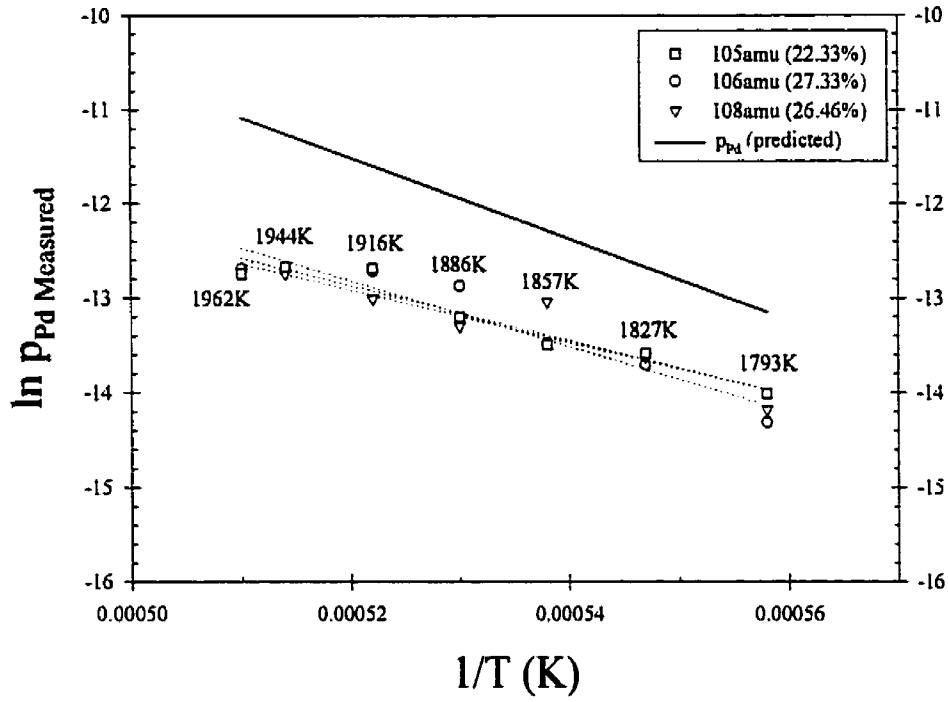

Figure 7-24. Plot of the Natural Logarithm of the Computed Partial Pressure for Pd against Reciprocal Temperature for Sample 7.

The coefficients of the linear regression are presented in Table 7-32 along with an R^2 assessment of adequacy of fit. The slopes of the linear regression lines in Figure 7-28 have a mean value of –30322 and a standard deviation of 3706.

Table 7-32. Linear regression analysis for Sample 7. The slope provides a measure of the partial heat of mixing for Pd.

Isotope	m (slope)	b (intercept)	R^2
^{105}Pd	-34544	5.140	0.9140
^{106}Pd	-27608	1.435	0.8722
^{108}Pd	-28815	2.109	0.9388
Model	-43071	10.884	

From the linear regression data, an expression for the partial pressure of Pd in this alloy can be derived, equation **(7.10)**.

$$\ln\left[p_{Pd\,(Sample\,7)}\right] = \frac{-30322}{T} + 2.895 \qquad (7.10)$$

From equation **(7.10)** the heat of sublimation in this temperature range is calculated as 252kJ/mol, which compares to the predicted value of 358kJ/mol. The difference is 106kJ/mol or 30% lower than predicted.

The calculated ratio of the partial pressure for Pd over the alloy to the measured partial pressure of pure Pd, along with the partial Gibbs energy of mixing for Pd in the alloy and as predicted by the model are listed in Table 7-33. A comparison of the measured partial Gibbs energy of mixing with the partial Gibbs energy of mixing predicted by the model is shown in Figure 7-25.

Table 7-33. Computed are: the ratio of the partial pressure for Pd over the alloy to the measured partial pressure of pure Pd; the partial Gibbs energy of mixing for Pd; and the partial Gibbs energy of mixing as calculated by the thermodynamic model for Sample 7.

Temperature (K)	**Experimental** $\frac{p_{Pd\,(alloy\,7)}}{p^{\circ}_{Pd\,(pure)}}$	**Experimental** $\Delta\overline{G}^{M}_{Pd}$ **(kJ/mol)**	**Model** $\Delta\overline{G}^{M}_{Pd}$ **(kJ/mol)**
1793	0.118	-31.9	-37.3
1827	0.099	-35.1	-38.3
1857	0.085	-38.0	-39.2
1886	0.075	-40.7	-40.0
1916	0.065	-43.5	-40.8
1944	0.058	-46.1	-41.6
1962	0.053	-47.8	-42.0

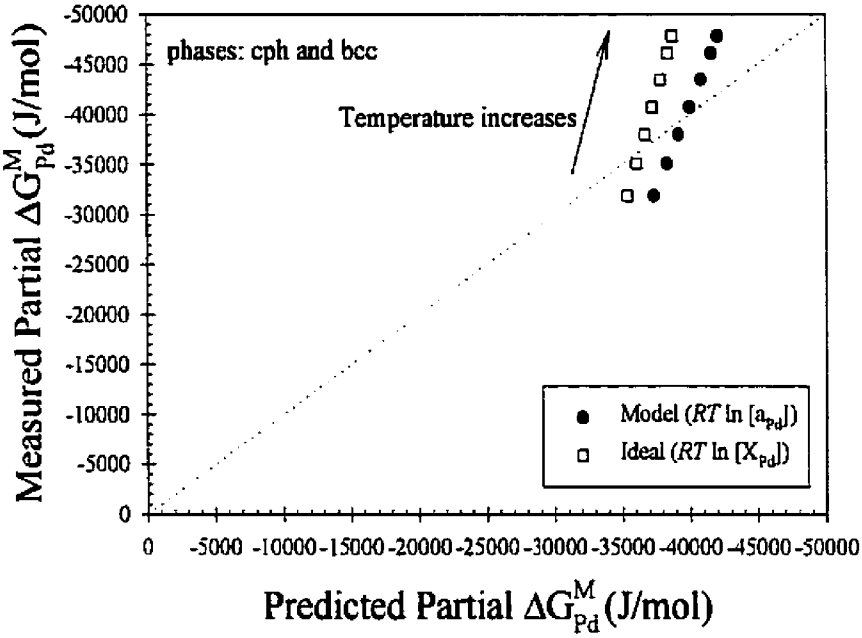

Figure 7-25. Comparison of Measured Partial Gibbs energy of mixing with the Partial Gibbs energy of mixing predicted by the model. Sample 7.

7.3.3.2 Sample 8 – 70.0%Mo/10.0%Ru/10.0%Pd/10.0%Rh

The intensity results for Sample 8 are shown in Table 7-34.

Table 7-34. Intensity (peak maximum) data for Sample 8.

Temperature (K)	^{105}Pd	^{106}Pd	^{108}Pd
1687	400	700	600
1713	900	700	400
1738	1200	800	800
1761	1100	1300	1300
1782	1600	1500	1700
1806	1700	1800	2000
1829	1800	2400	1900
1850	2600	3400	3000
1869	3500	4000	3300
1892	4900	4500	4000

A plot of the natural log of intensity multiplied by temperature versus the reciprocal of temperature for the sample 8 is shown in Figure 7-26.

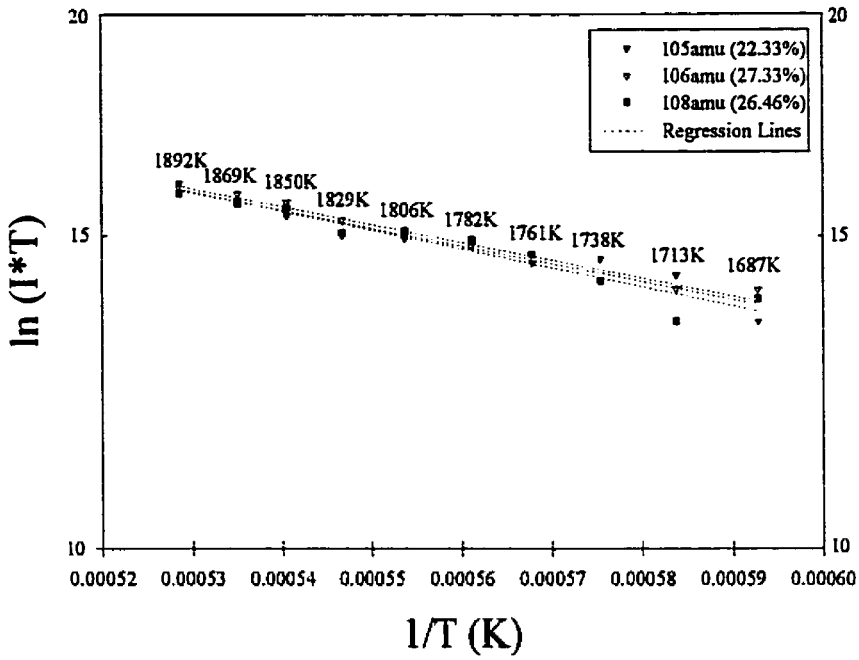

Figure 7-26. Natural log (I*T) versus 1/T for the primary isotopes of Pd for Sample 8 along with the results of the regression analysis.

The results from the linear regression analysis are presented in Table 7-35. The average slope of the line is –1021.4 with a standard deviation of 36.3.

Table 7-35. Data for the linear regression analysis for Sample 8.

Isotope	m (slope)	b (intercept)	R^2
^{105}Pd	-999.21	1.7297	0.9323
^{106}Pd	-1001.80	1.7331	0.9750
^{108}Pd	-1063.31	1.7640	0.9218

A plot of $\ln p_{Pd\,Measured}$ $vs\,\frac{1}{T}$ is shown in Figure 7-27.

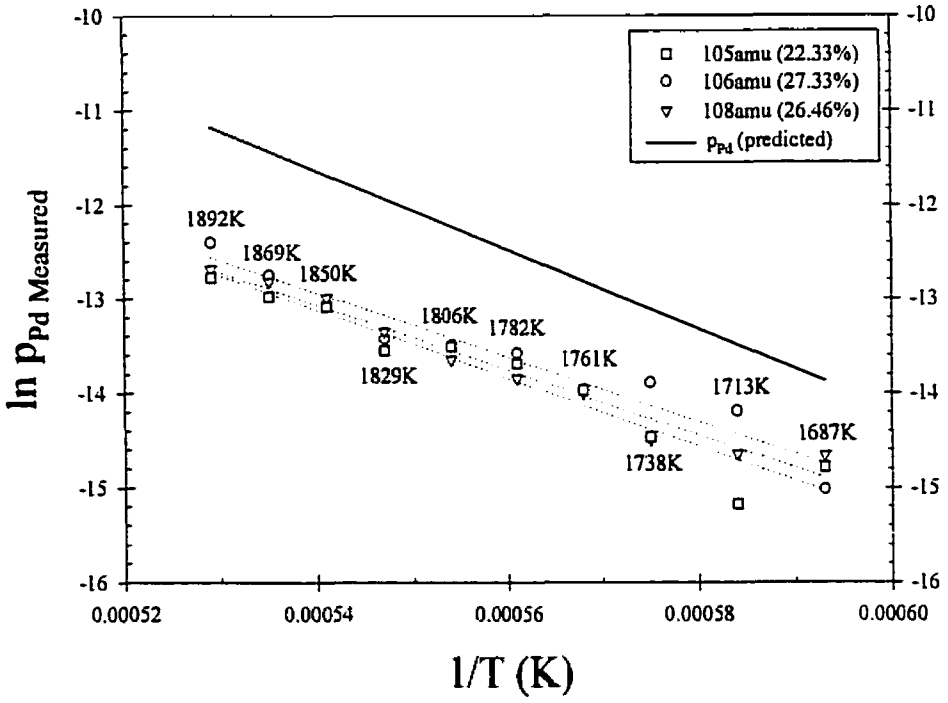

Figure 7-27. Plot of the Natural Logarithm of the Computed Partial Pressure for Pd against Reciprocal Temperature for Sample 8.

The coefficients of the linear regression are presented in Table 7-36 along with an R^2 assessment of adequacy of fit. The slopes of the linear regression lines in Figure 7-27 have a mean value of –34905 and a standard deviation of 1060.

Table 7-36. Linear regression analysis for Sample 8. The slope provides a measure of the partial heat of mixing for Pd.

Isotope	m (slope)	b (intercept)	R^2
^{105}Pd	-34120	5.484	0.9384
^{106}Pd	-34485	5.553	0.9715
^{108}Pd	-36111	6.378	0.9298
Model	-42098	11.096	

From the linear regression data, an expression for the partial pressure of Pd in this alloy can be derived, equation **(7.11)**.

$$\ln\left[p_{Pd\,(Sample\,8)}\right] = \frac{-34905}{T} + 5.805 \qquad (7.11)$$

From equation **(7.11)** the heat of sublimation in this temperature range is calculated as 290kJ/mol, which compares to the predicted value of 350kJ/mol. The difference is 60kJ/mol or 17%.

The calculated ratio of the partial pressure for Pd over the alloy to the measured partial pressure of pure Pd, along with the partial Gibbs energy of mixing for Pd in the alloy and as predicted by the model are listed in Table 7-37. A comparison of the measured partial Gibbs energy of mixing with the partial Gibbs energy of mixing predicted by the model is shown in Figure 7-28.

Table 7-37. Computed are: the ratio of the partial pressure for Pd over the alloy to the measured partial pressure of pure Pd; the partial Gibbs energy of mixing for Pd; and the partial Gibbs energy of mixing as calculated by the thermodynamic model for Sample 8.

Temperature (K)	**Experimental** $\frac{p_{Pd\,(alloy\,8)}}{p^{\circ}_{Pd\,(pure)}}$	**Experimental** $\Delta\overline{G}^{M}_{Pd}$ (kJ/mol)	**Model** $\Delta\overline{G}^{M}_{Pd}$ (kJ/mol)
1687	0.254	-19.2	-33.1
1713	0.229	-21.0	-33.8
1738	0.207	-22.8	-34.5
1761	0.189	-24.4	-35.1
1782	0.175	-25.8	-35.6
1806	0.160	-27.5	-36.3
1829	0.147	-29.1	-36.9
1850	0.137	-30.6	-37.4
1869	0.128	-31.9	-37.9
1892	0.119	-33.5	-38.5

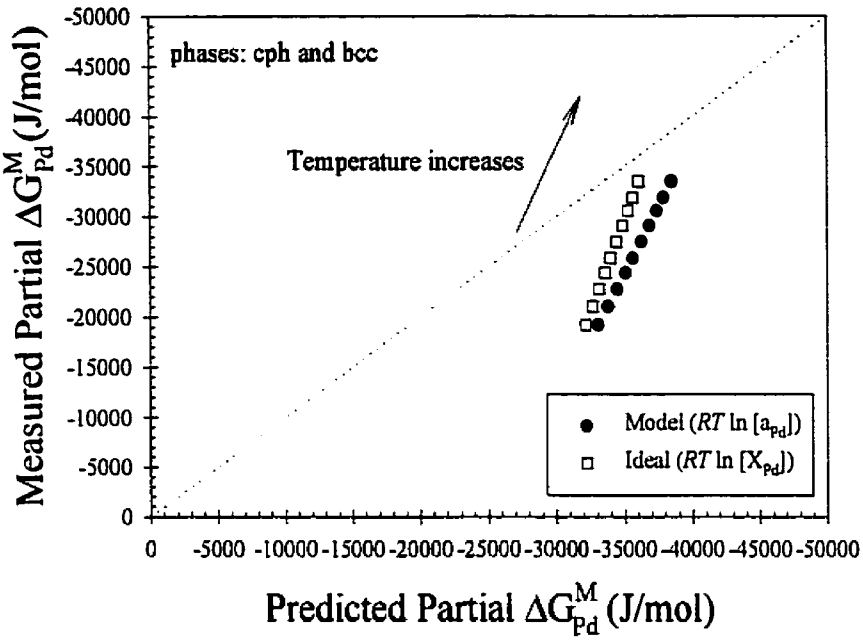

Figure 7-28. Comparison of Measured Partial Gibbs energy of mixing with the Partial Gibbs energy of mixing predicted by the model. Sample 8.

7.3.4 Summary of the Results - Rationale for Concluding Experimentation

7.3.4.1 Saturation of the Knudsen Cell

In analysing the results for possible reasons to account for the discrepancies between the measured partial pressures and the predicted partial pressures, the question must be asked as to whether or not there was saturation of Pd vapour in the Knudsen Cell. In all cases the heats of sublimation calculated from the results agreed with the heats of sublimation predicted by theory. This suggests that saturation did occur. Furthermore, there were not any systematic trends in the discrepancies in the absolute pressure measured over the alloys or the pure palladium sample.

7.3.4.2 Error Analysis

A comparison between the measured partial Gibbs energy of mixing with the partial Gibbs energy of mixing predicted for all seven alloys at 1800K is shown in Figure 7-29.

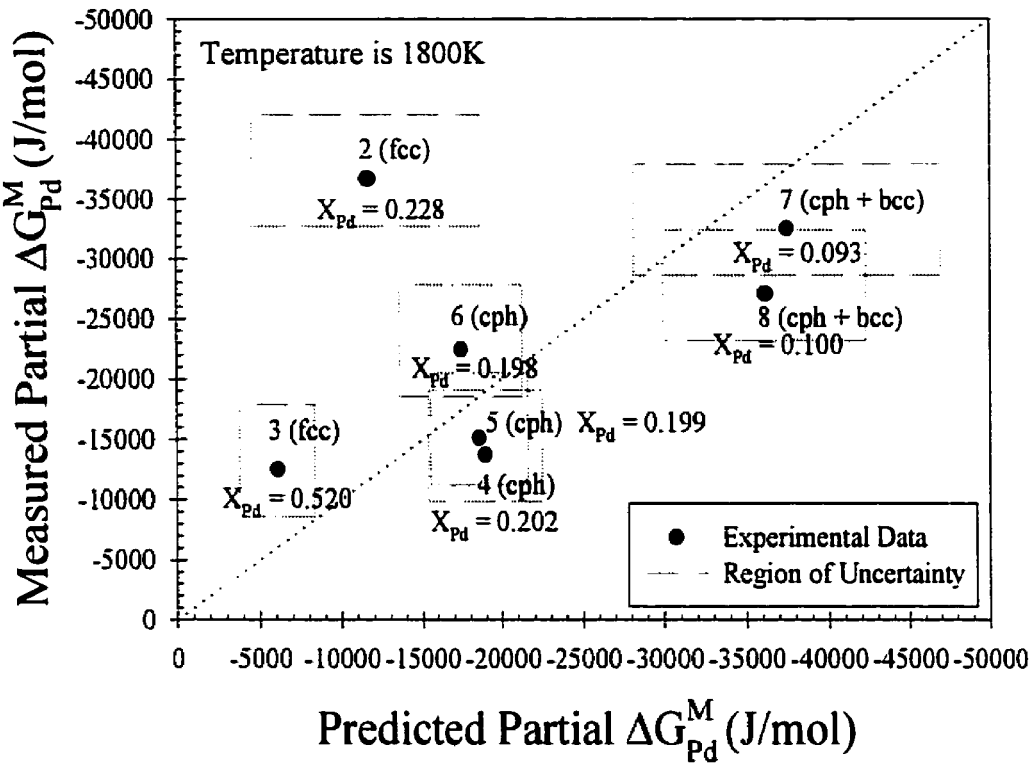

Figure 7-29. Comparison of Measured Partial Gibbs energy of mixing with the Partial Gibbs energy of mixing predicted by the model for all alloys at 1800K.

Compositional Key for Figure 7-29 (Atomic Percent)				
Sample 2:	22.8% Pd	77.2% Rh		
Sample 3:	52.0% Pd	48.0% Rh		
Sample 4:	20.3% Mo	19.8% Ru	20.2% Pd	39.7% Rh
Sample 5:	20.1% Mo	30.1% Ru	19.9% Pd	29.9% Rh
Sample 6:	20.3% Mo	39.9% Ru	19.8% Pd	20.1% Rh
Sample 7:	50.5% Mo	40.2% Ru	9.3% Pd	
Sample 8:	70.0% Mo	10.0% Ru	10.0% Pd	10.0% Rh

From Figure 7-29 it can be seen that the agreement between the experimentally determined partial Gibbs energy of mixing for palladium and the values predicted by the improved thermodynamic model is reasonable, except for Sample 2.

By computing the partial pressures of the alloys relative to the measured partial pressure of pure Pd, the need for exactly determining the ionization cross-section, σ_{Pd},

was eliminated. However, errors associated with the variations in the experiment-to-experiment parameters, namely f and s, were reduced but not eliminated. This means that the errors associated with the ratio of the partial pressures for each experiment probably ranged up to 30%. In Figure 7-29, the error associated with the measured partial Gibbs energy of mixing for Pd is based on this uncertainty. This allowed an upper and lower bound to be placed on the measured partial Gibbs energy of mixing for Pd.

The predicted partial Gibbs energy of mixing for Pd was calculated by:

$$\Delta\bar{G}^{M}_{Pd} = RT\ln\left[a_{Pd}\right] = \underbrace{RT\ln\left[X_{Pd}\right]}_{ideal\ term} + \underbrace{RT\ln\left[\gamma_{Pd}\right]}_{excess\ term} \tag{7.12}$$

where X_{Pd} represents the mole fraction of Pd in the alloy, and γ_{Pd} represents the activity coefficient.

The error in the predicted partial Gibbs energy of mixing for Pd can be apportioned to errors in the ideal term and errors in the excess term. During each experiment, mass loss occurs in the sample and this was attributed to vaporization of Pd. Therefore, the mole fraction of Pd varied slightly over the course of the experiment. The error in the ideal term was ascribed to the variation in the mole fraction of Pd. The maximum error in the ideal term was calculated by equation **(7.13)**, using values for the mole fraction of Pd found in Table 6-7.

$$error_{ideal\ term} = \left| RT\ln\left[X_{Pd\ initial}\right] - RT\ln\left[X_{Pd\ final}\right] \right| \tag{7.13}$$

The error in a generally small excess term was judged to be 50%. In absolute terms the maximum error was 5500J/mol (Sample 2). The total error for the predicted partial Gibbs energy of mixing for Pd was the sum of the error in the ideal term and the excess term.

7.3.4.3 Further Experimentation

In light of the precision suggested by the results shown in Figure 7-29, the justification for further expensive experimentation on highly specialized equipment could not be made. The results, however, generally confirm agreement between the measured and predicted partial Gibbs energies of mixing for Pd... as well as one might expect at 1800K. The one outlying point in Figure 7-29 is the result from Sample 2, which lies well off the line of agreement. Two possible reasons for the discrepancy associated with the results for Sample 2 are that there were crucible effects or complications associated with too small an orifice in the Knudsen cell lid. From Table 6-6, it can be seen that the zirconia crucible was from the Pinawa batch (unlike any of the others) and the orifice diameter was much smaller than that for any other sample. In addition, Sample 2 was the first experiment involving an alloy. Any or all of these three factors may have caused this outlying point.

8. Application of the Thermodynamic Model to Provide an Improved Fission Product Release Model

8.1 Preliminary Remarks

As mentioned previously, a rupture in the water coolant system of a CANDU nuclear reactor could lead to a loss-of-coolant-accident. For the purposes of safety analysis, modelling the behaviour of the fuel rod/cladding system is extremely important (see **Appendix E**). By understanding the behaviour of the fuel and the fission products that it contains, as they are exposed to and interact with the surrounding atmosphere, it is possible to predict the species (radioactive and inert) that will escape into the containment system of the reactor. Consideration of this problem led to the development of the fission product release model published by Lewis et al.[12].

A modified schematic diagram describing the fission product release model is shown in Figure 8-1. At the points marked "A", steam in the system reacts with the Zircalloy cladding via reaction **(8.1)**, resulting in a steam and hydrogen gas mixture.

$$Zr_{(from\ Zircalloy)} + 2H_2O_{(vapour)} \xrightleftharpoons{elevated\ T} ZrO_{2(solid)} + 2H_{2(vapour)} \qquad \textbf{(8.1)}$$

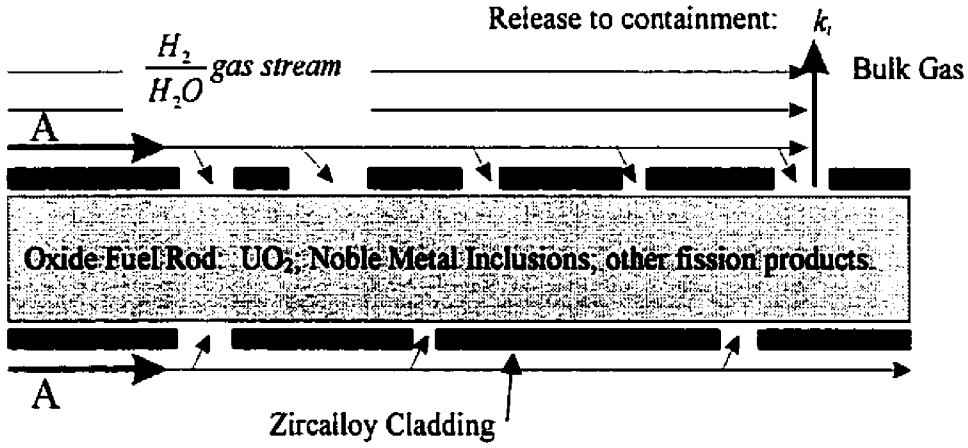

Figure 8-1. A modified schematic diagram of the fission product release model.

The $\frac{H_2}{H_2O}$ mixture resulting from reaction **(8.1)** establishes the oxygen potential in the system and subsequent reactions of that gas mixture. Furthermore, the amount of water that is involved is an important variable, since this will influence how much $H_{2\,(gas)}$ may be produced, and also affect the overall proportion of gas (H_2 and H_2O) to oxide fuel. These variables and the temperature determine the boundary conditions for thermodynamic calculations for the speciation of the oxide fuel as it comes into contact with the gas mixture. Once the speciation has been established, and the partial pressures for each calculated, the rate of transport for each species, R_i, can be calculated using equation **(1.7)**, and a measure of volatile radioisotope release can thus be obtained.

In order to determine the speciation and concentrations of the fission products being released it can be seen that a wide range of conditions may exist. Furthermore, since a typical inventory of UO_2 fuel after burn up consists of up to 60 elements*, the number of possible gaseous species that can result is very large. Obviously, calculations that are species and temperature specific would be voluminous, time consuming, and unwieldy to be effectively used in any safety analysis.

The fission product release model published by Lewis et al.[12] was developed by considering a large matrix of possible conditions, pertaining to likely conditions during a loss-of-coolant-accident. The three variables were:

1. Temperature- the range of 1000K to 3000K was selected. From 1000-2000K calculations were performed at 50K intervals. Above 2000K, the interval was 100K;
2. Reducing or Oxidizing Conditions- this was set by establishing the hydrogen

---

* The fission product inventory predicted by the ORIGEN2 code[2] has 60 elements; 26 are at trace levels.

gas to steam ratio, $\frac{H_2}{H_2O}$. Values used: 10^5, 10^4, 10^3, 10^2, 10, 1, 0.1, and 0.01. As mentioned previously, hydrogen gas is expected to develop as a result of the reaction of the Zircalloy cladding with water vapour;

3. Fission Product-to-Atmosphere Molar Ratio- calculated from the ratio of Cs to total atmosphere (i.e., $\frac{Cs}{(H_2+H_2O)}$). Values for this ratio: 10^{-4}, 10^{-5}, and 10^{-6}.

By using the ORIGIN2 code[2], the fission product inventory in a single channel of a CANDU reactor containing 13 bundles of uranium dioxide fuel with an equilibrium burn up of 100 MWh/kg U was calculated, shown in Table 8-1.

Table 8-1. Inventory of the fission products in a single channel of CANDU fuel with an equilibrium burn up of 100 MWh/kg U[2].

Element	Inventory (moles)	Element	Inventory (moles)	Element	Inventory (moles)
U*	1014.50	Cs	0.745	**Rh**	0.166
Pu	2.754	Sr	0.421	Te	0.138
Zr	1.442	Ba	0.389	Np	0.096
Mo	1.15	**Pd**	0.346	Nb	0.043
Ru	0.899	La	0.332	I_2	0.0385
Nd	0.859	Pr	0.265	Eu	0.025
Ce	0.824	Y	0.215	Sb	0.006

For a typical reaction of one channel in a CANDU reactor, the reactants would be expressed as:

$$\begin{aligned} &1014.5UO_2 + 2.754Pu + 1.442Zr + 1.15Mo + 0.899Ru + 0.859Nd + \\ &0.824Ce + \mathbf{0.745}Cs + 0.421Sr + 0.389Ba + 0.346Pd + 0.332La + \\ &0.265\mathrm{Pr} + 0.215Y + 0.166Rh + 0.138Te + 0.096Np + 0.043Nb + \\ &0.0385I_2 + 0.025Eu + 0.006Sb + \left(\frac{\mathbf{0.745}}{10^{-n}}\right)\left(xH_2O + (1-x)H_2\right) \xrightarrow{T,p} \end{aligned} \qquad \textbf{(8.2)}$$

where n represents the exponent of the ratio of Cs (**0.745**moles) to total atmosphere (i.e.,

---

* In subsequent calculations all uranium present initially was considered to be in the chemical form UO_2.

$\frac{Cs}{(H_2 + H_2O)}$), and x represents the fraction of H_2O that satisfies the appropriate hydrogen to steam ratio.

Gibbs energy minimization calculations at regular intervals of temperature will determine the equilibrium products for equation **(8.2)**. These products will consist of several condensed phases (solid or liquid) and an ideal vapour phase. For the vapour phase, the partial pressures of each gaseous species will also be calculated, which allows for equation **(1.7)** to be employed. However, even by restricting the calculations to specific temperatures, there is still far too much data to process rapidly for use as boundary conditions in additional computations.

8.2 The Method of Chemical Potentials

The Method of Chemical Potentials[12,18,90,91] was developed as a technique to extract the essence of the thermodynamic computations contained within the matrix of 24 conditions, over the 2000K temperature range. It was essential that this be a "stand-alone" technique, by which it was understood that time consuming Gibbs energy minimization calculations would be efficiently recorded only in such a manner that the computations could be retrieved rapidly at any temperature. This is essential so that calculations of the type embodied in equation **(8.2)** can be incorporated as boundary conditions into fission product release scenarios for safety analysis.

For the formation of any compound from its constituent elements, a general reaction can be written:

$$xA + yB + zC \underset{T}{\overset{K_{eq}}{\rightleftharpoons}} A_xB_yC_z \qquad \textbf{(8.3)}$$

where the equilibrium constant, K_{eq}, is defined as:

$$K_{eq} = \frac{p_{A_x B_y C_z}}{(p_A)^x (p_B)^y (p_C)^z} = \exp\left[\frac{-\Delta G^\circ}{RT}\right] \tag{8.4}$$

where, R represents the gas constant, T the temperature, and ΔG° the standard Gibbs energy change of the reaction. The standard Gibbs energy change, ΔG°, can be computed from the standard Gibbs energy of formation equations for the compounds (or the equivalent), by:

$$\Delta G^\circ = G^\circ_{A_x B_y C_z} - xG^\circ_A - yG^\circ_B - zG^\circ_C \tag{8.5}$$

where $G^\circ = \Delta H^\circ - TS^\circ$. G° is sometimes called the "absolute" Gibbs energy; numerically, this simply is a method to conveniently compute Gibbs energy *change*. Combining equations **(8.4)** and **(8.5)** gives:

$$p_{A_x B_y C_z} = \left((p_A)^x (p_B)^y (p_C)^z\right) \exp\left[\frac{xG^\circ_A + yG^\circ_B + zG^\circ_C - G^\circ_{A_x B_y C_z}}{RT}\right] \tag{8.6}$$

Equation **(8.6)** is specifically needed for the mass transfer model described by Equations **(1.7)** and **(1.8)**. From equation **(8.6)** it can be seen that to determine the partial pressure of any species, it is sufficient to represent accurately the partial pressure of the constituent elements (computed by time consuming Gibbs energy minimization) using an empirical series and the standard absolute Gibbs energy for the elements and the compound. This method of storing the equilibrium computations for gas species concentrations for a matrix of conditions (i.e., a specific $\frac{H_2}{H_2O}$ ratio and $\frac{Cs}{(H_2 + H_2O)}$ ratio, over the 1000K to 3000K temperature range), simply requires, in addition to the empirical series for each element, a table of Gibbs energies for all the compounds involved[12,18].

8.3 Demonstrating an Improved Fission Product Release Model

8.3.1 Typical FORM 2.0 Calculation

Using the fission product inventory predicted by the ORIGEN2 code[2], thermodynamic equilibrium calculations were performed over the temperature range for the twenty four different accident scenarios[18]. Gibbs energy minimization[17] was used to determine the equilibrium at a specified temperature and a total atmospheric pressure of 1 atm. For these calculations the following assumptions were made:

1. The gas phase is an ideal gas, therefore, for each species, i, $p_i = X_{i(vapour)} P_{tot}$;
2. All metallic liquids form an ideal metallic liquid solution, if they form a solution phase at all, therefore $a_{i(in\ liquid)} = X_{i(in\ liquid)}$;
3. All solids (i.e., intermetallics, oxides, and spinels) are treated as pure separate phases; and if $a_{solid} = 1$ the solid forms, but if $a_{solid} < 1$ the solid does not form.

A representative calculation is presented in Figure 8-2. The temperature for this calculation was 1800K, the ratio of $\frac{H_2}{H_2O}$ was 1, and the ratio $\frac{Cs}{(H_2 + H_2O)}$ was 10^{-5}. It should also be noted that the result for this calculation has been truncated for the sake of brevity. Only the first eleven gaseous species (in order of concentration) have been shown. For the gas phase, the total number of moles of gas is given first (i.e., 74511mol). The mole fractions for the gas species are listed next to each (e.g., the mole fraction of $H_{2(g)} = 0.50005$).

Because the "ideal metallic liquid" does not contribute to lowering the overall Gibbs energy, it does not form- there are zero moles of it. Finally, only the twelve solids and liquids that have a unit activity appear as distinct phases. Because this system has 23 components, the maximum number of separate coexistent phases that may form, as stated by the Gibbs Phase Rule, is 23, since temperature and pressure are fixed. Because a

distinct gas phase is present, the maximum number of solid and liquid phases that may form is 22, and as only twelve are present, the Phase Rule is respected.

1014.5 **UO_2** + 0.096 **Np** + 2.754 **Pu** + 0.824 **Ce** + 0.215 **Y** + 0.138 **Te** + 0.332 **La** + 1.442 **Zr** + 0.389 **Ba** + *0.899* ***Ru*** + *1.150* ***Mo*** + 0.265 **Pr** + 0.421 **Sr** + 0.0385 **I_2** + 0.859 **Nd** + 0.043 **Nb** + 0.006 **Sb** + 0.745 **Cs** + *0.166* ***Rh*** + *0.346* ***Pd*** + 0.025 **Eu** + 37250**H_2O** + 37250**H_2** =

Vapour Phase (Ideal Gas Mixture):

74511. mol	(	0.50005	H2
	+	0.49964	H2O
	+	0.25185E-03	H
	+	0.16990E-04	OH
	+	***0.15222E-04***	***H2MoO4***
	+	0.83348E-05	CsOH
	+	0.50686E-05	Ba(OH)2
	+	***0.30966E-05***	***PdOH***
	+	***0.22279E-05***	***RhO2***
	+	0.18223E-05	Te
	+	***0.15470E-05***	***Pd***

$p_{O_2} = 2.85 \times 10^{-9}$ atm

...

~Total of 179 gas species~ (1800K, 1 atm, gas_ideal)

"Ideal Metallic Liquid":

+ 0.0 mol **(Ru, Pd, Mo, Rh,** Te, Sb, Nb, Cs, Ba, Eu, Pr, La, Pu, Ce, Nd, Zr, U, Y)
(1800K, 1 atm, ideal liquid, a=0.52782)

12 Distinct Solid and Liquid Phases (maximum of 22 is possible):

+	1014.10000 mol	UO2	(1800K, 1 atm, S1, a= 1.0)
+	2.75390 mol	PuO2	(1800K, 1 atm, S1, a= 1.0)
+	***0.89897 mol***	***Ru***	(1800K, 1 atm, S1, a= 1.0)
+	0.42589 mol	(Nd2O3)(ZrO2)2	(1800K, 1 atm, S1, a= 1.0)
+	0.42100 mol	(SrUO4)	(1800K, 1 atm, S1, a= 1.0)
+	0.37522 mol	ZrO2	(1800K, 1 atm, S2, a= 1.0)
+	0.15849 mol	La2O3	(1800K, 1 atm, S1, a= 1.0)
+	0.13243 mol	Pr2O3	(1800K, 1 atm, S1, a= 1.0)
+	0.10750 mol	(Y2O3)(ZrO2)2	(1800K, 1 atm, S1, a= 1.0)
+	0.09600 mol	NpO2	(1800K, 1 atm, S1, a= 1.0)
+	0.04578 mol	Ce18O31	(1800K, 1 atm, S1, a= 1.0)
+	0.01911 mol	Nb2O5	(1800K, 1 atm, L1, a= 1.0)

Figure 8-2. Results from a typical Gibbs energy minimization calculation for a CANDU fuel channel. The metallic elements are treated as an *ideal liquid or at lower temperatures as separate pure solid phases.*

Highlighted in this calculation are the species that contain the noble metals. It can be seen that for Mo, Pd, and Rh, 100% of their inventory are found in the vapour phase, in which H_2MoO_4, PdOH, Pd, and RhO_2 are the dominant noble metal containing species. The Ru appears as a distinct solid phase as a consequence of the simplifying assumptions to treat noble metal reaction products at the time the original computations were made.

A reducing condition, where $\frac{H_2}{H_2O}$ = 100, and the $\frac{Cs}{(H_2+H_2O)}$ = 10^{-5}, is presented in Figure 8-3. The temperature is 1800K.

1014.5 **UO_2** + 0.096 **Np** + 2.754 **Pu** + 0.824 **Ce** + 0.215 **Y** + 0.138 **Te** + 0.332 **La** + 1.442 **Zr** + 0.389 **Ba** + *0.899* ***Ru*** + *1.150* ***Mo*** + 0.265 **Pr** + 0.421 **Sr** + 0.0385 **I_2** + 0.859 **Nd** + 0.043 **Nb** + 0.006 **Sb** + 0.745 **Cs** + *0.166* ***Rh*** + *0.346* ***Pd*** + 0.025 **Eu** + 737.55**H_2O** + 73762.45**H_2** =

Vapour Phase (Ideal Gas Mixture):

74514. mol	(	0.98992	H2
	+	0.97149E-02	H2O
	+	0.35435E-03	H
	+	0.84649E-05	Cs
	+	0.18036E-05	Te
	+	***0.76555E-06***	***RhO2***
	+	0.67054E-06	CsOH
	+	***0.57721E-06***	***Pd***

$p_{O_2} = 2.75\times10^{-13}$ atm

...

~Total of 179 gas species~ (1800K, 1 atm, gas_ideal)

"Ideal Metallic Liquid":

+ 0.28407 mol	(	***0.45016***	***Ru***
	+	***0.38272***	***Rh***
	+	***0.12845***	***Mo***
	+	***0.21654E-01***	***Pd***
	+	0.17008E-01	Nb

+ trace amounts of: Te, Sb, Ba, Pu, Cs, Pr, Eu, La, Zr, Ce, U, Nd, Y, Sr)
(1800K, 1 atm, liquid)

14 Distinct Solid and Liquid Phases (maximum of 22 is possible):

+	1014.00000 mol	UO2	(1800K, 1 atm, S1, a= 1.0)
+	2.75370 mol	PuO2	(1800K, 1 atm, S1, a= 1.0)
+	0.42908 mol	(Nd2O3)(ZrO2)2	(1800K, 1 atm, S1, a= 1.0)
+	0.42100 mol	(SrUO4)	(1800K, 1 atm, S1, a= 1.0)
+	0.41198 mol	Ce2O3	(1800K, 1 atm, S1, a= 1.0)
+	0.36884 mol	(BaO)(ZrO2)	(1800K, 1 atm, S1, a= 1.0)
+	***0.22270 mol***	***Mo5Ru3***	(1800K, 1 atm, S1, a= 1.0)
+	0.16444 mol	La2O3	(1800K, 1 atm, S1, a= 1.0)
+	0.13185 mol	Pr2O3	(1800K, 1 atm, S1, a= 1.0)
+	0.10750 mol	(Y2O3)(ZrO2)2	(1800K, 1 atm, S1, a= 1.0)
+	***0.10302 mol***	***Ru***	(1800K, 1 atm, S1, a= 1.0)
+	***0.09855 mol***	***UPd3***	(1800K, 1 atm, S1, a= 1.0)
+	0.09600 mol	NpO2	(1800K, 1 atm, S1, a= 1.0)
+	0.02624 mol	NbO2	(1800K, 1 atm, S3, a= 1.0)

Figure 8-3. Results from a Gibbs energy minimization calculation for a CANDU fuel channel under reducing conditions. The metallic elements are treated as an *ideal liquid*.

For the reducing condition shown in Figure 8-3 the ideal metallic liquid phase forms at 1593K (this calculation is not shown). It can also be seen that the partial oxygen pressure for the reducing condition is 4 orders of magnitude lower than for the condition shown in Figure 8-2.

8.3.2 Calculations with the Improved Thermodynamic Treatment for the Noble Metals

The physical reality that is not well represented in the second assumption of the FORM 2.0 calculations is addressed by the improved thermodynamic treatment for the noble metals. A calculation similar to that in Figure 8-2 is shown in Figure 8-4. The improved thermodynamic for the noble metals has been used. In this scenario, the ratio of $\frac{H_2}{H_2O}$ was 1, and the ratio $\frac{Cs}{(H_2+H_2O)}$ was 10^{-5}.

The results in Figure 8-4 show that Mo is found in both the gas phase and the cph-solid solution phase. The amount of Mo in the cph-solid solution was calculated by multiplying the total number of moles of the solid solution (i.e., 1.026 mols) by the concentration of Mo in the solid solution, 0.11764. The product is 0.1207 mols. Considering that the total inventory of Mo initially was 1.15 mols, the amount of Mo in the solid solution represents 10.5% of the total inventory. The balance of the inventory for Mo is contained in the gas phase. The amount of Mo in the gas phase was calculated by multiplying the total number of moles of gas (74511 mols) by the sum of the concentrations (or partial pressures) of each molybdenum bearing species. In this case the dominant species for Mo is H_2MoO_4, for which $p = 1.3625 \times 10^{-5}$. This represents 1.015 mols of Mo, or 88.3% of the total inventory. The balance of the Mo inventory, ≅1.2% is also found in the gas phase as other Mo containing species, which were not listed in Figure 8-4.

As was mentioned previously over 10% of the Mo was to be found in the cph-solid solution along with the entire Ru inventory, and 1.78% of the Pd inventory. There was also just over 0.1% of the Rh inventory in the cph-solid phase.

1014.5 **UO_2** + 0.096 **Np** + 2.754 **Pu** + 0.824 **Ce** + 0.215 **Y** + 0.138 **Te** + 0.332 **La** + 1.442 **Zr** + 0.389 **Ba** + *0.899* ***Ru*** + *1.150* ***Mo*** + 0.265 **Pr** + 0.421 **Sr** + 0.0385 **I_2** + 0.859 **Nd** + 0.043 **Nb** + 0.006 **Sb** + 0.745 **Cs** + *0.166* ***Rh*** + *0.346* ***Pd*** + 0.025 **Eu** + 37250**H_2O** + 37250**H_2** =

Vapour Phase (Ideal Gas Mixture):

74511. mol	(	0.50005	H2
	+	0.49965	H2O
	+	0.25184E-03	H
	+	0.16990E-04	OH
	+	***0.13625E-04***	***H2MoO4***
	+	0.83349E-05	CsOH
	+	0.50748E-05	Ba(OH)2
	+	***0.30416E-05***	***PdOH***
	+	***0.22251E-05***	***RhO2***
	+	0.18223E-05	Te
	+	***0.15195E-05***	***Pd***
	+	***0.34861E-13***	***Mo***

$p_{O_2} = 2.85 \times 10^{-9}$ atm

$a_{Mo(w.r.t.Mo_{bcc})} = 0.050$

...

~Total of 179 gas species~ (1800K, 1 atm, gas_ideal)

Solution Phase:

+ 1.0260 mol	(	***0.87617***	***Ru***
	+	***0.11764***	***Mo***
	+	***0.59887E-02***	***Pd***
	+	***0.19904E-03***	***Rh***)

(1800K, 1 atm, cphsolid)

Note: Only one metallic inclusion phase.

12 Distinct Solid and Liquid Phases (maximum of 22 is possible):

+	1014.10000 mol	UO2	(1800K, 1 atm, S1, a= 1.0)
+	2.75390 mol	PuO2	(1800K, 1 atm, S1, a= 1.0)
+	0.42589 mol	(Nd2O3)(ZrO2)2	(1800K, 1 atm, S1, a= 1.0)
+	0.42100 mol	(SrUO4)	(1800K, 1 atm, S1, a= 1.0)
+	0.37522 mol	ZrO2	(1800K, 1 atm, S2, a= 1.0)
+	0.15849 mol	La2O3	(1800K, 1 atm, S1, a= 1.0)
+	0.13243 mol	Pr2O3	(1800K, 1 atm, S1, a= 1.0)
+	0.10750 mol	(Y2O3)(ZrO2)2	(1800K, 1 atm, S1, a= 1.0)
+	0.09600 mol	NpO2	(1800K, 1 atm, S1, a= 1.0)
+	0.04578 mol	Ce18O31	(1800K, 1 atm, S1, a= 1.0)
+	0.01911 mol	Nb2O5	(1800K, 1 atm, L1, a= 1.0)

Figure 8-4. Results from a Gibbs energy minimization calculation, *which included the improved thermodynamic model*, for a CANDU fuel channel. Note the appearance of a solid metallic phase.

The cph-solid that forms in Figure 8-4 remains stable up to 2335K (this calculation is not shown), at which temperature it sublimes. It should be noted that the partial pressure of oxygen is the same in this result, as it was for the calculation shown in Figure 8-2. However, it is important to also note that because a solid phase containing Mo forms it is possible to determine and speak meaningfully of the activity of Mo with respect to solid Mo_{bcc}. In this case the a_{Mo} is 0.050.

The reducing calculation, similar to Figure 8-3, is shown in Figure 8-5. In this scenario the $\frac{H_2}{H_2O} = 100$, and the $\frac{Cs}{(H_2 + H_2O)} = 10^{-5}$, and the temperature is 1800K.

1014.5 **UO_2** + 0.096 **Np** + 2.754 **Pu** + 0.824 **Ce** + 0.215 **Y** + 0.138 **Te** + 0.332 **La** + 1.442 **Zr** + 0.389 **Ba** + *0.899* ***Ru*** + *1.150* ***Mo*** + 0.265 **Pr** + 0.421 **Sr** + 0.0385 **I_2** + 0.859 **Nd** + 0.043 **Nb** + 0.006 **Sb** + 0.745 **Cs** + *0.166* ***Rh*** + *0.346* ***Pd*** + 0.025 **Eu** + 737.55**H_2O** + 737623.45**H_2** =

Vapour Phase (Ideal Gas Mixture):

74514. mol	(	0.98992	H2
	+	0.97157E-02	H2O
	+	0.35435E-03	H
	+	0.84648E-05	Cs
	+	0.18036E-05	Te
	+	0.67059E-06	CsOH
	+	***0.57725E-06***	***Pd***
	+	***0.79419E-07***	***RhO2***

...

~Total of 179 gas species~ (1800K, 1 atm, gas_ideal)

$p_{O_2} = 2.75 \times 10^{-13}$ atm

$a_{Mo(w.r.t.Mo_{bcc})} = 0.719$

Solution Phases:

+ 1.8383 mol	(	***0.44915***	***Ru***
	+	***0.44722***	***Mo***
	+	***0.83122E-01***	***Rh***
	+	***0.20510E-01***	***Pd***)
		(1800K, 1 atm, cphsolid)	
+ 0.41993 mol	(	***0.78079***	***Mo***
	+	***0.17468***	***Ru***
	+	***0.27253E-01***	***Pd***
	+	***0.17285E-01***	***Rh***)
		(1800K, 1 atm, bccsolid)	

Note: Two metallic phases- under more reducing conditions.

12 Distinct Solid and Liquid Phases (maximum of 22 is possible):

+	1014.00000 mol	UO2	(1800K, 1 atm, S1, a= 1.0)
+	2.75370 mol	PuO2	(1800K, 1 atm, S1, a= 1.0)
+	0.42908 mol	(Nd2O3)(ZrO2)2	(1800K, 1 atm, S1, a= 1.0)
+	0.42100 mol	(SrUO4)	(1800K, 1 atm, S1, a= 1.0)
+	0.41198 mol	Ce2O3	(1800K, 1 atm, S1, a= 1.0)
+	0.36884 mol	(BaO)(ZrO2)	(1800K, 1 atm, S1, a= 1.0)
+	0.16444 mol	La2O3	(1800K, 1 atm, S1, a= 1.0)
+	0.13185 mol	Pr2O3	(1800K, 1 atm, S1, a= 1.0)
+	0.10750 mol	(Y2O3)(ZrO2)2	(1800K, 1 atm, S1, a= 1.0)
+	0.09600 mol	NpO2	(1800K, 1 atm, S1, a= 1.0)
+	***0.08422 mol***	***UPd3***	(1800K, 1 atm, S1, a= 1.0)
+	0.03107 mol	NbO2	(1800K, 1 atm, S3, a= 1.0)

Figure 8-5. Results from a Gibbs energy minimization calculation, *which included the improved thermodynamic model*, for a CANDU fuel channel under reducing conditions. Note the appearance of two metallic phases under more highly reducing condition than that shown in Figure 8-4.

The two solid solution phases shown in Figure 8-5 are predicted to coexist up to a

temperature of 2224K, at which point the bcc-solid disappears and a liquid solution containing the noble metals appears, coexisting with cph-solid. The cph-solid finally melts at 2266K. Note that these calculations are not shown.

In the case where the thermodynamic model for the noble metals was not used (Figure 8-3) the rhodium release to the vapour phase was predicted as 34.5% of the total inventory. However, for the second case where the model was used (Figure 8-5), only 3.6% (a full order of magnitude) of the rhodium inventory escapes to the vapour phase. Furthermore, an ideal *liquid phase* is predicted under strongly reducing conditions when not employing the *alloy models* developed in this research. This could have important transport implications. When using the *alloy models*, the noble metals are, for the most part, retained in *solid solution form*.

For the results shown in Figure 8-5, the activity of Mo with respect to solid Mo_{bcc} is 0.719. The partial pressure of oxygen was $p_{O_2} = 2.75 \times 10^{-13}$ atm, the same as it was in the results of Figure 8-3.

With the improved thermodynamic treatment, a realistic treatment of the noble metals is provided. This treatment allows for a meaningful calculation of the activity of Mo, present as a component in a solid phase or phases, with respect to pure bcc-solid Mo. This is important because previous experimentation has shown[11] that molybdenum oxidizes at oxygen potentials comparable to those of hyperstoichiometric UO_{2+x}. It has also been proposed that by measuring the Mo content of the noble metal inclusions, a measure of the local oxygen potential of the fuel can be made[92]. This was not possible from the FORM 2.0 calculations.

It can thus be seen that thermodynamic models for the alloy phases do make a difference in terms of describing the equilibrium condition of the fuel after exposure to a hydrogen-steam atmosphere. In the reducing condition, the Gibbs energy minimization calculation that treats the metals as able to form an ideal liquid, has the Rh inventory in the vapour phase over-predicted by an order of magnitude. However, by treating the noble metals as able to form distinct non-ideal solution phases, a more realistic prediction is made involving solid-solutions known to exist. The case of an atmosphere of equal parts hydrogen gas and steam shows significant differences in the Mo inventory in the vapour. Finally, the improved treatment better describes the behaviour of Mo in the solid phase, which has implications in the correlation to the local oxygen potential in the region near the fuel.

8.4 An Improved Method of Chemical Potentials

The Method of Chemical Potentials provides a straightforward methodology to record previously computed partial pressures of every vapour species, by using a mathematically derived expression for each of the computed partial pressures of the elements. This is a generic solution and relies on representing faithfully the computed partial pressures of each element. To complement the better treatment of the noble metals, an improved method of chemical potentials (IMCP) is proposed.

One concern with the Method of Chemical Potentials is that for some of the elements, the Gibbs energy minimization calculation determined that their vapour pressures were extremely low (e.g., the non-volatiles[6]: Sr, Nd, La, Y, Zr). Furthermore, during the release, these elements often combined with oxygen and hydrogen, and so the dominant chemical form in the vapour phase was not an elemental monatomic or

diatomic gas (e.g., $CsOH_{(g)}$ instead of $Cs_{(g)}$; $Ba(OH)_{2(g)}$ instead of $Ba_{(g)}$; and $RhO_{2(g)}$ instead of $Rh_{(g)}$), but an oxide, hydroxide, or hydride.

These two factors can combine to introduce numerical imprecision into the calculations. Small misrepresentations in the mathematically derived partial pressures of a non-volatile element can be amplified by equation **(8.6)**, especially if the compound is relatively volatile in comparison to one of its constituent elements.

In the improved method instead of deriving an expression for the partial pressure of the elements, an empirical representation for the partial pressure of the most dominant species containing each of the 23 component elements is suggested. These expressions can be manipulated in exactly the same manner as described in equations **(8.3)** through **(8.6)**.

For example, consider the scenario shown in Figure 8-4. The partial pressure of H_2 and H_2O are nearly equal and relatively large, while the associated equilibrium partial pressure of O_2 is 2.8530×10^{-9}. With the Improved Method of Chemical Potentials, expressions for H_2 and H_2O would be derived, as opposed to expressions for H_2 and O_2. The most dominant species containing Mo is $H_2MoO_{4\,(g)}$, for which the partial pressure, in this example, is 1.3625×10^{-5}. In order to obtain the partial pressure of $Mo_{(g)}$, the following equilibrium would be employed:

$$3H_2 + H_2MoO_4 \underset{T}{\overset{K_{eq}}{\rightleftharpoons}} Mo + 4H_2O \qquad \textbf{(8.7)}$$

In a similar manner to that described for the Method of Chemical Potentials, the partial pressure for $Mo_{(g)}$ is given by:

$$p_{Mo} = \frac{\left(p_{H_2}\right)^3 \left(p_{H_2MoO_4}\right)}{\left(p_{H_2O}\right)^2} \exp\left[\frac{G^\circ_{H_2MoO_4} + 3G^\circ_{H_2} - G^\circ_{Mo} - 4G^\circ_{H_2O}}{RT}\right] \quad \textbf{(8.8)}$$

At 1800K, this expression will give $p_{Mo} = 3.4861 \times 10^{-14}$ atm, which is identical to that shown for p_{Mo} in Figure 8-4. The value of p_{Mo} can be also be compared to the value that would be calculated for p_{Mo} using the FORM 2.0 code[18]. From the FORM 2.0 code[18], under the same postulated accident conditions, $p_{Mo} = 1.8695 \times 10^{-13}$ atm. This represents a full order of magnitude difference, and suggests that calculations for other species, which are based on the partial pressure of molybdenum gas, would compound this error.

When all the partial pressures of the elements have been determined in a similar manner, the partial pressures of all other gaseous compounds can be computed using equation **(8.6)**.

There is one important consideration to the Improved Method of Chemical Potentials. Because the dominant chemical species, which contains any particular element, may change from reducing to oxidizing conditions, it is a matter of judgement to decide which species will have partial pressures fit to mathematical expressions in temperature.

9. Conclusions

The thermodynamic behaviour of the five component Mo-Pd-Rh-Ru-Tc system, the Noble Metals, in nuclear parlance, is now well understood. For this system, all ten of the binary subsystems have now been thermodynamically modelled, with self-consistent and complete mathematical expressions for all observed phases. These binary models, have been combined into a quinary model, using the Kohler interpolation scheme with departure terms.

For the first time the Mo-Ru system has been evaluated in conjunction with thermodynamic implications, as have the four binary systems that contain technetium. These evaluations contribute to part of the original content of this thesis.

For the first time the solidus-liquidus region of the Pd-Rh system has been experimentally examined. Direct measurements of the solidus and liquidus confirmed the predicted behaviour of positive deviations from ideality in the liquid and solid solutions. This experimental contribution in the Pd-Rh system is another aspect of the original content in this thesis.

Direct measurements of vapour pressures over noble metal alloys were made that confirm that these alloys exhibit only small positive deviations from ideal behaviour. In general, these measurements supported the quinary thermodynamic solution model. For the first time, such a model exists. This too is original to this research.

With the thermodynamics of the noble metal alloys understood, it is possible to incorporate the thermodynamic models for these alloy phases into Gibbs energy minimization calculations to better predict the behaviour of nuclear fuel during a LOCA.

10. Future Work

To balance the thermodynamic treatment of the noble metal alloy phases, it is felt that future work in the analysis of the behaviour of fission products during loss-of-coolant-accident should be directed towards other non-stoichiometric or solution phases within the fuel. In particular, a similar study and assessment of the uranium-oxygen system should be undertaken. Specifically, modelling the thermodynamic properties of $UO_{2\pm x}$ would enable the effect that this solid solution phase has on the partial pressure of O_2 (and by extension the H_2 and H_2O pressures) to be predicted. Furthermore, the modelling should allow for the dissolution of low concentrations of other fission products into the parent $UO_{2\pm x}$ phase.

Another consequence of having developed the thermodynamic model is that the system containing the nuclear fuel can be extended. For example, it is known that the hydrogen vapour to steam ratio is controlled by the Zircalloy cladding. By incorporating the presence of the cladding into the calculation, better fission product release predictions would be made. To do this would first entail modelling the Zr-Sn system (an original thermodynamic evaluation of this system is included in **Appendix E**), followed by a Gibbs energy minimization calculation for steam/cladding reactions.

Regardless of whether the Zircalloy cladding is included or not, further Gibbs energy minimization calculations using the noble metal alloy model to predict fission product release during loss-of-coolant-accidents should be performed. Furthermore, these should be combined with the Improved Method of Chemical Potentials in an updated version of the FORM 2.0[18] and the SOURCE 2 safety codes.

Finally, the thermodynamic evaluations of all the technetium phase diagrams are based on limited experimental results. While it is acknowledged that such experiments are costly and complex, it would be of scientific interest to undertake limited validation.

11. References

1. N.N. Greenwood and A. Earnshaw, Chemistry of the Elements, 2nd Edition, Pergamon Press plc, Oxford, England, (1997).
2. A.G. Croff, "ORIGEN2- A Revised and Updated Version of the Oak Ridge Isotope Generation and Depletion Code", Report ORNL-5621, (July 1980).
3. Technical Information published by Atomic Energy of Canada.
4. J.R. Lamarsh, Introduction to Nuclear Engineering, 2nd Edition, Addison-Wesley Publishing Company, Reading, Massachusetts, (1983).
5. S. Glasstone and A. Sesonske, Nuclear Reactor Engineering, 3rd Edition, Van Nostrand Reinhold Company, New York NewYork, (1981).
6. S.G. Prussin, D.R. Olander, W.K. Lau, and L. Hansson, "Release of Fission Products (Xe, I, Te, Cs, Mo, and Tc) from Polycrystalline UO_2", *Journal of Nuclear Materials*, **154** (1988), 25-37.
7. H. Kleykamp, "The Chemical State of the Fission Products in Oxide Fuels", *Journal of Nuclear Materials*, **131** (1985), 221-246.
8. H. Kleykamp, "The Chemical State of the Fission Products in Oxide Fuels within the Different Stages of the Nuclear Fuel Cycle", High Tech Ceramics, edited by: P. Vincenzini, Elsevier Science Publishers, Amsterdam, (1987), 2769-2798.
9. H. Kleykamp, "The Chemical State of Fission Products in Oxide Fuels at Different Stages of the Nuclear Fuel Cycle", *Nuclear Technology*, **80** (1988), 412-422.
10. P.G. Lucuta, R.A. Verrall, Hj. Matzke, and B.J. Palmer, "Microstructural Features of SIMFUEL- Simulated High-Burn-up UO_2-based Nuclear Fuel", *Journal of Nuclear Materials*, **178** (1991), 48-60.
11. H. Kleykamp, J.O.A. Paschoal, R. Pejsa, and F. Thümmler, "Composition and Structure of Fission Product Precipitates in Irradiated Oxide Fuels: Correlation with Phase Studies in the Mo-Ru-Rh-Pd and BaO-UO_2-ZrO_2-MoO_2 Systems" *Journal of Nuclear Materials*, **130** (1985), 426-433.
12. B.J. Lewis, B.J. Corse, W.T. Thompson, M.H. Kaye, F.C. Iglesias, P. Elder, R. Dickson, and Z. Liu, "Low Volatile Fission Product Release and Fuel Volatilization During Severe Reactor Accident Conditions", *Journal of Nuclear Materials*, **252** (1998), 235-256.
13. D. Cubicciotti, "A Model for Release of Fission Gases and Volatile Fission Products from Irradiated UO_2 in Steam Environment", *Nuclear Technology*, **53** (1981), 5-7.
14. D. Cubicciotti, "Vaporization Thermodynamics of Fission Products from Fuel under Nuclear-Accident Conditions", *Advances in Ceramics*, **17** (1986), 211-222.

15. D. Cubicciotti and B.R. Sehgal, "Vapour Transport of Fission Products in Postulated Severe Light Water Reactor Accidents", *Nuclear Technology*, **65** [5] (1984), 266-291.

16. D. Cubicciotti, "Vapour Transport of Fission Products under Nuclear-Accident Conditions", *Journal of Nuclear Materials*, **154** (1988), 53-61.

17. C.W. Bale, A.D. Pelton, and W.T. Thompson. "Facility for the Analysis of Chemical Thermodynamics - User Manual 2.1", Ecole Polytechnique de Montreal/ McGill University, (1996).

18. B.J. Corse, "FORM 2.0- Fuel Oxidation and Release Model- A Computer Code to Predict the Low Volatile Fission-Product Release and Fuel Volatilization from Uranium Dioxide Fuel Under Severe Reactor Accident Conditions", *Master's Thesis*, The Royal Military College, (1997).

19. M. Hillert and M. Schalin, "How Can Calphad Develop Further as a Science", *Journal of Phase Equilibria*, **19** [3] (1998), 206-212.

20. M.W. Chase, "Heats of Transition of the Elements", *Bulletin of Alloy Phase Diagrams*, **4** [1] (1983), 124.

21. D.R. Stull and H. Prophet, "JANAF Thermochemical Tables", U.S. Department of Commerce, Washington, D.C., (1985).

22. E.H.P. Cordfunke and R.J.M. Konings, Thermochemical Data for Reactor Materials and Fission Products, Elsevier Science Publishers, Amsterdam, (1990).

23. D.D. Wagman et al., "Selected Values of Chemical Thermodynamic Properties", National Bureau of Standards Series 270, U.S. Department of Commerce, Washington, D.C., (1968-1971).

24. I. Barin, O. Knacke, and O. Kubaschewski, Thermochemical Properties of Inorganic Substances, Springer-Verlag, Berlin, (1977).

25. L. Brewer, Molybdenum: Physico-Chemical Properties of Its Compounds and Alloys, O. Kubaschewski, Ed., Atomic Energy Review Special Issue No. 7, International Atomic Energy Agency, Vienna, (1980).

26. D.W. Oxtoby and N.H. Nachtrieb, Principles of Modern Chemistry, 2nd edition, Holt, Reinhart, and Winston, Orlando, Florida, (1990).

27. *Journal of Phase Equilibria*, American Society for Metals, Metals Park, Ohio.

28. T.B. Massalski, Binary Alloy Phase Diagrams, **1** & **2**, American Society for Metals, Metals Park, Ohio, (1986).

29. JANAF Thermochemical Tables, US Department of Commerce, National Bureau of Standards/Institute for Applied Technology, Washington, D.C., (June 1971, supplements 1974, 1975).

30. R. Hultgren, R.L. Orr, D. Anderson, and K.K. Kelley, Selected Values of Thermodynamic Properties of Metals and Alloys, John Wiley and Sons, New York, New York, (1974).

31. R. Gürler, "A Computer Assessment of the Molybdenum-Palladium Phase Diagram", *Journal of Alloys and Compounds*, **191** (1993), 83-86.

32. R. Gürler and J.N. Pratt, "A Computer Assessment of the Molybdenum-Rhodium Phase Diagram", *Journal of Alloys and Compounds*, **189** (1992), 97-100.

33. R. Gürler, L.A. Cornish, and J.N. Pratt, "Computer Assessment of the Palladium-Rhodium System", *Journal of Alloys and Compounds*, **191** (1993), 165-168.

34. R. Gürler, "A Computer Assessment of the Ru-Rh and Ru-Pd Systems", *Journal of Alloys and Compounds*, **191** (1993), 31-35.

35. M.H. Rand and P.E. Potter, "Thermodynamics and Phase Diagrams of Mo-Pd-Ru and Related Systems", *Physics*, **103B** (1981), 21-30.

36. Lide D. R. (ed), CRC Handbook of Chemistry and Physics, CRC Press, Boca Raton, Louisiana, (2000).

37. J.B. Mann, "Ionization Cross Sections of the Elements Calculated from Mean-Square Radii of Atomic Orbitals", *Journal of Chemical Physics*, **46** [5] (1967), 1646-1651.

38. T. Muromura, T. Adachi, H. Takeishi, Z. Yoshida, T. Yamamoto, and K. Ueno, "Metallic Phases Precipitated in UO_2 Fuel", *Journal of Nuclear Materials*, **151** (1988), 318-326.

39. T. Matsui and K. Naito, "Vaporization Study on Fission-Produced Noble Metal Alloys by Mass-Spectrometric Method", *Thermochimica Acta*, **139** (1989), 299-312.

40. E. Raub, "Die Legierungen der Platinmetalle mit Molybdän", *Zeitschrift Fuer Metallkunde*, **45** (1954), 23-30.

41. C.W. Haworth and W. Hume-Rothery, "The Constitution of Molybdenum-Rhodium and Molybdenum-Palladium Alloys", *Journal of the Institute of Metals*, **87** (1958-59), 265-272.

42. E. Anderson, "The Equilibrium Diagram of the System Molybdenum-Palladium", *Journal of the Less-Common Metals*, **6** (1964), 81-84.

43. E.M. Savitskii, M.A. Tylkina, and O.Kh. Khamidov, "The Molybdenum-Palladium System", *Russian Journal of Inorganic Chemistry*, **9** [12] (1964), 1475-1477.

44. W. Zaiss, S. Steeb, and T. Krabichler, "Diffusionsuntersuchungen im System Molybdän-Palladium mit Hilfe einer Mikrosonde", *Zeitschrift Fuer Metallkunde*, **63** (1972), 180-184.

45. P. Greenfield and P.A. Beck, "Intermediate Phases in Binary Systems of Certain Transition Elements", *Transactions of the Metallurgical Society of AIME*, **206** (1956), 265-276.

46. A. Maldonado and K. Schubert, "The Structures of Some Systems Homologous and Quasi-Homologous to T^5-T^{10}", *Zeitschrift Fuer Metallkunde*, **55** (1964), 619-626.

47. H. Kleykamp, "Constitution and Thermodynamics of the Mo-Ru, Mo-Pd, Ru-Pd, and Mo-Ru-Pd Systems", *Journal of Nuclear Materials*, **167** (1989), 49-63.

48. R. Gürler and J.N. Pratt, "Constitutional Studies of Molybdenum-Palladium Alloys Using Ultra-Rapidly Solidified Samples", *Journal of the Less-Common Metals*, **175** (1991), 71-78.

49. H. Okamoto, "Comment on Mo-Pd (Molybdenum-Palladium)", *Journal of Phase Equilibria*, **15** [4] (1994), 452-453.

50. A.A. Rudnitskii and R.S. Polyakova, "The Palladium-Ruthenium System", *Russian Journal of Inorganic Chemistry*, **4** [6] (June 1959), 631-636.

51. A.S. Darling and J.M. Yorke, "The Ruthenium-Palladium System", Platinum Metal Review, **4** [3] (1960), 104-110.

52. W. Obrowski and G. Zwingmann, "Beitrag zum Aufbau des Systems Palladium-Ruthenium und über Eigenschaften der palladiumreichen Legierungen", *Zeitschrift Fuer Metallkunde*, **53** (1962), 453-455.

53. S.N. Tripathi, S.R. Bharadwaj, and S.R. Dharwadkar, "The Pd-Ru System (Palladium-Ruthenium)", *Journal of Phase Equilibria*, **14** [5] (1993), 638-642.

54. J.O.A. Paschoal, "Der Aufbau der Systeme Mo-Ru-Rh-Pd und UO_2-ZrO_2-MoO_2-BaO und ihre Korrelation mit Spaltproduktausscheidungen in bestrahlten Brennstoffen", Kernforschungszentrum Karlsruhe Report, KfK 3473 (1983).

55. J.O.A. Paschoal, H. Kleykamp, and F. Thümmler, "The Constitution of the Ru-Rh System", *Journal of the Less-Common Metals*, **98** (1984), 279-284.

56. S.N. Tripathi, S.R. Bharadwaj, and M.S. Chandrasekharaiah, "The Rh-Ru System (Rhodium-Ruthenium)", *Journal of Phase Equilibria*, **17** [4] (1996), 362-365.

57. H. Okamoto, "Comment on Rh-Ru (Rhodium-Ruthenium)", *Journal of Phase Equilibria*, **15** [2] (1994), 232.

58. E. Anderson and W. Hume-Rothery, "The Equilibrium Diagram of the System Molybdenum-Rhodium", *Journal of the Less-Common Metals*, **2** (1960), 19-28.

59. H. Okamoto, "Comment on Mo-Rh (Molybdenum-Rhodium)", *Journal of Phase Equilibria*, **15** [3] (1994), 368.

60. B.C. Giessen, U. Jaehnigen, and N.J. Grant, "Ordered AB and AB_3 phases in T_6-T_9 Alloy Systems and a Modified Mo-Ir Phase Diagram", *Journal of the Less-Common Metals*, **10** (1965), 147-150.

61. E. Anderson and W. Hume-Rothery, "The Equilibrium Diagram of the System Molybdenum-Ruthenium", *Journal of the Less-Common Metals*, **2** (1960), 443-450.

62. B.F. Kieffer and K. Sedlatschek, "An Investigation of the Ternary Systems Molybdenum-Rhenium-Niobium and Molybdenum-Rhenium-Ruthenium", Symposium on High-Temperature Refractory Metals, Gordon and Breach Science Publishers, New York, New York, (1969), 441-464.

63. H. Kleykamp, "The Constitution of the Mo-Ru System", *Journal of the Less-Common Metals*, **136** (1988), 271-275.

64. H. Kleykamp, "Thermodynamics of the Mo-Ru System", *Journal of the Less-Common Metals*, **144** (1988), 79-86.

65. M.H. Kaye, W.T. Thompson, and B.J. Lewis, "Toward a Comprehensive Thermodynamic Treatment of Noble Metal Inclusions", *Transactions of the American Nuclear Society*, **79** (1998), 123-125.

66. R. Gürler, "Constitutional Studies of Molybdenum-Ruthenium Alloys Using Ultra-Rapidly Solidified Samples", *Journal of Alloys and Compounds*, **285** (1999), 133-136.

67. V.B. Compton, E. Corenzwit, J.P. Maita, B.T. Matthias, and F.J. Morin, "Superconductivity of Technetium Alloys and Compounds", *Physical Review*, **123** [5] (September 1961), 1567-1568.

68. J.B. Darby, Jr. and S.T. Zegler, "Comments on Superconducting Phases in the Mo-Tc System", *Physics and Chemistry of Solids*, **23** (1962), 1825-1827.

69. J.B. Darby, Jr., D.J. Lam, L.J. Norton, and J.W. Downey, "Intermediate Phases in Binary Systems of Technetium-99 with Several Transition Elements", *Journal of the Less-Common Metals*, **4** (1962), 558-563.

70. N.V. Ageev, C.V. Kopetskii, E.M. Savitskii, and V.S. Shekhtman, "Sigma-Phase Formation in the Systems Rhenium-Manganese and Rhenium-Iron", *Doklady Akademii Nauk S.S.S.R.*, **129** (1959), 87-88.

71. J.B. Darby, Jr., L.J. Norton, and J.W. Downey, "A Survey of the Binary Systems of Technetium with Group VIII Transition Elements", *Journal of the Less-Common Metals*, **5** (1963), 397-402.

72. J. Niemiec, "X-ray Analysis of Technetium Alloys with Rhodium, Palladium, and Platinum", "Bulletin de L'Académie Polonaise Des Sciences", **11** [12] (1963), 665-669.

73. D.R. Gaskell, Introduction to Metallurgical Thermodynamics, McGraw-Hill, New York, New York, (1981).

74. E. Raub, "Metals and Alloys of the Platinum Group", *Journal of the Less-Common Metals*, **1** (1959), 3-18.

75. E. Raub, H. Beeskow, and D. Menzel, "Palladium-Rhodium Legierungen und Allotropieverhältnisse beim Rhodium", *Zeitschrift Fuer Metallkunde*, **50** (1959), 428-431.

76. K.M. Myles, "Thermodynamic Properties of Solid Rhodium-Palladium Alloys", *Transactions of the Metallurgical Society of AIME*, **242** (1968), 1523-1526.

77. J.E. Shield and R.K. Williams, "The Study of the Pd-Rh System by Electrical Resistivity Measurements", *Scripta Metallurgica*, **21** [11] (1987), 1475-1479.

78. H. Okamoto, "Comment on Pd-Rh (Palladium-Rhodium)", *Journal of Phase Equilibria*, **15** [3] (1994), 369.

79. K.T. Jacob, S. Priya, and Y. Waseda, "Thermodynamic Mixing Properties and Solid-State Immiscibility in the Systems Pd-Rh and Pd-Rh-O", *Journal of Phase Equilibria*, **19** [4] (1998), 340-350.

80. P. Chartrand and A.D. Pelton, "On the Choice of 'Geometric' Thermodynamic Models, *Journal of Phase Equilibria*, **21** [2], (2000), 141-147.

81. F. Kohler, "Zur Berechnung der thermodynamischen Daten eines ternären Systems aus den zugehörigen binären Systemen", *Monatshefte Für Chemie*, **91**, (1960), 738-740.

82. J.O.A. Paschoal, H. Kleykamp, and F. Thümmler, "Phase Equilibria in the Quaternary Molybdenum-Ruthenium-Rhodium-Palladium System", *Zeitschrift Fuer Metallkunde*, **74** (1983), 652-664.

83. K. Naito, T. Tsuji, T. Matsui, and A Date, "Chemical State, Phases, and Vapour Pressures of Fission-Produced Noble Metals in Oxide Fuel", *Journal of Nuclear Materials*, **154** (1988), 3-13.

84. R. Gürler and J.N. Pratt, "A Constitutional Investigation of the Mo-Pd-Rh Ternary System at 1100°C", *Journal of Nuclear Materials*, **186** (1991), 39-46.

85. R. Gürler and J.N. Pratt, "A Computer Calculation of the Ternary Mo-Pd-Rh Phase Diagram", *Journal of Nuclear Materials*, **200** (1993), 16-23.

86. H.R. Haines, P.E. Potter, and M.H. Rand, "Some Phase-Diagram Studies of Systems with Fission-Product Elements for Fast Reactor Fuels", Proceedings of an IAEA Symposium on Thermodynamics of Nuclear Materials, 1, (1979), 471-501.

87. M.H. Kaye, K.M. Jaansalu, and W.T. Thompson, "Experimental Thermodynamics ~ Phase Equilibrium in Metallic Systems", IUPAC, (*accepted March 6, 2001*). *Included as Appendix A*

88. ASTM, "Standard Practice for Temperature Calibration of Differential Scanning Calorimeters and Differential Thermal Analyzers", ASTM Designation E 967-83 (re-approved 1987), (1983), 588.

89. D.R. Gaskell, Introduction to Metallurgical Thermodynamics, McGraw-Hill, New York, New York, (1981).

90. M.H. Kaye, W.T. Thompson, B.J. Lewis, and F.C. Iglesias, "Oxidation of Nuclear Fuel Rods During a Loss-of-Coolant Accident",8th Canadian Material Science Conference, London, Ontario, (June 12, 1996).

91. W. T. Thompson, G. Eriksson, C.W. Bale, and A.D. Pelton, "Applications of F*A*C*T in High Temperature Materials Chemistry", High Temperature Materials Chemistry IX, K.E. Spear (ed.), The Electrochemical Society, Inc., Pennington, New Jersey, (1997), 16-30.

92. R. McEachern, "Oxidation Behaviour of Noble-Metal Inclusions in Used UO_2 Nuclear Fuel", Report AECL-11818, (July 1997).

Appendices

Note to Reader:

The appendices have been constructed as self-standing documents. For the sake of convenience the references cited are to be found at the end of each appendix.

Appendix A

Copy of the manuscript submitted to:

IUPAC VOLUME

EXPERIMENTAL THERMODYNAMICS

Phase Equilibrium in Metallic Systems

M.H. Kaye[*], K.M. Jaansalu[†], and W. T. Thompson[*,†]

[*] Department of Materials and Metallurgical Engineering,
Queen's University, Kingston, Ontario, Canada, K7L 3N6

[†] Department of Chemistry and Chemical Engineering,
The Royal Military College, Kingston, Ontario, Canada, K7K 7B4.

Submitted for review: March 6, 2001.

1. Introduction

Phase equilibrium in binary metallic systems has been extensively studied in support of metallurgical engineering. The early work, a century or more ago, put emphasis on such experimental methods as thermal analysis and metallography and resulted in the landmark collection of phase diagrams by Hansen in 1936.[1] In the years following, the greater range of superior experimental methods and a developing interest in the underlying thermochemical principles of phase equilibria led to the international metallic phase diagram evaluation programs[2-5] culminating in the volumes edited by Massalski.[6]

Phase equilibrium for a binary metallic system is usually represented on an isobaric temperature-composition diagram. This very common selection of axes recognizes the major variables of interest in metallurgical processing. Although it is most often secondary to the intended use, these diagrams may be regarded as maps showing the phase or phases that provide the lowest Gibbs energy at a particular temperature, pressure, and composition. In principle, the phase diagram may be developed from an independent knowledge of the relative Gibbs energies for the various possible phases. Although this has been recognized since the landmark paper of Gibbs[7], it is seldom a reliable practical approach to phase diagram construction, since relatively small uncertainties in measured Gibbs energy differences between components in the phases generate substantial uncertainties in the placement of the phase boundaries.

The matters that make the computation of phase diagrams unreliable when based on a variety of independent direct thermochemical measurements imply that thermochemical properties can be quite well inferred from a phase diagram when the underlying principles are applied. Indeed, the determination of any feature of a phase diagram (by whatever method) constitutes a *bona fide* method to establish thermochemical properties that are quite reliable. Therefore, compilations of assessed phase diagrams constitute a rich source of thermochemical solution properties. The development of phase diagrams from Gibbs energies may appear to have limited practical value. It may seem that the exercise does little more than demonstrate that the features of the diagram are

consistent with the constraints of thermodynamic principles – reassuring but not far reaching. However, the process of critical analysis (modelling) brings together in a *self-consistent way* various kinds of independent thermochemical property measurements with the phase diagram as the keystone. As a result, the analysis isolates improbable measurements and places bounds on accuracy. Until the widespread use of advanced computers, this approach was impractical, but in the past 25 years it has become well recognized.

The solution properties inferred from phase diagram modelling are valuable in other ways. For example, thermochemical data on the behaviour of a binary metallic solution, when combined with other data, such as the Gibbs energy of formation of metal oxides, may be useful in understanding equilibrium in a three component metal-metal-oxygen system. Another example of interest is in the vacuum processing of alloys, where a phase diagram showing the placement of the vapour field under reduced pressure can be calculated. Furthermore, reasonable predictions of phase diagrams can be computed for multi-element metallic systems based upon an understanding of the component binary metallic systems. The predictions, at the very least, guide experimental investigations toward regions of particular interest.

2. Solution Thermodynamics Relevant to Metallic Phase Diagram Development

Since the principles of phase equilibrium computations are well covered elsewhere (Darken[8], Oonk[9], Gaskell[10], Lupis[11]), only the cornerstone ideas will be highlighted here. The underlying principle in extracting thermodynamic data from phase diagrams is the equality of chemical potential or partial molar Gibbs energy for each of the components in the coexisting phases. Therefore, for component A, distributed between coexisting phases α and β:

$$\overline{G}_A^{\alpha} = \overline{G}_A^{\beta} \tag{1}$$

With reference to Figure 1, the partial molar Gibbs energy for component A in the α phase, can be interpreted graphically as the intercept of a tangent to the Gibbs energy of the α phase at the composition of interest.

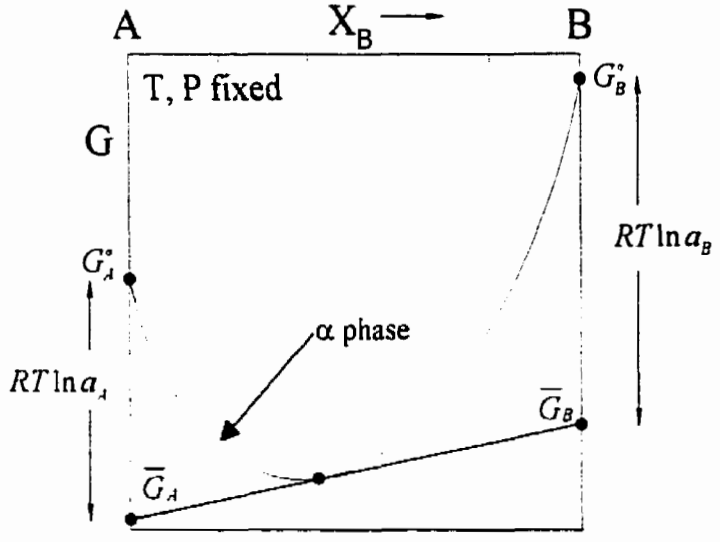

Figure 1. Relationship of molar Gibbs energy of a solution to the partial molar Gibbs energies and activities of the components.

The partial molar Gibbs energy must be expressed relative a standard condition of concentration. For pure A, the difference illustrated in Figure 1 can be related to the activity of the component in solution α at the composition given by the point of tangency. That is:

$$\overline{G}_A^{\alpha} - \overline{G}_A^{\circ\alpha} = RT\ln a_A^{\alpha} \tag{2}$$

where a_A^α is the activity at temperature T.

The temperature-composition phase diagram for the Sn-Bi system is shown in Figure 2.

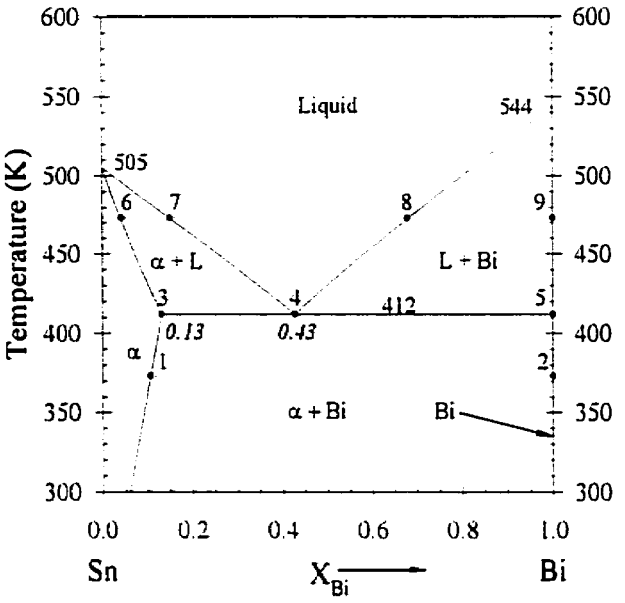

Figure 2. Isobaric Sn-Bi temperature–composition phase diagram.

A thermodynamic model for the Sn-Bi system[12] is given in Table 1.

Table 1. Gibbs Energy Data for Sn-Bi binary system.[12]

1. Sn (Pure Component): $G_{Sn}^{\circ(Liquid\rightarrow Liquid)} = 0 \;\; J/mol$ (Reference Phase) $G_{Sn}^{\circ(Liquid\rightarrow tI4_{(\alpha-solid)})} = -7029.1+13.917T \;\; J/mol.$
2. Bi (Pure Component): $G_{Bi}^{\circ(Liquid\rightarrow Liquid)} = 0 \;\; J/mol$ (Reference Phase) $G_{Bi}^{\circ(Liquid\rightarrow hR2_{(solid)})} = -11296.8+20.766T \;\; J/mol.$ $G_{Bi}^{\circ(Liquid\rightarrow tI4_{(\alpha-solid)})} = -4331.8+20.766T \;\; J/mol$
3. Sn-rich tI4 solution (α-solid phase): For $(1-x)Sn_{\alpha-solid}+(x)Bi_{\alpha-solid} = \left((1-x)Sn+(x)Bi\right)_{\alpha-solid\ solution}$ $\Delta G = (1-x)RT\ln(1-x)+(x)RT\ln(x) \;\; J/mol$
4. Liquid Phase: For $(1-x)Sn_{Liquid}+(x)Bi_{Liquid} = \left((1-x)Sn+(x)Bi\right)_{Liquid\ solution}$ $\Delta G = (1-x)RT\ln(1-x)+(x)RT\ln(x)+(1-x)(x)\left(606+194(1-x)\right) \;\; J/mol$

Gibbs energy isotherms for all phases (liquid, Sn-rich solid solution (α), and virtually pure solid Bi) are shown in Figure 3 at three temperatures. The hydrostatic pressure is understood to be constant at 1 atm, although for practical purposes there is little influence on the Gibbs energy of condensed phases for changes of a few atmospheres.

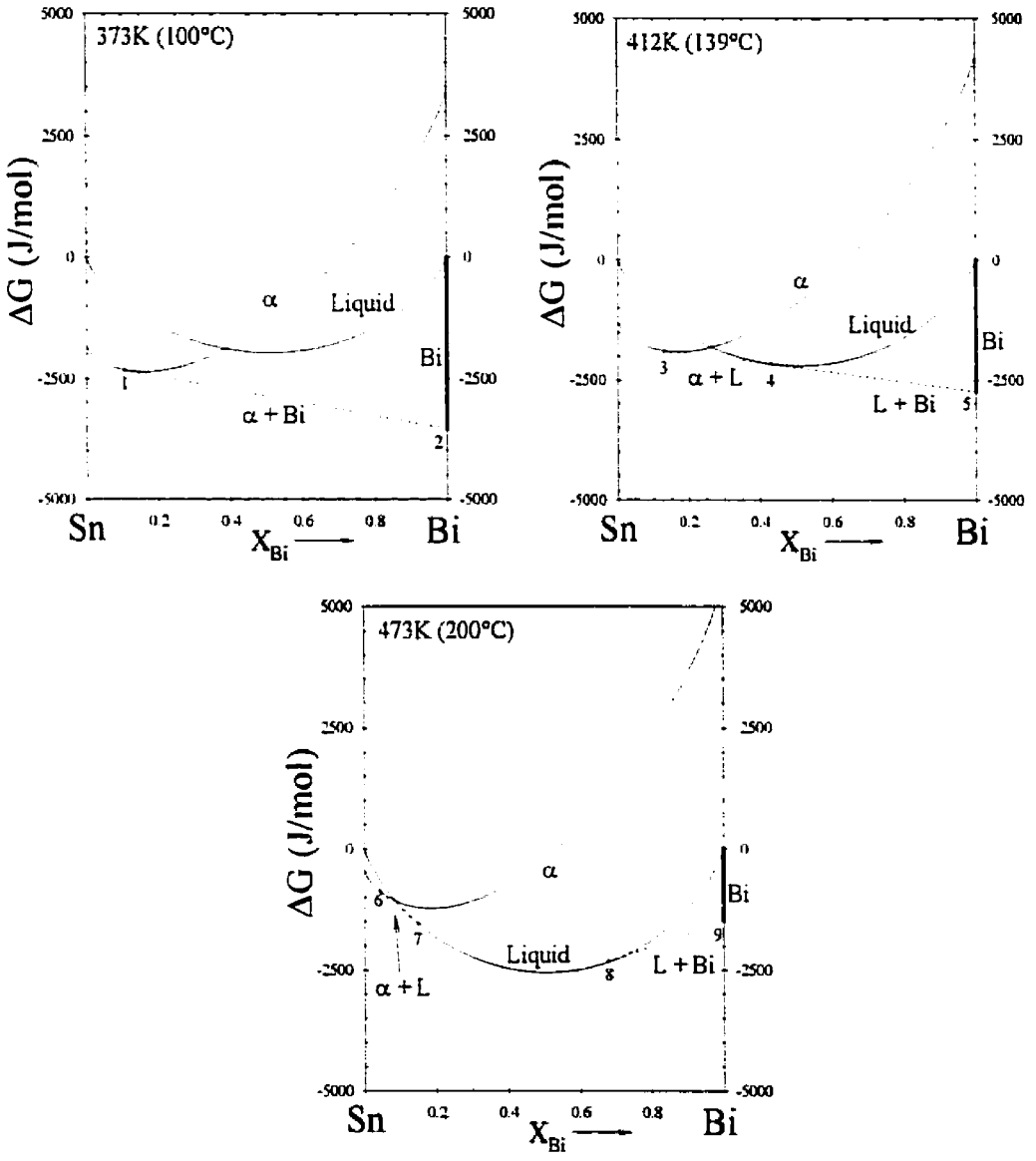

Figure 3. Gibbs energy Isotherms for Sn-Bi system.

At 473K it is possible to construct a common tangent between the Gibbs energy isotherms for the Sn-rich solid solution phase and the liquid, α + L. In view of the

significance of the tangent intercepts at the extremes of composition, this construction satisfies the basic requirement of equation (1) for both components simultaneously. Moreover, it is clear that no other phase between the points of tangency has a Gibbs energy lower than a mixture of these two phases. This collection of ideas, leading to the ends of the tie line (points 6 and 7) shown in Figure 2 at 473K, is termed the *lowest common tangent* construction. At 473K, when the overall Bi concentration is higher, there is another pair of coexisting phases (points 8 and 9). The construction can still be described as *lowest common tangent* if the point representing the Gibbs energy of pure solid Bi is interpreted as the lower extremity of a "curve" which ascends sharply upward near the right edge of the figure. This might be offered as a thermochemical explanation of the negligible solubility of Sn in solid Bi.

At 412K, the temperature of the eutectic, the two common tangents are now collinear. That is to say, one tangent touches all three isotherms simultaneously (points 3, 4, and 5). This situation typically arises only at one temperature or, in the language of the Phase Rule, when the system is invariant. At 373K, there is only one common tangent connecting virtually pure solid Bi to the Sn-rich α-solid solution (points 1 and 2). The liquid phase isotherm does not cut this tangent and is, therefore, not as stable as the two solid phase combination depicted on the phase diagram.

It is useful to mention in connection with Figure 3 the concept of *lattice stability* attributed to Kaufman[13], and with data compiled and reviewed by Dinsdale.[14] It might not be possible to locate the Gibbs energy isotherm for the α-solid solution in an experimental sense relative to the other phases for high concentrations of Bi. However, the meaning of the Bi rich extreme of the isotherm is the Gibbs energy Bi *would have if it could exist* in the α-phase (tI4).[15] This lattice stability of Bi in the tI4 structure can be expressed relative to Bi in its more stable rhombohedral structure (hR2).[16] In Table I this is treated as a constant: $\left(-4331.8-\left(-11296.8\right)\right)=6965 J/mol$.

Of course, when Gibbs energies all phases are known as functions of temperature, the enthalpy and entropy contributions to the Gibbs energy are, in effect, known as well. This opens the possibility of calculating other phase diagrams for the same system using

other co-ordinates. In Figure 4, the temperature, or thermal potential, axis in Figure 2 has been replaced by the relative thermal energy or enthalpy change, with respect to a mechanical mixture of the two pure solid components at 298K.

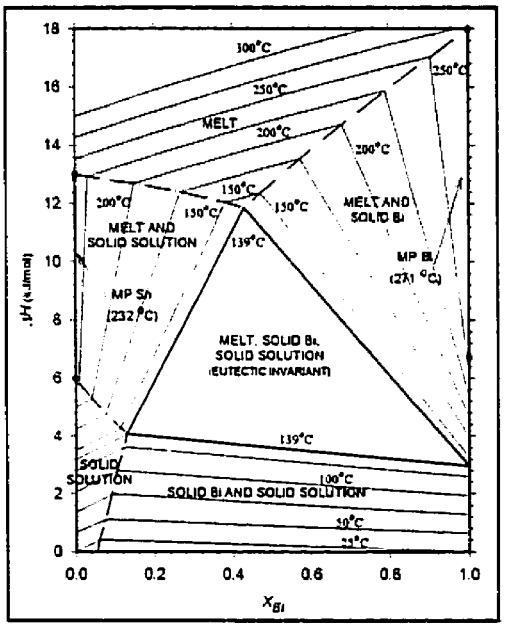

Figure 4. Enthalpy-composition phase diagram for Sn-Bi.

This diagram not only connects phase equilibrium with scanning calorimetry but is useful in a practical sense to understand thermal effects associated with solidification or melting – a matter of interest for this particular alloy system in view of its use in lost core moulding of hollow polymer components, which involves repetitive melting and solidification.

Since, for the case of most metallic solution phases, the component atoms interchange on lattice sites, the ideal Gibbs energy of mixing for a mole of solution represented by:

$$X_A(A) + X_B(B) = (A-B)_{Solution} \tag{3}$$

is given by:

$$\Delta G = X_A RT \ln X_A + X_B RT \ln X_B \tag{4}$$

a form used in Table 1 for the liquid and α-phases.

The Gibbs energy provided by equation (4) is brought into agreement with thermochemical measurements or phase diagram features by the addition of an excess Gibbs term, G^E, that itself can be subdivided into an enthalpy and excess entropy contribution:

$$G^E = \Delta H - TS^E \tag{5}$$

The simplest form is given by an empirical series, which is usually arranged as follows:

$$G^E = X_A X_B \left(a + bX_B + cX_B^2 + \ldots\right) \tag{6}$$

For many systems G^E is not very dependent on temperature, which implies that S^E is near zero, and the random atomic mixing assumption inherent in the form of equation (4) provides a close approximation to the actual entropy of mixing. In this case, the excess Gibbs energy is numerically equivalent to the enthalpy of mixing. When G^E is temperature dependent each coefficient in equation (6) may be expressed by an expansion in T; usually linear is sufficient.

To complete the mathematical positioning of a Gibbs energy isotherm, for example the liquid phase in Figure 3, the ends of the curve at each extreme of composition must be located. This may be done by arbitrarily selecting a reference phase for each component (the phases need not be the same) and expressing the ends of the isotherm with respect to these selections. For the Sn-Bi system shown in Table 1, the point of reference for each component is the pure liquid.

Figure 5 shows the phase diagram for Mg-Si. Five phases are involved, of which two are solution phases. All of the numerical data to establish the relative placement of the Gibbs energy curves consistent with Figure 5 is given in Table 2. This provides the basis for constructing the Gibbs energy isotherms in Figure 6 at 1300K.

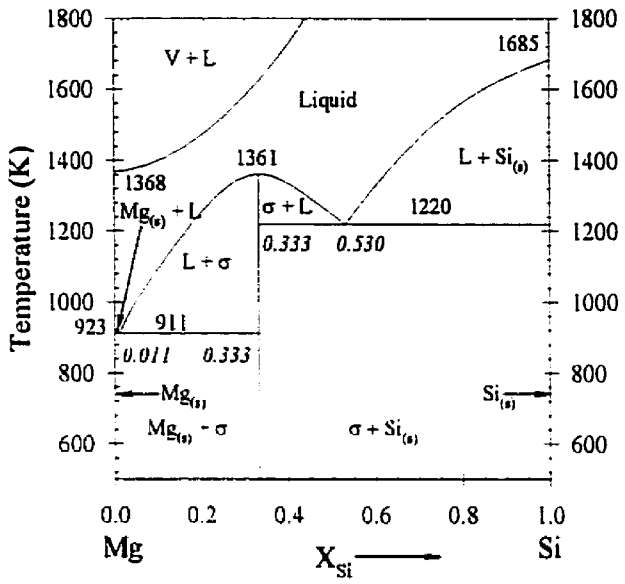

Figure 5. Computed binary phase diagram for the Mg-Si system using the data in Table 2. The pressure is 1 atm.

Table 2. Gibbs energy data used in the construction of Figures 5 through 8.

1. Mg (Pure Component):

$G_{Mg}^{\circ(Liquid \rightarrow Liquid)} = 0 \ J/mol$ (Reference Phase)

$G_{Mg}^{\circ(Liquid \rightarrow Solid)} = -8479 + 9.186T \ J/mol$

$G_{Mg}^{\circ(Liquid \rightarrow Vapour)} = 127847 - 93.476T + RT\ln(P) \ J/mol$

2. Si (Pure Component):

$G_{Si}^{\circ(Liquid \rightarrow Liquid)} = 0 \ J/mol$ (Reference Phase)

$G_{Si}^{\circ(Liquid \rightarrow Solid)} = -50212 + 29.80T \ J/mol$

$G_{Si}^{\circ(Liquid \rightarrow Vapour)} = 384540 - 109.613T + RT\ln(P) \ J/mol$

3. Mg_2Si (Intermetallic Compound, σ):

For $\frac{2}{3}Mg_{Liquid} + \frac{1}{3}Si_{Liquid} = \frac{1}{3}Mg_2Si_{Solid}$

$\Delta G = -211373 + 1096.8T - 133.427T\ln T \ J/mol;$

4. Vapour Phase:

For $(1-x)Mg_{(gas,\,P\,atm)} + (x)Si_{(gas,\,P\,atm)} = \left((1-x)Mg + (x)Si\right)_{(gaseous\ solution,\ P\ atm)}$

$\Delta G = (1-x)RT\ln(1-x) + (x)RT\ln(x) \ J/mol;$

5. Liquid Phase:

For $(1-x)Mg_{Liquid} + (x)Si_{Liquid} = \left((1-x)Mg + (x)Si\right)_{Liquid\ solution}$

$\Delta G = (1-x)RT\ln(1-x) + (x)RT\ln(x)$

$+(1-x)(x)(-26751 - 70.809T) + (1-x)(x)^2(74838) \ J/mol.$

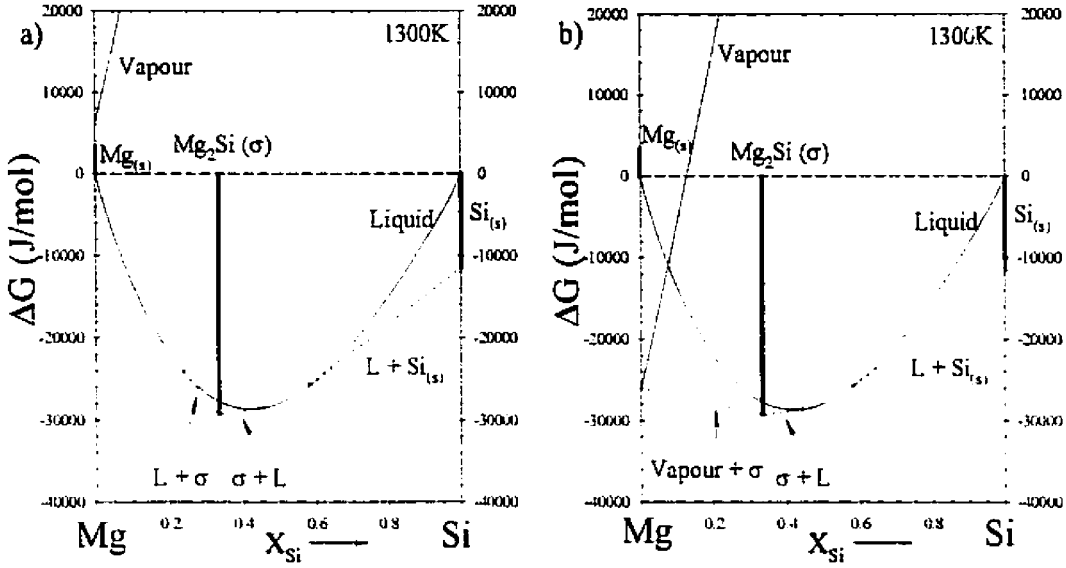

Figure 6. Gibbs energy isotherms for the Mg-Si system at 1300K. The effect of pressure reduction on the placement of the vapour phase isotherm is shown in b).

By applying the lowest common tangent construction it is seen that Figure 5 and Figure 6a are self-consistent at this temperature. As for Table 1, the data in Table 2 may be regarded as a formal way of storing the phase diagram, or as thermodynamic data useful for other purposes. Consider the development of the temperature-composition diagram at a constant pressure of 0.05 atm. The isotherm for the vapour phase in Figure 6b is lowered by $RT \ln P$ and the lowest common tangent construction is repeated. The resulting phase diagram is shown in Figure 7.

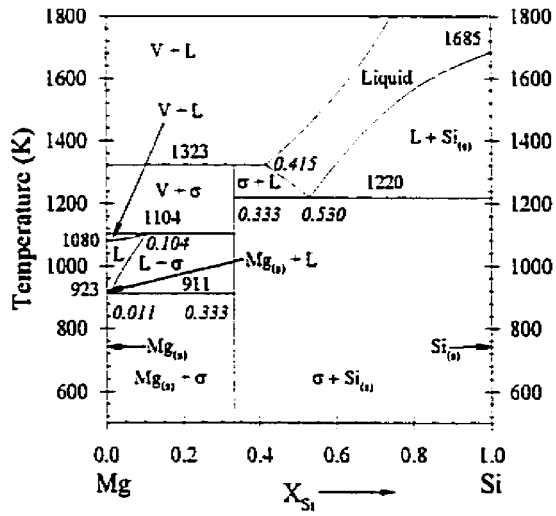

Figure 7. Computed binary phase diagram for the Mg-Si system using the data in Table 2. The pressure is 0.05 atm.

The ability to rapidly compute the diagram at various pressures naturally leads to an isothermal *log P-composition* diagram, shown in Figure 8 at 1300K.

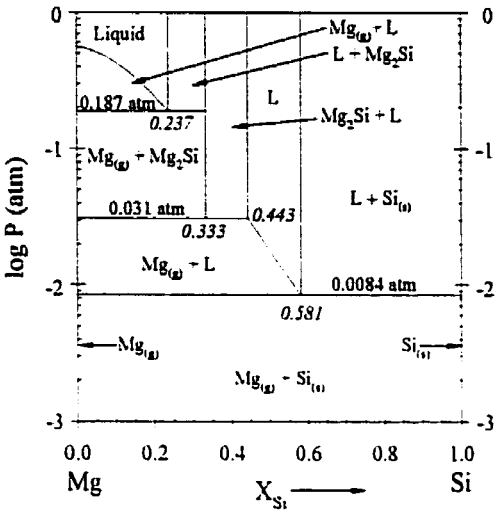

Figure 8. Computed isothermal pressure versus composition phase diagram for the Mg-Si system using the data in Table 2. The temperature is 1300K.

The data in Table 2 are reasonably reliable insofar as relative Gibbs energies are concerned. The computed diagram, in which the eutectic compositions and temperatures are well represented, is evidence. However, the enthalpy and entropy changes inferred from the Gibbs energies are less reliable. For example, the constant preceding the $T \ln T$ term in the Gibbs energy for the formation of Mg_2Si implies a large difference in the heat capacities between the product and reactants associated with the formation of Mg_2Si. Further, the magnitude of the temperature dependence in the Gibbs energy of mixing of the liquid phase implies a large departure from random atom mixing. This underlines the need to couple phase diagram modelling to experimental measurement.

3. Experimental Methods

A very wide variety of experimental techniques bear upon the study of phase equilibrium in metal systems. It is typical of a great fraction of the experimental work reported that specialized equipment, unique to the alloy under study, has been custom assembled for a particular purpose. A catalogue of specific techniques would, therefore, imply a degree of experimental standardization and off the shelf equipment that does not exist. The approach here will be to broadly classify the main techniques used, with reference to binary systems, although all of the techniques can apply to multi-component systems. The selection of a particular technique is usually dictated by heating requirements, available materials of construction, and the chemical reactivity or volatility of component elements. Materials of construction pose a major problem and, if this matter is not a part of the experimental plan from the outset, the containment materials may become inadvertent minor components of the system under study.

3.1 Microscopic Phase Examination

The detection of phases by microscopic means for alloys of known composition and thermal history is a cornerstone in the development of metallic phase diagrams. By working backwards with the computational ideas discussed in the previous section, thermodynamic information of the phases can be deduced.

Optical microscopic methods for metals are based on the reflection of light from polished and etched metal surfaces.[16] To determine the liquidus and solidus, an alloy is heated (annealed) in a protective atmosphere at a known temperature. A rapid quench follows which freezes in the microstructure at that temperature.[17] By examining the microstructure, the number and identity of the phases present at temperature can be determined.[18] An example of a typical optical micrograph for a Mo-Rh alloy is shown in Figure 9.[19] Several days or even weeks of annealing may be required to reach equilibrium depending on the temperature. Alloys with an increasing fraction of a second element are examined and the composition when a second phase appears at a particular temperature is noted. The relative mass or atomic fraction of the phases can be obtained from the

observed phase fractions, which in turn can be related to a tie line on the phase diagram.

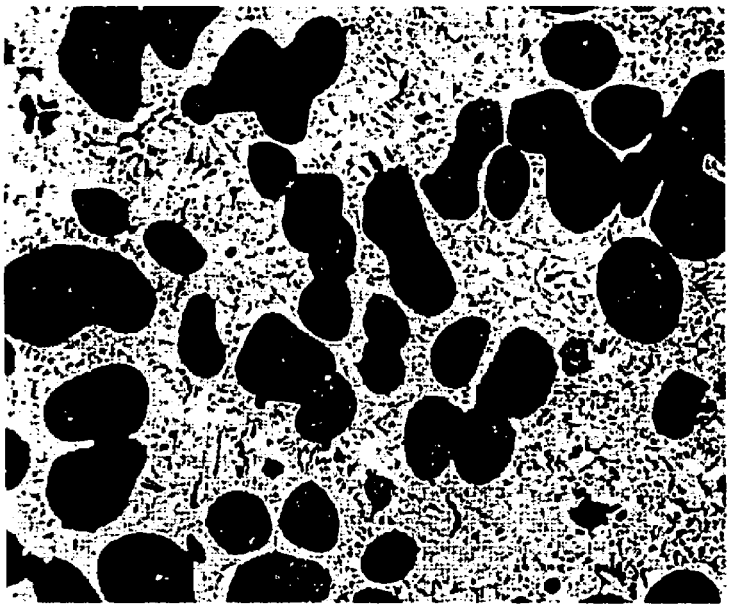

Figure 9. Mo-30 atomic% Rh alloy quenched from the condition identified in Figure 10, at a temperature just above the eutectic in the two phase field (α + liq). The dark regions are the Mo-rich phase (α-Mo), surrounded by the two phase mixture associated with the eutectic solidification of the liquid phase. Sample was etched in solutions diluted from a stock solution of: 9g NaOH, 2.5g $K_3Fe(CN)_6$, and 380g H_2O. Magnification is 200X.[19]

By plotting the phase assemblages determined by microscopy at each alloy composition against temperature, a general indication of the phase diagram is obtained. The example for the molybdenum-rhodium system is shown in Figure 10.[19] Note that the relative proportions of α–Mo and transformed liquid phase (from Figure 9) are consistent with the lever rule construction in Figure 10.

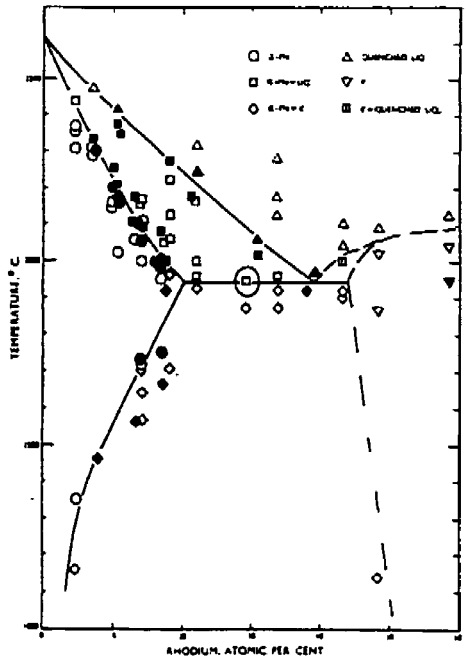

Figure 10. A partial phase diagram for Mo-Rh as determined by metallography.[19] Note the point (as circled) for the Mo-30 atomic% Rh alloy depicted in Figure 9.

A superior method, in principle, is hot stage microscopy where the phases can be directly observed at temperature in a vacuum or protective atmosphere. This approach does not depend on interpretational matters that arise when phase transformations occur during quenching, but is otherwise similar to the venerable annealing-quenching technique.

For the scanning electron microscope (SEM) or electron probe microanalyser (EPMA), an electron beam interacts with the atoms in the sample, and X-rays are emitted that are characteristic of the elements present. These X-rays are detected and analysed using energy dispersive (EDS) or wave-length dispersive spectrometers (WDS). SEMs are routinely coupled to an EDS system for concurrent chemical analysis. For microchemical analysis in metallurgical work, an EPMA has one or more wavelength dispersive spectrometers (WDS) attached. The SEM and EPMA instruments make use of the same physical principles, but the emphasis is different. The SEM is an imaging device; EPMA a chemical analysis tool. As such with an EPMA, the instrument is designed to control the position of the electron beam which must be held stationary for long periods of time, tightly aimed, and focussed. Detailed information on these techniques and their applications can be found in Scanning Electron Microscopy[20], the ASM Handbooks[21,22],

and in ASTM Standard E-1508-98.[23] The relative merits of the WDS, sometimes called a crystal dispersive spectrometer, over the EDS is that the WDS has a higher resolution of the X-ray spectrum and better detection limits of trace elements, but this comes at the cost of increased data collection times. The impact of these differences is well discussed by Lifshin.[24]

In the study of phase equilibrium, the main advantage of an SEM/EDS system is the capability to provide relatively rapid compositional information, that can be used to locate the ends of tie-lines. Routinely, images are collected that indicate the distribution of specific elements. This requires some capability of the SEM to hold the electron beam at a specific location for a pre-set time, similar to the EPMA. As the EDS system acquires the entire spectrum, as opposed to the WDS which scans only the wavelengths of interest, data collection for the EDS system is relatively rapid.

Advances in SEM/EDS have resulted in better and faster means of determining the composition of the phases. In particular, the advances in detector technology, digital pulse processing, and computer storage have expanded the utility of energy-dispersive spectrometry.[25] Older detection systems are restricted to detecting aluminum and heavier elements. Detector construction and the development of atmospheric thin windows have improved the detectability of light elements, such as carbon and oxygen, to the point where they can be detected reliably and their proportions derived. Present day systems can detect elements as light as beryllium. Of particular note are the advances in low voltage electron microscopy, which prevents charge build-up on the sample. Thus conductive coatings are not required and a better EDS analysis is obtained for light elements.

The transmission electron microscope (TEM) is an extremely valuable tool in examining precipitates on the order of a few hundred nanometers. Although it is primarily used for the investigation of sub-micron features of microstructures, the TEM has also been used to provide information relating to the placement of phase boundaries for metallic systems.[21] In a TEM, an electron beam is passed through a thin section of material. Similar to the SEM or EPMA, the X-rays emitted can be analysed with a EDS

or WDS system to give the composition of the phase examined. An electron diffraction pattern is also obtained concurrently, giving the structure of the phase.

3.2 X-ray Diffraction

Since the first structure determination by W.L. Bragg in 1912[26], X-ray diffraction has been used to characterise the arrangement of atoms.[27] Metallic phases and their crystal structures have been so extensively studied that the method is now used to identify phases and is primarily used as a complement to metallographic or microscopic techniques. X-ray powder diffractometry has been reviewed in great detail recently[28] and application to metallurgy can be found in general texts[29-31] and in specific publications.[27]

Construction of phase diagrams from X-ray data exploits the fact that there is a continuous change in the lattice parameter with changing proportions of atoms of different size. Typically, alloy specimens equilibrated at high temperature are quenched to room temperature to preserve the equilibrium. For a continuous solid solution, such as Co-Ni alloys, the lattice parameter varies nearly linearly with composition (Vegard's law). This variation is shown for the Co-Ni system in Figure 11.[32]

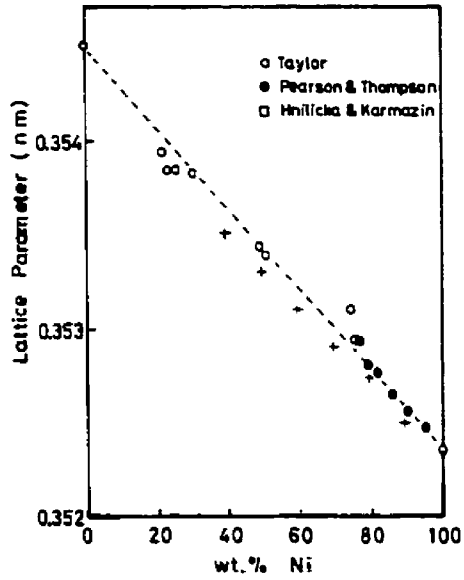

Figure 11. Lattice parameter of Co-Ni alloys at room temperature.[32]

Where there are two phases possible at a particular temperature, there is an arrest in the lattice parameter variation with composition and diffraction peaks associated with a second phase begin to appear. This is evident for the Ni-Ti system shown in Figure 12.[33]

The discontinuity identifies the phase boundary or solid solubility at 1023K.

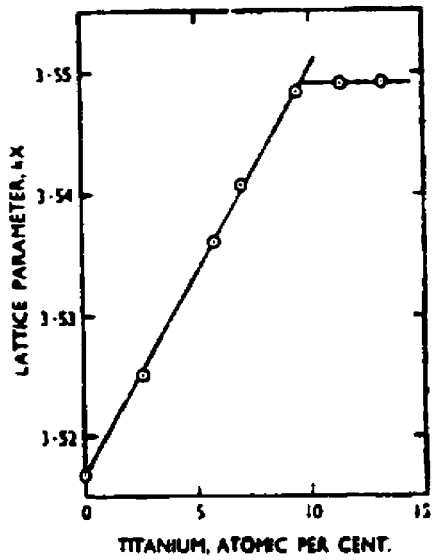

Figure 12. Lattice parameter of Ni-Ti alloys, nickel rich region at 1023K.[33]

For comparison purposes, the Ni-Ti phase diagram[6] is shown in Figure 13, with the point on the phase boundary determined in Figure 12 circled.

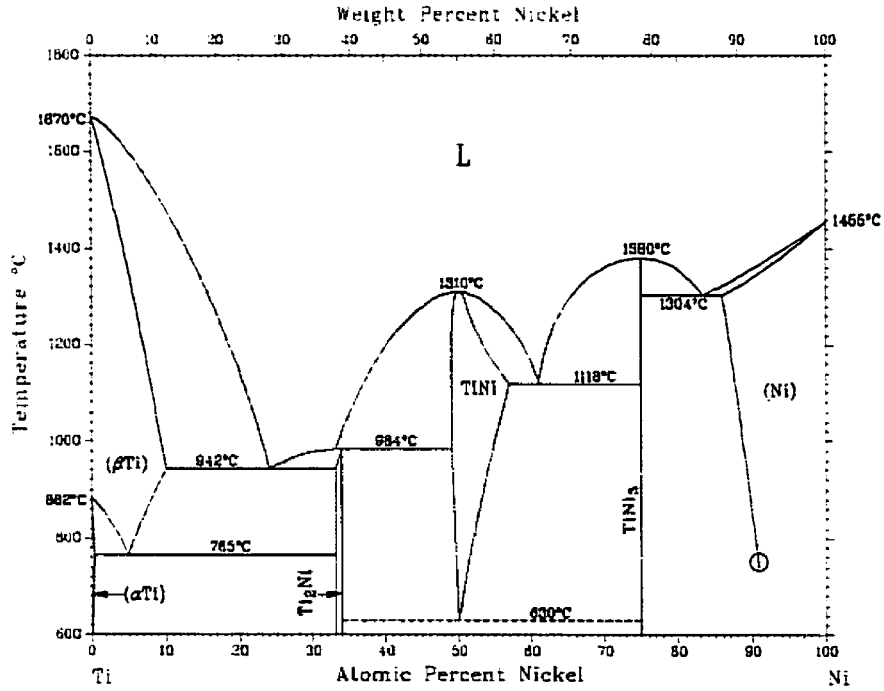

Figure 13. The Ni-Ti phase diagram.[6] The circled point on the lower right relates to the discontinuity shown in Figure 12.

Approximate relative proportions of the phases in the powder, usually accurate to a few percent, can be determined by intensity variation. To do so requires that standards

of known proportions be prepared and used to create a calibration plot. Relative proportions can also be determined by Rietveld refinement, which is growing in popularity.[34] This technique originally grew out of the analysis of neutron diffraction patterns and has been applied to X-ray diffraction patterns. The interpretational software requires some knowledge of the space group, and atomic positions within the unit cell. This is generally not a problem for metallic systems. One recent application has been to quantitatively determine the mass fraction and mean size evolution of the δ' precipitates in an Al-Li alloy.[35,36] The software is freely available[37] and guidelines for the Rietveld refinement have been published recently.[38]

3.3 Emf Cells

Generally speaking, this approach provides the relative partial molar Gibbs energy of one component in the system as a voltage measured under open circuit conditions.[39] The experimental program must first demonstrate reproducibility in the measured potentials following a disturbance, such as the momentary passage of a small current or excursion in temperature. By gathering sufficient information on the compositional dependence of one component over the extremes of composition change, the Gibbs-Duhem equation may be integrated to determine the relative partial molar Gibbs energy of the other component and the Gibbs energy of mixing, depicted in Figure 1.

Consider a binary system M-N in which M is the more easily oxidized element. An electrochemical concentration cell may be constructed of the type:

$$- \quad M \left| M^{z+} \right| M - N \quad + \tag{7}$$

The electrolyte containing the M^{z+} ion must be suitably conductive and non-volatile at the temperature of interest. Typically, a molten salt mixture is employed to provide a suitably low eutectic.[40-42] The diluent salts for the M^{z+} ion must be sufficiently stable so that there is no chemical exchange with the alloying elements. The reversible open circuit cell voltage E gives the relative partial Gibbs energy of M by:

$$\Delta \overline{G}_M = -z\Im E \tag{8}$$

where $\Im$ is the Faraday constant.

To permit measurements at higher temperatures, where even a molten electrolyte may be too volatile, a solid electrolyte may be employed. In this technique, a metal/metal oxide equilibrium may be used to establish an oxygen partial pressure in the half-cells. The difference in the effective oxygen partial pressure on either side of the solid O^{2-} conducting electrolyte generates an emf that can be related to the activity of the metal component under study in the alloy phase.

To take the case of palladium-rhodium alloys, the thermodynamic properties have been measured between 950K and 1350K.[43] The galvanic cell, shown in Figure 14, is schematically represented by:

$$- \underbrace{Rh, Rh_2O_3}_{(P_{O_2})_1} \Big| \underbrace{Y_2O_3 \cdot ZrO_2}_{\text{solid oxide electrolyte}} \Big| \underbrace{Pd_{1-x}Rh_x, Rh_2O_3}_{(P_{O_2})_2} + \qquad (9)$$

where the oxygen partial pressure at each electrode is controlled by:

$$2Rh + \tfrac{3}{2}O_2 \rightleftharpoons Rh_2O_3 \qquad (10)$$

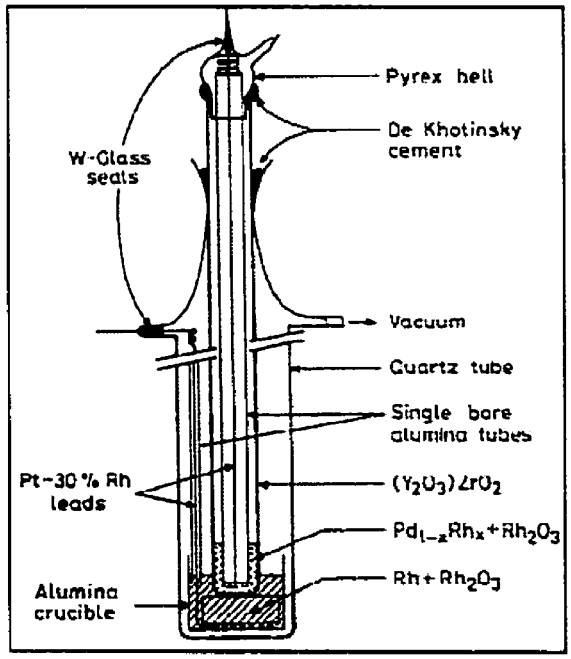

Figure 14. Schematic diagram of a galvanic cell.[43]

The results take the form of plots of E (in volts) versus temperature for each alloy composition, as shown in Figure 15.

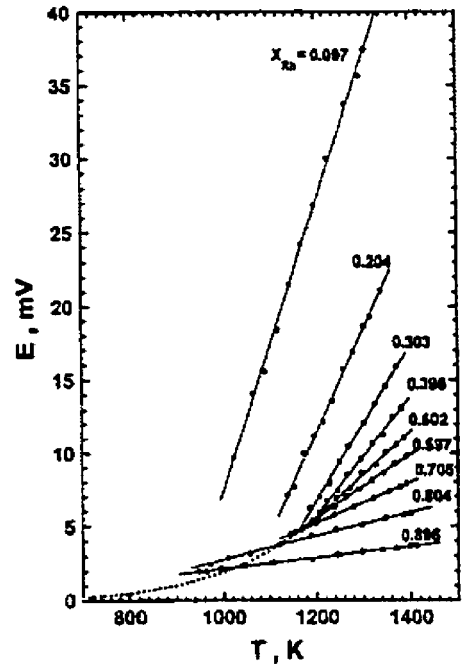

Figure 15. Sample set of results for emf measurements for Pd-Rh alloys.[43]

The emf, corresponding to the virtual oxygen transfer, reaction (11), is given by equation (12):

$$O_{2(alloy-side\ 2)} \xrightarrow{4\Im} O_{2(pure\ Rh-side\ 1)} \tag{11}$$

$$E = \frac{-RT}{4\Im} \ln\left[\frac{(P_{O_2})_1}{(P_{O_2})_2}\right] \tag{12}$$

Combining the previous concepts, the activity of the rhodium (a_{Rh}) is directly related to the emf by equation (13)[43]:

$$-3\Im E = \Delta\overline{G}_{Rh} = RT \ln a_{Rh} \tag{13}$$

From the temperature dependence of the activity, the partial enthalpy and entropy for Rh can be computed. By using the Gibbs-Duhem equation, the corresponding properties for Pd can be derived. This leads to a thermodynamic model describing the solution behaviour of the solid in the Pd-Rh system, in the range of temperatures where continuous solid solutions can be expected, as shown in Figure 16.[44] The form of the equation is similar to that shown in Table 1 for the liquid phase of the Sn-Bi system (small positive deviations from ideal behaviour).

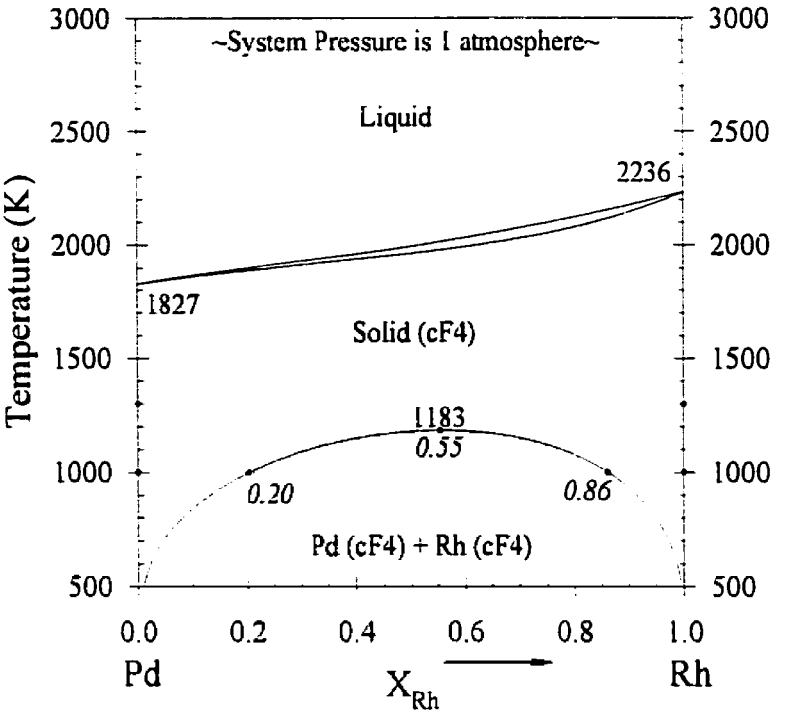

Figure 16. Pd-Rh phase diagram.[44]

Gibbs energy isotherms for the Pd-Rh system at 1000K and 1300K are shown in Figure 17. Notice that in Figure 17a), the miscibility gap depicted on the phase diagram is defined by the common tangent to the cF4-phase.

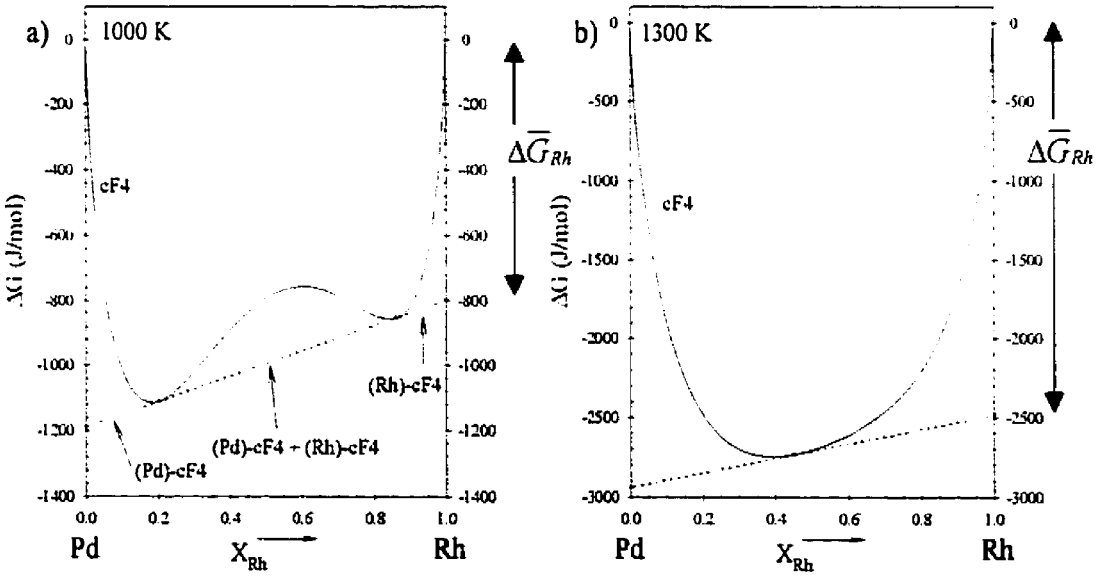

Figure 17. Gibbs Energy Isotherms for the Pd-Rh System at 1000K and 1300K.

3.4 Vapour Pressure Techniques

Vapour pressure measurements provide another way of measuring a relative partial molar Gibbs energy. Since the temperatures involved in most metal system investigations are relatively high and the partial pressure of the most volatile component is typically low, it is quite appropriate to employ ideal gas behaviour in the following way:

$$\Delta\overline{G}_i = \overline{G}_i - G_i^\circ = RT\ln\left[\frac{P_i}{P_i^\circ}\right] = RT\ln[a_i] \qquad (14)$$

This experimental approach of gathering Gibbs energy data is limited to systems where there is only one component that is a substantial contributor to the vapour phase and also when the molecular weight of the volatile species is not in question. Fortunately for most metals, the dominant vapour species is usually monatomic.

In the transpiration or transport technique, an inert gas is passed through or over a condensed sample such that the partial pressure of the vapour is taken to be in equilibrium with the condensed phase.[45-47] The mass transport is monitored through the weight loss of the condensed phase or through the weight gain of a cold finger or trap that is positioned downstream. The vapour species are condensed and analysed with a suitable technique. A simple transpiration apparatus is presented at Figure 18.[46] Such an apparatus would be used for the determination of the vapour pressures of solids. Care must be taken to ensure that the flow of the carrier gas is slow enough for equilibrium to be reached but also fast enough to render insignificant any diffusion of the vapour downstream to the cold trap. Material depletion is another factor: material evaporated from the condensed system must not affect the overall composition to a significant extent.

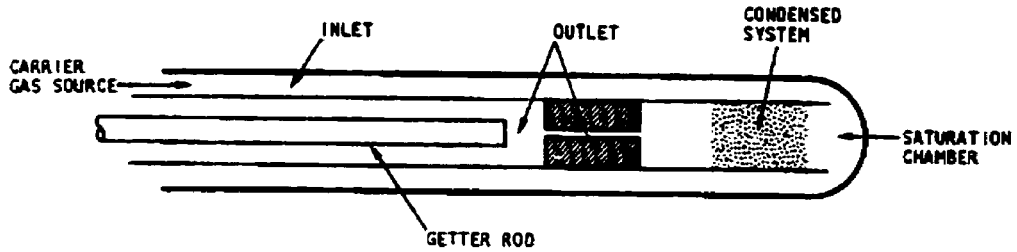

Figure 18. Simple high temperature transpiration apparatus, after Norman and Winchell.[46]

In principle the transpiration technique could be applied to the Mg-Si system

mentioned in Section 2. The measurements for a particular composition and temperature would give, in effect, a point on the vapour phase boundary in Figure 7. The collection of sufficient data of this type yields the relative partial molar Gibbs energy of Mg in the liquid phase as a function of temperature. By the application of the Gibbs-Duhem equation, the corresponding relative partial molar Gibbs energy for Si could be derived. The Gibbs energy of mixing could then be found, which becomes the basis for the computation of the phase diagram for Mg-Si, by the lowest common tangent methodology.

The modern embodiment of vapour pressure methods employs superior detection systems. One such arrangement, appropriate to systems with quite low volatility, for example Pd-Rh, is shown in Figure 19.[48] A Knudsen cell made of inert material encloses the alloy under study. The effusing vapour is detected by mass spectrometric means.

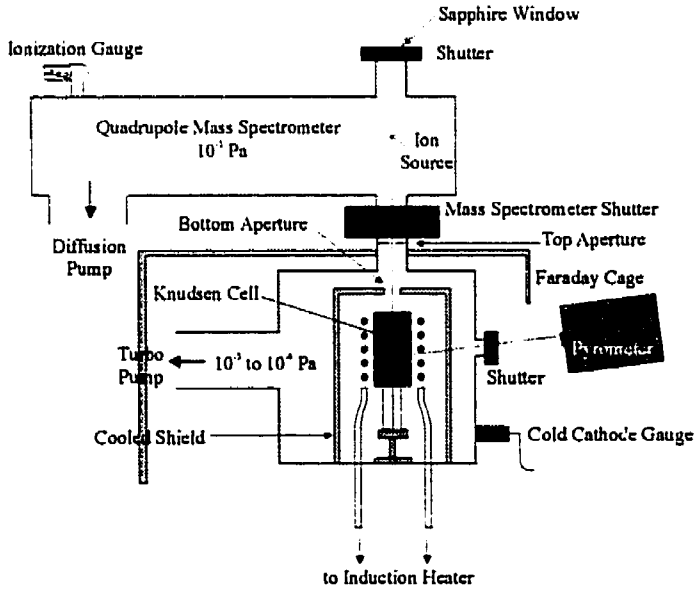

Figure 19. Mass Spectrometer/Knudsen Cell apparatus.

The signal provides a partial pressure for each isotope of Pd, the more volatile element. The relative isotopic abundance of vapour species is used to refine the computation of the total partial pressure expressed in equation (14) as P_i. Typical data for a Pd-Rh alloy is shown in Figure 20 for both pure Pd and an alloy.[48] The displacement of the two lines provides a measurement of the activity of Pd in the alloy. In this case, it is slightly greater than the atomic fraction of Pd in the condensed phase.

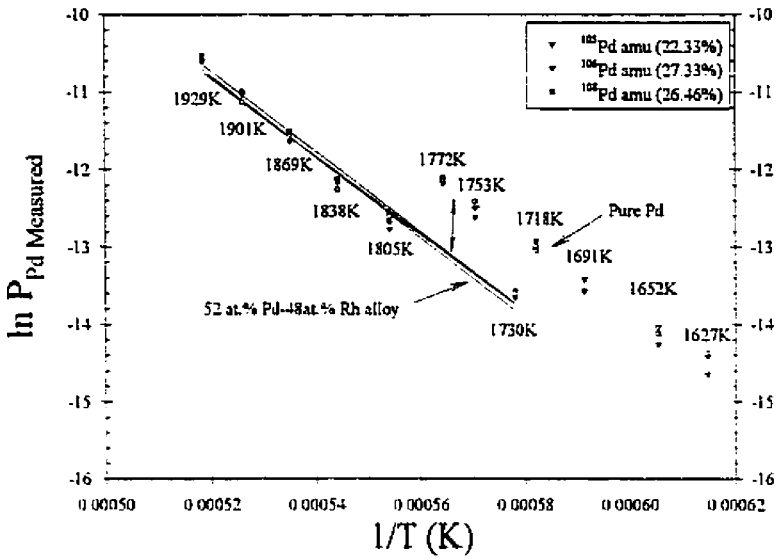

Figure 20. Typical partial pressure data for a 52 at.%Pd-48 at.% Rh alloy.[48]

When the volatility is much higher, continuous recording thermogravimetric (TGA) means could be employed in the detection system. Vapour effusing from the hot Knudsen cell, swept away by an inert carrier gas, condenses in a cold trap downstream. The mass loss from a chamber (in which saturation must be demonstrated) provides the partial pressure using classical effusion equations.

3.5 Thermal Methods

In the simplest embodiment of this technique, the temperature is continuously recorded during slow heating or cooling. Phase changes that take place alter the rate of temperature change with time due to the heat effects associated with the transformation. The most effective use of this technique is the study of liquid-solid transformation since the phase transformations are generally not sluggish in metallic systems.

A variation on this technique is differential thermal analysis (DTA) in which two thermocouples are used. One is placed in a non-transforming reference material and the other in the system under study. A spike occurs in the temperature difference when a transformation is encountered. An example of the application of DTA is shown in Figure 21 for a Pd-Rh alloy.[48]

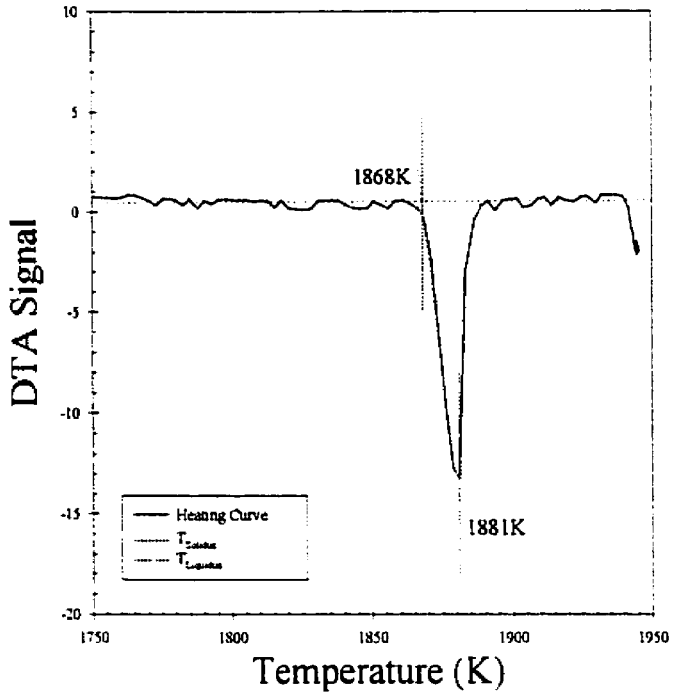

Figure 21. A typical DTA curve for an 80 at.% Pd- 20 at.% Rh alloy. The extrapolated onset indicates that the solidus temperature is 1868K.[48]

Thermal analysis techniques put emphasis on the temperature at which a transformation commences, since the temperature at which a transformation concludes may not be reliably detected. For example, the solidus in a cooling binary metal system is usually effected by segregation associated with the slow diffusion of the components in the crystallizing solid. An advancement on DTA is the quantification of the thermal effect associated with the peak height/area, which leads to scanning calorimetry.

3.6 Scanning Calorimetry

There are the two principal types of differential scanning calorimeters (DSC). Boersma[49] introduced the heat flux DSC in 1955, and Watson and O'Neill[50,51] developed the Power Compensation DSC in 1963. With these two techniques it is possible to make quantitative measurements of the transformation energy, which had not been possible with traditional DTA.[52] In the heat flux method, the heat of tranformation is detected as a temperature difference with respect to an adjacent reference material.[49] In the power compensating method, the power required to keep the sample and the reference material at the same temperature is recorded.[50]

A typical result for a Sn-Bi alloy is shown in Figure 22. It can be seen from this figure that the onset of transformation temperature is calculated as 412K. This corresponds to the eutectic temperature in Figure 2.[53]

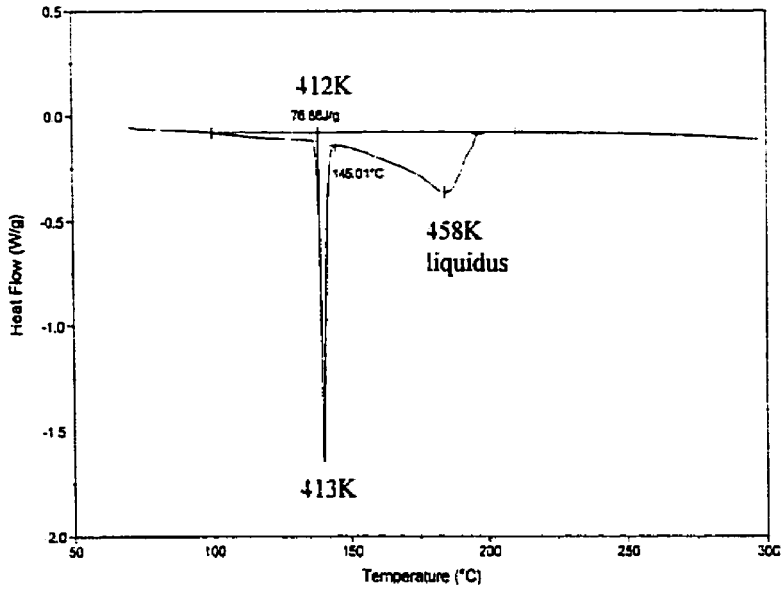

Figure 22. DSC heating profile for a 20at.%Bi in Sn alloy. The eutectic temperature, determined by the extrapolated onset, is 412K; and the liquidus temperature is 458K.[53]

Table 3 summarizes the experimental work[53] for several additional compositions of Sn-Bi alloys. For the process of raising the temperature from 373K to 483K, with all accompanying phase changes, a measured ΔH is recorded in Table 3. This can be compared to the calculated ΔH, determined from Figure 4. The difference in the values is typical of the precision that may be expected from scanning calorimetry as it applies to alloy transformations that involve melting.

Table 3. Thermal effects for fusion of Sn-Bi Alloys.

X_{Bi}	Measured ΔH (J/mol)	Calculated ΔH (J/mol)	Difference (J/mol)	%
0.197	10103	10496	-393.1	-3.75
0.312	10890	11074	-184.3	-1.66
0.390	11846	11455	391.7	3.42
0.475	11623	11863	-240.0	-2.02

The liquidus temperatures were determined from the return to baseline, as marked

in Figure 22. These are shown in Table 4 and compared with modelled temperatures from Figure 2.

Table 4. Liquidus Temperatures for the Sn-Bi Alloys.

X_{Bi}	Observed Liquidus (K)	Modelled Liquidus (K)
0.197	458	463
0.312	430	438
0.390	425	421
0.475	423	424

Heating rates affect the results obtained using scanning calorimetry to a limited degree. An indication of this is shown in Table 5

Table 5. Effect of Heating Rate on Observed Parameters for Sample 3 (X_{Bi} = 0.39)

Heating Rate C°/min	Observed Eutectic (K)	Observed Liquidus (K)
10	412.6	425.2
2	412.6	424.1
0.5	412.5	423.7

Figure 23 shows a series of representative DSC curves for various alloy compositions in a more complex binary system.[54] At compositions indicated by 1, 2, and 3 (pure B; compound D with a congruent melting temperature; and the eutectic composition, respectively), the curves have very sharp peaks, indicating a temperature invariant phase change. However, alloys 4 to 8 have melting ranges as indicated on the phase diagram. For alloys 4 to 7, the eutectic and peritectic temperatures correspond to the extrapolated onset of the sharp peak, but the heating curve does not return almost immediately to the baseline, which is similar to the behaviour shown in Figure 22. In the cases where the cooling path only passes through one region of solid plus liquid (alloys 4, 6, and 7) the DSC curve moves towards a second extreme value, which corresponds to the liquidus temperature. For curve 5, the eutectic and peritectic temperatures are indicated by sharp peaks, and the liquidus by the final peak.

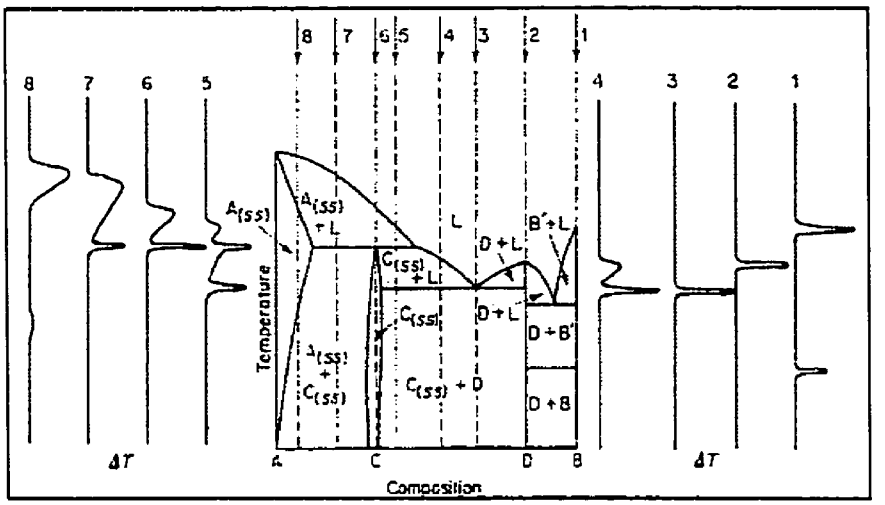

Figure 23. The A-B phase diagram, showing representative DSC curves for various alloy compositions, indicated by the dashed lines.[54]

Alloy 8 in Figure 23 has a path that does not cross a eutectic or peritectic tie line. Instead, the solidus is determined by where the extrapolated onset occurs for the larger peak, with the liquidus occurring at the peak extremity, similar to that of Figure 21. The temperature of the solvus is approximately indicated by the bump in the DSC curve at the lower temperature, however, the heat effect here is rather small and difficult to resolve. X-ray diffraction (Section **3.2**) would be better suited to determining the placement of this phase boundary.

3.7 Calorimetric Methods

Although enthalpies of formation and heat capacity do not deal directly with the subject matter of this review, these data do bear upon phase transformations since they contribute to the development of Gibbs energy equations (e.g., Mg_2Si in Table 2).

The calorimetric techniques applied to metallurgy are well reviewed in Materials Thermochemistry.[45] Practical considerations in reaction calorimetry are well reviewed in Chapter 3A of Physicochemical Measurements in Metals Research.[55] With respect to solution calorimetry, the IUPAC has recently published a book by that title which describes the various techniques now commonplace today. In particular, Chapter 6 of Solution Calorimetry[56] gives an excellent review of this technique as applied to metallurgical systems.

4. Multi-Component Systems

Phase equilibrium in systems of contemporary commercial interest almost invariably involve more than two components. Experimental studies, based upon methods outlined in the previous sections, are being guided to a considerable degree, by predictive methods based upon the substantial body of thermodynamic data collected over the past 25 years.[6,57] Two types of multi-component systems may be distinguished; those involving a solvent element with several dilute solutes, and those covering the extremes of composition for all components.

When there is a dominant metal component, the simplifications associated with dilute solution thermodynamics may be applied. There are many systems of commercial interest that fall into this category. Principally, a knowledge of the Henrian activity coefficient for each solute and its variation with temperature is required. In many cases, it is sufficient to treat the activity coefficients as independent of composition within the limited range of concentration for those dilute solutes and to ignore, as an initial approximation, the effect of one solute on the activity coefficient of another.

Consider the case of a lead battery electrode alloy containing small concentrations of Ca, Sn, and Ag. The activity of Ca dissolved in Pb can be found by formulating the solubility product from the Gibbs energy of formation of $CaPb_3$, via reaction (15), and using a portion of the binary Pb-Ca phase diagram, shown in Figure 24.[58-60]

$$Ca + 3Pb \rightleftharpoons CaPb_3 \qquad (15)$$

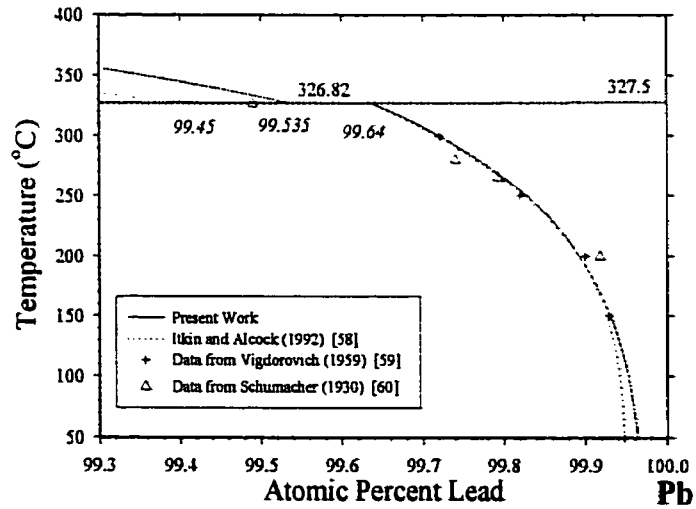

Figure 24. The Ca-Pb phase diagram, enlarged at the Pb-rich side.

Taking the activity of Pb in the lead rich phase to be the atom fraction, the activity coefficient of Ca can be found for alloys saturated with $CaPb_3$, using equation (16).

$$\Delta G^{\circ} = RT\ln[X_{Ca}] + RT\ln[\gamma_{Ca}] + RT\ln[X_{Pb}] \qquad (16)$$

The Henrian activity may be found, broadly speaking, in a similar manner for the other solutes. The phase equilibrium involving the possible coexistence of the lead-rich solid solution with intermetallic phase(s) can now be calculated. Figure 25 depicts the compositions of all the possible intermetallic phases involving the four elements in question.

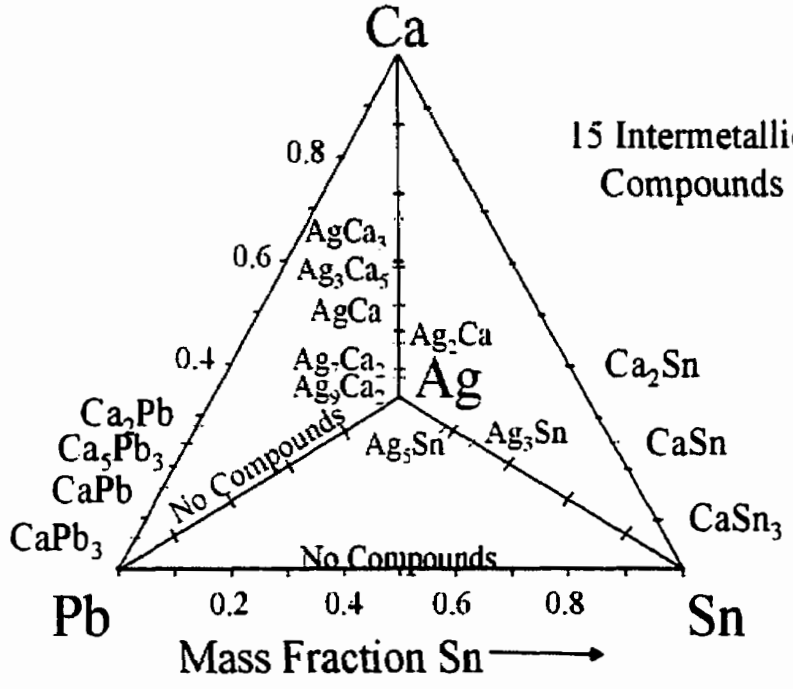

Figure 25. The Pb-Sn-Ca-Ag quaternary system.

With the Gibbs energy of formation for these nearly stoichiometric phases, there is sufficient data to develop the phase diagram in the lead-rich corner by Gibbs energy minimization methods incorporated into computational software.[61] The estimated phase equilibrium is depicted in Figure 26 for 523K.

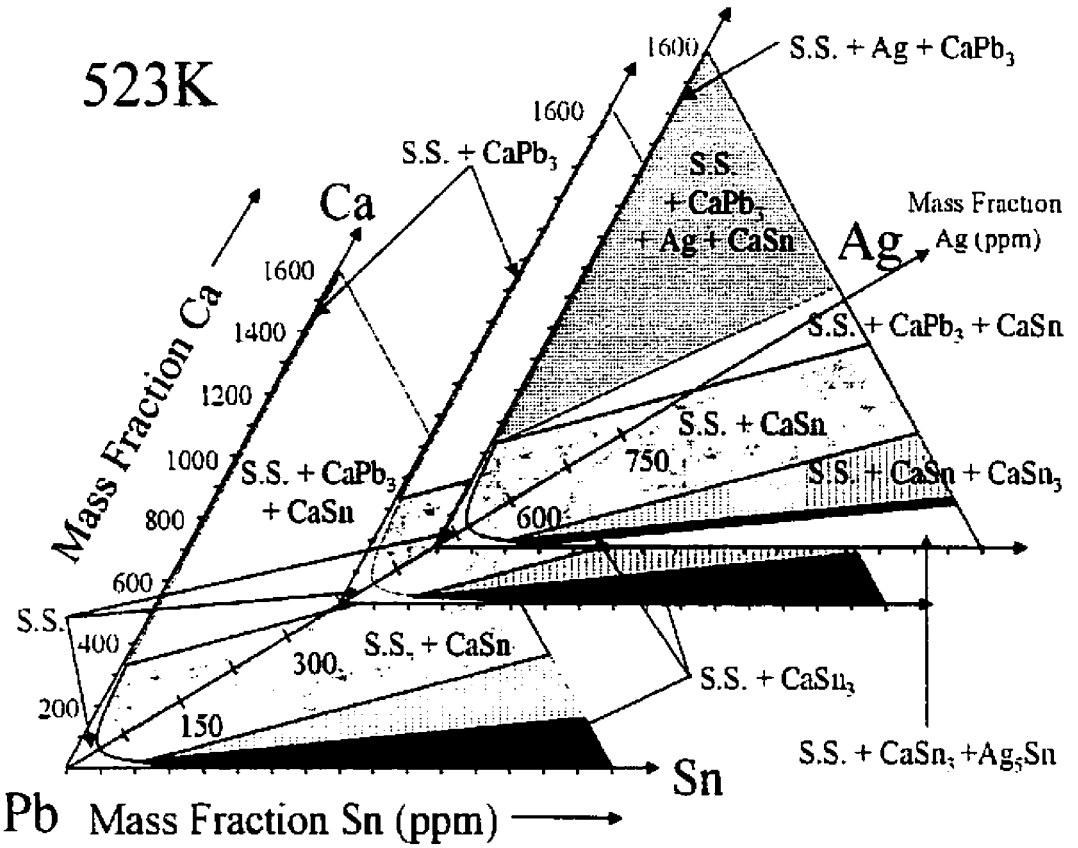

Figure 26. Ternary slices from Pb-Sn-Ca-Ag quaternary, at constant levels of Ag.

It is also possible to compute, for a series of temperatures, the most stable phase assemblages and identify the critical temperatures associated with the appearance of new phases. These results are organized in Table 6, with the asterisks indicating the critical temperature for the appearance of a new phase. This information, made possible by bringing together a variety of experimental measurements, modelling the binary phase diagrams to rationalize those data, and using modern computational tools, is revealing in terms of the genesis of phases. In particular, it is important to know from which phase (solid or liquid) a particular intermetallic precipitate first appears. This effects the metallurgical microstructure with a consequent impact on mechanical properties.

Table 6. The mass percentages of the various phases for the slow cooling of a Pb alloy with 600 ppm Ca, 6000 ppm Sn, and 500 ppm Ag.

Temperature (K)	Liquid Solution	$CaSn_3$	Solid Solution	Ag_5Sn
773.0	100			
727.0	100	*		
599.5	99.475	0.525	*	
589.7	0	0.564	99.436	
534.0	0	0.592	99.408	*
473.0	0	0.593	99.365	0.042

When the phase equilibrium is to be developed for a system where dilute solution simplifications do not apply, interpolation methods may be used to estimate Gibbs energies based upon experimental studies for the binary metal combinations. Consider the case of Mo-Pd-Rh-Ru alloys. This system is encountered as metallic inclusions in spent nuclear fuel. The Kohler interpolation scheme[62], which will here suffice to represent others[63], proportionally weights, from each binary system, the contribution of the thermodynamic property of interest, as given in equation (17).

$$G_p^E = (1-X_X)^2 G_a^E + (1-X_Y)^2 G_b^E + (1-X_Z)^2 G_c^E \qquad (17)$$

This is illustrated in Figure 27, where the Gibbs energy of mixing at point ***p***, is estimated from the known Gibbs energy of mixing at points ***a***, ***b***, and ***c***, which are found by extending line segments from each of the corners on the ternary diagram, to the opposite binary system.

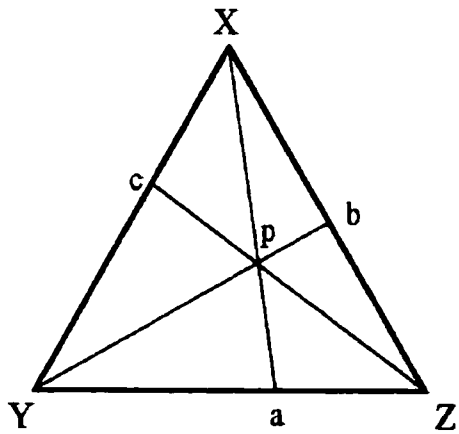

Figure 27. Representation of Kohler Interpolation; the property (G^E) at *p* may be estimated from a knowledge of properties at compositions *a*, *b*, and *c*.[62]

The form of the interpolation scheme for the excess Gibbs energy is consistent with regular solution behaviour of each component dissolved in a solvent involving a fixed proportion of the other two components. This methodology has been found suitable in many cases as a predictive approach to provide ternary and multi-component excess solution property estimates when no experimental data exists. As experimental data is gathered for the multi-component system, departure terms may be added to the basic interpolation. These terms (usually only 1 or 2 are necessary or justified) take the form of products of all mole fractions raised to different powers times a temperature dependent coefficient. The correction terms vanish in the binary subsystems. Figure 28 shows the phase equilibrium for the ternary faces of the quaternary alloy at 2000K computed using this interpolation method.[64] The phase boundaries for the Pd-Rh binary alloy may be compared with the binary diagram in Figure 16.

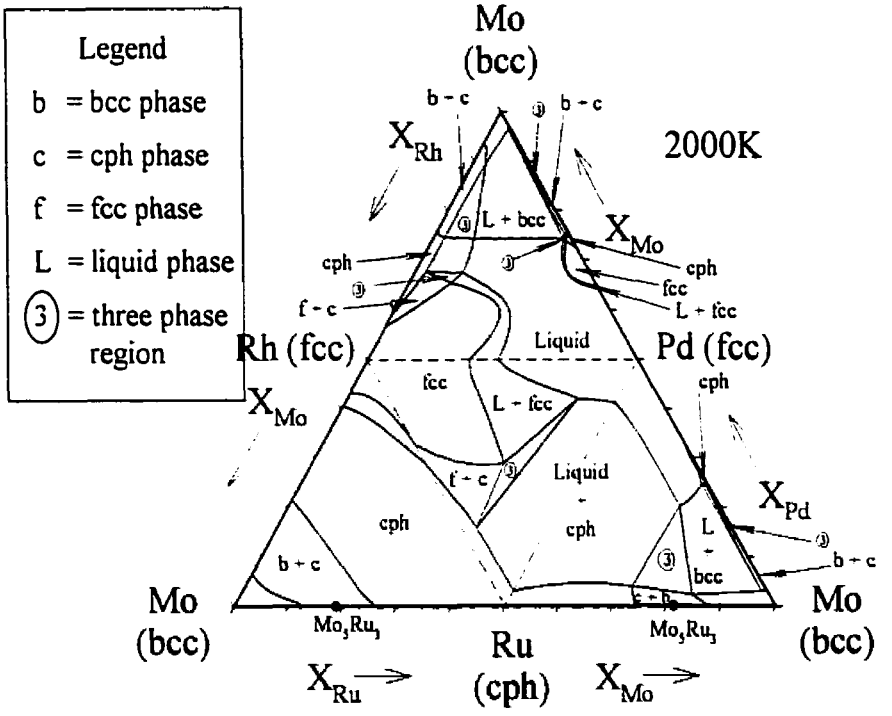

Figure 28. Four ternary diagrams for the Mo-Pd-Rh-Ru System at 2000K.[64]

5. Conclusion

Phase equilibrium expressed using temperature-composition binary phase diagrams has long been recognized as central to metallurgical processing. For the greater part of the last century, the development of these diagrams was almost exclusively undertaken as an experimental activity involving the substantial use of microscopy, X-ray diffraction, and thermal analysis. The widespread use of computers in the past 25 years awakened a more fundamental understanding of the thermodynamic principles of phase diagram construction that was dormant for a century. This has enabled experimental measurements of thermodynamic solution properties to contribute in greater measure to phase diagram development and assist in major international assessment programs leading to comprehensive compilations. This modelling/assessment process not only gives assurance that the phase diagram is self-consistent and respects underlying principles, but also provides a degree of confidence in extrapolating to conditions of temperature, pressure, or composition that may be difficult to study experimentally. Furthermore, phase equilibrium information, stored as self-consistent equations for the thermochemical properties of the phases, permits diagrams with unconventional axes to be rapidly developed for special applications. With the addition of interpolation equations to forecast multi-component solution behaviour from the binary sub-systems, likely phase diagrams for systems with many components can now be calculated to help focus future time-consuming experimental effort.

6. References for Appendix A

1. M. Hansen. Der Aufbau der Zweistofflegierungen, Springer Verlag, Berlin (1936).
2. M. Hansen. Constitution of Binary Alloys, McGraw-Hill, New York, NY (1958).
3. R.P. Elliott. Constitution of Binary Alloys-First Supplement, McGraw-Hill, New York, NY (1965).
4. F.A. Shunk. Constitution of Binary Alloys-Second Supplement, McGraw-Hill, New York, NY (1969).
5. W.G. Moffatt. The Handbook of Binary Phase Diagrams, G.E. Company, Schenectady, NY (1977).
6. T.B. Massalski. Binary Alloy Phase Diagrams, **1 & 2**, ASM, Metals Park, OH (1986).
7. J.W. Gibbs. In The Collected Works of J. Willard Gibbs, **Volume I - Thermodynamics**, Yale University Press, New Haven, CT, 55-371 (1957).
8. L.S. Darken. Thermodynamics in Physical Metallurgy, ASM, Cleveland, OH (1952).
9. H.A.J. Oonk. Phase Theory: The Thermodynamics of Heterogeneous Equilibria, Studies in Modern Thermodynamics 3, Elsevier Scientific, Amsterdam (1981).
10. D.R. Gaskell. Introduction to Metallurgical Thermodynamics, McGraw-Hill, New York, NY (1981).
11. C.H.P. Lupis. Chemical Thermodynamics of Materials, Elsevier Science Publishers, Amsterdam (1983).
12. W.T. Thompson, B.R. Davis. 29th International Metallographic Society, Pittsburgh, PA, (1996).
13. L. Kaufman. Phase Stability in Metals and Alloys, P.S. Rudman, J. Stringer, R.I. Jaffee, (Eds.), McGraw-Hill, New York, NY (1967).
14. A.T. Dinsdale. *CALPHAD* **15**, 317-425 (1991).
15. H. Okamoto. *J. Phase Equilibr.* **12**, 623-643 (1991).
16. H.E. Boyer, T.L. Gall (Eds.). Metals Handbook Desk Edition, ASM, Metals Park, OH (1985).
17. K. Chu-Kun, L Zu-Xiang, Y. Dong-Sheng. High Temperature Phase Equilibria and Phase Diagrams, Pergamon Press, Beijing (1990).
18. G.L. Kehl. The Principles of Metallographic Laboratory Practice, McGraw-Hill, New York, NY (1949).
19. C.W. Haworth, W. Hume-Rothery. *Inst. Met. J.* **87**, 265-272 (1958-59).

20. J.I Goldstein, D.E. Newbury (Eds.). Scanning Electron Microscopy and X-Ray Microanalysis: A Text for Biologists, Materials Scientists, and Geologists, 2nd Edition, Plenum Press, New York, NY (1992).

21. "Metallography and Microstructures", ASM Handbook, **9**, ASM International, Materials Park, OH (1985).

22. "Materials Characterization", ASM Handbook, **10**, ASM International, Materials Park, OH, 473-476 (1986).

23. ASTM Standard E 1508-98, "Standard Guide for Quantitative Analysis by Energy-Dispersive Spectroscopy," ASTM (1999).

24. E. Lifshin. "Electron Microprobe Analysis", In Characterization of Materials E. Lifshin (Ed.) Volume **2B** of Materials Science and Technology, R.W. Cahn, P. Haasen, E.J. Kramer, (Eds.). VCH, New York, NY, 351-421 (1994).

25. J.J. Freil, V.A. Greenhut. *Adv. Mater Processes* **156**, 28-32 (1999).

26. W.L. Bragg. The Crystalline State: Volume 1 – General Survey, W.H. Bragg, W.L. Bragg (Eds.) G.Bell and Sons, London, 268-286 (1933).

27. A. Taylor. X-ray Metallography, John Wiley & Sons, New York, NY (1961).

28. R. Jenkins, R.L. Snyder. Introduction to X-ray Powder Diffractometry, Chemical Analysis Volume 138, John Wiley & Sons, New York, NY (1996).

29. B.D. Cullity. Elements of X-Ray Diffraction 2nd edition, Addison-Wesley, Reading, MA. (1978).

30. R.E. Reed-Hill. Physical Metallurgy Principles, Van Nostrand, Princton, NJ (1964).

31. G. Kostorz. "Chapter 12. X-ray and Neutron Scattering" In Physical Metallurgy, 3rd edition, (R.W. Cahn, P. Haasen, Eds.), North-Holland, New York, NY (1983).

32. P. Nash (Ed.). Phase Diagrams of Binary Nickel Alloys, ASM International, Materials Park, OH (1991).

33. A. Taylor, R.W. Floyd. *Inst. Met. J.* **80**, 577-587 (1951-52).

34. R.A. Young (Ed.). The Rietveld Method, IUCr Monographs on Crystallography 5, Oxford University Press, Oxford, (1993).

35. J.I. Pérez-Landazábal, M.L. Nó, G. Madariaga, J. San Juan. *J. Appl. Crys.* **30**, 107-113 (1997).

36. J.I. Pérez-Landazábal, M.L. Nó, G. Madariaga, V. Recarte, J. San Juan. *Acta Mater.* **48**, 1283-1296 (2000).

37. Collaborative Computational Project Number 14 - Single Crystal and Powder Diffraction, Homepage is: http://www.ccp14.ac.uk/main.htm

38. L.B. McCusker, R.B. Von Dreele, D.E. Cox, D. Louër, P. Scardi. *J. Appl. Crys.* **32**, 36-50 (1999).

39. A. Mikula. High Temperature Materials Chemistry IX, K.E. Spear (Ed.), The Electrochemical Society, Inc., 187-193 (1997).

40. W.T. Thompson, A. Leung, D.G. Hurkot. *Can. Metal. Q.* **12**, 421-433 (1973).

41. O.J. Kleppa. *Am. Chem. Soc. J.* **71**, 3275-3280 (1949).

42. O.J. Kleppa. *Am. Chem. Soc. J.* **72**, 3346-3352 (1950).

43. K.T. Jacob, S. Priya, Y. Waseda. *J. Phase Equilibr.* **19**, 340-350 (1998).

44. R. Gürler, L.A. Cornish, J.N. Pratt. *J. Alloys Compd.* **191**, 165-168 (1993).

45. O. Kubaschewski, C.B. Alcock, P.J. Spencer. Materials Thermochemistry, 6th edition, Pergamon Press, 64-112 (1993).

46. J.H. Norman P. Winchell. In Physicochemical Methods in Metal Research, Part I, R.A. Rapp (Ed.), in Series "Techniques of Metals Research," **IV**, John Wiley and Sons, New York, (1970).

47. J.L.Margrave. "Vapour Pressure". In Physicochemical Measurements at High Temperatures, J.O'M. Bockris, J.L. White, J.D. Mackenzie (Eds.), Butterworths, 225-246 (1959).

48. M.H. Kaye. Ph.D. Thesis, *in preparation.*

49. S.L. Boersma. *Am. Cer. Soc. J.* **38**, 281-284 (1955).

50. E.S. Watson, M.J. O'Neill, J. Justin, N. Brenner. *Anal. Chem.* **36**, 1233-1238 (1964).

51. M.J. O'Neill. *Anal. Chem.* **36**, 1238-1245 (1964).

52. C. Sykes. *Proc. Roy. Soc.* **148**, 422-446 (1935).

53. From unpublished experimental work performed by M.H. Kaye.

54. W. Gutt, A.J. Majumdar. "Chapter 29- Phase Studies". In Differential Thermal Analysis, **2**, R.C. Mackenzie (Ed.), Academic Press, London, 79-117 (1972).

55. J.S.L. Leach. In Physicochemical Methods in Metal Research, Part I, R.A. Rapp (Ed.), in Series "Techniques of Metals Research," **IV**, John Wiley and Sons, New York, (1970).

56. K.N. Marsh, P.A.G. O'Hare (Eds.). "Solution Calorimetry" In Experimental Thermodynamics, **IV**, IUPAC Chemical Data Series #39, Blackwell Scientific Publications, London (1994).

57. *J. Phase Equilibr.* (previously *Bull. Alloy Phase Diagrams*), ASM, Metals Park, OH.

58. V. Itkin, C.B. Alcock. *J. Phase Equilibr.* **13**, 162-169 (1992).

59. V.N. Vigdorovich, A. Ya. Nashel'skii. *Russ. J. Inorg. Chem.* **4**, 922-925 (1959).

60. E.E. Schumacher, G.M. Bouton. *Met. Alloys* **1**, 405-409 (1930).

61. C.W. Bale, A.D. Pelton, W.T. Thompson. "Facility for the Analysis of Chemical Thermodynamics - User Manual 2.1", Ecole Polytechnique de Montreal / McGill University, (1996).

62. F. Kohler. *Monats. Chem.* **91**, 738-740 (1960).

63. P. Chartrand, A.D. Pelton. *J. Phase Equilibr.* **21**, 141-147 (2000).

64. M.H. Kaye, W.T. Thompson, B.J. Lewis. *Trans. Am. Nucl. Soc.* **79**, 123-125 (1998).

APPENDIX B - SELECTED TERNARY PHASE DIAGRAMS FROM LITERATURE

For comparison purposes, ternary phase diagrams proposed by other researchers are shown here. Figure B-1 shows Mo-Pd-Rh at 1973K, by Paschoal et al.[1].

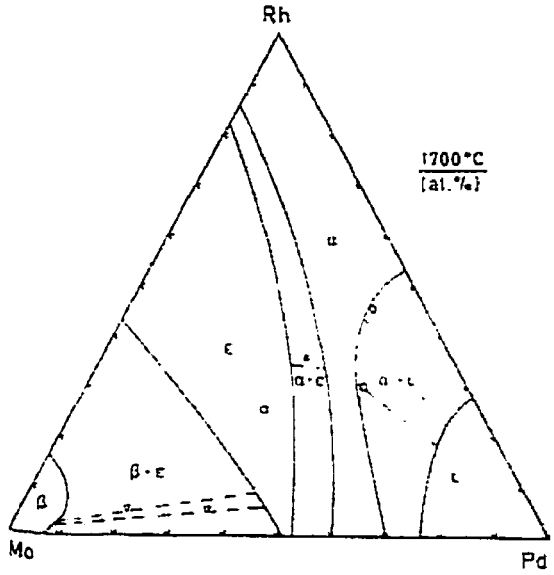

Figure B-1. Mo-Pd-Rh from Paschoal et al.[1]. The temperature is 1973K.

The ternary diagram for Pd-Rh-Ru at 1973K, by Paschoal et al.[1] is shown in Figure B-2.

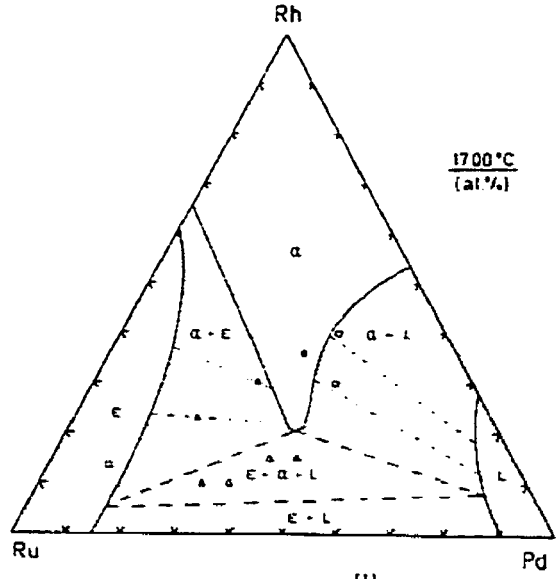

Figure B-2. Pd-Rh-Ru from Paschoal et al.[1]. The temperature is 1973K.

The ternary diagram for Mo-Rh-Ru at 1973K, by Paschoal et al.[1] is presented in Figure B-3.

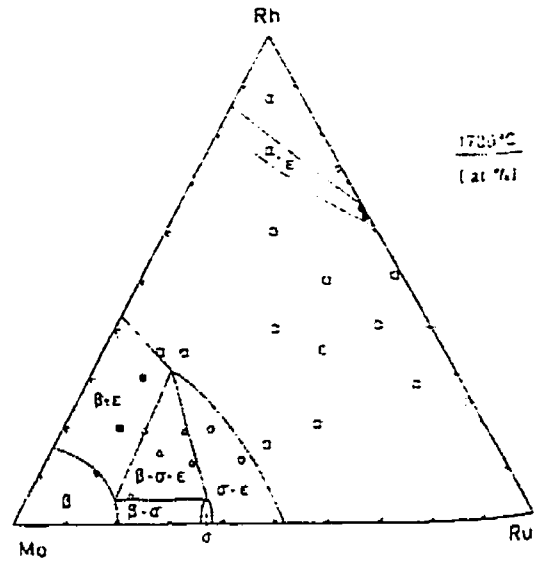

Figure B-3. Mo-Rh-Ru from Paschoal et al.[1]. The temperature is 1973K.

The ternary diagram for Mo-Pd-Ru at 1973K, by Paschoal et al.[1] is presented in Figure B-4.

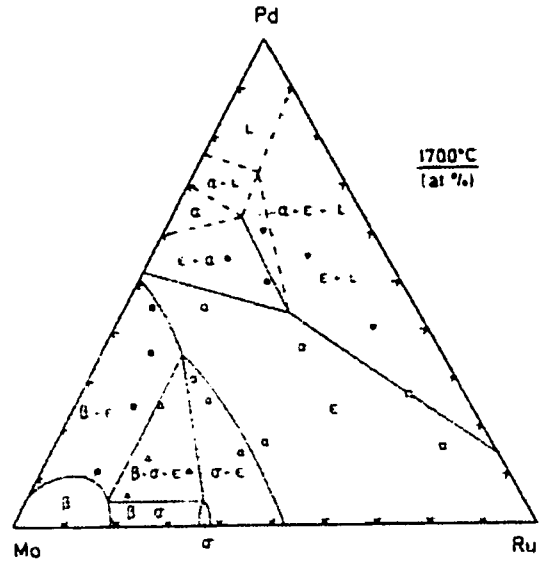

Figure B-4. Mo-Pd-Ru from Paschoal et al.[1]. The temperature is 1973K.

The ternary diagram for Mo-Pd-Rh experimentally determined by Gürler and Pratt[2], is shown in Figure B-5.

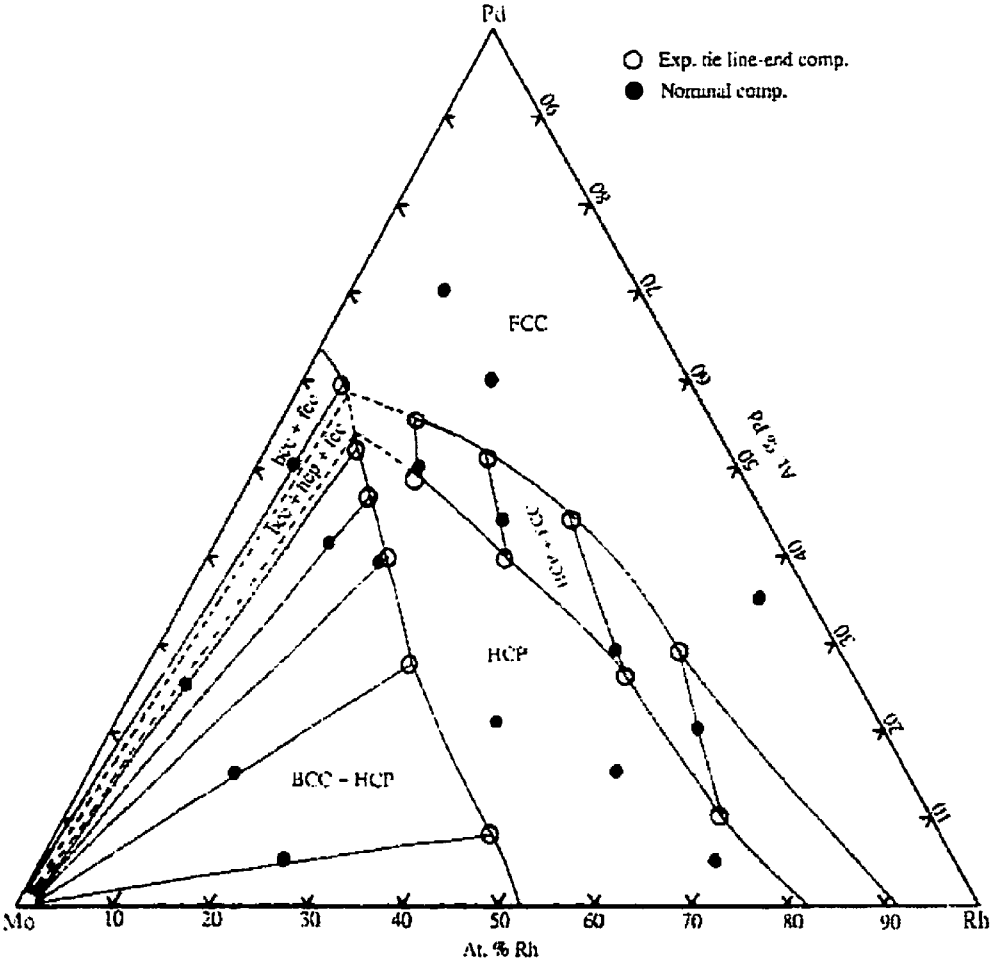

Figure B-5. Mo-Pd-Rh from Gürler and Pratt[2]. The temperature is 1373K.

References for Appendix B

1. J.O.A. Paschoal, H. Kleykamp, and F. Thümmler, "Phase Equilibria in the Quaternary Molybdenum-Ruthenium-Rhodium-Palladium System", *Zeitschrift Fuer Metallkunde*, **74** (1983), 652-664.

2. R. Gürler and J.N. Pratt, "A Constitutional Investigation of the Mo-Pd-Rh Ternary System at 1100°C", *Journal of Nuclear Materials*, **186** (1991), 39-46.

APPENDIX C - RESULTS FROM DTA EXPERIMENTS

The complete set of results for the differential thermal analysis measurements of Pd-Rh alloys is presented here.

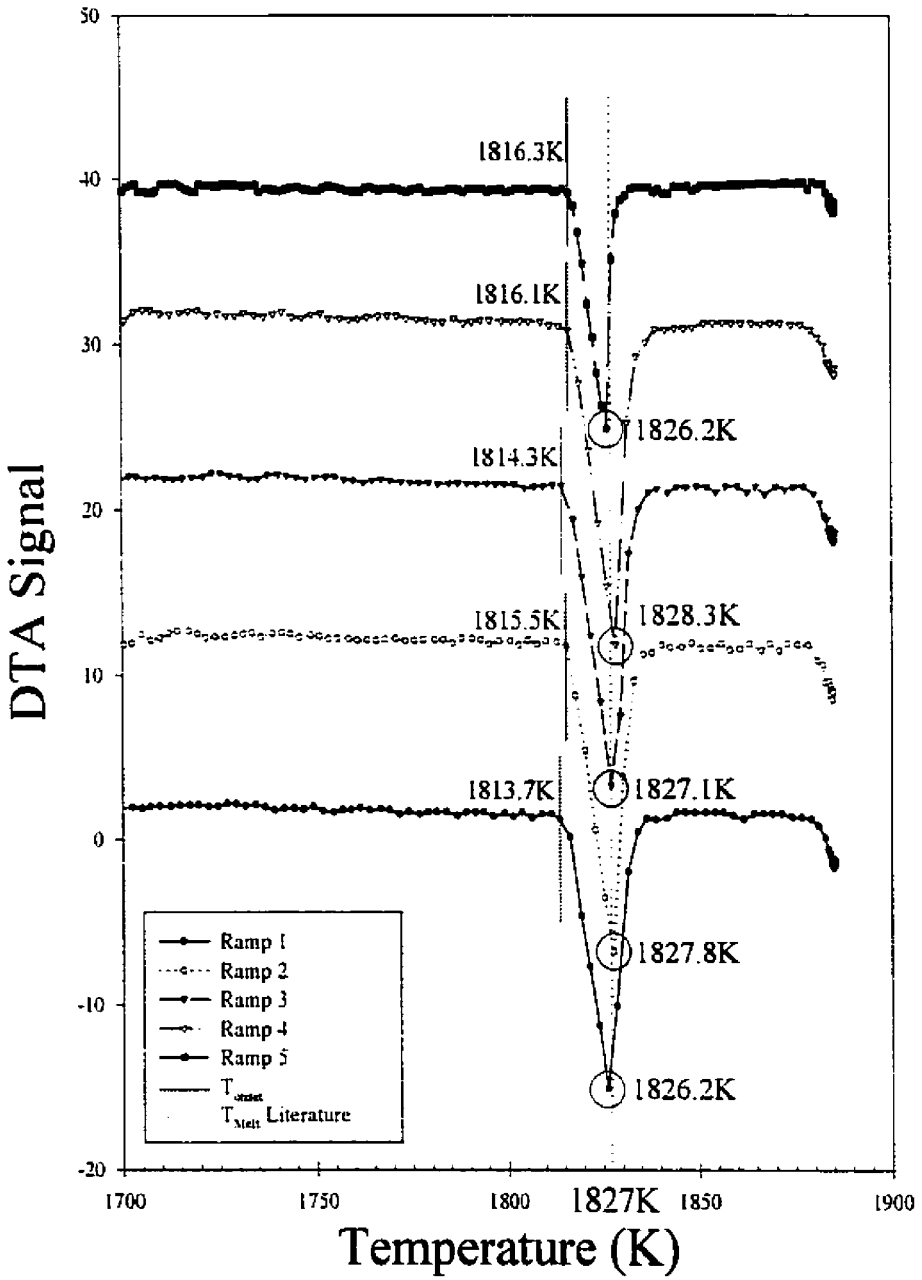

Figure C-1. DTA results for **Sample A- Pure Pd.** The average melting temperature is 1827.1K.

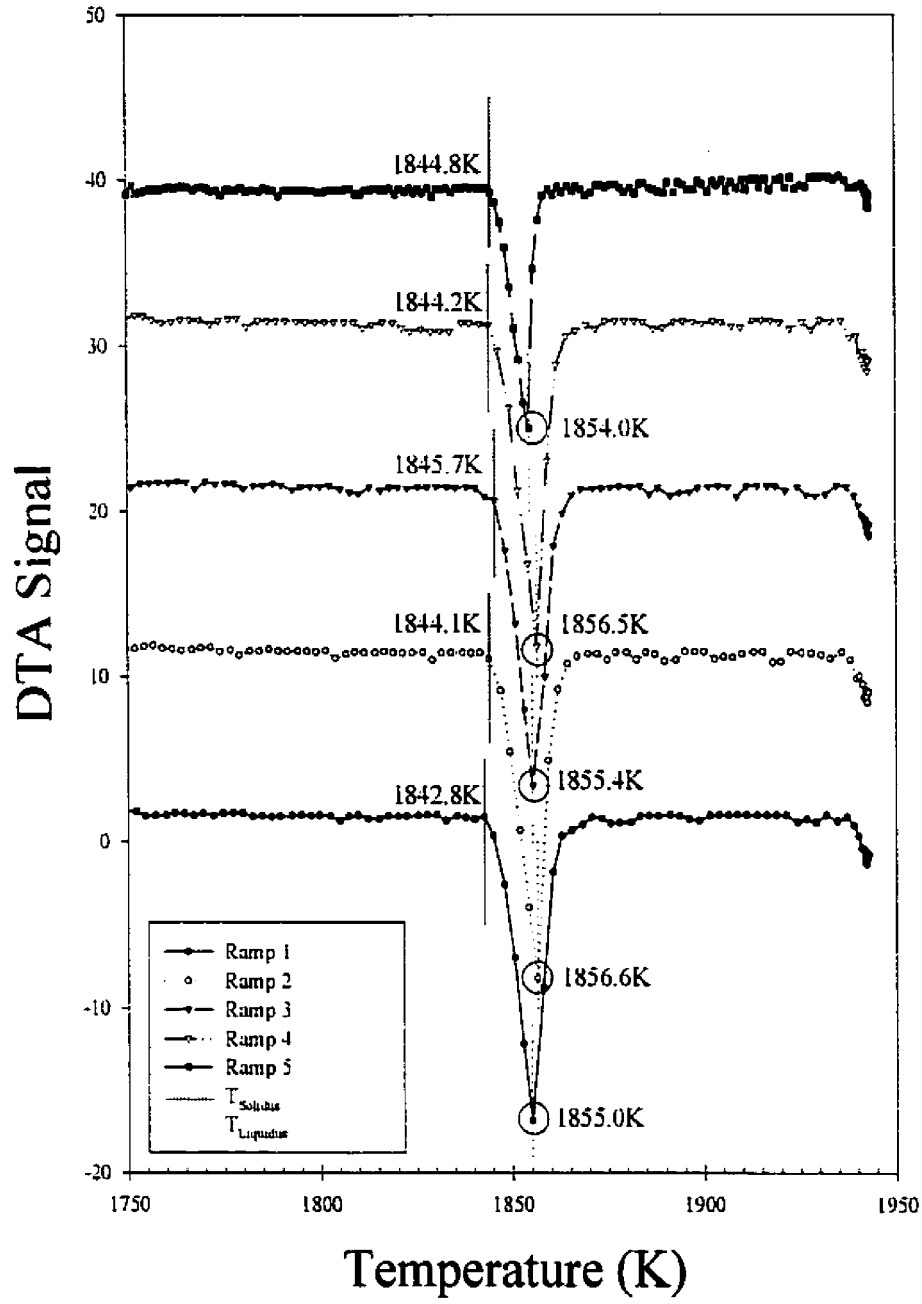

Figure C-2. DTA results for **Sample B- 88at.% Pd:12at.%Rh**.
The average solidus temperature is 1844K. The average liquidus temperature is 1856K.

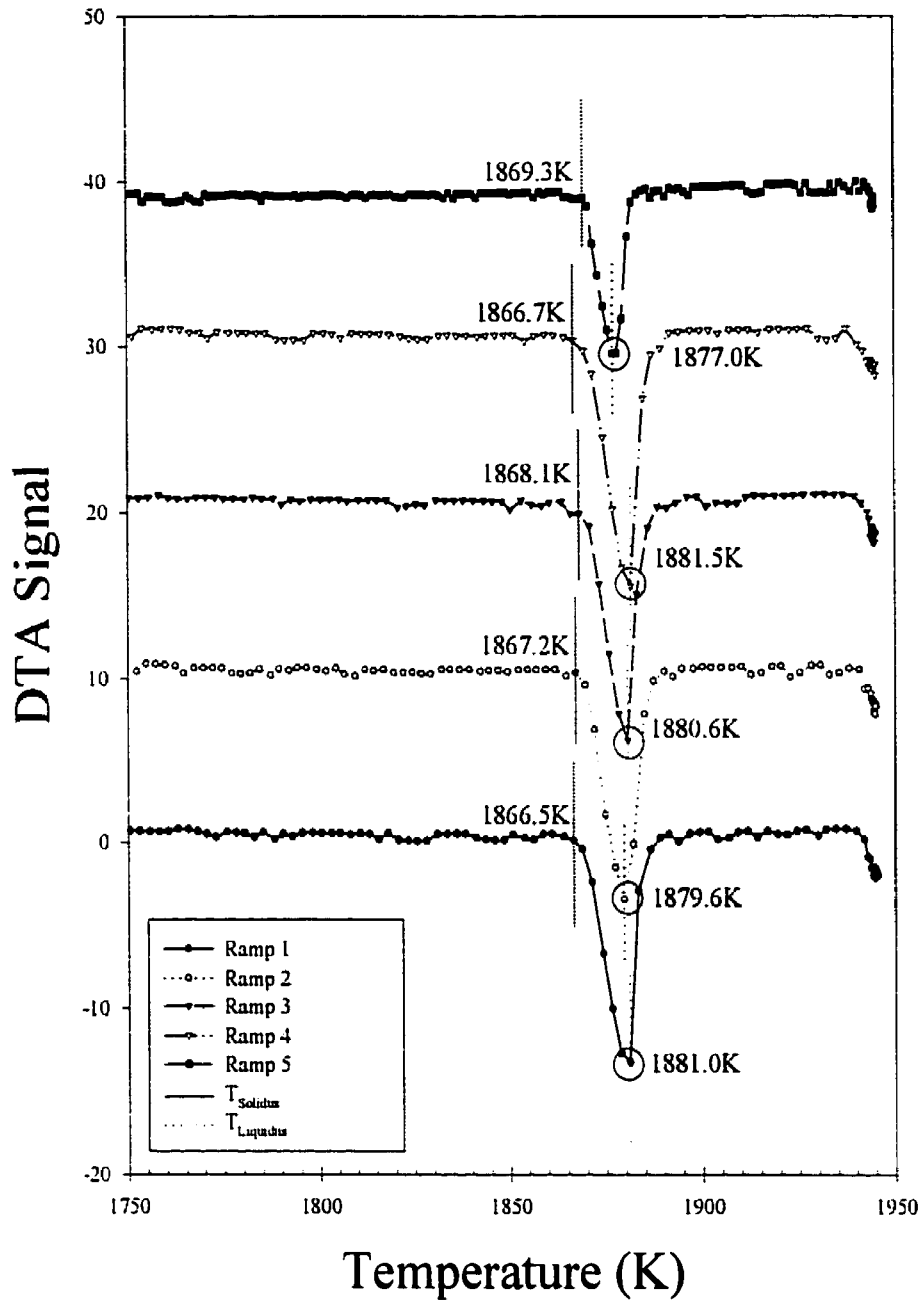

Figure C-3. DTA results for **Sample C- 80at.% Pd:20at.%Rh**.
The average solidus temperature is 1868K. The average liquidus temperature is 1880K.

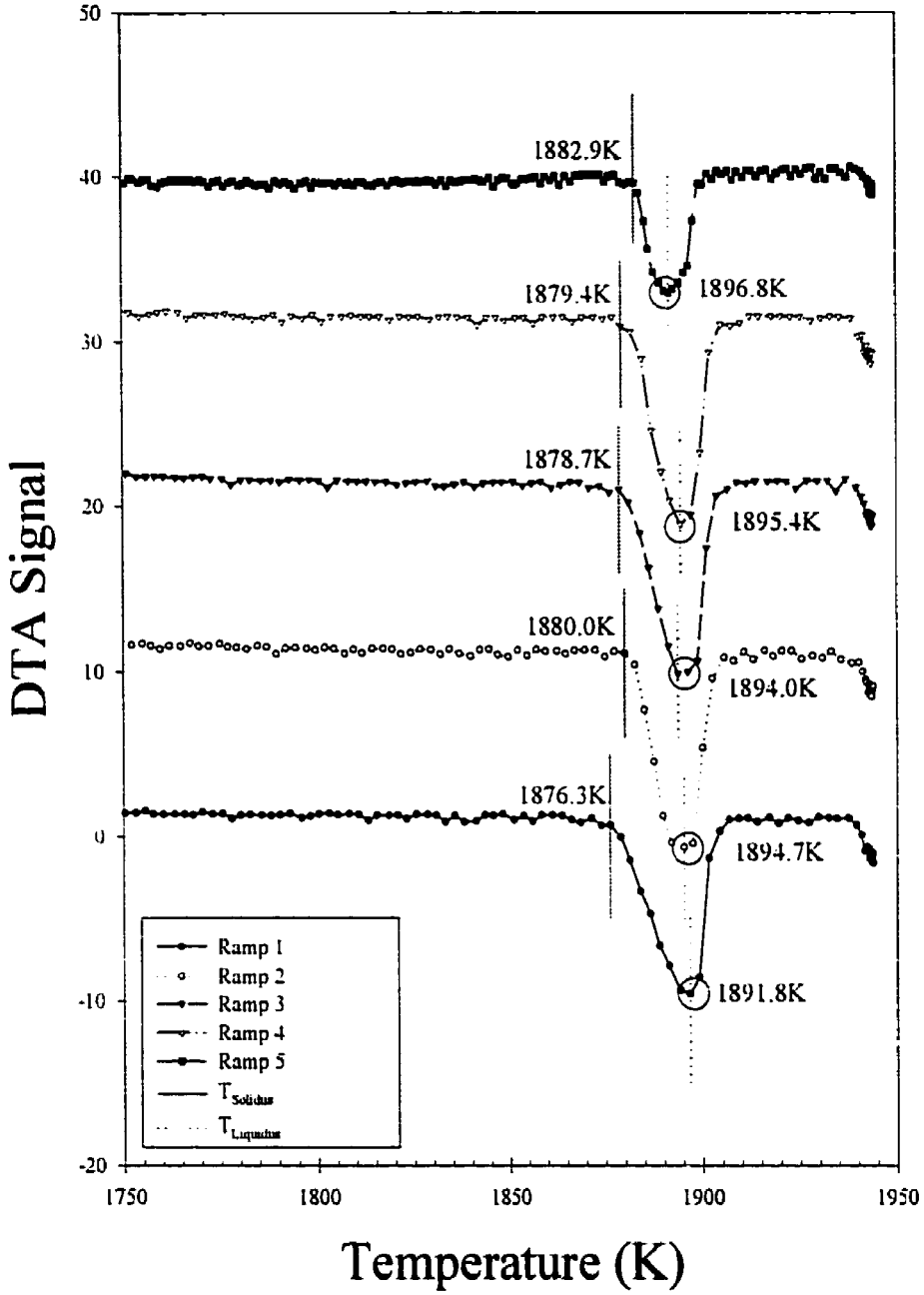

Figure C-4. DTA results for **Sample D- 74at.% Pd:26at.%Rh**.
The average solidus temperature is 1879K. The average liquidus temperature is 1895K.

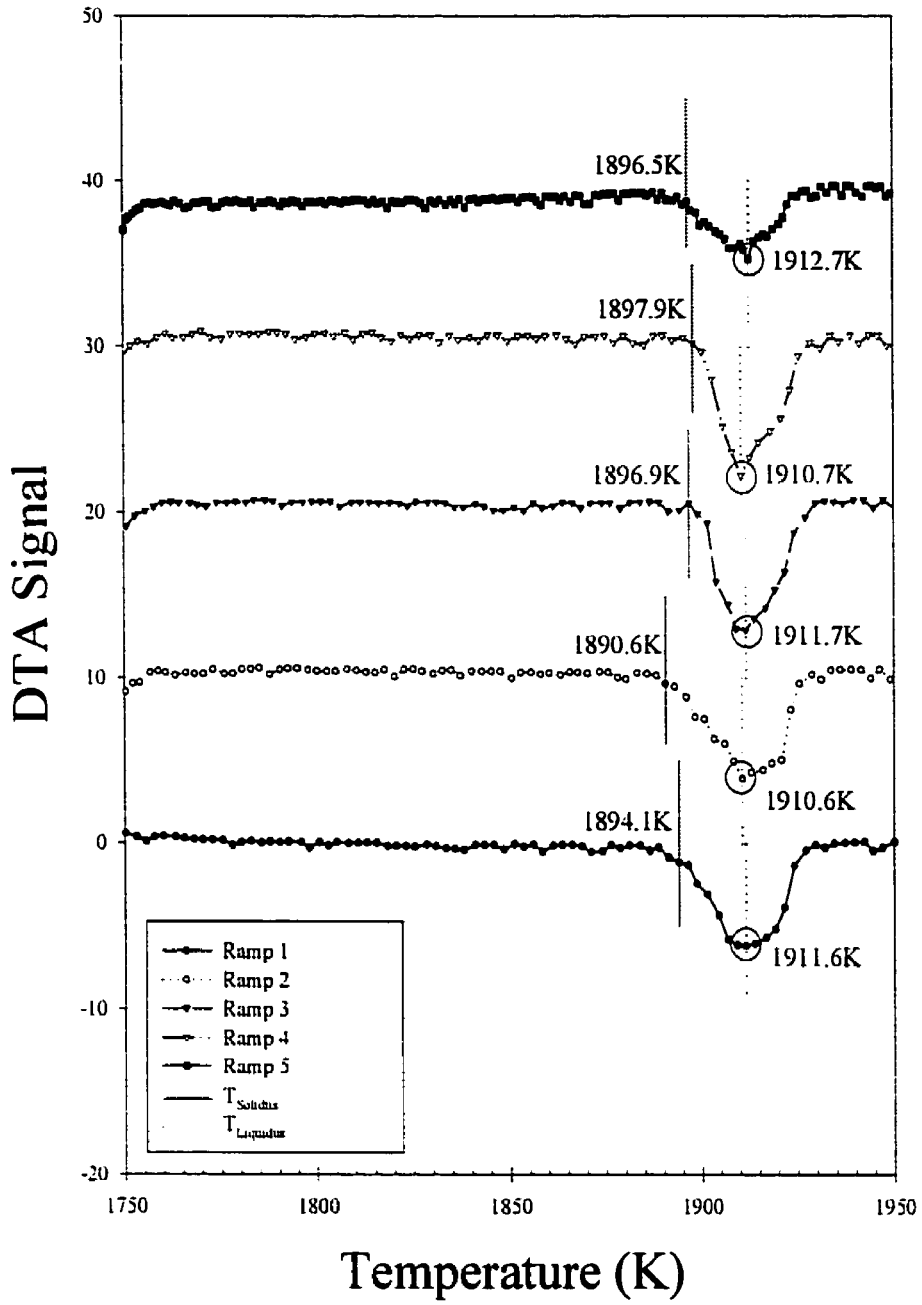

Figure C-5. DTA results for **Sample E- 69at.% Pd:31at.%Rh.**
The average solidus temperature is 1895K. The average liquidus temperature is 1911K.

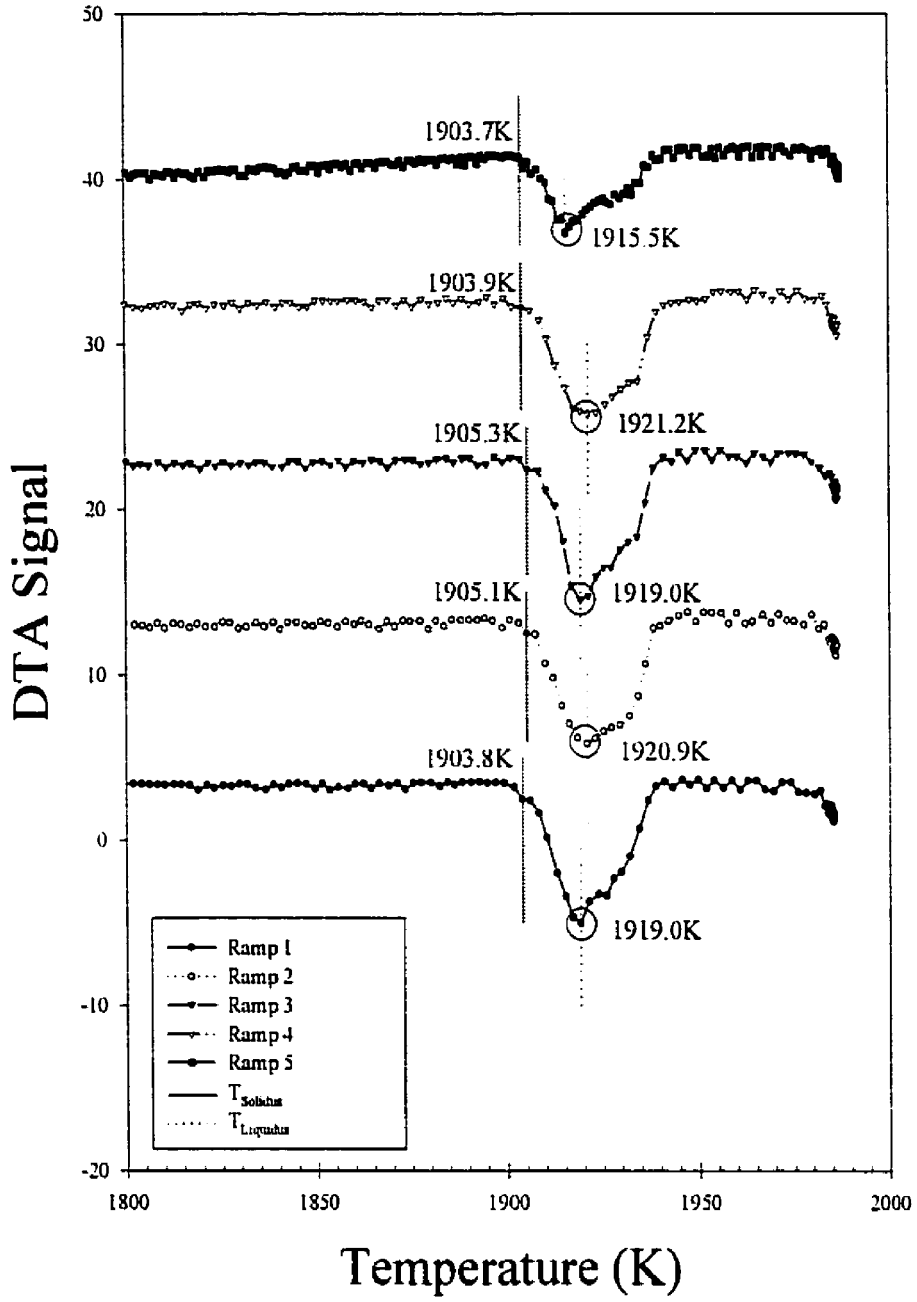

Figure C-6. DTA results for **Sample F- 64at.% Pd:36at.%Rh**.
The average solidus temperature is 1904K. The average liquidus temperature is 1919K.

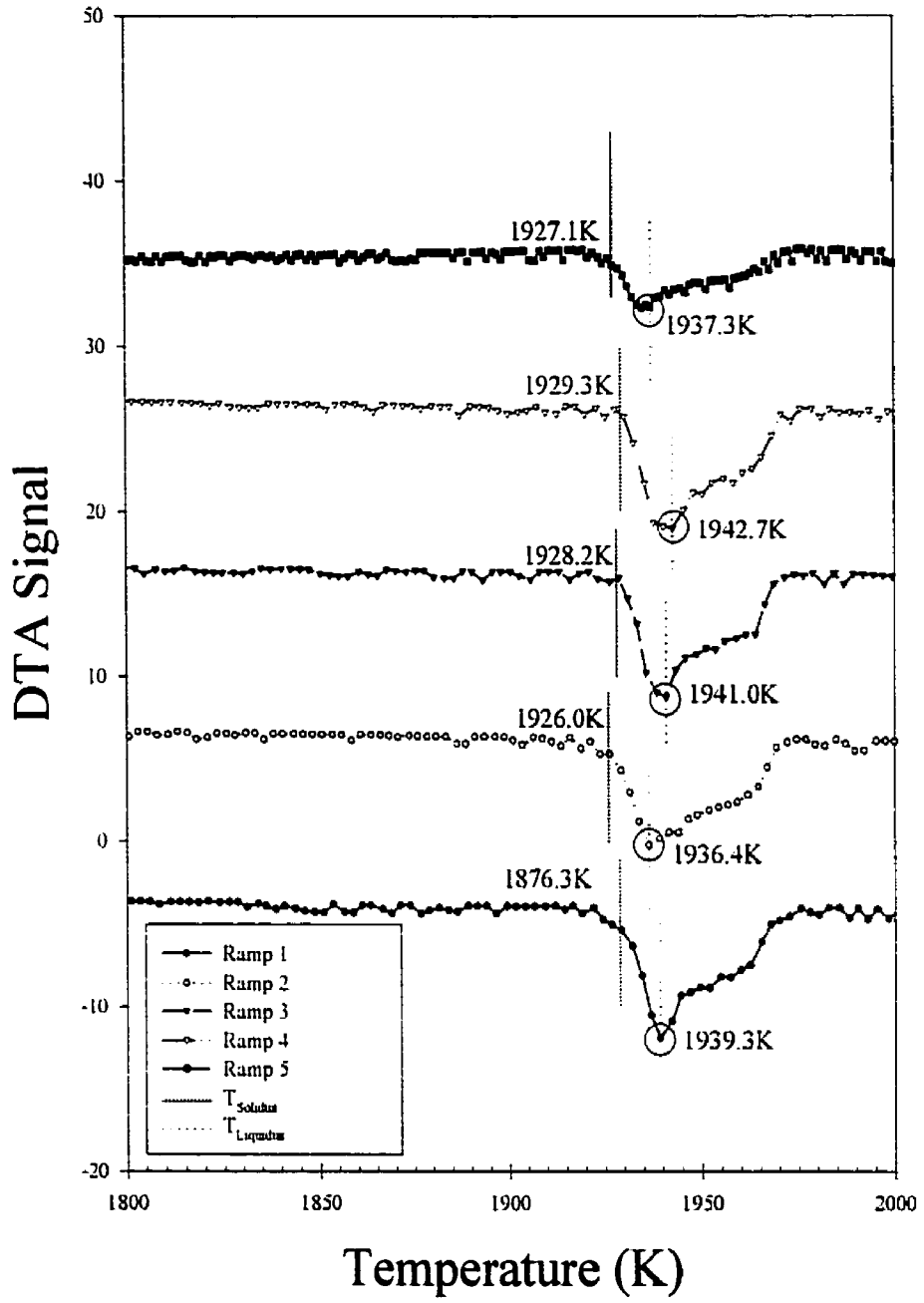

Figure C-7. DTA results for **Sample G- 59at.% Pd:41at.%Rh**.
The average solidus temperature is 1928K. The average liquidus temperature is 1939K.

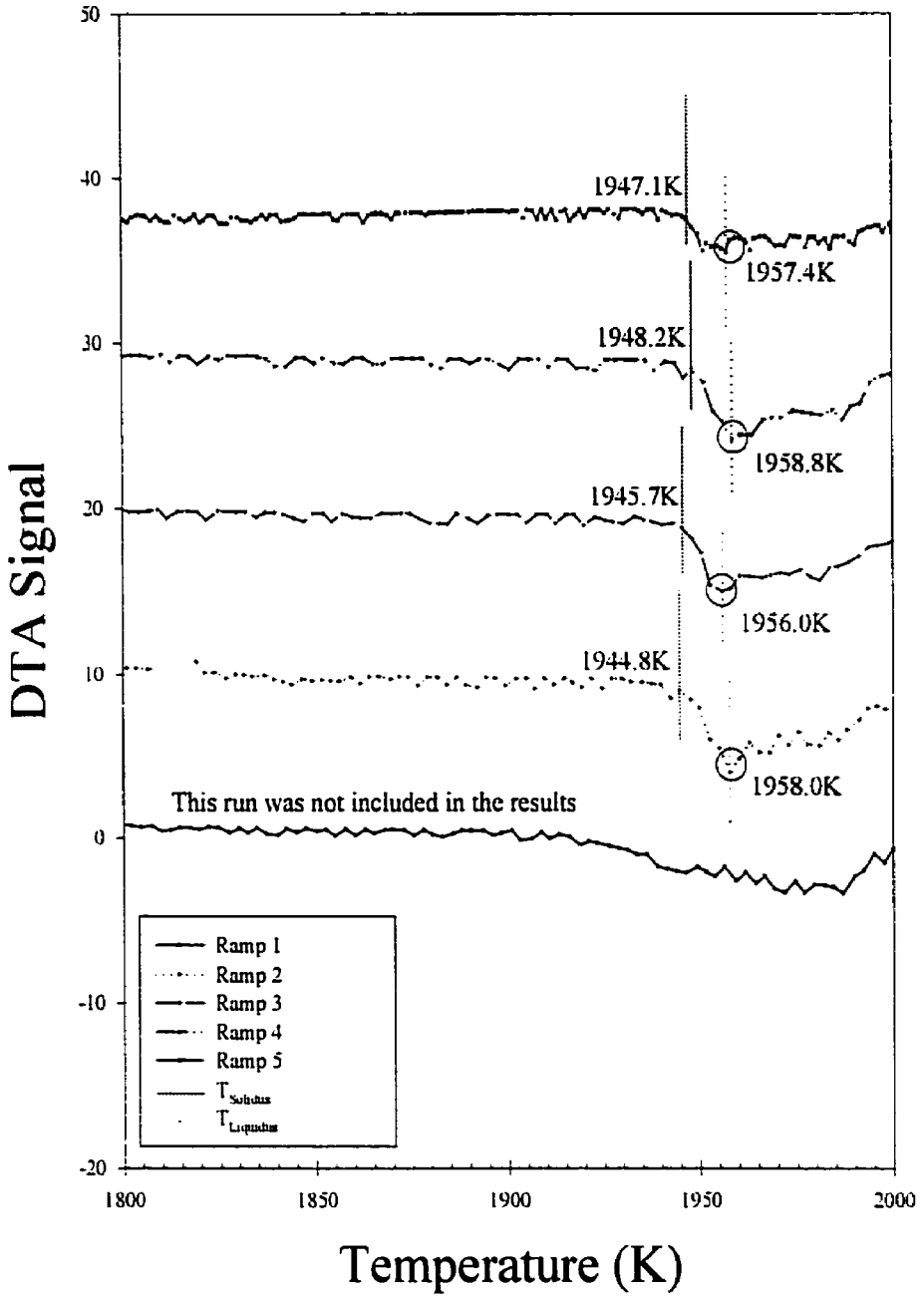

Figure C-8. DTA results for **Sample H- 53at.% Pd:47at.%Rh**.
The average solidus temperature is 1946K. The average liquidus temperature is 1958K.

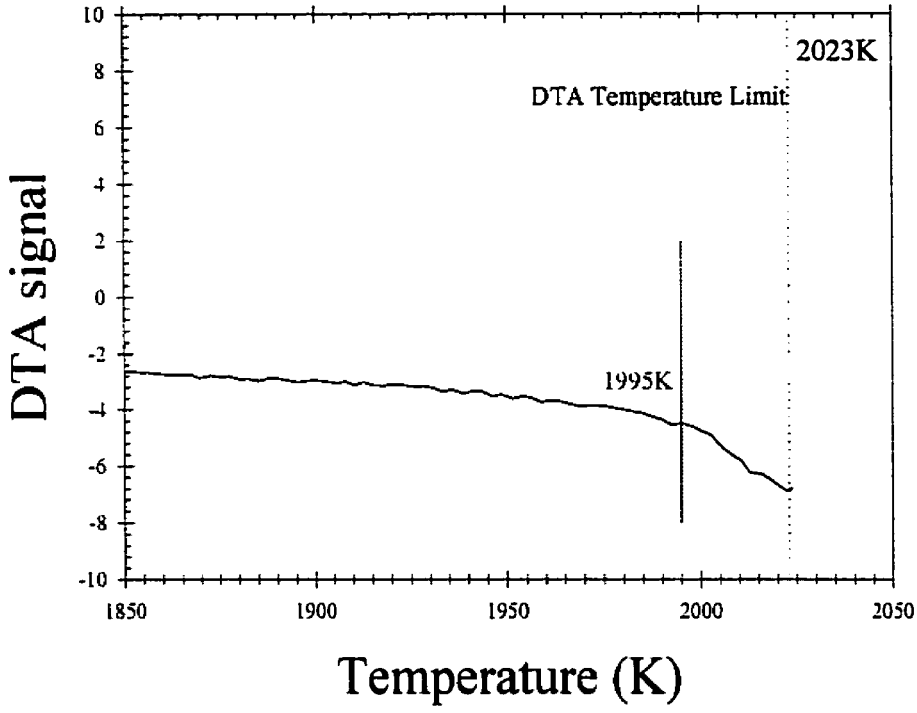

Figure C-9. DTA results for **Sample J- 34at.% Pd:66at.%Rh**.
The solidus temperature is approximately 1995K. The liquidus temperature is above the maximum operating temperature for the DTA.

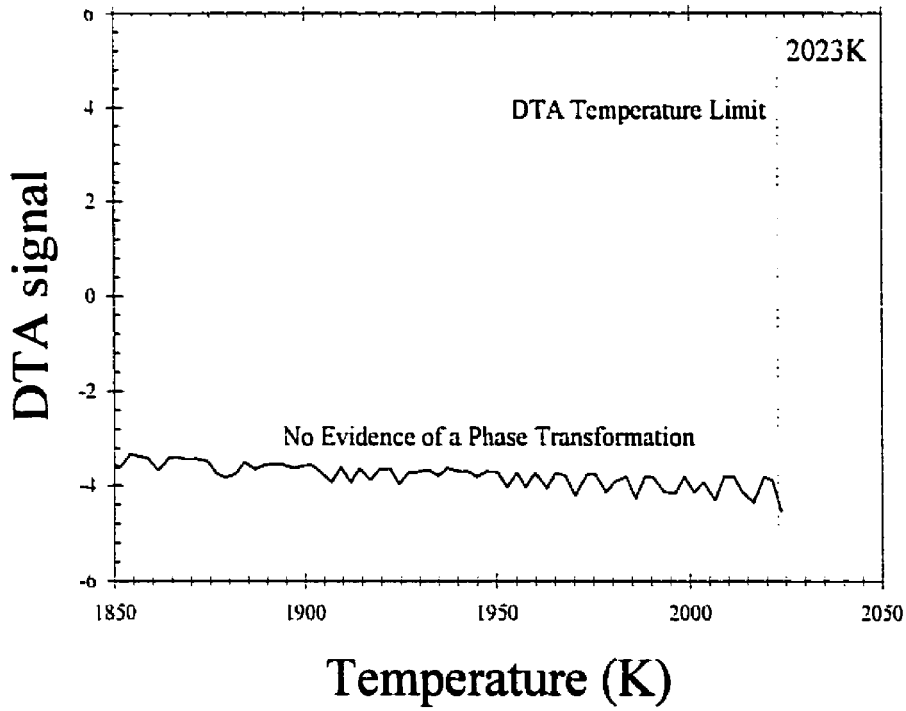

Figure C-10. DTA results for **Sample K- 19at.% Pd:81at.%Rh**.
The average solidus temperature is 1904K. The average liquidus temperature is 1919K.

APPENDIX D - DATA FROM KNUDSEN CELL/MASS SPECTROMETER WORK

The complete set of results for Samples 2-8 is presented here in tabular form. Note that the intensity, measured in counts, was derived from the maximum peak height in a 1amu band of the spectrum centred around the amu number for the isotope of interest. The results for Samples 2-8 are shown in Table D-1 through Table D-7.

Table D-1. Intensity (peak maximum) data for Sample 2.

Temperature (K)	^{102}Pd	^{104}Pd	^{105}Pd	^{106}Pd	^{108}Pd	^{110}Pd
1741	100	200	300	400	500	200
1799	300	200	700	900	800	300
1850	200	600	1200	900	1100	400
1893	200	800	2100	2000	1900	800
1922	200	1300	3000	2700	3200	1000
1953	300	1400	2600	3100	2700	1500
1982	300	2700	3700	4800	4100	2200
2015	300	2700	5100	6300	5900	3200
2031	500	4100	6900	7000	7200	3200

Table D-2. Intensity (peak maximum) data for Sample 3.

Temperature (K)	^{102}Pd	^{104}Pd	^{105}Pd	^{106}Pd	^{108}Pd	^{110}Pd
1638	100	400	800	600	500	400
1730	200	700	1100	1300	1200	900
1805	200	900	2600	3400	2800	1500
1838	200	3000	4400	4700	5000	2000
1869	700	4000	8000	9300	8400	3200
1901	700	7100	13100	14000	15000	6900
1929	1400	10100	20600	23500	23000	10200

Table D-3. Intensity (peak maximum) data for Sample 4.

Temperature (K)	^{102}Pd	^{104}Pd	^{105}Pd	^{106}Pd	^{108}Pd	^{110}Pd
1715	500	1000	1100	900	800	400
1737	300	1000	1200	1100	1300	700
1757	300	800	1400	1300	1400	700
1779	200	1600	1600	1800	1400	900
1802	200	1400	2000	2400	2100	1100
1824	300	1500	2200	3100	2400	1000
1844	200	2200	2800	3100	3200	1600
1861	400	2200	3200	3700	2900	1400
1885	500	3000	4000	3800	3700	2000
1910	200	4600	4800	4600	4200	1700

Table D-4. Intensity (peak maximum) data for Sample 5.

Temperature (K)	^{102}Pd	^{104}Pd	^{105}Pd	^{106}Pd	^{108}Pd	^{110}Pd
1684	200	800	900	1200	700	900
1703	100	1100	1200	1100	1000	500
1723	100	1400	1800	1100	1300	600
1743	200	1400	1500	2100	1800	800
1759	300	1400	2700	3000	2400	1700
1786	400	2800	3200	2900	3100	1400
1812	400	2600	3700	3800	3800	1700
1837	400	3000	4700	5000	3800	2300
1858	400	4300	6000	5800	6200	2400
1874	400	3800	5900	6100	6000	2400

Table D-5. Intensity (peak maximum) data for Sample 6.

Temperature (K)	^{102}Pd	^{104}Pd	^{105}Pd	^{106}Pd	^{108}Pd	^{110}Pd
1661	100	600	300	300	300	200
1686	100	500	400	500	400	300
1705	100	700	500	400	600	400
1734	100	800	900	800	600	200
1760	300	700	1000	700	700	300
1787	100	1000	1600	1300	1400	600
1813	200	1500	2300	2200	1500	1100
1833	100	1800	2200	2400	1600	800
1853	100	2200	2800	3000	3200	1300
1875	400	2300	3900	3600	2800	1900

Table D-6. Intensity (peak maximum) data for Sample 7.

Temperature (K)	^{102}Pd	^{104}Pd	^{105}Pd	^{106}Pd	^{108}Pd	^{110}Pd
1793	100	700	500	700	800	300
1827	100	700	900	1200	1200	500
1857	100	800	1100	2100	1300	700
1886	200	1200	2000	1600	1700	800
1916	200	1000	2300	2100	2800	1300
1944	200	1500	2300	2700	2800	1400
1962	200	1800	2300	2700	2600	1400

Table D-7. Intensity (peak maximum) data for Sample 8.

Temperature (K)	^{102}Pd	^{104}Pd	^{105}Pd	^{106}Pd	^{108}Pd	^{110}Pd
1687	100	600	400	700	600	400
1713	100	500	900	700	400	500
1738	100	700	1200	800	800	400
1761	200	700	1100	1300	1300	400
1782	100	1000	1600	1500	1700	800
1806	100	1300	1700	1800	2000	1100
1829	100	1700	1800	2400	1900	900
1850	300	2800	2600	3400	3000	1100
1869	400	1900	3500	4000	3300	1400
1892	300	2600	4900	4500	4000	1300

APPENDIX E - ORIGINAL EVALUATION OF ZR-SN PHASE DIAGRAM

The cladding reaction with H_2O to generate a steam-hydrogen gas mixture is almost as important as the reaction of the gas mixture with the fuel in the totality of a fission product release code. Unfortunately, a thermodynamic model for the Zirconium-Tin binary system, that is consistent with the latest phase diagram, does not exist[1]. Therefore a modelling of the Zr-Sn phase diagram was undertaken, the results of which are shown in Figure E-1.

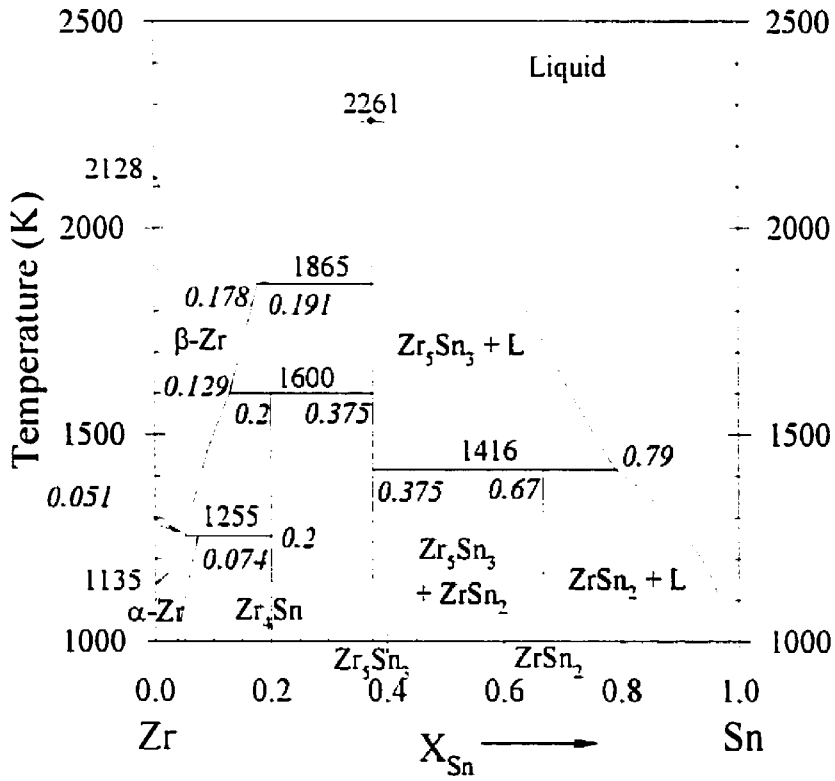

Figure E-1. The Evaluated Zr-Sn equilibrium phase diagram.

For the pure components, the following Gibbs energy expressions were used:

$$G_{Zr}^{\circ(Liquid \rightarrow Liquid)} = 0 \text{ J/mol (reference phase)} \qquad \textbf{(E.1)}$$

$$G_{Zr}^{\circ(Liquid \rightarrow \alpha - solid)} = -24967 + 13.384T \text{ J/mol} \qquad \textbf{(E.2)}$$

$$G_{Zr}^{\circ(Liquid\rightarrow\beta-solid)} = -20950 + 9.845T \quad \textbf{(E.3)}$$

$$G_{Sn}^{\circ(Liquid\rightarrow Liquid)} = 0 \text{ J/ mol (reference phase)} \quad \textbf{(E.4)}$$

$$G_{Sn}^{\circ(Liquid\rightarrow Sn\text{-}Solid)} = -7029.1 + 13.917T \text{ J/mol} \quad \textbf{(E.5)}$$

$$G_{Sn}^{\circ(Liquid\rightarrow\alpha-Zr\ solid)} = 4578.69 - 13.917T \text{ J/mol (hypothetical transition)} \quad \textbf{(E.6)}$$

$$G_{Zr}^{\circ(Liquid\rightarrow\beta-Zr\ solid)} = -4620.44 + 13.917T \text{ J/mol (hypothetical transition)} \quad \textbf{(E.7)}$$

The excess properties of mixing for the solution phases in the Zr-Sn system are:

$$\Delta G_{Liquid}^{E} = X_{Zr}X_{Sn}\left[-120920 + 75658X_{Sn}\right] \text{ J/mol} \quad \textbf{(E.8)}$$

$$\Delta G_{\alpha-Zr}^{E} = X_{Zr}X_{Sn}\left[-80170\right] \text{ J/mol (for } X_{Sn} < 0.1) \quad \textbf{(E.9)}$$

$$\Delta G_{\beta-Zr}^{E} = X_{Zr}X_{Sn}\left[-63000 - 30.08T\right] \text{ J/mol (for } X_{Sn} < 0.2) \quad \textbf{(E.10)}$$

For the Zr_4Sn, Zr_5Sn_3, and $ZrSn_2$, the Gibbs energy expressions used were:

$$\Delta G_{Zr_4Sn}^{\circ} = -41940 + 10.1T \text{ J/mol (per } \tfrac{1}{5} \text{ mol of } Zr_4Sn) \quad \textbf{(E.11)}$$

$$\Delta G_{Zr_5Sn_3}^{\circ} = -56737 + 10T \text{ J/mol (per } \tfrac{1}{8} \text{ mol of } Zr_5Sn_3) \quad \textbf{(E.12)}$$

$$\Delta G_{ZrSn_2}^{\circ} = -33951.4 + 7T \text{ J/mol (per } \tfrac{1}{3} \text{ mol of } Zr_5Sn_3) \quad \textbf{(E.13)}$$

Note that equations **(E.11)**, **(E.12)**, and **(E.13)** refer to zirconium and tin in their liquid states (i.e, $Zr_{(liq)}$ and $Sn_{(liq)}$). These equations were derived in a manner that provided peritectoid reactions at 1600K and 1255K, and a peritectic reaction at 1416K.

A detailed view of the Zr-rich side of the diagram is shown in Figure E-2.

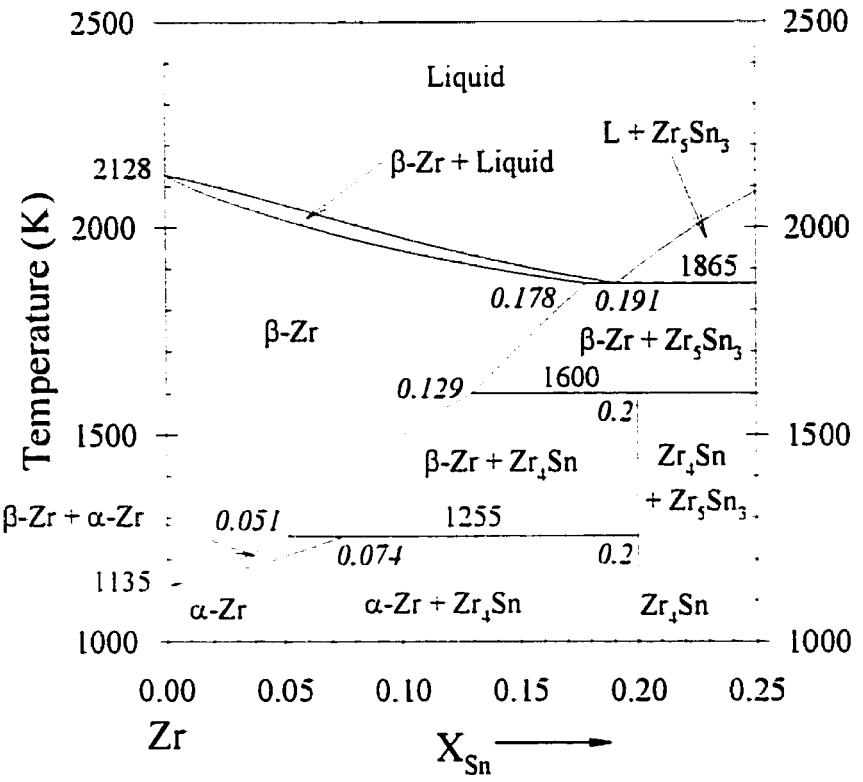

Figure E-2. A detailed section of the Zr-Sn phase diagram at the Zr-rich side.

For comparison the Zr-Sn phase diagram from the assessment of Abriata et al.[1] is shown in Figure E-3. It can be seen that the agreement along the β-Zr solvus is within the experimental uncertainty of ±0.3at.%Sn at the ends of the lowest tie line (i.e., 1255K or 982°C), and within the scatter of the experimental data for the tie lines at higher temperatures, where the data is scarce.

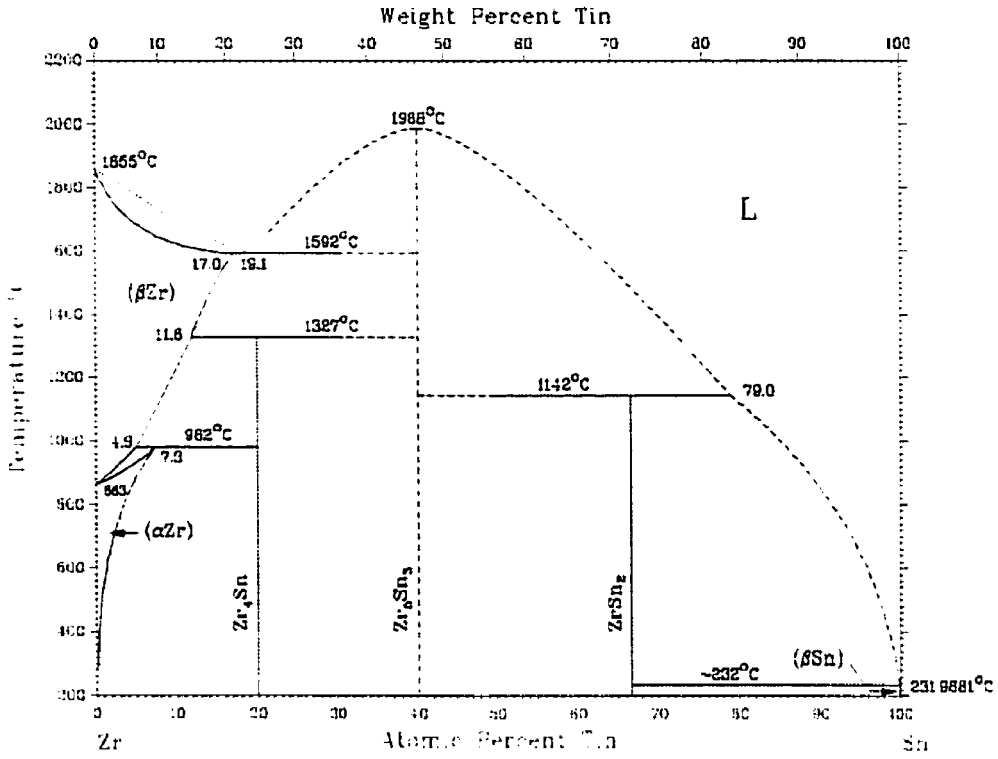

Figure E-3. The Zr-Sn phase diagram at the Zr-rich side.

Because this system describes the principal components of Zircalloy, the solution properties that have been determined for α-Zr and β-Zr can now be used to perform a Gibbs energy minimization calculation for Zircalloy reacting with water.

$$Zircalloy + H_2O \xrightleftharpoons{elevated\ T} products + H_2 \qquad \textbf{(E.14)}$$

Reference for Appendix E

1. J.P. Abriata, J.C. Bolcich, and D. Arias, "The Sn-Zr (Tin –Zirconium) System", *Bulletin of Alloy Phase Diagrams*, **4** [2] (1983), 147-154.